

INFORMATION TO USERS

This manuscript has been reproduced from the microfilm master. UMI films the text directly from the original or copy submitted. Thus, some thesis and dissertation copies are in typewriter face, while others may be from any type of computer printer.

The quality of this reproduction is dependent upon the quality of the copy submitted. Broken or indistinct print, colored or poor quality illustrations and photographs, print bleedthrough, substandard margins, and improper alignment can adversely affect reproduction.

In the unlikely event that the author did not send UMI a complete manuscript and there are missing pages, these will be noted. Also, if unauthorized copyright material had to be removed, a note will indicate the deletion.

Oversize materials (e.g., maps, drawings, charts) are reproduced by sectioning the original, beginning at the upper left-hand corner and continuing from left to right in equal sections with small overlaps. Each original is also photographed in one exposure and is included in reduced form at the back of the book.

Photographs included in the original manuscript have been reproduced xerographically in this copy. Higher quality 6" x 9" black and white photographic prints are available for any photographs or illustrations appearing in this copy for an additional charge. Contact UMI directly to order.

U·M·I

University Microfilms International
A Bell & Howell Information Company
300 North Zeeb Road, Ann Arbor, MI 48106-1346 USA
313/761-4700 800/521-0600

Order Number 9500099

The motion of deformable drops and bubbles at low Reynolds numbers: Applications to selected problems in geology and geophysics

Manga, Michael, Ph.D.

Harvard University, 1994

Copyright ©1994 by Manga, Michael. All rights reserved.

U·M·I

**300 N. Zeeb Rd.
Ann Arbor, MI 48106**

HARVARD UNIVERSITY
THE GRADUATE SCHOOL OF ARTS AND SCIENCES



THESIS ACCEPTANCE CERTIFICATE

The undersigned, appointed by the

Division

Department Earth and Planetary Sciences

Committee

have examined a thesis entitled

"The motion of deformable drops and bubbles:
Applications to selected problems in geology
and geophysics"

presented by Michael Manga

candidate for the degree of Doctor of Philosophy and hereby
certify that it is worthy of acceptance.

Signature *[Signature]*

Typed name Prof. Richard J. O'Connell

Signature *[Signature]*

Typed name Prof. Howard A. Stone (DAS)

Signature *[Signature]*

Typed name Ass't. Prof. Carl B. Agge

Ass't. Prof. Göran A. Ekström

Date May 13, 1994

The motion of deformable drops and bubbles at
low Reynolds numbers: Applications to selected
problems in geology and geophysics

A thesis presented

by

Michael Manga

to

The Department of Earth and Planetary Sciences

in partial fulfillment of the requirements

for the degree of

Doctor of Philosophy

in the subject of

Geophysics

Harvard University

Cambridge, Massachusetts

May, 1994

©1994 by Michael Manga
All rights reserved.

Abstract

Many geological and geophysical processes may be characterized by low Reynolds number multiphase fluid flows. This thesis focuses on the dynamics of deformable drops and bubbles in multiphase fluid systems. Specifically, several model flow problems are considered: the interactions of buoyant drops and bubbles in suspensions, the motion of drops and bubbles through fluid-fluid interfaces, and the deformation of buoyant volumes of fluid in externally-imposed flows. A combination of numerical calculations, laboratory experimental results and analytical methods are used to study the model flow problems.

Free-boundary problems of interface deformation in Stokes flows are solved numerically using the boundary integral method for axisymmetric, two-dimensional and three-dimensional geometries. Boundary integral equations of the second kind involving only the unknown interfacial velocities are presented for problems with multiple fluid-fluid interfaces. Laboratory experiments are presented for two bubbles interactions, and the motion of particles through fluid-fluid interfaces. The experimental results for bubble interactions are used to develop a model for coalescence in suspensions; the model is then used in population dynamics simulations. Analytical results for the far-field interactions of deformable drops are determined using a combination of the method of reflections, domain perturbation methods and the Lorentz reciprocal theorem.

Geological applications considered in this thesis include the interaction of bubbles in magmas and lavas, the ascent of mantle plume heads in a compositionally layered Earth, the stability of continental roots, the entrainment of the D" layer at the base

of the mantle by a convecting mantle, and the formation and evolution of Venusian coronae and highlands.

Bubble deformation leads to a greatly enhanced rate of coalescence in magmas and lavas if the bubbles have radii greater than a few millimeters. An instability is predicted to occur in suspensions of deformable bubbles which will result in spatial variations of bubble concentrations. Plume heads passing from the lower mantle into a less viscous upper mantle become extended vertically and develop a cylindrical geometry. Continental roots must be several orders of magnitude more viscous than the surrounding mantle (in order not to sink, spread or be entrained). If D'' is approximately 2-3% more dense than the lower mantle, it is possible that D'' is not entrained into the convecting mantle (due to compositional buoyancy) but may still become thermally unstable and form thermal plumes. The surface expression of rising and spreading plume heads or diapirs is consistent with many features associated with coronae on Venus. The surface expression of crustal thickening above downwellings, notably the plateau-shaped topography and pattern of surface stresses, is characteristic of many of the plateau-shaped highlands on Venus. Variations of the thickness of the lithosphere, associated with ocean-continent boundaries, results in large-amplitude and short-wavelength deviatoric stresses and dynamic topography near the ocean-continent boundary.

Acknowledgements

During the last several years I have been fortunate to be supported by many people and resources. I would like to thank

Howard Stone for an education;

Rick O'Connell for ideas and opportunities;

Carl Agee, Jeremy Bloxham and Göran Ekström for interesting classes and discussions;

Lorraine Tringali and Joan Donahue for invaluable assistance;

The fluid mechanics group: John Bush, Steve Lucas, Gareth McKinley, Steve Spiegel and John Tanzosh; Jeremy's postdocs: Mike Bergman, Wei-jia Kuang and Martin St. Pierre; and my colleagues in geophysics: Joe Durek, Carl Gable, Richard Holme, Dorothy Koch, Mark Linker, Jeff Love, Lucia Lovison, Peggy Shannon, Bernhard Steinberger, Wei-jia Su, Winston Tao and Stephen Zatzman, for support;

Harvard University for its excellent libraries;

Joe Rice for assisting with the experiments; Karin Riley and Jamie Billett for assisting with the photography;

The Harvard undergraduates in my sections for inspiration and motivation;

Jafar Arkani-Hamed for an introduction to research in science;

My family for encouragement;

Susan for a sense of humour, and patience.

Contents

1	Introduction	1
1.1	Governing equations	3
1.1.1	Boundary conditions	3
1.1.2	Further approximations and assumptions	6
1.2	Free-boundary problems	7
1.2.1	Integral representation of Stokes equations	7
1.2.2	Integral equations for problems with one and two deformable fluid-fluid interfaces	9
1.3	Translation of a single deformable drop in an unbounded fluid at low Reynolds number	10
1.4	Thesis overview	15
1.4.1	Part I. Buoyancy-driven drops in suspensions	15
1.4.2	Part II. The motion of drops through fluid interfaces	19
1.4.3	Part III. Dynamics of continental roots and mantle dregs and the formation of the Venusian highlands	20
2	Interaction of two axisymmetric buoyancy-driven drops	22
2.1	Introduction	22
2.2	Problem formulation	26
2.3	On-axis Interaction of Axisymmetric Drops	28
2.3.1	Effect of interfacial tension	29
2.3.2	The style of film drainage	31

2.3.3	Rate of film drainage and dimple formation	32
2.3.4	History effects	36
2.3.5	Comparison with analytical results	37
2.3.6	Cusps and tails	40
2.4	Concluding remarks	41
3	Interaction and stability of offset drops	42
3.1	Introduction	42
3.2	Interaction of offset bubbles: Experimental results	44
3.3	Flow-induced deformation leading to alignment	46
3.4	Numerical results: Two-dimensional calculations	48
3.5	Numerical results: Three-dimensional calculations	53
3.5.1	Effects of interfacial tension (Bond number)	56
3.5.2	Effects of horizontal offset	57
3.5.3	Effects of relative drop size	59
3.6	Concluding remarks	60
4	Long range drop interactions	61
4.1	Scaling analysis: An overview of drop alignment by flow-induced shape changes	61
4.1.1	Translation of a single drop in an unbounded fluid	62
4.1.2	Method of reflections	63
4.1.3	Shape distortion	63
4.1.4	Quasi-steady assumption	64
4.2	Migration of spherical drops: Application of the method of reflections	65
4.3	Shape calculation	67
4.4	Translational velocity from the Reciprocal theorem	68
4.5	Concluding remarks	72
5	Three drops, four drops, clouds of drops and suspensions	74
5.1	Introduction	75

5.2	Three drops and four drops	76
5.2.1	Three drops	77
5.2.2	Four drops	80
5.3	Clouds of drops	80
5.4	Coalescence in suspensions	81
5.4.1	Collision-frequency function	82
5.4.2	The Smoluchowski model	84
5.5	Monodisperse suspensions	84
5.6	Collision-frequency in polydisperse suspensions	87
5.6.1	Experimental apparatus and procedure	87
5.6.2	Experimental results	89
5.7	Population dynamics simulations	95
5.7.1	The population dynamics model	96
5.7.2	Isotropic polydisperse suspensions with a homogeneous concen- tration distribution	97
5.7.3	“Sedimentation” and separation in a polydisperse suspension .	101
5.7.4	Limitations of the population dynamics simulations	105
5.8	Concluding remarks	105
6	Interactions between bubbles in magmas and lavas: Effects of bubble deformation	107
6.1	Introduction	108
6.2	Applications to bubbles in magmas and lavas	109
6.2.1	The formation of instabilities of bubble concentration	110
6.2.2	Applications to volcanic systems	112
6.2.3	Application to bubbles in lava flows	114
6.3	Concluding remarks	117
7	The low Reynolds number motion of drops, bubbles and rigid par- ticles through fluid-fluid interfaces	119

7.1	Introduction	120
7.2	Problem formulation	124
7.3	Results	126
7.3.1	Drop and interface deformation	126
7.3.2	Mode of drop deformation	130
7.3.3	Rise speed	133
7.3.4	Drop surface area	135
7.3.5	Gap thickness	136
7.4	Experimental results	138
7.4.1	Experimental apparatus	139
7.4.2	A single bubble passing through an interface	140
7.4.3	Multiple particles passing through interfaces	144
7.4.4	The motion of two vertically aligned bubbles through a fluid- fluid interface	150
7.5	The motion of slender bodies through a fluid-fluid interface	150
7.5.1	The motion of a slender body passing into a less viscous fluid	151
7.5.2	The motion of a slender body passing into a more viscous fluid	152
7.6	Concluding remarks	153
8	The Interaction of Plume Heads With Compositional Discontinuities in the Earth's Mantle	156
8.1	Introduction	157
8.2	Problem Formulation	159
8.3	Results	162
8.3.1	Plume head moving away from a deformable interface	162
8.3.2	Plume head passing through an interface	165
8.3.3	Plume head approaching the surface of the Earth	167
8.4	Discussion	172
8.5	Concluding remarks	177

9	Deformation of continental roots, the formation of Venusian highlands and “dregs” at the base of the mantle	178
9.1	Introduction	179
9.2	Problem formulation	180
9.3	Continental roots	181
9.3.1	The tectosphere hypothesis	181
9.3.2	Effect of viscosity ratio	183
9.3.3	Remarks	184
9.4	Highlands and coronae on Venus	186
9.4.1	Crustal thickening above a downwelling	186
9.4.2	Comparison with ascending plume models	190
9.4.3	Remarks	190
9.5	“Dregs” at the base of the mantle	193
9.5.1	Dynamics of mantle “dregs”	194
9.5.2	Scaling analysis for the steady-state radius of dregs	196
9.5.3	Remarks	198
A	The Boundary integral method (BIM)	200
A.1	Introduction	201
A.2	Analytic formulation	202
A.2.1	Equations and boundary conditions	204
A.2.2	Green’s functions	206
A.2.3	Integral representation of Stokes equations	208
A.2.4	Integral equation for a fluid-fluid interface	210
A.2.5	Application to a rigid particle near a fluid-fluid interface . . .	212
A.2.6	Generalization to multiple fluid-fluid interfaces	214
A.3	Numerical implementation	216
A.3.1	Interface description	217
A.3.2	Calculation of the interfacial velocity (solution of the integral equation)	218

A.3.3	Interface evolution	218
A.3.4	Miscellaneous remarks	219
A.4	Summary	220
B	Axisymmetric problems	221
C	Three-dimensional problems	223
C.1	Numerical solution of the integral equations	224
C.1.1	Numerical mesh	224
C.1.2	Integration method	226
C.1.3	Calculating curvature and normal vectors	227
D	The reciprocal theorem applied to the translation of nonspherical drops	233
D.1	Perturbation solution for the translation of a non-spherical drop . . .	233
D.2	Application of the Reciprocal theorem	236
E	The effect of radial and lateral viscosity variations near the Earth's surface on the surface expression of mantle flow	238
E.1	Radial viscosity variations	238
E.2	Lateral viscosity variations: Variations of lithosphere thickness	241
	Bibliography	245

List of Figures

1.1	Geometry of the generic two fluid problem	4
1.2	Geometry of one and two interface free-boundary problems	9
1.3	Deformation of a single buoyant drop: Effect of initial shape	11
1.4	Streamlines for nonspherical buoyant drops	12
1.5	Deformation of a single buoyant drop: Effect of interfacial tension on initially oblate and prolate drops	13
1.6	Deformation of a single buoyant drop: Effect of viscosity ratio	14
1.7	Drop geometries studied in the thesis	15
1.8	Geometries studied for the motion of a drop normal to a fluid-fluid interface	18
1.9	Illustration of features of mantle dynamics	20
2.1	Two vertically aligned air bubbles in corn syrup	24
2.2	Geometry of two drop problem	26
2.3	Effect of interfacial tension	30
2.4	Effect of a point force on drop deformation	32
2.5	Three modes of film drainage	33
2.6	Effect of Bond number on film drainage	34
2.7	Effect of viscosity ratio on film drainage	35
2.8	Dimple formation	37
2.9	Effect of initial drop separation distance	38
2.10	Comparison with analytical results	39

3.1	Alignment of offset bubbles in corn syrup	45
3.2	Illustration of the interaction between spherical drops	46
3.3	Illustration of the alignment of initially offset drops	47
3.4	Streamlines calculated for translating drops	49
3.5	Effect of horizontal offset for 2D drops	50
3.6	Effect of Bond number and viscosity ratio for offset 2D drops	51
3.7	Effect of Bond number on the entrainment of offset 2D drops	52
3.8	Effect of Bond number on the alignment of offset 3D drops	54
3.9	Trajectories of offset 3D drops: effect of interfacial tension	55
3.10	Effect of horizontal offset on the alignment of offset 3D drops	56
3.11	Trajectories of offset 3D drops: effect of interfacial tension	57
3.12	Effect of relative drop size on the alignment of offset 3D drops	58
3.13	Trajectories of 3D drops: effect of relative drop size	59
4.1	Geometry of two drop problem studied analytically	62
4.2	The function $c(\lambda)$	70
4.3	Trajectories of bubbles computed from the analytical far-field results	71
4.4	Interaction between drops in thermocapillary motion	73
5.1	Three three-dimensional drops	77
5.2	Trajectories of three three-dimensional drops	78
5.3	Interaction of four three-dimensional drops	79
5.4	Collection radius of interacting drops	82
5.5	Interaction of two drops in a suspension	85
5.6	Interaction of two equal-size drops	86
5.7	Experimental apparatus for two bubble experiments	90
5.8	Three modes of bubble interactions	91
5.8	Three modes of bubble interactions (continued)	92
5.9	Capture cross-section of deformable bubbles	93
5.10	Coalescence rate of deformable bubbles	95

5.11	Bubble-size distribution in an isotropic homogeneous suspension . . .	98
5.12	Average bubble volume as a function of time in isotropic homogeneous suspension	99
5.13	Average bubble volume and volume flux of bubbles emerging from the top of a tank as a function of time in for different Bond numbers . . .	100
5.14	Volume fraction distribution within a tank	101
5.15	Bubble-size distribution at the top of a tank	102
5.16	Average bubble volume and volume flux of bubbles at the top of a tank as a function of time for different tank heights	103
6.1	The formation of concentration instabilities	111
6.2	Bubble interaction in volcanic conduits	113
6.3	Vesicle distribution in solidified lavas	115
7.1	Different features characteristic of the motion of bubbles through fluid- fluid interfaces	123
7.2	Geometry for the problem of a drop passing through an interface . . .	124
7.3	Effect of drop viscosity ratio	127
7.4	Effect of changing ratio of upper to lower fluid viscosity	128
7.5	Effect of drop Bond number	129
7.6	Effect of interface Bond number	130
7.7	Mode of deformation	131
7.8	Mode of deformation and surface area	132
7.9	Rise speed	134
7.10	Surface area	135
7.11	Gap thickness	137
7.12	Photographs of an air bubble passing from a higher to lower viscosity fluid	141
7.13	Photographs of an air bubble passing from a lower to higher viscosity fluid	142

7.14	Photographs of a sphere passing from a higher to lower viscosity fluid	143
7.15	Streamlines for a drop passing through an interface	145
7.16	Photographs of two spheres passing from a higher to lower viscosity fluid	146
7.17	Photographs of spheres passing from a higher to lower viscosity fluid .	147
7.18	Photographs of two spheres passing from a lower to higher viscosity fluid	148
7.19	Photographs of two vertically aligned bubbles passing from a lower to higher viscosity fluid	149
7.20	Slender-body geometry	151
7.21	Photographs of a slender passing from a higher to lower viscosity fluid	152
7.22	Photographs of a slender body passing from a lower to higher viscosity fluid	153
8.1	Problem geometry: Ascending plume head	160
8.2	Plume attached to a free-surface	163
8.3	Plume head moving away from an interface	164
8.4	Effect of upper to lower mantle viscosity ratio on an ascending plume head	166
8.5	Effect of plume to lower mantle viscosity ratio	167
8.6	Plume approaching the surface of the Earth	168
8.7	Cross-sections of the surface topography produced by a spreading plume head	169
8.8	Evolution of the surface topography produced by a spreading plume head	170
8.9	Surface deviatoric stresses produced by a spreading plume head . . .	171
9.1	Model geometry and properties	181
9.2	S-wave heterogeneity in the upper mantle	182
9.3	Rate of deformation of a buoyant blob	184
9.4	Thickening crust above a downwelling: streamlines	187
9.5	Thickening crust above a downwelling: surface stresses	188

9.6	Pattern of surface deformation above a downwelling	189
9.7	Topography of a thickened crust above a downwelling	190
9.8	Stresses produced by a rising plume head	191
9.9	Pattern of surface deformation produced by a rising plume head . . .	192
9.10	Mantle dregs: Evolution to a steady shape	195
9.11	Entrainment of mantle dregs: Streamlines	196
9.12	Steady shape of mantle dregs as a function of the entrainment parameter	197
A.1	Summary of free-boundary problems studied using the boundary inte- gral method	203
A.2	Translating and deforming drop in an unbounded fluid	205
A.3	Geometry used to define the fundamental singular solution to Stokes equations	207
A.4	Sphere and drop approaching a fluid-fluid interface	213
C.1	Numerical mesh	225
C.2	Test: Interaction of two axisymmetric drops	228
C.3	Calculation of interfacial curvature	229
C.4	Test: Relaxation of a prolate drop	231
E.1	Model geometry used to study radial viscosity variations	239
E.2	Effect of radial viscosity variations on surface topography	240
E.3	Effect of radial viscosity variations on the geoid-topography ratio . .	241
E.4	Model geometry used to study variations of lithospheric thickness . .	242
E.5	Effect of variations of lithosphere thickness on surface topography and surface stresses	243

List of Tables

7.1	Tank geometries used in experiments	139
A.1	Selected Green's functions for Stokes flow	208
C.1	Gaussian weights and abscissas for integration	226
C.2	Comparison of steady drop deformation in a shear flow for $\lambda = 1$. . .	230

Chapter 1

Introduction

Many processes in geology and geodynamics involve, or may be characterized by, the motion of fluids. Some geological processes, such as the coalescence of bubbles in lavas, involve more than one fluid phase. In the case of bubbles in a lava flow, the two phases are the molten rock and the gas bubbles. Flows involving two or more fluid phases are referred to as multiphase flows. In many geological flows, for example flowing lavas or problems in mantle dynamics, viscous effects are very important. Qualitatively, viscously dominated flows occur where *(i)* fluids have very high viscosities, *(ii)* the characteristic length scales are small, *(iii)* velocities are small, or *(iv)* some combination of *(i)*-*(iii)*. Such flows for Newtonian fluids are described by the equations of low Reynolds number hydrodynamics. The low Reynolds number assumption requires that viscous forces are large compared to inertial forces. Consider a particle with characteristic size a translating with velocity U in a fluid with viscosity μ and density ρ . The low Reynolds number assumption requires that

$$\mathcal{R} = \frac{\rho U a}{\mu} \ll 1, \quad (1.1)$$

an approximation typically valid when the length scale is small (in many biological fluid processes and chemical engineering applications), or the viscosity is very large (in many Earth Science applications), or flows are slow (low Reynolds number flows are often called “creeping” flows).

We consider a number of low Reynolds number multiphase flow problems and focus on limits in which substantial deformation of fluid-fluid interfaces occurs. The dynamics of interface deformation in low Reynolds number flows are of interest in a wide variety of fields including chemical and petroleum engineering, solid-earth geophysics, hydrology, and biology. Typical applications span an immense range of length scales from microns to hundreds of kilometers: biological studies of cell deformation; chemical engineering studies of coalescence, flotation, coating flows and the dynamics of thin films; and geophysical studies of mantle plumes, lithospheric slabs and bubbles in magmas and lavas.

In this thesis we study flows driven by density variations, referred to hereafter as buoyancy-driven flows. In particular we will focus on three model problems:

1. the buoyancy-driven motion and interaction of deformable drops and bubbles
2. the motion of drops, bubbles and rigid particles normal to a deformable fluid-fluid interface, and
3. the dynamics of drops attached to a free-surface.

Geological applications of the three model problems include bubble dynamics in magmas and lavas, bubble and crystal separation in stratified magma chambers, the ascent of mantle plume heads in the Earth's mantle, the formation of coronae and highlands on Venus, and the dynamics of continental roots and mantle dregs. We employ a combination of numerical, analytical and experimental methods in our studies.

We begin this chapter with a discussion of the governing equations and then end this chapter with a brief overview of the problems and applications discussed in the remaining chapters of this thesis.

1.1 Governing equations

A point-wise statement of a balance of linear momentum (Newton's second law) for a Newtonian fluid gives rise to the Navier-Stokes equations

$$\rho \left[\frac{\partial \mathbf{u}}{\partial t} + \mathbf{u} \cdot \nabla \mathbf{u} \right] = -\nabla p + \mu \nabla^2 \mathbf{u} + \rho \mathbf{g}, \quad (1.2)$$

where ρ is the fluid density, μ is the fluid viscosity, p is the pressure, \mathbf{u} is the fluid velocity and \mathbf{g} is the gravitational acceleration. Conservation of mass gives rise to the continuity equation

$$\frac{\partial \rho}{\partial t} + \nabla \cdot (\rho \mathbf{u}) = 0. \quad (1.3)$$

For the low Reynolds number limit, in which viscous forces, the right-hand side of equation (1.2), dominate over inertial forces, the left-hand side of equation (1.2), and for incompressible flows, the Navier-Stokes and continuity equations simplify to the Stokes equations

$$\nabla \cdot \mathbf{T} = -\nabla p + \mu \nabla^2 \mathbf{u} = \mathbf{0} \quad (1.4)$$

and

$$\nabla \cdot \mathbf{u} = 0. \quad (1.5)$$

The stress tensor \mathbf{T} in the Stokes equations (1.4) has been defined to include hydrostatic pressure variations, and thus is divergence free,

$$\mathbf{T} = -p\mathbf{I} + \mu(\nabla \mathbf{u} + \nabla \mathbf{u}^T) + \rho(\mathbf{g} \cdot \mathbf{x})\mathbf{I}. \quad (1.6)$$

With the definition of the stress tensor (1.6), the body force will appear in the boundary conditions involving pressure.

1.1.1 Boundary conditions

We are concerned with the evolution of deformable fluid-fluid interfaces. Consider a fluid-fluid interface, denoted by S , separating fluids 1 and fluids 2 with viscosities μ_1 and μ_2 and densities ρ_1 and ρ_2 respectively (see figure 1.1).

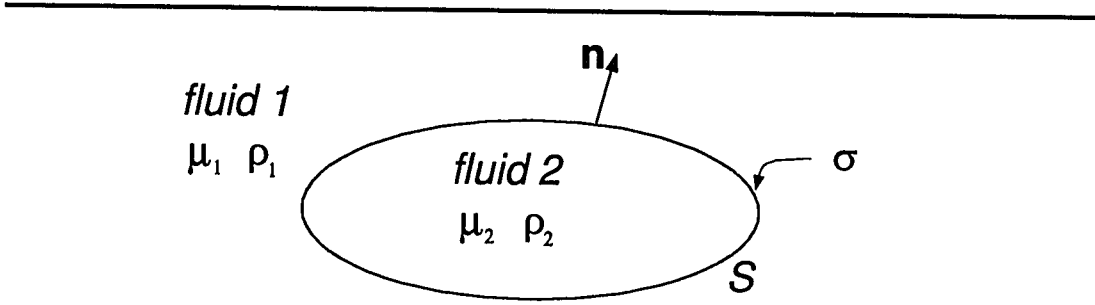


Figure 1.1: Geometry of the generic two fluid problem. Fluid 1 has density ρ_1 and viscosity μ_1 , and fluid 2 has density ρ_2 and viscosity μ_2 . The two fluids are separated by a fluid-fluid interface S , which is characterized by the interfacial tension σ .

(a) *Boundary conditions on velocity*

Fluid velocities are continuous across fluid interfaces

$$\mathbf{u}_1(\mathbf{x}) = \mathbf{u}_2(\mathbf{x}) \quad \mathbf{x} \in S, \quad (1.7)$$

where \mathbf{x} is a position vector. Additionally, there is a boundary condition on velocity far away from the interface,

$$\mathbf{u}(\mathbf{x}) = \mathbf{0} \quad \text{as } |\mathbf{x}| \rightarrow \infty \quad (1.8)$$

if the ambient fluid is at rest far away from the fluid interface, or

$$\mathbf{u}(\mathbf{x}) = \mathbf{u}^\infty(\mathbf{x}) \quad \text{as } |\mathbf{x}| \rightarrow \infty \quad (1.9)$$

if there is an externally-imposed flow $\mathbf{u}^\infty(\mathbf{x})$.

(b) *Boundary conditions on stress*

The stress jump, $[\mathbf{n} \cdot \mathbf{T}]$, across the fluid interface is given by

$$[\mathbf{n} \cdot \mathbf{T}] \equiv \mathbf{n} \cdot \mathbf{T}_1 - \mathbf{n} \cdot \mathbf{T}_2 = \sigma (\nabla_s \cdot \mathbf{n})\mathbf{n} - \nabla_s \sigma - (\rho_2 - \rho_1)\mathbf{g} \cdot \mathbf{x}\mathbf{n} \quad \text{on } S. \quad (1.10)$$

Here σ denotes the interfacial tension, $\nabla_s = (\mathbf{I} - \mathbf{n}\mathbf{n}) \cdot \nabla$ is the gradient operator tangent to the interface, $\nabla_s \cdot \mathbf{n}$ is the mean curvature of the interface, and \mathbf{n} is a unit

normal vector directed from fluid 2 into fluid 1 (see figure 1.1). Since the body forces are incorporated into the definition of the stress tensor, equation (1.6), the buoyancy forces appear in the boundary conditions involving stress, equation (1.10).

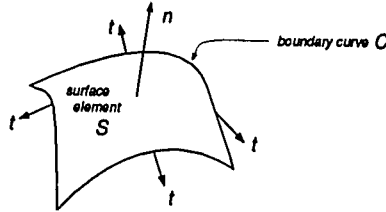
The contribution to the stress jump from interfacial tension stresses *normal* to the interface is given by $\sigma (\nabla_s \cdot \mathbf{n})\mathbf{n}$. If there are interfacial tension variations, produced as a result of variations of surfactant concentration or temperature variations, there is a contribution to the stress jump *tangent* to the interface of $\nabla_s \sigma$.¹

The stress jump may be nondimensionalized by choosing $U = \Delta \rho g a^2 / \mu_1$ and a as characteristic velocity and length scales, respectively, so that the characteristic stress is $\mu_1 U / a$ and the characteristic advective timescale is $\mu_1 / \Delta \rho g a$. The dimensionless boundary condition for stress (if there are no interfacial tension variations) is given

¹In a macroscopic description, whereby the interface is treated as a two-dimensional surface separating two distinct bulk fluid, the interfacial tension σ acts as a tensile force per unit length of a curve in the interface. In the absence of buoyancy forces, a local force balance over a surface element S bounded by curve C (the contour C is traversed counterclockwise) requires that

$$\int_S (\mathbf{n} \cdot \mathbf{T}_1 - \mathbf{n} \cdot \mathbf{T}_2) dS = - \oint_C \sigma \mathbf{t} dl, \quad (1.11)$$

where \mathbf{n} is a unit normal vector outward from S , and \mathbf{t} is a unit vector tangent to S and perpendicular to the bounding curve C (see the sketch below).



Applying Stokes theorem (see Leal [1992])

$$\oint_C \sigma \mathbf{t} dl = \int_S \nabla_s \sigma dS - \int_S \sigma \mathbf{n} \nabla_s \cdot \mathbf{n} dS. \quad (1.12)$$

Thus the local boundary condition on the stress jump (neglecting buoyancy forces) becomes

$$\mathbf{n} \cdot \mathbf{T}_1 - \mathbf{n} \cdot \mathbf{T}_2 = \sigma (\nabla_s \cdot \mathbf{n})\mathbf{n} - \nabla_s \sigma \text{ on } S. \quad (1.13)$$

by

$$\mathbf{n} \cdot \hat{\mathbf{T}}_1 - \lambda \mathbf{n} \cdot \hat{\mathbf{T}}_2 = \frac{1}{\mathcal{B}} (\nabla_s \cdot \mathbf{n}) \mathbf{n} - \hat{\mathbf{g}} \cdot \hat{\mathbf{x}} \mathbf{n} \text{ on } S, \quad (1.14)$$

where the $\hat{\cdot}$ is used to denote dimensionless variables, and $\hat{\mathbf{g}}$ is a unit vector in the direction of \mathbf{g} . Two non-dimensional parameters appear: the viscosity ratio

$$\lambda = \frac{\mu_2}{\mu_1} \quad (1.15)$$

and the Bond number

$$\mathcal{B} = \frac{(\rho_2 - \rho_1) g a^2}{\sigma}. \quad (1.16)$$

The Bond number represents the ratio of buoyancy to interfacial tension stresses.

(c) *Kinematic condition*

Additionally, if the interface is deforming, motion of material elements which define the fluid interface satisfies a kinematic constraint which requires that points on the interface remain on the interface for all time; formally, the constraint, expressed from a Lagrangian point of view, is given by

$$\frac{d\mathbf{x}}{dt} = \mathbf{u}(\mathbf{x}) \text{ on } S. \quad (1.17)$$

1.1.2 Further approximations and assumptions

We have already discussed the low Reynolds number approximation which requires that the Reynolds number

$$\mathcal{R} = \frac{\rho U a}{\mu} \ll 1. \quad (1.18)$$

We will further assume that the fluids of interest are homogeneous (constant density and viscosity) in each fluid domain. The Peclet number, which represent the ratio of advection to diffusion must be large in order to neglect diffusive processes which may affect the fluid density and viscosity. Thus, the Peclet number

$$Pe = \frac{U a}{\kappa} \gg 1, \quad (1.19)$$

where U and a are typical velocity and length scales, respectively, and κ is a diffusivity. The diffusivity may be a thermal diffusivity if temperature variations are large, Brownian diffusion if the particles are small, or represent chemical diffusion of, for example, gas from a liquid into a bubble. Furthermore, we will assume that interfacial tension variations and thus Marangoni effects are negligible, *i.e.* $\nabla_s \sigma = 0$.

1.2 Free-boundary problems

The principal difficulty with solving free-boundary problems, problems in which the fluid-fluid interface shown in figure 1.1 is deformable, is that the position of the interface is unknown *a priori* and must be determined as part of the solution to the boundary value problem. Thus, the problem of determining the time-dependent interface shape is inherently nonlinear even though the governing equations of motion, the Stokes equations (1.4-5), are linear.

1.2.1 Integral representation of Stokes equations

The Stokes equations may be solved numerically using the boundary integral method. The method is well established and has been used, for example, to study drop deformation in extensional flows [Rallison & Acrivos 1978; Stone 1994] and the buoyancy-driven motion and stability of translating drops [Koh & Leal 1989; Pozrikidis 1990]. The boundary integral approach involves recasting the Stokes equations, which are differential equations, as integral equations. The resulting integral equations involve only information on fluid interfaces and boundaries if the fluids are assumed to be homogeneous, and thus there is a reduction of the geometric dimension of the numerical problem: a two-dimensional flow problem reduces to one involving one-dimensional line integrals and a three-dimensional problem reduces to one involving two-dimensional surface integrals. In appendix A we derive the basic equations and provide a summary of the application of the boundary integral method to Stokes flow problems.

The Stokes equations (1.4-5) may be recast as integral equations

$$\frac{1}{\mu} \int_S \mathbf{n} \cdot \mathbf{T} \cdot \mathbf{J}(\mathbf{x} - \mathbf{y}) dS_y + \int_S \mathbf{n} \cdot \mathbf{K}(\mathbf{x} - \mathbf{y}) \cdot \mathbf{u} dS_y = \begin{cases} \mathbf{u}(\mathbf{x}) & \mathbf{x} \in V, \\ \frac{1}{2}\mathbf{u}(\mathbf{x}) & \mathbf{x} \in S, \\ \mathbf{0} & \mathbf{x} \notin V. \end{cases} \quad (1.20)$$

where S includes all surfaces bounding the fluid domain V (S is assumed to be a Lyapunov smooth boundary). The kernels \mathbf{J} and \mathbf{K} map a force at \mathbf{y} to the field at position \mathbf{x} in an unbounded three-dimensional domain:

$$\mathbf{J}(\mathbf{x} - \mathbf{y}) = \frac{1}{8\pi} \left(\frac{\mathbf{I}}{|\mathbf{x} - \mathbf{y}|} + \frac{(\mathbf{x} - \mathbf{y})(\mathbf{x} - \mathbf{y})}{|\mathbf{x} - \mathbf{y}|^3} \right) \quad (1.21)$$

and

$$\mathbf{K}(\mathbf{x} - \mathbf{y}) = -\frac{3}{4\pi} \frac{(\mathbf{x} - \mathbf{y})(\mathbf{x} - \mathbf{y})(\mathbf{x} - \mathbf{y})}{|\mathbf{x} - \mathbf{y}|^5}. \quad (1.22)$$

The analogous equation to (1.20) for the pressure is given by,

$$\frac{1}{4\pi} \int_S \mathbf{n} \cdot \mathbf{T} \cdot \frac{(\mathbf{x} - \mathbf{y})}{|\mathbf{x} - \mathbf{y}|^3} dS_y + \frac{\mu}{2\pi} \int_S \mathbf{n} \cdot \nabla \left(\frac{\mathbf{x} - \mathbf{y}}{|\mathbf{x} - \mathbf{y}|^3} \right) \cdot \mathbf{u} dS_y = \begin{cases} p(\mathbf{x}) & \mathbf{x} \in V, \\ \frac{1}{2}p(\mathbf{x}) & \mathbf{x} \in S, \\ 0 & \mathbf{x} \notin V, \end{cases} \quad (1.23)$$

Equations (1.20) and (1.23) for the velocity and pressure, respectively, represent formal integral equation solutions for the velocity and pressure fields $\mathbf{u}(\mathbf{x})$ and $p(\mathbf{x})$ of the generic Stokes flow problem. A more complete discussion of the boundary integral equations is provided in appendix A.

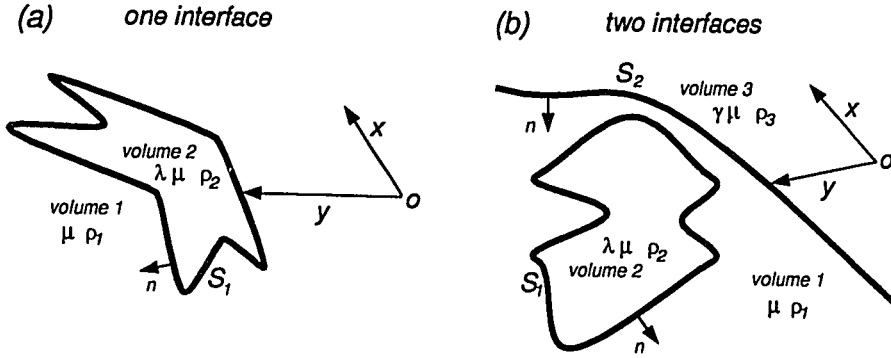


Figure 1.2: Geometry of (a) one and (b) two interface free-boundary problems.

1.2.2 Integral equations for problems with one and two deformable fluid-fluid interfaces

Integral equations of the form of equation (1.20) can be applied to problems involving single and multiple fluid-fluid interfaces (see appendix A).

First, consider a problem with one fluid-fluid interface, denoted S_1 , separating fluids 1 and 2, with viscosities μ and $\lambda\mu$, respectively (see figure 1.2a). The unit normal vector is outward from fluid 2. The integral equations for a single fluid-fluid interface are given by

$$\begin{aligned}
 & -\frac{1}{\mu} \int_{S_1} [\mathbf{n} \cdot \mathbf{T}] \cdot \mathbf{J}(\mathbf{x} - \mathbf{y}) \, dS_y \\
 & - (1 - \lambda) \int_{S_1} \mathbf{n} \cdot \mathbf{K}(\mathbf{x} - \mathbf{y}) \cdot \mathbf{u}_1 \, dS_y = \begin{cases} \mathbf{u}_1(\mathbf{x}) & \mathbf{x} \in V_1, \\ \frac{1 + \lambda}{2} \mathbf{u}_1(\mathbf{x}) & \mathbf{x} \in S_1, \\ \lambda \mathbf{u}_2(\mathbf{x}) & \mathbf{x} \in V_2. \end{cases} \quad (1.24)
 \end{aligned}$$

Second, consider a problem with two fluid-fluid interfaces, denoted S_1 and S_2 , separating fluids 1 and 2, and 1 and 3, respectively (see figure 1.2b). The unit normal vector is an outward normal from fluids 2 and 3 directed into fluid 1. We assume the fluid viscosities are μ , $\lambda\mu$ and $\gamma\mu$ in fluids 1, 2 and 3, respectively. The integral

equations for a pair of fluid-fluid interfaces are given by

$$\begin{aligned}
& -\frac{1}{\mu} \int_{S_1} [\mathbf{n} \cdot \mathbf{T}^I] \cdot \mathbf{J} dS_y - (1-\lambda) \int_{S_1} \mathbf{n} \cdot \mathbf{K} \cdot \mathbf{u}_1 dS_y - \frac{1}{\mu} \int_{S_2} [\mathbf{n} \cdot \mathbf{T}^{II}] \cdot \mathbf{J} dS_y \\
& - (1-\gamma) \int_{S_2} \mathbf{n} \cdot \mathbf{K} \cdot \mathbf{u}_1 dS_y = \begin{cases} \mathbf{u}_1(\mathbf{x}) & \mathbf{x} \in V_1, \\ \lambda \mathbf{u}_2(\mathbf{x}) & \mathbf{x} \in V_2, \\ \gamma \mathbf{u}_3(\mathbf{x}) & \mathbf{x} \in V_3, \\ \frac{1+\lambda}{2} \mathbf{u}_1(\mathbf{x}) & \mathbf{x} \in S_1, \\ \frac{1+\gamma}{2} \mathbf{u}_1(\mathbf{x}) & \mathbf{x} \in S_2, \end{cases} \quad (1.25)
\end{aligned}$$

where $[\mathbf{n} \cdot \mathbf{T}^I]$ and $[\mathbf{n} \cdot \mathbf{T}^{II}]$ are the stress jumps across S_1 and S_2 , respectively, and account for the different density contrasts.

1.3 Translation of a single deformable drop in an unbounded fluid at low Reynolds number

In this thesis we study a number of problems involving the deformation of two or more drops or the motion of a drop through an interface. A useful starting point for this thesis is thus to review the dynamics of a single deformable drop translating in an unbounded fluid. In this section we summarize the numerically observed deformation of translating drops as a function of \mathcal{B} , λ and initial drop shape. Since a spherical drop translating with the Hadamard-Rybczyński velocity

$$\mathbf{U} = -\frac{2(1+\lambda)}{3(2+3\lambda)} \frac{(\rho_2 - \rho_1)a^2}{\mu} \mathbf{g} \quad (1.26)$$

is an exact solution to the Stokes equations and satisfies *all* boundary conditions, then a spherical drop is a steady shape provided the drop is far from all boundaries. However, Kojima, Hinch & Acrivos [1984] presented a stability analysis and some experimental results which demonstrate that a *deformed* drop is unstable to shape perturbations, unstable in the sense that the drop will deform continuously, for

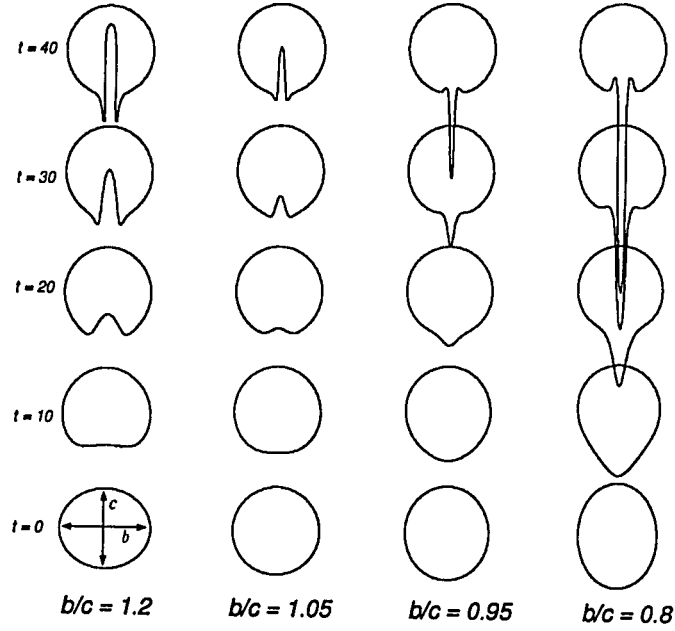


Figure 1.3: Interface shapes during the buoyancy-driven translation of initially non-spherical drops for $b/c = 1.2, 1.05, 0.95$ and 0.8 ; $\mathcal{B} = \infty$, $\lambda = 1$.

sufficiently low values of interfacial tension. Numerical results calculated using the boundary integral method were presented by Koh & Leal [1989] and Pozrikidis [1990a] for a wide range of viscosity ratios λ (defined in figure 1.2a) and initial drop shapes. Both numerical studies demonstrate that for large enough values of the Bond number initially prolate drops will develop a long tail behind the drop whereas initially oblate drops develop a cavity at the back of the drop. For sufficiently low values of the interfacial tension an annular tail will develop at the back of an initially oblate drop, and the tail will surround the cavity inside the drop. Koh & Leal [1989] determined the critical Bond number for a given viscosity ratio and shape above which the drop deforms continuously and below which the drop eventually assumes a spherical shape. Koh & Leal [1990] also successfully compared numerical and experimental results.

In figures 1.3-6 we present interface shapes for single translating axisymmetric drops at different times during the translation of the drop and evolution of the drop

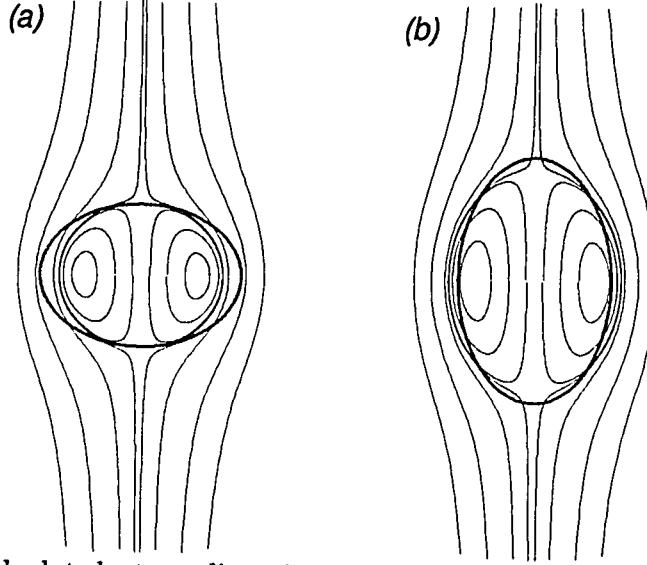


Figure 1.4: Calculated streamlines in a frame of reference translating with the Hadamard-Rybczyński velocity for (a) an oblate drop with $b/c = 1.5$ and (b) a prolate drop with $b/c = 2/3$; $\mathcal{B} = \infty$, $\lambda = 1$. Similar streamlines for a spherical drop do not intersect the drop surface since the drop surface is a streamsurface.

shape. Interface shapes are shown at positions corresponding to the actual displacement relative to the initial position of the drop. The initial shape and position of the drop are labeled $t = 0$. Time is normalized by $\mu/\Delta\rho ga$. In figure 1.3 we assume $\mathcal{B} = \infty$ and $\lambda = 1$ and vary the initial shape of the drop: results are shown for aspect ratios of $b/c = 1.2, 1.05, 0.95$ and 0.8 . The aspect ratio b/c is defined in figure 1.3. The volume of the drops in the four simulations is the same. Oblate drops, $b/c > 1$ develop an enlarging cavity at the back of the drop, and an annular tail forms behind the drop surrounding the cavity, *e.g.* drop shape at $t = 40$ for $b/c = 1.2$. In order to help understand the two distinct modes of deformation, we present calculated streamlines for an oblate drop (figure 1.4a) and prolate drop (figure 1.4b) in a frame of reference translating with the Hadamard-Rybczyński velocity. For the oblate drop, the sides of the drop will be swept around the drop leading to the formation of a cavity. For the prolate drop, an extensional flow (in a frame of reference translating

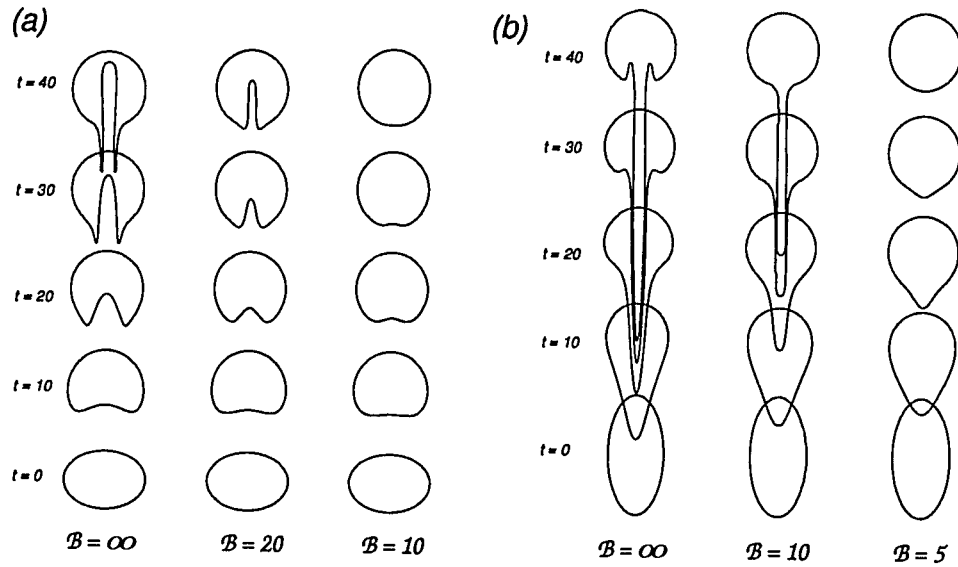


Figure 1.5: (a) Interface shapes during the buoyancy-driven translation of initially oblate drops for $B = \infty, 20$ and 10 ; $b/c = 1.5$, $\lambda = 1$. (b) Interface shapes during the buoyancy-driven translation of initially prolate drops for $B = \infty, 10$ and 5 ; $b/c = 0.5$, $\lambda = 1$.

with the drop) develops at the front and back of the drop. The extensional flow at the front the drop will flatten the drop whereas the extensional flow at the back of the drop will lead to the formation of a tail.

In figure 1.5 we consider the effect of changing the Bond number on the evolution of drop shapes. In figure 1.5a we present three simulations for $B = \infty, 20$ and 10 for oblate drops; $b/c = 1.5$, $\lambda = 1$. For large Bond numbers, $B = \infty$ a cavity develops inside the drop and an annular tail forms behind the drop. For smaller Bond numbers, $B = 20$, a cavity still forms inside the drop but no tail develops. For still smaller Bond numbers, $B = 10$, the drop returns to a spherical shape. In figure 1.5b we present three simulations for $B = \infty, 10$ and 5 for prolate drops; $b/c = 0.5$, $\lambda = 1$. For large Bond numbers, $B = \infty$, a long tail forms behind the drop and a small amount of the external fluid is entrained inside the nearly spherical "head" of the drop. For smaller

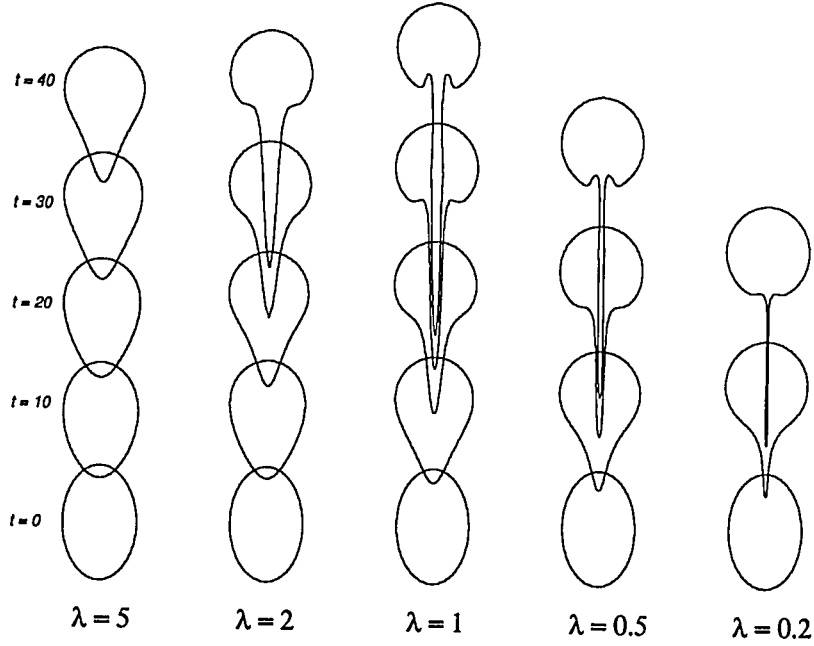


Figure 1.6: Interface shapes during the translation of initially nonspherical buoyancy-driven drops for $\lambda = 5, 2, 1, 0.5$ and 0.2 ; $\mathcal{B} = \infty$, $b/c = 2/3$.

Bond numbers, $\mathcal{B} = 10$, a tail still forms behind the drop but the “head” of the drop remains nearly spherical. For still smaller Bond numbers, $\mathcal{B} = 5$, the drop returns to a spherical shape.

Finally, in figure 1.6, we present simulations for different viscosity ratios for $\lambda = 5, 2, 1, 0.5$ and 0.2 ; $\mathcal{B} = \infty$, $b/c = 2/3$. The effect of increasing the viscosity ratio is to decrease the rate of deformation. Koh & Leal [1989] showed numerically that the rate of deformation scales as $1/(1 + \lambda)$ for large Bond numbers (a limit in which interfacial tension has little effect on deformation). as suggested by the form of the integral equations, for example (1.24).

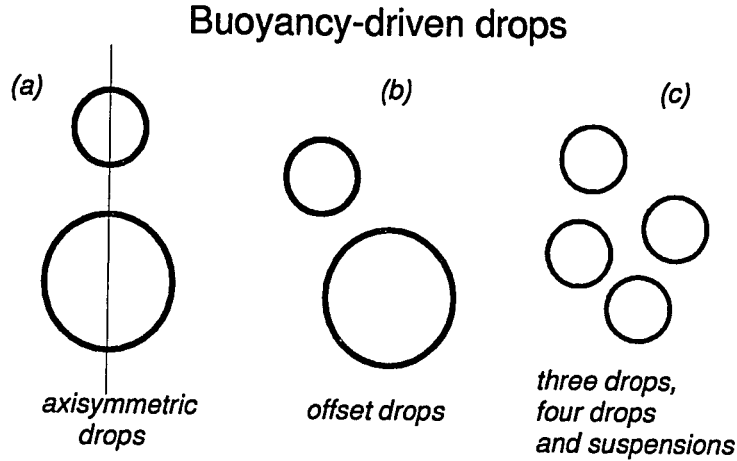


Figure 1.7: Geometries considered for the buoyancy-driven translation, interaction, and deformation of deformable drops and bubbles.

1.4 Thesis overview

Below we present a brief outline and summary of the thesis.

1.4.1 Part I. Buoyancy-driven drops in suspensions

In part I of this thesis we consider the time-dependent interactions between two buoyancy-driven deformable drops in the low Reynolds number flow limit for sufficiently large Bond numbers that the drops become significantly deformed. Chapter 2 considers the interaction and deformation of axisymmetric drop configurations (see figure 1.7a). Boundary integral calculations are presented for Bond numbers in the range $0.25 \leq \mathcal{B} < \infty$ and viscosity ratios in the range $0.2 \leq \lambda \leq 20$. Specifically, the case of a large drop following a smaller drop is considered, which typically leads to the smaller drop coating the larger drop for $\mathcal{B} \gg 1$. Three distinct drainage modes of the thin film of fluid between the drops characterize axisymmetric two drop interactions: (i) rapid drainage for which the thinnest region of the film is on the axis of symmetry, (ii) uniform drainage for which the film has a nearly constant thickness, and

(iii) dimple formation. The initial mode of film drainage is always rapid drainage. As the separation distance decreases, film flow may change to uniform drainage and eventually to dimpled drainage. Moderate Bond numbers, typically $\mathcal{B} = O(10)$ for $\lambda = O(1)$, enhance dimple formation compared to either much larger or smaller Bond numbers. The numerical calculations also illustrate the extent to which lubrication theory and analytical solutions in bipolar coordinates (which assume spherical drop shapes) are applicable to deformable drops.

We next consider the ‘stability’ of axisymmetric drop configurations. Two-dimensional and three-dimensional boundary integral simulations and laboratory experiments are used in chapter 3 to study the interactions between two horizontally offset drops (see figure 1.7*b*). For sufficiently deformable drops, alignment occurs so that the small drop may still coat the large drop, whereas for large enough drop viscosities or high enough interfacial tension, the small drop will be swept around the larger drop. If the large drop is sufficiently deformable, the small drop may then be “sucked” into the larger drop as it is being swept around the larger drop. In chapter 4 we explain the alignment process by calculating the shape and translation velocities of widely separated, nearly spherical drops using the method of reflections and a perturbation analysis for the deformed shapes. The perturbation analysis demonstrates explicitly that drops will tend to be aligned for $\mathcal{B} > O(d/a)$ where d is the separation distance between the drops.

Finally we demonstrate that the deformation of drops and bubbles in suspensions enhances the rate of coalescence. Three-dimensional numerical simulations demonstrate that two drop interactions are representative of the interactions between groups of drops (see figure 1.7*c*). The analytical results developed in chapter 4 are used to determine the rate of coalescence in dilute monodisperse suspensions. The coalescence rate of bubbles in a dilute polydisperse suspension is determined experimentally. We find that the rate of coalescence of deformable bubbles with $\mathcal{B} \approx 10$ may be more than one order of magnitude greater than the equivalent rate of coalescence of spherical bubbles. Population dynamics calculations are then presented for (i) homogeneous

and isotropic suspensions of bubbles, and *(ii)* suspensions of bubbles in which separation of the dispersed phase may occur due to differential rise speeds of bubbles with different radii.

Large Bond numbers are characteristic of many problems in solid-earth geophysics and geology because of the large length scales in these systems. The Reynolds number is generally much less than 1 since the viscosity of the mantle is about 10^{21} Pa s and the viscosity of magmas ranges from $10-10^7$ Pa s. For example, mantle plumes, which are believed to be low viscosity (relative to the rest of the mantle) and low density instabilities produced in a thermal boundary layer at the base of a convecting mantle, may be described to a good approximation as buoyant drops since the Peclet number is very large [Singer & Olson 1985; Griffiths et al. 1989]. Mantle plumes are believed to consist of a large nearly spherical plume head followed by a tail or conduit attached to the thermal boundary layer [Griffiths & Campbell 1990]. On the basis of the results presented in this thesis, we expect that mantle plume heads (which may be described as buoyant drops) in close spatial and temporal proximity would tend to merge. Mantle plume heads form frequently enough and rise slow enough that situations may arise in which plumes may interact, particularly during the Cretaceous period when many plumes erupted on the surface of the Earth. The interaction of plumes may explain some of the variation in inferred plume size [Richards et al. 1989] and some of the variation in the size of highlands and coronae on Venus which are thought to be produced by plumes spreading beneath the planet's surface [Koch 1993].

At smaller length scales, geological applications associated with high Bond number dynamics include air bubbles in magmas, where bubble radii are less than a few centimeters. The coalescence and interactions of bubbles in ascending magmas and in magma chambers may be important processes governing the style of volcanic eruptions [Jaupart & Vergnolle 1989]. Understanding the interactions between bubbles may aid in the interpretation of the distribution of bubbles in solidified volcanic flows and the process of bubble formation in magmas. Chapter 6 contains an extended discussion of the importance of deformation on bubble dynamics in magmas and lavas and

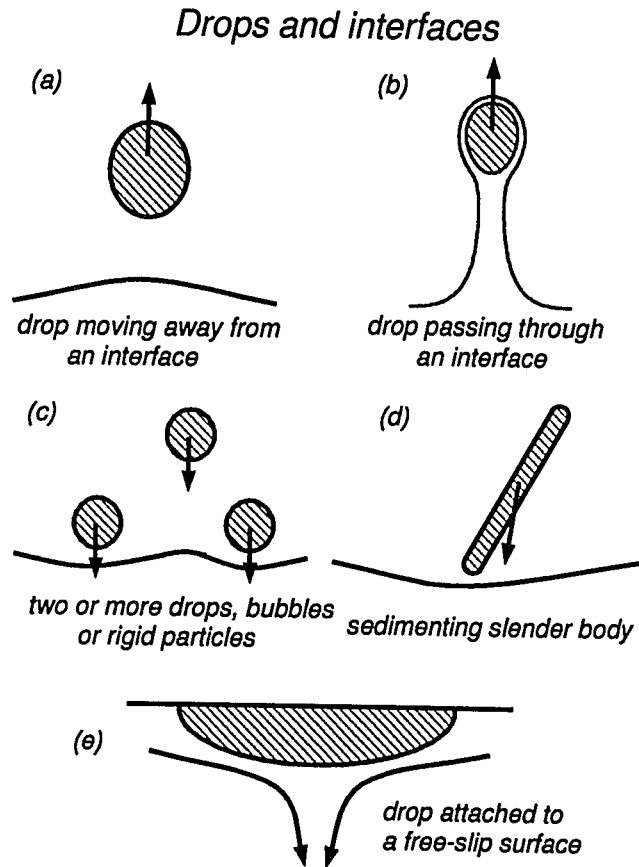


Figure 1.8: Geometries considered for studying the translation and deformation of drops, bubbles and rigid particles translating normal to a fluid-fluid interface.

provides an overview of some of the implications of bubble dynamics for the eruption of basaltic magmas and evolution of bubble concentration in effusive lavas. We also discuss an instability which may develop in suspensions of deformable bubbles owing to deformation: local velocity gradients produced as a result of variations of bubble concentration will lead to a migration, due to deformation, of bubbles from regions of lower to higher bubble concentration. In addition, at small length scales, the rate of coalescence of drops of liquid iron during the earliest stages of the Earth's history may have affected the rate of segregation of the Earth's core and also the amount of iron and other heavy metals that are removed from the mantle.

1.4.2 Part II. The motion of drops through fluid interfaces

The motion of a single drop through a fluid-fluid interface serves as a useful model for understanding the dynamics and evolution of separating multiphase flows, *e.g.*, the separation of gas bubbles or sedimenting particles in stratified fluids. In chapter 7 we consider the time-dependent deformation of a drop passing through a deformable fluid-fluid interface. The initially flat fluid-fluid interface will be referred to hereafter as the interface. Drops passing from a higher to lower viscosity fluid become extended vertically (and thus accelerate), whereas drops which do not accelerate substantially develop a cavity at the back of the drop as they pass through the interface. The two modes of deformation are analogous to the two modes of deformation of a single drop in an unbounded fluid, *e.g.* figure 1.3. We then consider experimentally the dynamics of one or more particles passing through fluid-fluid interfaces. We find that, in agreement with numerical calculations, rigid particles entrain more fluid through the interface than bubbles entrain.

We also consider the motion of slender bodies, rigid particles with aspect ratios much greater than one (such as rods and fibers), sedimenting through a fluid-fluid interface. We find that an initially inclined slender body entering a lower viscosity fluid will become oriented parallel to gravity. Slender bodies entering a more viscous fluid do not become oriented perpendicular to gravity. The dynamics of particles passing through interfaces suggest that in some limits, as discussed in chapter 7, structures may form in the separating phase in a stratified fluid.

In chapter 8 we apply the results of the study of drops passing through interfaces to the ascent of mantle plume heads passing through compositional discontinuities in the Earth's mantle. The effect of a viscosity decrease in the upper mantle, generally thought to be a factor of 10 to 30 [Hager & Clayton 1989], results in the vertical extension of plume heads, and may play a role in creating hotspots which persist following the emplacement of continental flood basalts. We also consider two other problems with application to mantle plumes: the motion of a plume head away from an interface and a plume head spreading beneath the surface of the Earth. The surface

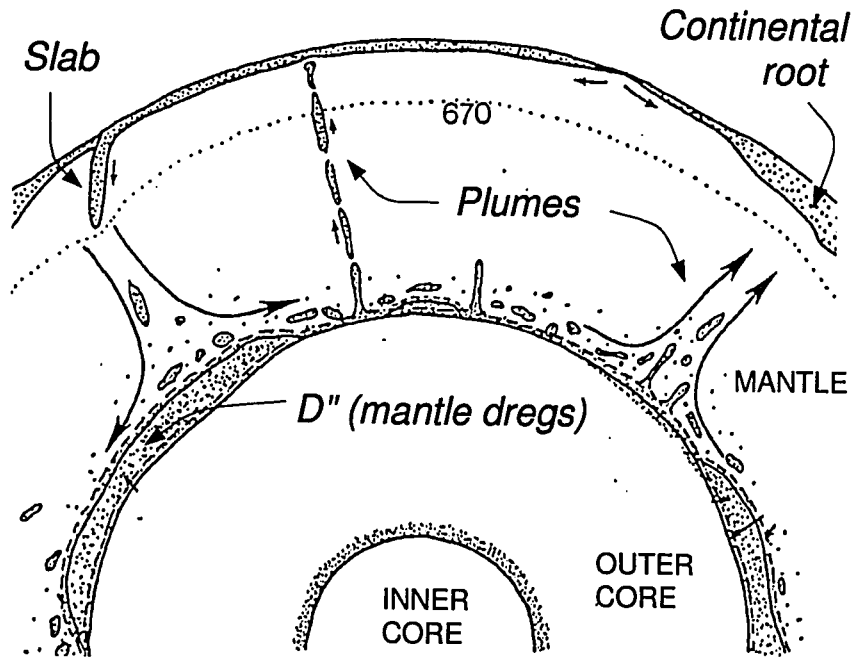


Figure 1.9: Schematic illustration of various components of the convecting mantle [after Lay 1993]: continental roots, mantle plumes and mantle dregs (D" layer).

dynamics and stresses associated with a rising and spreading plume head appear to be consistent with the emplacement of continental flood basalts and the formation of coronae on Venus.

1.4.3 Part III. Dynamics of continental roots and mantle dregs and the formation of the Venusian highlands

In chapter 9 we consider a few features associated with buoyancy-driven flow in the mantle where the fluid domains under consideration may have different viscosities. Although we will be approximating regions of the mantle as having a uniform viscosity and density, the simplified geometry and model may help provide a better physical understanding of some of the buoyancy-driven features associated with mantle con-

vection. Specifically we will consider the effect of viscosity contrasts on the surface expression of flow in the mantle, the dynamics of continental roots, the formation of Venusian highlands above downwellings, and the dynamics of mantle dregs.

Continental roots, regions of anomalously fast seismic velocity extending to depths of up to 500 km beneath continental shields, have been interpreted by Jordan [1975] to be compositionally distinct mantle and named the “tectosphere”. The presence of seismic anomalies beneath all continents requires that the continental root be very viscous and in order not to be sheared apart from the continent by mantle convection stresses and not be too dense that it delaminates from the overlying continent.

The Venusian highlands, topographically elevated plateau-like regions with diameters of 1000 to 3000 km, are thought to be caused by either upwelling mantle plumes [Kiefer & Hager 1991ab], or form as a result of crustal convergence and thickening above a downwelling [Bindschadler et al. 1990]. We re-examine the latter hypothesis in order to consider the dynamic feasibility of the crustal thickening model.

Finally we end chapter 9 by discussing the dynamics of mantle dregs, an expression used to describe the compositionally unknown material which constitutes the D” layer at the base of the mantle. Proposals for the composition of D” include, among others, reaction products between the core and mantle, accumulated dense components from subducted slabs or residual material remaining from early Earth differentiation. We examine the dynamics of compositionally distinct dregs beneath a convecting mantle in order to determine the limits in which material from D” may be entrained into the convecting mantle.

Chapter 2

Interaction of two axisymmetric buoyancy-driven drops

In this chapter, we consider the hydrodynamic interactions between two buoyant drops in a viscously dominated flow. Our contribution to the subject area is to investigate the case where buoyancy forces are much larger than the restoring forces due to interfacial tension, and hence large drop distortions are possible. We use the boundary integral method to study numerically the on-axis interaction of two deformable translating drops. In the following two chapters we will consider the interaction of drops which are initially horizontally offset.

2.1 Introduction

The low Reynolds number study of the buoyancy-driven interaction between a pair of drops or a drop and an interface serves as a useful model for understanding the dynamics of multiphase systems, *e.g.* liquid-liquid extraction which eventually requires the coalescence of a drop with its homophase, or the evolution of the dispersed phase volume fraction in multiphase flows common to industrial processing. Most previous studies of two drop interactions assume spherical drop shapes, a limit which requires that interfacial tension forces are large compared to viscous and pressure forces. For

example, the Stokes flow field around two translating spherical drops, as well as the rise speed and associated drag forces, have been examined theoretically using bipolar coordinates [*e.g.* Stimson & Jeffrey, 1926; Haber et al., 1973, Chervenivanova & Zaprjanov, 1987], the method of images [*e.g.* Fuentes et al., 1988], and the method of reflections [*e.g.* Hestroni & Haber, 1978; Reed & Anderson, 1980].

Coalescence of two drops requires that the separation distance between the two drops eventually becomes very small; thus, the thin film geometry and flow characteristic of the near contact between two drops has received much attention. Most studies make *ad hoc* approximations for some features of the thin film flow geometry, though two recent studies obviate this deficiency. An approximate lubrication theory description of the two drop geometry, valid for two nearly touching spherical drops, is presented by Davis et al. [1989] and Barnocky & Davis [1989].

Yiantsios & Davis [1990] extend the lubrication approach to account for interface deformation in the limit that interfacial tension is sufficiently strong to allow only small deformations. The evolution of drop shape as a function of viscosity ratio between the two fluids is determined and the formation of a dimpled shape is demonstrated without any *ad hoc* approximations other than assuming the validity of the lubrication approximation. The finite deformation and associated film drainage of a drop approaching a deformable fluid-fluid interface, in particular the effects of viscosity contrasts and interfacial tension, is addressed by Chi & Leal [1989] using a boundary integral method. The studies of Yiantsios & Davis and Chi & Leal thus describe the complete time evolution of an isolated drop interacting with a deformable boundary, at least for cases where only modest drop deformation occurs.

In the limit of low interfacial tension, drops may become highly deformed even when separation distances are large. Large shape distortions lead to a number of different types of two drop interactions at low Reynolds numbers. The flows are characterized by large values of the Bond number, $\mathcal{B} = \Delta\rho g a_1^2 / \sigma$, which represents the ratio of buoyancy forces to interfacial tension forces: $\Delta\rho$ is the density difference between the drop and surrounding fluid, g is the gravitational acceleration, a_1 is the

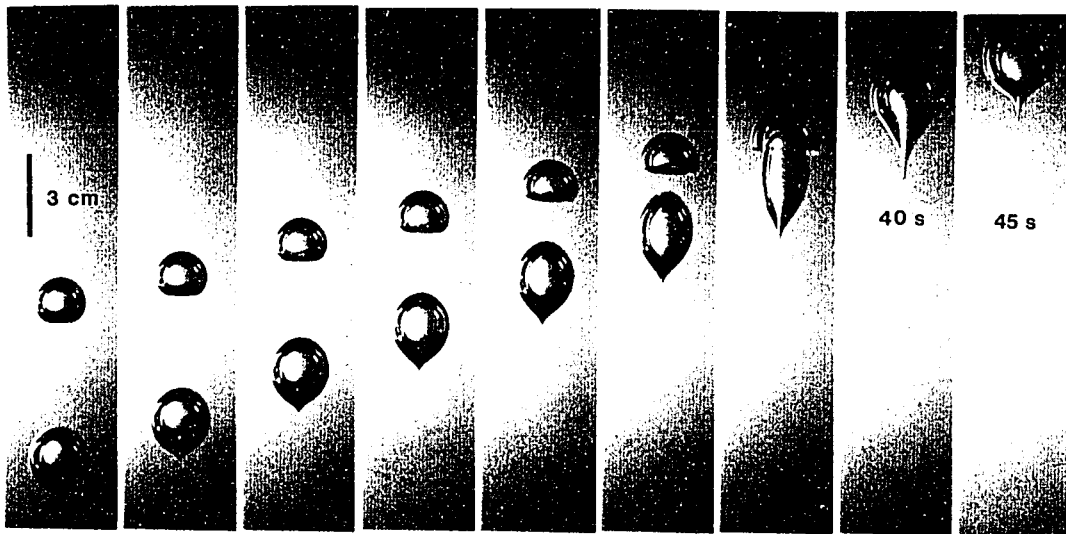


Figure 2.1: Sequence of photographs of air bubbles in corn syrup. The Bond number based on the larger drop is $\mathcal{B} \approx 50$ and the Reynolds number is $\mathcal{R} \approx 10^{-3}$. Photographs are shown at 5 second intervals. The trailing bubble has a small tail which develops initially as the bubble is released and the tail is about one bubble radius long. Owing to the large viscosity of corn syrup, the tail does not completely relax before the first photograph is taken.

radius of the larger of the two drops, and σ is the interfacial tension. In figure 2.1 we show the interaction that results from two air bubbles translating along their line-of-centers in a large container of corn syrup. The Bond number for this experiment is large, $\mathcal{B} \approx 100$, and the Reynolds number based on the bubble radius a_1 and rise speed U is small, $\mathcal{R} = \rho U a_1 / \mu \approx 10^{-2}$. This series of photographs illustrates that deformation may be large even when separation distances are large, and that the spherical drop assumption commonly used to study drop interactions is not always a reasonable approximation.

We note here that for situations where the interfacial tension forces are weak, such as the experiments illustrated in figure 2.1, the flow-field created by the trailing

drop (radius a_1) will tend to flatten the leading drop into an oblate shape. The velocity difference thus generated across the leading drop (radius a_2) is approximately $\Delta u \approx a_2 U_1 / d$ for large separation distances d in a viscously dominated flow where U_1 is the speed of the trailing drop. Consequently, neglecting interfacial tension, the total strain or deformation experienced by the leading drop is $\tau \Delta u / a_2$, where τ is a characteristic time for the deformation to occur. Choosing $\tau = a_1 / U_1$, which is the advective time scale characteristic of interaction of the two drops, gives a strain a_1 / d experienced by the leading drop as a consequence of motion of the trailing drop. Thus, for separation distances of 4 drop radii, we can expect strains of 25%, or aspect ratios of about 3/2. We will see that even such modest shape distortions are important when considering the interaction of two drops which are not aligned initially along the vertical direction. The two drop interaction shown in figure 2.1, characterized by large distortions owing to large Bond numbers, is the primary focus of this chapter.

The spherical shape assumption is justified in many chemical engineering systems involving aqueous media so long as the drop radii are smaller than $O(10\mu m)$. Larger drops may be characterized by Bond numbers greater than $O(1)$ and significant deformation should be expected. We note that the study here is also relevant to a number of geological and geophysical problems where the Reynolds number is small because of high viscosities and the Bond number is large because of large length scales. At the longest length scales, the behaviour of mantle plumes and diapirs with length scales ranging from 10 km to 1000 km, can be modeled as buoyancy-driven drops [Manga et al. 1993; Koch 1993]. At smaller length scales, bubbles with typical radii of 1 mm to 1 cm, in high viscosity silicate magmas, have Bond numbers greater than $O(1)$. Large Bond numbers may also be achieved owing to the presence of surfactants which may substantially decrease interfacial tension, though surfactants also induce motion because of gradients of interfacial tension. Such Marangoni motions are outside the scope of this investigation (but see the discussion in §4.5).

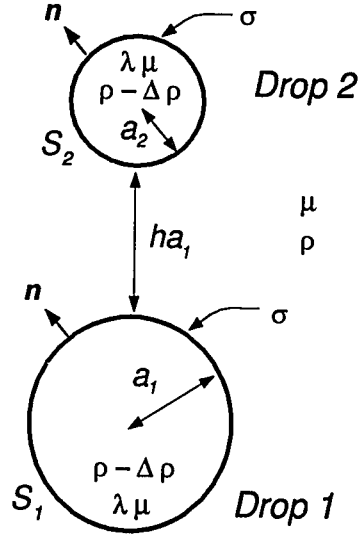


Figure 2.2: Geometry of the problem considered in chapter 2. The unit normal vector \mathbf{n} is outward from the drops. Drops 1 and 2 have radii a_1 and a_2 , respectively. The drops have viscosity $\lambda\mu$ and density $\rho - \Delta\rho$; the external fluid has viscosity μ and density ρ . The interfacial tension is denoted by σ . The separation distance between the drops is ha_1 . The surfaces of the drops are denoted by S_1 and S_2 .

2.2 Problem formulation

The interaction of drops translating parallel to their line-of-centers is modeled by considering three fluid domains, the ambient fluid and the two drops, as shown in figure 2.2. To reduce the number of parameters we assume that the drops are composed of the same fluid, which corresponds to the most common problems of physical interest. We denote the fluid domains by subscripts 1 and 2 for drops 1 and 2, respectively, and by the subscript *ext* for the external fluid.

We require that the velocity decays to zero far from the drops,

$$\mathbf{u}_{ext} \rightarrow \mathbf{0} \text{ as } |\mathbf{x}| \rightarrow \infty \quad (2.1)$$

and that the velocity is continuous across all interfaces,

$$\mathbf{u}_1 = \mathbf{u}_{ext} \text{ on } S_1 \quad \text{and} \quad \mathbf{u}_2 = \mathbf{u}_{ext} \text{ on } S_2, \quad (2.2)$$

where S_1 is the surface bounding drop 1, and S_2 is the surface bounding drop 2. The stress jump $[\mathbf{n} \cdot \mathbf{T}]_i$ across interface i is balanced by the density contrast and interfacial tension forces, which depend on the local curvature $\nabla_s \cdot \mathbf{n}$ of the interface:

$$[\mathbf{n} \cdot \mathbf{T}]_1 = \mathbf{n} \cdot \mathbf{T}_{ext} - \mathbf{n} \cdot \mathbf{T}_1 = \sigma (\nabla_s \cdot \mathbf{n})\mathbf{n} + \mathbf{n}\Delta\rho\mathbf{g} \cdot \mathbf{x} \quad \text{on } S_1 \quad (2.3)$$

$$[\mathbf{n} \cdot \mathbf{T}]_2 = \mathbf{n} \cdot \mathbf{T}_{ext} - \mathbf{n} \cdot \mathbf{T}_2 = \sigma (\nabla_s \cdot \mathbf{n})\mathbf{n} + \mathbf{n}\Delta\rho\mathbf{g} \cdot \mathbf{x} \quad \text{on } S_2, \quad (2.4)$$

where σ denotes the constant interfacial tension, \mathbf{n} is the unit normal directed into the external fluid, and $\nabla_s = (\mathbf{I} - \mathbf{n}\mathbf{n}) \cdot \nabla$ is the gradient operator tangent to the interface. Additionally there is a kinematic constraint, which requires that a fluid element on a fluid-fluid interface remain on that interface for all time; formally, the kinematic constraint may be expressed with the Lagrangian description

$$\frac{d\mathbf{x}}{dt} = \mathbf{u}(\mathbf{x}) \quad \text{for } \mathbf{x} \in S_1, S_2. \quad (2.5)$$

For convenience, the trailing drop is labeled drop 1, and the leading drop is labeled drop 2. The equations are nondimensionalized by choosing the characteristic length as the radius of the trailing drop, radius a_1 , the velocity scale as $\Delta\rho g a_1^2 / \mu$ and an advective time scale of $\mu / \Delta\rho g a_1$. For a given initial configuration (dimensionless separation distance h in figure 2.2), three dimensionless parameters characterize the flow: the ratio of drop radii, a_1/a_2 , the viscosity ratio, λ , and a Bond number based on the properties of the trailing drop

$$\mathcal{B} = \frac{\Delta\rho g a_1^2}{\sigma}. \quad (2.6)$$

The Bond number characterizing the deformation of drop 2 with radius a_2 is $\mathcal{B}(a_2/a_1)^2$. In this chapter we will assume that the drops are of comparable sizes, and often use a to denote a typical drop radius.

We solve for the time-dependent deformation and translation of the drops by recasting the Stokes equations as a pair of coupled integral equations of the second kind for the interfacial velocities, equations (1.25). The integral equations involve only stress jumps, equations (2.3) and (2.4), across the interfaces and the unknown velocities along the interfaces. For the axisymmetric configuration considered in this chapter, the azimuthal integration may be performed analytically (see appendix B) reducing the surface intergrals to line integrals. The integral equations are solved by a collocation procedure and integration is performed using Gauss-Legendre quadrature. The interface shapes are described by taut cubic splines [deBoor 1978] parameterized in terms of arc length. Typically, we use 50-120 collocation points on each half-interface.

Cumulative numerical error, estimated by monitoring the volume change of the drops, may occasionally be as high as 5-10% for the most severe distortions and the times of the longest numerical simulations, particularly for problems involving large viscosity contrasts. Such volume changes are larger than those reported in previous studies because of the large distances over which the drops translate in the simulations. Typically, calculated interfacial velocities for a single spherical drop in an unbounded fluid differ by less than 1% from the exact Hadamard-Rybczyński result. In the results presented in this chapter, the volume changes were always less than 10% and no volume rescaling was implemented.

2.3 On-axis Interaction of Axisymmetric Drops

The numerical results presented below illustrate the interaction between two axisymmetric drops translating along their line-of-centers. Qualitatively, the numerical results have some similarities with the problem of a drop approaching a deformable interface presented by Chi & Leal [1989]. Most notably, the style of film drainage between the two drops is similar to the film formed between a drop and a fluid-

fluid interface, though we allow for much larger interface distortions since the zero interfacial tension limit is studied.

We consider the case of a large drop following a smaller drop so that interaction eventually occurs; the two drops are composed of the same fluid and the radius ratio $a_1/a_2 = 2$ in all the simulations. Thus, the Bond number for the smaller drop is $0.25\mathcal{B}$. Both drops are assumed to be initially spherical and the initial separation distance between the two drops (the distance h shown in figure 2.2) is usually chosen as one half the radius of the large drop. Changing the ratio of drop sizes and the initial drop separation distance results in only modest qualitative changes in drop behaviour. However, the history of deformation is important for the understanding the detailed drop deformation in the high Bond number limit owing to the long-range nature of Stokes flows; in §2.3.4 we summarize typical results observed when the initial separation distance is changed.

2.3.1 Effect of interfacial tension

In figure 2.3 we illustrate the effect of interfacial tension on the shapes of translating drops. A sequence of interface shapes at equal time increments is shown for Bond numbers $\mathcal{B} = \infty, 10$ and 1 . For all Bond numbers the smaller leading drop initially deforms into an oblate shape and the larger trailing drop deforms into a prolate shape; both types of deformation are a result of the flow produced by the neighbouring drop. For example, as schematically indicated in figure 3.4 using the simple idealization of treating the translating drop as a point force, the trailing drop becomes elongated (prolate distortion) owing to the viscous stresses associated with the convergence of streamlines in the flow produced by the leading drop. Conversely, the leading drop becomes flattened (oblate distortion) owing to the viscous stresses associated with the divergence of streamlines in the flow produced by the trailing drop (analytical descriptions of the nonspherical shapes are given in chapter 4).

For translational motions in an unbounded fluid the spherical drop shape is stable to infinitesimal perturbations provided the interfacial tension is finite, *i.e.* $\mathcal{B} < \infty$

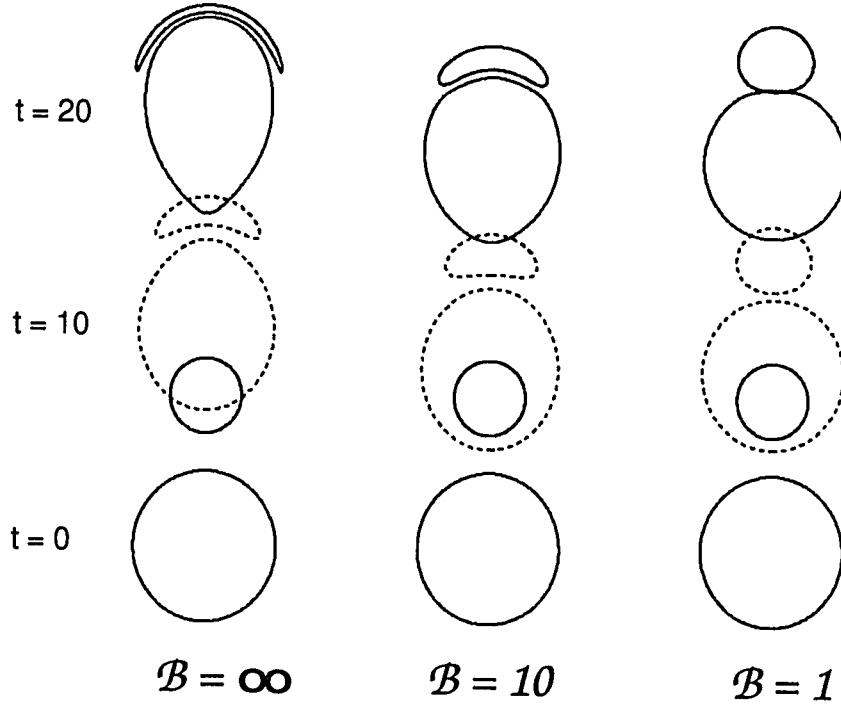


Figure 2.3: Effect of interfacial tension on drop deformation; $B = \infty, 10, 1$; $\lambda = 1$; $a_1/a_2 = 2$. Interface shapes are shown at times $t = 0, 10$ and 20 .

[Kojima et al. 1984]. However, finitely deformed drop shapes are unstable, and subsequently undergo a continual deformation, if the restoring interfacial tension forces are not sufficiently large: prolate drops will develop long tails and oblate drops will develop cavities [Koh & Leal 1989; Pozrikidis 1990; see figure 1.5]. For the isoviscous drops shown in figure 2.3, Bond numbers of the order 10 appear to be sufficient to prevent the large drop from developing a tail (see figure 2.6 for shapes at longer times). As the restoring interfacial tension force is reduced, the smaller leading drop deforms substantially, spreading over the surface and thus coating the larger drop, as illustrated for the $B = \infty$ and $B = 10$ simulations (figure 2.3). At longer times, the separating film thins substantially, the drops numerically make contact, and the simulation is terminated. The same manner of interaction and deformation

was shown previously for the two air bubbles interacting in corn syrup (figure 2.1). In the experiments, coalescence occurs shortly after the final photograph shown in figure 2.1.

2.3.2 The style of film drainage

The interaction over long times and possible coalescence of two nearly touching drops is controlled by the dynamics of the thin film between the drops. Interest in the coalescence process has been the primary motivation for the extensive study of the film drainage problem. The use of a boundary integral method allows us to study the complete evolution of the thin film for large drop deformations. When the interfaces are deformable, three distinct modes of film drainage characterize the interaction of two drops, analogous to the three modes described in Chi & Leal [1989] for a drop approaching its initially planar homophase. The three styles of interface deformation, which provide insight into the probable manner and location of coalescence, are referred to as (i) rapid drainage, (ii) uniform drainage and (iii) dimple formation, depending on the thickness profile of the film and the manner in which the film thins.

Numerical simulations illustrating the three modes of film flow are presented in figure 2.5. The film profiles (gap thickness as a function of radial position) are also shown. We note that ‘uniform drainage’ characterizes an almost (but not exact) uniform film thickness between two drops.

The three modes of film drainage also characterize different stages in the evolution of a given film. As we will see in the following sections, as the separation between the drops decreases, the characterization of the drainage flow may change from rapid to uniform drainage and then dimple formation. For the range of viscosity ratios considered in this chapter, the separation distance h , at which dimple formation begins, decreases with decreasing viscosity ratio λ for a given Bond number. In the study by Yiantsios & Davis [1990], which is restricted to small Bond numbers, $\mathcal{B} \ll 1$, dimple formation is always predicted to eventually occur. However, in our high Bond number calculations (*e.g.* $\mathcal{B} = \infty$ shown later in figure 2.6) and experiments with air

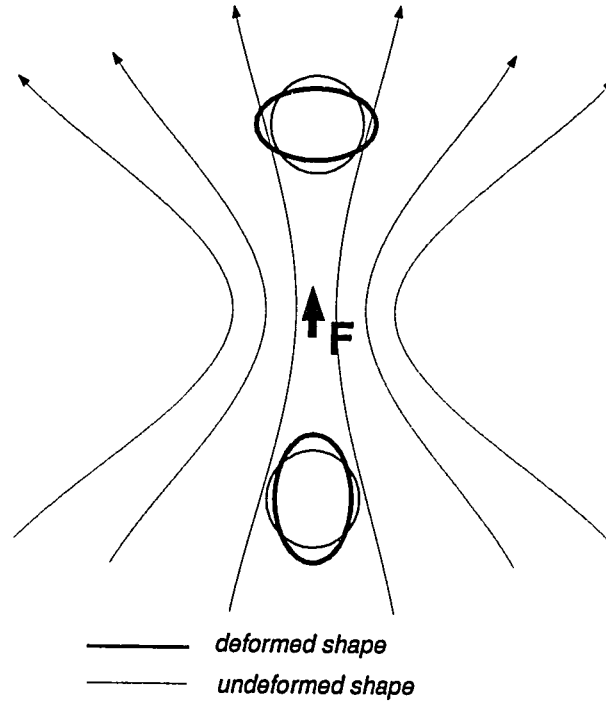


Figure 2.4: Illustration of the effect of a point force, F , on drop deformation. Drops in front of a point force, which models the presence of a second drop, become oblate spheroids. Conversely, drops behind a point force become prolate spheroids.

bubbles (*e.g.* figure 2.1) dimple formation never appears to occur prior to coalescence. In the following section we discuss the effects of interfacial tension and drop viscosity on the style of drainage and outline the physical mechanisms responsible for the corresponding drainage mode.

2.3.3 Rate of film drainage and dimple formation

In figure 2.6 we present the time evolution of the gap thickness measured at $r = 0$, shown with a solid line, for different values of the Bond number and $\lambda = 1$. Corresponding drop shapes at different stages of the interaction are shown and identified with the letters a, b, c, etc. The minimum separation distance between the two drops

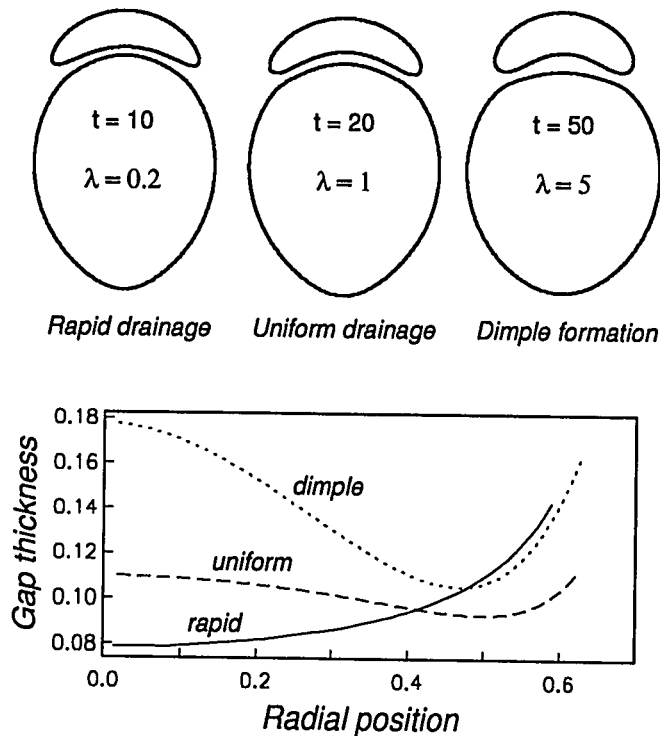


Figure 2.5: The three modes of film drainage, analogous to the three modes described in Chi & Leal [1989]: (i) rapid drainage, (ii) uniform drainage, and (iii) dimple formation. Examples of calculated shapes for each mode are shown for $\mathcal{B} = 10$; $\lambda = 0.2, 1$ and 5 ; $a_1/a_2 = 2$. On the bottom we plot gap thickness versus radial distance to illustrate more clearly the differences in gap geometry.

is shown with a dashed line. Dimple formation in the thin film thus begins when the solid and dashed lines diverge indicating that the smallest separation distance is no longer along the centerline. The solid and dashed curves for $\mathcal{B} = 1$ and ∞ overlap since no dimple develops. The film thickness decreases most rapidly for the large interfacial tension simulation ($\mathcal{B} = 1$), and most slowly for the moderate interfacial tension simulation ($\mathcal{B} = 10$) which forms a dimpled film.

In order to explain the variation of film thickness with time, we note that for smaller Bond numbers (hence smaller distortions), film drainage is more rapid because

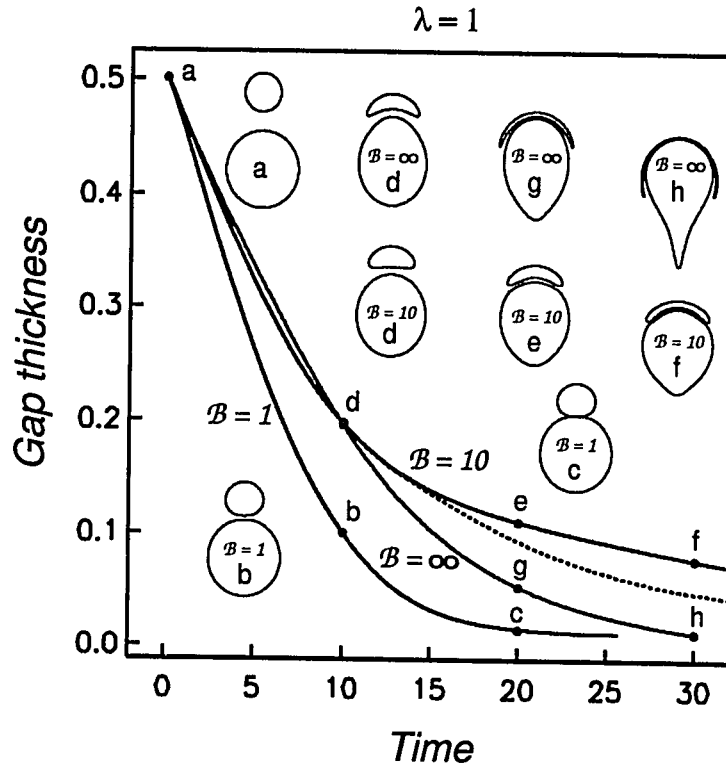


Figure 2.6: The rate of film drainage versus time for drops with Bond numbers $B = 1$, 10 and ∞ ; $\lambda = 1$; $a_1/a_2 = 2$. The solid curve corresponds to the thickness of the film on the axis of symmetry, $r = 0$, and the dashed curve corresponds to the minimum film thickness. Drop shapes at different times are shown for reference.

the two drops remain nearly spherical and thus fluid in the gap is not forced to flow over too large a surface area. For the case of vanishing interfacial tension ($B = \infty$), the smaller drop coats the larger drop, so that the increase in surface area provides additional resistance to fluid motion in the narrow gap which delays film thinning. Dimple formation for moderate Bond numbers ($B = 10$; see also figure 2.5) means that the narrowest portion of the film is away from the centerline; this geometric constriction further slows the rate of film drainage. From the results shown in figure 2.6, we observe that in the absence of interfacial tension ($B = \infty$) the thin film has a nearly uniform thickness over the entire near-contact surface and no dimpled film

For low viscosity drops, corresponding to a more mobile interface [Davis et al. 1989], the rate of film drainage is enhanced. For high viscosity drops the interface becomes immobile, and not only offers additional resistance to fluid flow in the thin film, but also enhances the formation of dimples thus leading to a slower rate of drainage. We observe that in the higher viscosity ratio simulations, such as the case $\lambda = 5$ shown in figure 2.7, the gap thickness along the axis of symmetry actually increases after a certain stage in the development of a dimpled film. Since very large pressures exist at $r = 0$ in order to squeeze fluid out of the thinning film, it becomes easier for the drop to distort such that the thickness of the gap increases at the film midpoint. This behaviour is associated with moderate values of the Bond number and is to be contrasted with the qualitatively different, monotonically thinning, low Bond number film profiles determined by Davis et al. [1989] and calculated by Chi & Leal [1989]. Although the thin film thickens along the axis of symmetry, the volume of fluid contained within the thin film region continues to decrease with time.

For drops that remain nearly spherical (small Bond numbers), the radius of the dimple can be predicted by balancing the pressure in the film against the buoyancy force, giving a dimple radius of $r_d = O(a_1 \mathcal{B})^{1/2}$ [*e.g.* Yiantsios & Davis 1990]. In figure 2.8 we plot the dimple radius against time for the case of $\mathcal{B} = 10$ and $\lambda = 1, 5$ and 20. For all cases the initial dimple radius is about $0.15a_1$ and increases with time. The low Bond number estimate is not valid for these highly deformed drops since dimple radii greater than the drop radius are predicted. Predicting dimple radii for highly deformed drops is difficult since simple analytical approximations of drop shapes and pressure in the gap are not yet available.

2.3.4 History effects

For each of the above calculations we have assumed that the initial separation distance is $0.5a_1$. In figure 2.9 we show the rate of decrease of gap thickness, dh/dt , for initial separation distances of $0.5a_1$ and $2.5a_1$ and different viscosity ratios. The Bond number is taken to be large enough, $\mathcal{B} = 10$, that large distortions are possible. The

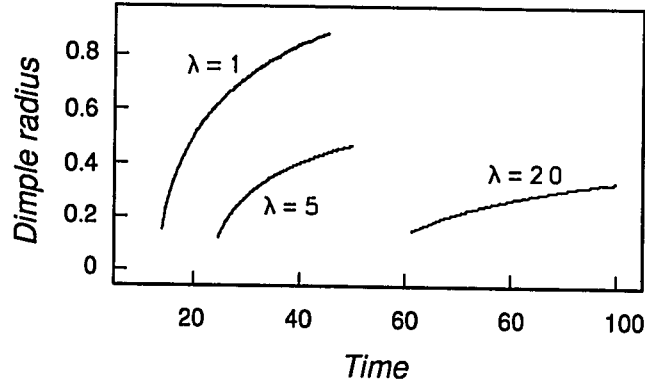


Figure 2.8: Dimple radius (normalized to a_1) as a function of time for viscosity ratios $\lambda = 1, 5$ and 20 ; $B = 10$; $a_1/a_2 = 2$. The initial dimple radius is about $0.15a_1$ for all cases.

results in figure 2.9 demonstrate that for small dimensionless separation distances h , the approach velocity dh/dt is smaller at a given h for larger initial separations. If the initial separation distance is large ($2.5a_1$), the corresponding drop distortions are larger: larger initial separations provide more time for deformation.

From the numerical simulations, we observe that for the drop pairs with $\lambda = 1$ and 5 , the dimple forms at larger separations h which leads to smaller rates of approach dh/dt when two different initial conditions are compared at the same separation distance. For the case with $\lambda = 0.2$ dimples do not develop during the simulation. We note that although dh/dt initially increases for $\lambda = 0.2$ for the small initial separation distance (because the large trailing drop becomes a prolate ellipsoid and is extended) the separation distance between the center-of mass of the two drops decreases monotonically.

2.3.5 Comparison with analytical results

Here we consider the extent to which analytical results may be applied to describe the on-axis interaction of deformable drops. In figure 2.10 we show the rate of decrease

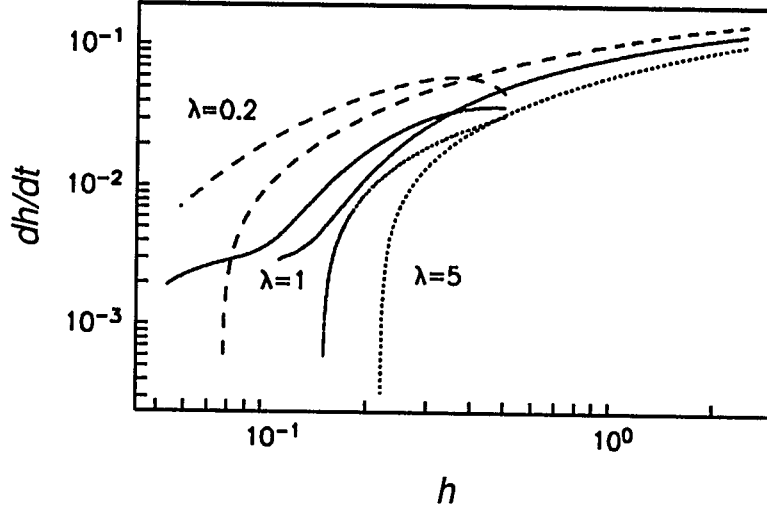


Figure 2.9: The effects of initial drop separation distances. Examples are shown for $\lambda = 0.2, 1$ and 5 with $\mathcal{B} = 10$ and initial separation distances of $0.5a$ and $2.5a$; $a_1/a_2 = 2$. The initial configuration does not change results qualitatively.

of gap thickness, dh/dt , as a function of the dimensionless separation distance h , for (i) two numerical simulations ($\mathcal{B} = 1$ and 10 ; $\lambda = 1$) indicated by the solid curves, (ii) the results of a lubrication analysis indicated by a dotted line, and (iii) an exact solution for spherical drops in bipolar coordinates indicated by a dashed curve.

The lubrication analysis which combines lubrication theory and boundary integral methods [Barnocky & Davis 1989; Davis et al. 1989] is applicable to spherical shapes characteristic of small Bond numbers, $\mathcal{B} \ll 1$, and not surprisingly differs significantly from the behaviour of moderately distorted drop pairs characteristic of larger Bond numbers, $\mathcal{B} > 1$. Exact solutions in bipolar coordinates for spherical drops [Haber et al. 1973] are reasonably accurate for deformable drops when separation distances are large and thus the drops have not distorted to a significant degree. As the separation distance decreases, the analytical result for the rate of approach overpredicts the deformable drop result. The calculated and analytical results differ by less than 10% for separation distances greater than $0.8a_1$ for $\mathcal{B} = 10$ and $0.07a_1$ for $\mathcal{B} = 1$.

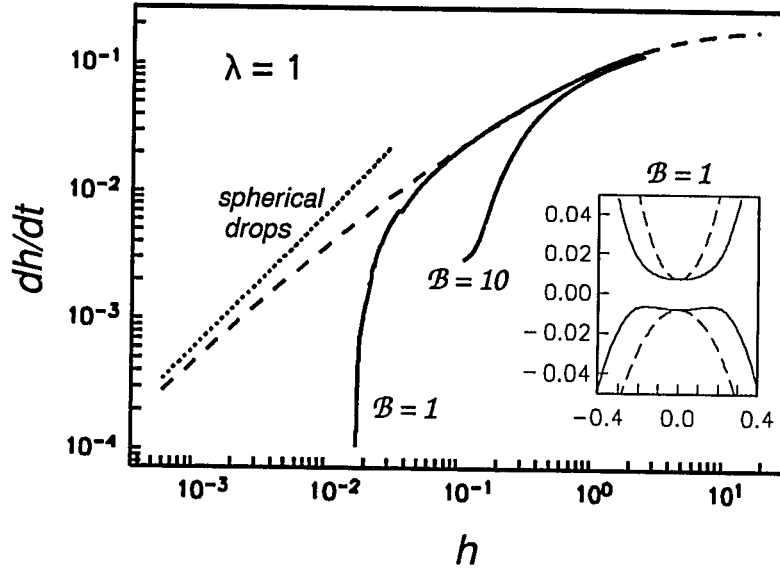


Figure 2.10: Comparison of boundary integral results with analytical results for spherical drops; $\lambda = 1$; $a_1/a_2 = 2$. Numerical results are shown by solid curves for $B = 1$ and $B = 10$. The bipolar coordinate solution is shown by a dashed curve [Haber et al. 1973]. The combined lubrication theory and boundary integral analysis for spherical drops is shown by a dotted line [Davis et al. 1989]. The inset shows a (distorted) magnification of the geometry of the gap between the drops with solid curves for $B = 1$ at $h = 0.02$; the shapes of spherical drops, with the same volume, are shown by dashed curves.

Although the drops for $B = 1$ appear to be nearly spherical (figure 2.6c), the inset of figure 2.10 shows a magnification of the thin gap between the deformable drops (solid line) and undeformed spherical drops with the same volume (dashed line). Clearly, the area over which fluid in the gap is squeezed is much larger for the deformed drops, and the mode of film flow is characterized by uniform drainage. For comparison, the results of Yiantsios & Davis [1990] show that for drops with $B \ll 1$ approaching a deformable surface, the rate of film drainage decreases from $dh/dt \propto h^{1/2}$ for large and moderate gap thicknesses h , (characteristic of spherical drop solutions [Davis et al. 1989; Haber et al. 1973] to $dh/dt \propto h^4$ along the axis of

symmetry and $dh/dt \propto h^{5/2}$ for the minimum gap thickness (at the rim of the dimple) when h becomes very small. For comparison, we find numerically that $dh/dt \propto h^{4.3}$ at $h = 0.02$ and $r = 0$ for the case with $B = 1$ in figure 2.10.

2.3.6 Cusps and tails

In the experiments (later stages in figure 2.1) and in the calculations (*e.g.* figure 2.6*h*), regions of very high curvature develop at the back of the trailing drop or bubble. Two features of the flow contribute to the development and maintenance of interfaces with high curvatures. First, by analogy to the formation of pointed ends on a drop in a steady extensional flow, where the radius of curvature of the end of the drop scales as B^{-3} [*e.g.* Acrivos 1983], we might expect that the flow behind the trailing drop, which locally resembles an extensional flow, may allow a tail with a region of high curvature to develop. Second, while the spherical drop shape exactly satisfies the normal stress balance [Batchelor 1967] and is stable to infinitesimal distortions for $B < \infty$, the effect of the leading drop is to allow the trailing drop to become prolate, and thus to become unstable for large Bond numbers [Koh & Leal 1989; Pozrikidis 1990]. The combination of the local extensional flow and a distorted prolate shape allow the drop to be extended and the tail to develop.

Regions of very high curvature also develop at the rim or edge of the coating drop (see figure 2.1 and figure 2.6*c*) where the flow is locally extensional. Near the rim of the coating drop the flow is locally two-dimensional since the thickness of the coating drop is much smaller than the radius of the larger drop.

Recent studies of two-dimensional free-surface flows by Joseph et al. [1991] (experiments) and Jeong & Moffatt [1992] (experiments and theory) have demonstrated that regions of very high curvature, which may appear macroscopically to be cusps, may develop even for systems with finite interfacial tension. The two drop interactions shown here fall into the category of flows which allow regions of high curvature to develop.

2.4 Concluding remarks

In this chapter we have considered the time-dependent buoyancy-driven interaction between two axisymmetric low Reynolds number deformable drops in the limit that buoyancy forces dominate over restoring interfacial tension forces. For axisymmetric configurations, the film drainage between the drops may be characterized by three distinct modes: (i) rapid drainage for which the thinnest region of the film is on the axis of symmetry, (ii) uniform drainage for which the film has a nearly constant thickness, and (iii) dimple formation. As the separation distance between the two drops decreases, the mode of film drainage may change from rapid drainage to uniform drainage and eventually a dimple may form. The numerical calculations presented here cover Bond numbers $1 \leq \mathcal{B} < \infty$ and viscosity ratios $0.2 \leq \lambda \leq 20$. For a given viscosity ratio (*e.g.* $\lambda = 1$) the separation distances at which the dimple begins to form is larger for intermediate Bond numbers ($\mathcal{B} = 10$) than for very large or very small Bond numbers ($\mathcal{B} = \infty$ and 1). The separation distance between the drops at which a dimple begins to form decreases as the drop viscosity contrast decreases. Lubrication theory results and combined lubrication theory–boundary integral analyses [Barnocky & Davis 1989; Yiantsios & Davis 1990; Davis et al. 1989], which are appropriate for $\mathcal{B} \ll 1$, differ significantly from the behaviour of drops for $\mathcal{B} > 1$. Exact solutions in bipolar coordinates for spherical drops [Haber et al. 1973] are reasonably accurate for deformable drops when drop separation distances are large.

Chapter 3

Interaction and stability of offset drops

In this chapter we consider the hydrodynamic interaction between two horizontally offset deformable drops and bubbles. We present experimental results for air bubbles in corn syrup, and two-dimensional and three-dimensional boundary integral calculations in order to demonstrate that the effects of deformation due to drop interactions may result in the alignment and eventual coalescence of initially horizontally offset drops. The effects of deformation which promote the coalescence of drops should lead to an enhanced rate of coalescence in suspensions of buoyant deformable drops and bubbles.

3.1 Introduction

We consider the stability of the axisymmetric drop configuration studied in chapter 2. Stability is examined by considering the tendency for an initially off-axis configuration to evolve either towards or away from an aligned configuration. Again we consider the case of a large drop translating behind a smaller drop, however, the centers-of-mass are initially offset horizontally. Experimental results are presented in §3.2, and a qualitative explanation for the evolution of off-axis configurations is presented in

§3.3. Numerical solutions of an analogous two-dimensional geometry are presented in §3.4 to provide an improved quantitative understanding. In general the two drop free-boundary problem is difficult for nonaligned drops, and numerical solutions are complicated by the necessity of treating three-dimensional geometries. Previous analytical studies of two drop interactions have been limited to spherical shapes. Some of the features characteristic of drop interaction and deformation at low Reynolds numbers have been observed in finite-difference/front-tracking numerical studies at finite Reynolds numbers for both two-dimensional and three-dimensional drops [Unverdi & Trygvasson 1992]. In §3.5 we present some three-dimensional boundary integral calculation to demonstrate the importance of relative drop size, interfacial tension characterized by the Bond number, and viscosity ratios on the deformation and alignment of horizontally offset drops and the expected eventual coalescence of drops.

The interactions between two drops model a great many two body interactions common in multiphase sedimentation processes – a quantitative understanding of two particle interactions is the starting point for studies which attempt to characterize the behaviour (sedimentation rate and coagulation rate) of suspensions. In chapter 4 we consider analytically the two drop problem studied numerically and experimentally in this chapter. The results presented below demonstrate that sufficiently deformable drops (moderate to large Bond numbers, low viscosity ratios) with only modest horizontal displacements will interact in a manner which induces alignment. The alignment of deformable drops owing to hydrodynamic interactions increases the likelihood of coalescence of buoyancy-driven drops. Hence final configurations similar to the results presented in chapter 2 are obtained. We note that drop interaction and alignment may produce uneven concentrations of drops and bubbles in dispersed multiphase systems, analogous to the inhomogeneities which develop in suspensions of nonspherical particles [*e.g.* Koch & Shaqfeh 1989], see chapter 6.

3.2 Interaction of offset bubbles: Experimental results

In figures 3.1 we show examples of two types of interactions between air bubbles rising in a large container of corn syrup. The interactions leading to alignment arise as a consequence of the *deformation* of the bubbles. The Reynolds numbers in these experiments are small, $\mathcal{R} \approx 5 \times 10^{-3}$, and the Bond numbers are large, $\mathcal{B} \approx 20$.

The experiment in figure 3.1*a* illustrates a process we will refer to as drop alignment, which is a far-field interaction, where the long-range, interaction-induced deformation of the bubbles leads to a lateral component of translation and the eventual alignment of the bubbles. The two bubbles start about one bubble radius apart and eventually align and coalesce over a translational distance of about five bubble radii.

The experiment in figure 3.1*b* illustrates a short range process in which the small bubble is advected around the larger bubble and is “sucked” or entrained into the larger bubble, finally translating vertically with an almost axisymmetric configuration prior to eventually coalescing. Coalescence occurs shortly after the last photographs shown in each sequence in (a) and between the last two photographs shown in (b). The difference between the experiment shown in figure 3.1*b* and the experiment shown in figure 3.1*a* is that the initial horizontal separation distance was sufficiently large that the small bubble does not coat the larger trailing bubble.

The experimental results indicate that the axisymmetric two drop configuration studied in chapter 2 is a stable geometry in the limit of large Bond numbers since bubble and drop deformations lead to alignment. For both experiments shown in figure 3.1 we note the large degree and complexity of deformation of both bubbles and the formation of tails and regions of high curvature.

In the chapter 5 we present a more detailed experimental analysis of the two air bubble interaction.

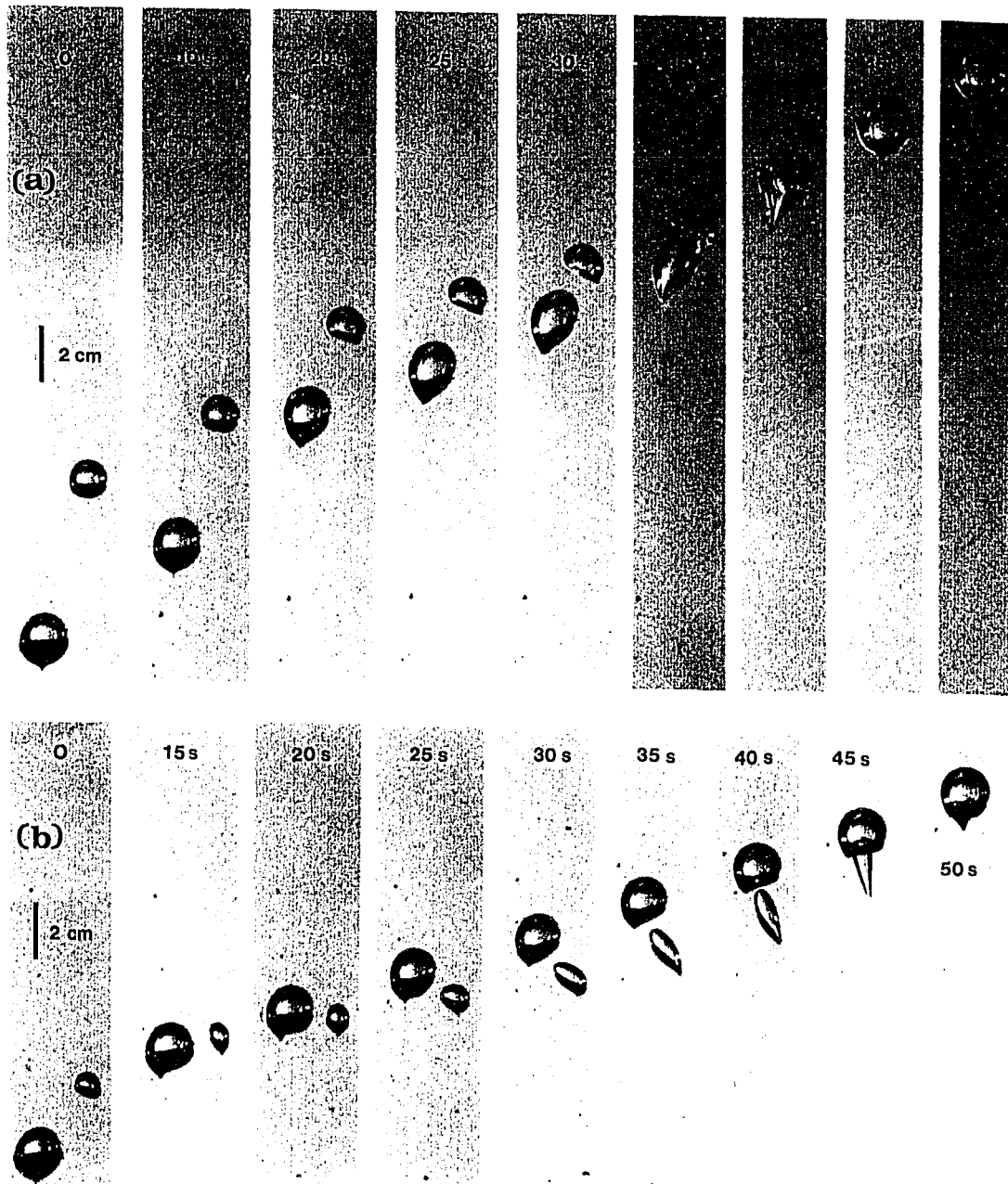


Figure 3.1: Interaction and deformation of two air bubbles rising in a large container of corn syrup: (a) alignment and (b) "suction" or entrainment of bubbles which are initially horizontally offset. The Reynolds number, $\mathcal{R} \approx 10^{-3}$, and the Bond number, $\mathcal{B} \approx 20$. Times and a scale bar are shown on the photographs.

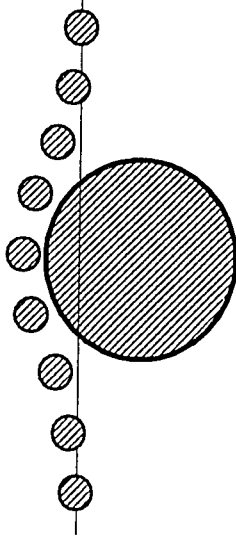


Figure 3.2: Illustration of the interaction between non-deformable spherical drops. Owing to the reversibility property of Stokes flows, the horizontal offset between the drops is preserved as the small drop is swept around the larger drop.

3.3 Flow-induced deformation leading to alignment

As a preliminary, we note that the corresponding problem of two translating spherical drops evolves so that, relative to a reference frame translating with the larger sphere, the small sphere is swept around toward the back, as shown in figure 3.2. The off-axis configuration is unstable as a consequence of the hyperbolic stagnation point at the front of the larger drop (the stagnation point at the front and back of the large drop exists in a frame of reference moving with the large drop).

For the dynamics shown in figure 3.1a, it is straightforward to provide a qualitative explanation, schematically illustrated in figure 3.3, for the alignment of offset deformable drops. The alignment occurs since the long range effect of drop interactions (figure 2.4) is to deform the trailing drop into a prolate shape, suitably inclined with respect to the vertical; the leading drop is deformed into an oblate shape. Owing

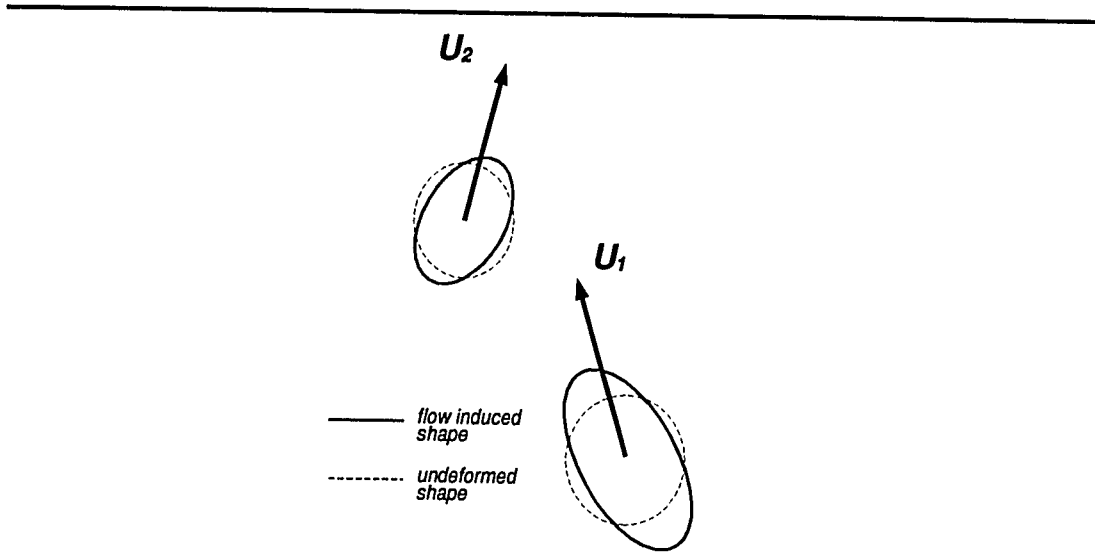


Figure 3.3: Illustration of the mechanism for the alignment of two rising deformable drops. The deformation of each drop by the flow produced by the other drop, as shown in figure 2.4, allows the drops to translate with velocities U_1 and U_2 which have horizontal components that favour alignment.

to the deformation, each drop has a horizontal component of velocity in a direction opposite to that shown in figure 3.2. If deformation is sufficiently large, the horizontal velocities may favour alignment, as indicated in figure 3.3. In chapter 4 we calculate the deformation-induced velocity in the limit of small shape distortions.

We suggest that the second type of two drop interaction (figure 3.1*b*), in which the small drop is first advected around the larger drop and then sucked in from behind, is the result of short range dynamics owing to the deformation of the larger drop. The dynamics are dictated by the continual deformation of the larger drop so that in a frame of reference moving with the larger drop, streamlines will not be contained entirely within the drop, as they are for spherical drops. Deformation at the back of the drop results in closed streamlines which leave and re-enter the drop defining a vortex or “wake”, which is illustrated numerically in figure 3.4*a* for an axisymmetric drop. Thus, a neutrally buoyant fluid element in the region behind the leading drop

may be advected into the cavity which develops behind the deforming leading drop. In figure 3.4*b* we show numerical calculations of the streamlines (again in a frame of reference moving with the front of the leading drop) for an axisymmetric two drop geometry (the volume of trailing drop is $1/4$ the volume of the leading drop). The effect of the second drop is to increase the extent of the vortex outside the leading drop. A sufficiently deformable drop partly located in the vortical region will tend to be entrained. At higher Reynolds numbers a similar entrainment phenomenon occurs for two spherical drops owing to the formation of a low pressure wake [*e.g.* deNevers & Wu 1972]. We emphasize the distinction between the high Reynolds number dynamics, and the low Reynolds number dynamics shown in figure 3.1*b* which rely on the deformation of the drop.

3.4 Numerical results: Two-dimensional calculations

A full three-dimensional treatment of the boundary integral equations (the geometry required to study offset drops) requires the numerical description of a twice differentiable three-dimensional surface. The boundary integral method has been used to study three-dimensional free-surface problems, but has been limited to modest deformations [*e.g.* deBruijn 1989; Pozrikidis 1992]. We first introduce a simplification and consider two-dimensional (cylindrical) drops. A two-dimensional geometry allows us to consider the most important feature of the problem, namely, the horizontal offset. To the extent that such two-dimensional simulations represent the important dynamical processes of the three-dimensional problem, the results presented below provide an improved understanding of the nature of two drop interactions. We will see that the two-dimensional calculations reproduce the qualitative behaviour of two drop systems for both types of two drop interactions observed in the experiments shown in figure 3.1. Three-dimensional calculations are presented in §3.5 and chapter 5.

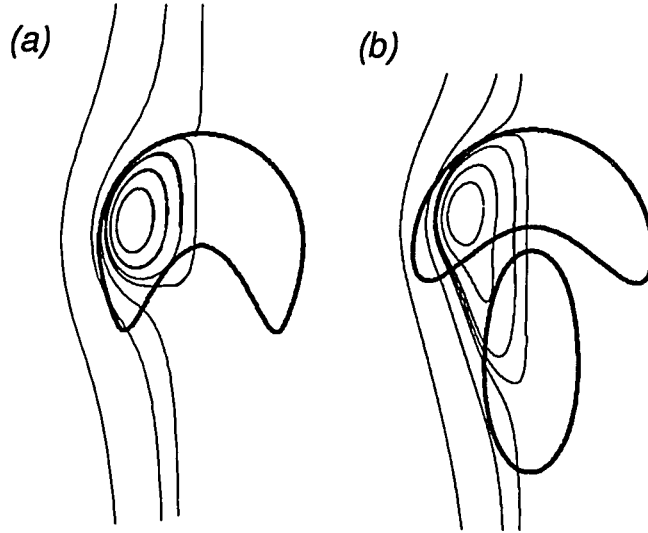


Figure 3.4: Streamlines, relative to the translating drop, (a) for a single deforming drop, and (b) for a pair of drops (the volume of the trailing drop is $1/4$ the volume of the leading drop); $\mathcal{B} = 50$; $\lambda = 1$. Notice that the streamlines leave the drop and travel through the developing cavity at the back of the drop. Thus, fluid elements in the cavity will be entrained into the drop. The effect of the second drop is to further extend the vortex outside the leading drop. An axisymmetric geometry is assumed and the streamlines are calculated using the boundary integral method described in Appendix A and chapter 2.

The boundary integral method has had limited application to buoyancy-driven two-dimensional free-boundary problems [e.g. Newhouse & Pozrikidis 1990]. An important consideration with two-dimensional Stokes flows is the logarithmic behaviour of the velocity kernel which in unbounded domains leads to Stokes paradox. We eliminate this difficulty by including a planar free-slip lower surface; boundary conditions for the planar surface are accounted for by using the appropriate image system. The lower boundary has the physical effect of creating tails on drops due to viscous resistance by the planar surface. However, the development of a tail does not have a noticeable effect on the dynamics of drop interaction. The parameters which describe

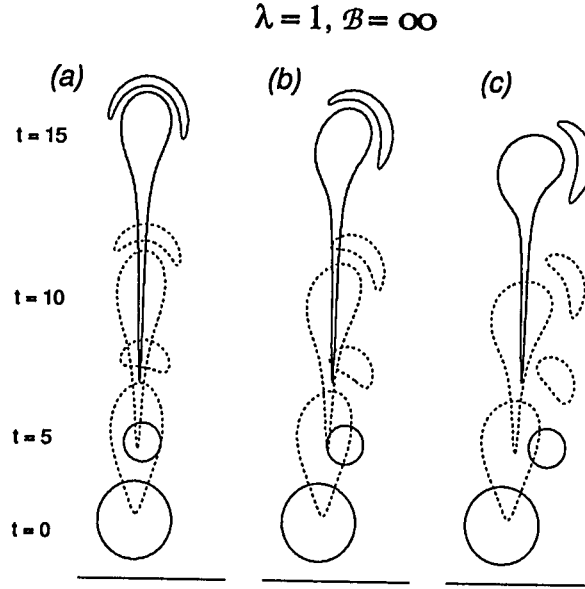


Figure 3.5: The effect of initial configuration. Results are shown for three different offsets; $\lambda = 1$; $\mathcal{B} = \infty$; $a_1/a_2 = 2$. The horizontal line represents a free-slip lower planar surface.

the two-dimensional problem are the same as the parameters describing axisymmetric drops. The numerical implementation follows the discussion given in chapter 2 and Appendix A; the kernel functions and image singularities are given in Appendix A.

In figure 3.5 we show three simulations for different horizontal offsets for the case $\lambda = 1$ and zero interfacial tension. As the initial horizontal offset increases, the tendency of the smaller leading drop to spread over the larger trailing drop decreases. Even for large offsets, the deformation of the leading drop is large owing to the long range nature of Stokes flows. For the axisymmetric two drop interactions studied in chapter 2, a tail develops on the trailing drop owing to the deformation induced by the leading drop, and the natural instability of nonspherical shapes when the interfacial tension is small [Kojima et al. 1984]; the tail which develops in the two-dimensional calculations is larger because of the presence of a nearby free-slip surface.

In figure 3.6 we show that provided the drops can sufficiently resist deformation,

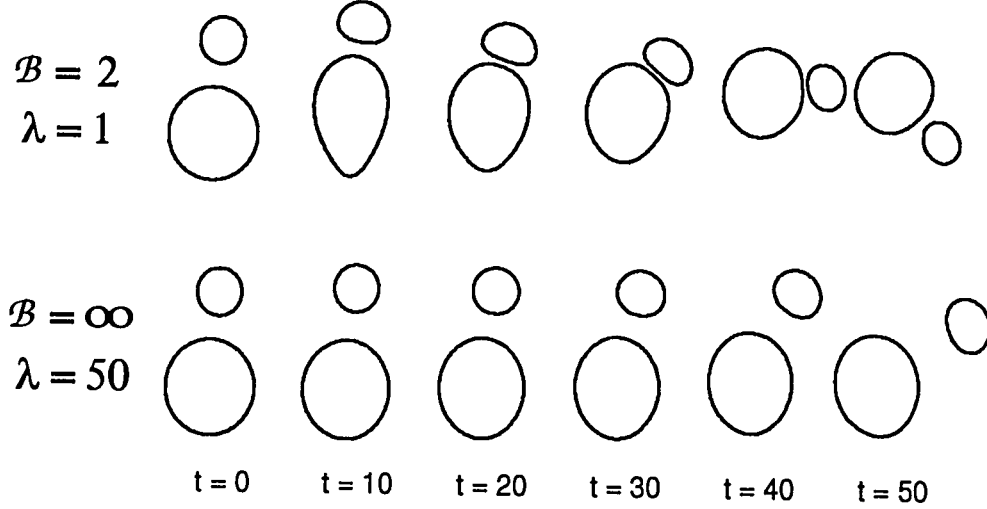


Figure 3.6: The effect of interfacial tension and drop viscosity on drop interactions illustrated in a frame of reference translating with the drops. The initial geometry is the same as the initial geometry in figure 3.5a. Calculations are shown for $\lambda = 1$ and $\mathcal{B} = 2$ and $\lambda = 50$ and $\mathcal{B} = \infty$; $a_1/a_2 = 2$. For both cases the small drop is swept around the leading drop, whereas in the previous figure the small drop coats the large drop. The horizontal planar surface is not shown.

by either having a large viscosity contrast or large interfacial tension, then the small drop may be swept around the large drop. Specifically we show calculations for $\lambda = 50$ and $\mathcal{B} = \infty$, and $\lambda = 1$ and $\mathcal{B} = 2$. Since the drops translate very large distances in the simulations shown in figure 3.6, typically about 40 drop radii, we show drop shapes at different times in a frame of reference moving with the drops. The initial drop configuration is the same as the initial configuration for the drops in figure 3.5a. In both cases shown in figure 3.6 the small drop is swept around the large drop. However, the interaction between the two drops differs in the two cases. For large viscosity ratios (such as the $\lambda = 50$ case) the separation distance between the drops remains large since the fluid between the drops is squeezed out slowly due to the small amount of flow in the drop. For the case of $\lambda = 1$ the fluid can drain more quickly

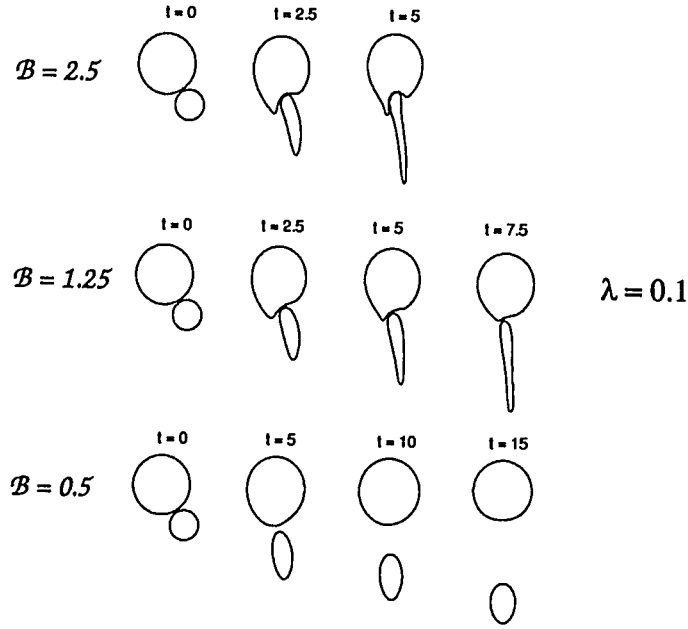


Figure 3.7: The effect of interfacial tension on the interactions between a small drop trailing a larger drop illustrated in a frame of reference moving with the drops. Calculations are shown for $\mathcal{B} = 2.5, 1.25$ and 0.5 ; $\lambda = 0.1$; $a_1/a_2 = 2$ (Bond number based on the trailing drop). For large enough Bond numbers, the small drop may be entrained into the larger drop owing to the deformation of the larger drop. The horizontal planar surface is not shown.

and the drops remain in very close proximity.

Finally, in figure 3.7, we illustrate the importance of drop deformation on the “suction” or entrainment of a small trailing drop by a larger drop. As in figure 3.6, we show drop shapes at different times in a frame of reference translating with the front of the large drop. Simulations are shown for $\lambda = 0.1$ (which allows for rapid and larger drop distortions) and $\mathcal{B} = 0.5, 1.25$ and 1.5 (where the Bond number is based on the radius of the smaller trailing drop). For large interfacial tension, $\mathcal{B} = 0.5$, the small drop is left behind. Notice however that the drops are eventually aligned. For smaller interfacial tension, $\mathcal{B} = 2.5$, the larger drop is indented and the trailing small

drop is advected into the developing cavity. At times greater than $t = 5$ the drops numerically make contact and the simulation is stopped. In the two-dimensional simulations, we found that the initial separation distance needed to be very small in order for the small drop to be entrained into the larger drop. This quantitative feature is not a feature of the experimental results presented in figure 3.1*b*.

3.5 Numerical results: Three-dimensional calculations

The numerical solution of three-dimensional free-boundary problems is difficult and only limited work has been done using the boundary integral approach. Previous work has considered the deformation of neutrally buoyant drops in shear flows in the limit of modest shape distortions [*e.g.* Rallison 1981; Kennedy et al. 1993; deBruijn 1989]. Below we present three-dimensional numerical calculations of the buoyancy-driven translation of drop which we believe are the first for buoyancy-driven interactions and deformations, and the first simulations to consider large interface distortions. Details of the numerical procedure and implementation are discussed in Appendix C. Briefly, the numerical method involves discretizing the drop surfaces by a mesh of 3200 triangular surface elements and a grid of 382 collocation points. All surface variables (normals and curvatures) are assumed to vary linearly over each surface element. Integration is performed using 7 point Gaussian quadrature. The interface is advected at each time step using an Euler time step. Typically we use 500 time steps in the simulations reported below. Since the three-dimensional calculations are extremely expensive computationally, calculations were performed for drops with the same viscosity as the surrounding fluid ($\lambda = 1$).

In figures 3.8, 3.10 and 3.12 we show interface shapes of buoyant translating drops at different times. In figure 3.8 we consider the effect of the initial horizontal offset, in figure 3.10 we consider the effect of interfacial tension characterized by the Bond number, and in figure 3.12 we consider the effect of the relative drop size. Corre-

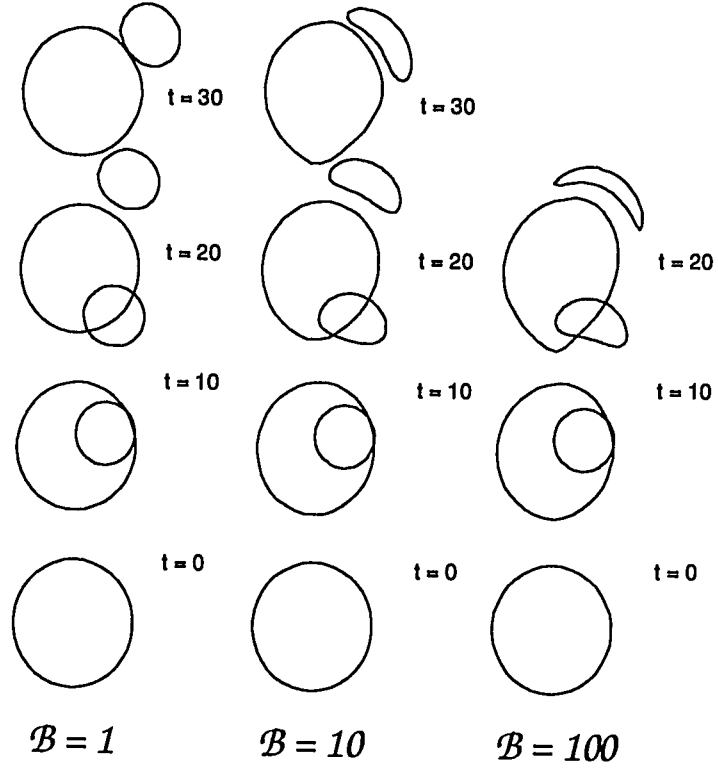


Figure 3.8: Three-dimensional boundary integral calculations illustrating the effect of interfacial tension (Bond number) on the alignment of three-dimensional offset drops for $\mathcal{B} = 1, 10$ and 100 ; $\lambda = 1$, $a_2/a_1 = 0.5$.

sponding to the simulations presented in figures 3.8, 3.10 and 3.12 we also present computed trajectories of the center-of-masses of the drops in figures 3.9, 3.11 and 3.13, respectively. Presenting the drop trajectories allows for a more direct and quantitative comparison of the importance of deformation and relative drop orientation on drop interactions.

We begin by presenting a few results, derived in the following chapter, which will provide insight into the hydrodynamics of interacting drops. First, the relative

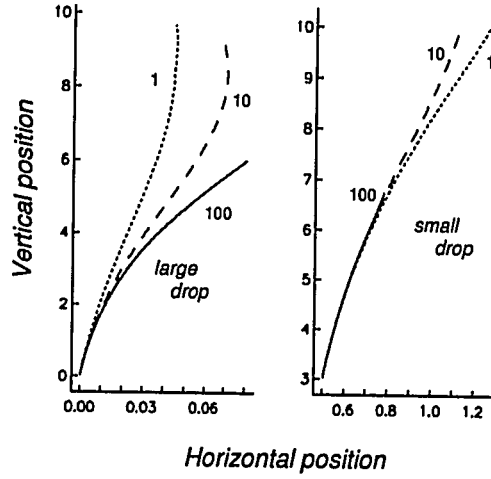


Figure 3.9: The effect of interfacial tension (Bond number) on the trajectories of three-dimensional offset drops for $B = 1, 10$ and 100 corresponding to dotted, dashed and solid curves, respectively; $\lambda = 1$, $a_2/a_1 = 0.5$. Trajectories correspond to the drop shapes presented in figure 3.8.

magnitude of drop distortion ϵ_i of drop i is given by (§4.2.3)

$$\frac{\epsilon_1}{\epsilon_2} = \left(\frac{a_2}{a_1} \right)^2. \quad (3.1)$$

Second, to leading order, the correction to the rise speed of each drop is described by the first reflection (a “push” on the leading drop by the trailing drop and a “pull” on the trailing drop by the leading drop). The additional speed of drop 1, δU_1 , due to drop 2 is given by (§4.1.2)

$$\delta U_1 = O \left(\frac{\Delta \rho g a_2^3}{\mu d} \right) \quad (3.2)$$

and the additional speed of drop 2, δU_2 , due to drop 1

$$\delta U_2 = O \left(\frac{\Delta \rho g a_1^3}{\mu d} \right) \quad (3.3)$$

where d is the separation distance between the drops. Finally, we note that in the limit of small distortions the magnitude of drop deformation is $O(aBa^2/d^2)$ and thus the correction to the rise speed of the drop is $O(U^{(0)}Ba^2/d^2)$, where $U^{(0)}$ is the Hadamard-Rybzinski rise speed (§4.4).

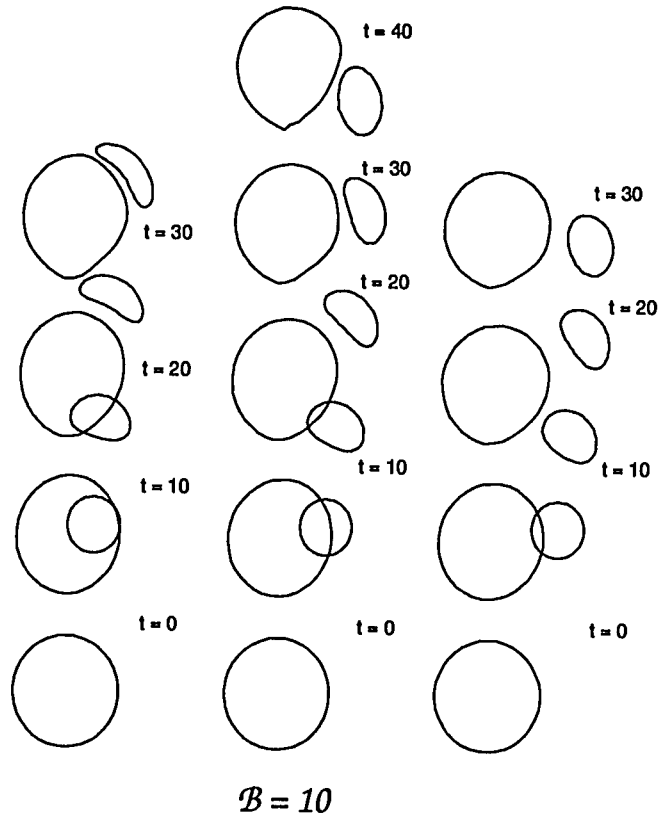


Figure 3.10: Three-dimensional boundary integral calculations illustrating the effect of initial horizontal offset on the alignment of three-dimensional offset drops for initial horizontal offsets of $0.5a_1$, $0.9a_1$ and $1.3a_1$; $\mathcal{B} = 10$, $\lambda = 1$, $a_2/a_1 = 0.5$.

3.5.1 Effects of interfacial tension (Bond number)

In figures 3.8-9 we consider the effect of interfacial tension, described by the Bond number, on the alignment of drops. We present three simulations for the same initial condition but different Bond numbers; $\mathcal{B} = 1$, 10 and 100, $\lambda = 1$, and $a_2/a_1 = 0.5$. For $\mathcal{B} = 1$ the drops remain nearly spherical and the small drop does not coat the larger drop, whereas for $\mathcal{B} = 100$ the small drop is flattened by the trailing drop and coats the trailing drop. The thickness of the film of fluid trapped between the drops also decreases most rapidly for the $\mathcal{B} = 1$ simulation, similar to the observations presented

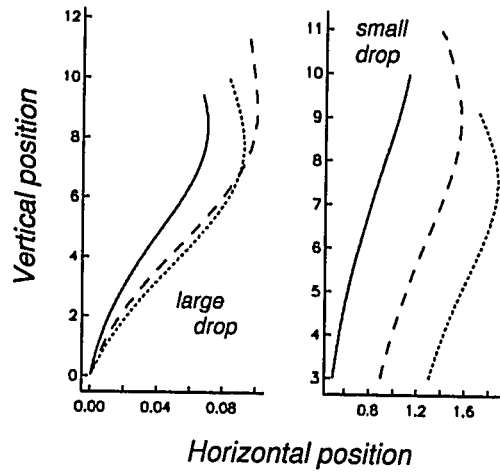


Figure 3.11: The effect of initial horizontal offset on the trajectories of three-dimensional offset drops for initial horizontal offsets of $0.5a_1$, $0.9a_1$ and $1.3a_1$ corresponding to solid, dashed and dotted curves, respectively; $\mathcal{B} = 10$, $\lambda = 1$, $a_2/a_1 = 0.5$. Trajectories correspond to the shapes presented in figure 3.10.

in figures 2.3 and 2.6. The effects of deformation on the translation of the drops are observed in the trajectories shown in figure 3.9. For the simulation with $\mathcal{B} = 100$, the larger trailing drop experiences a greater horizontal drift, due the greater shape distortion. The effects of deformation on the trajectories of the small drops is less noticeable since the effects of deformation are small compared to contribution from the first reflection, equation (3.5).

3.5.2 Effects of horizontal offset

In figure 3.10-11 we consider the effect of the initial horizontal offset of the alignment of drops. Results are presented for initial horizontal offsets of $0.5a_1$, $0.9a_1$ and $1.3a_1$; $\mathcal{B} = 10$, $a_2/a_1 = 0.5$ and $\lambda = 1$. As the initial horizontal offset is increased the magnitude of deformation decreases. There are two reasons for the decrease in the magnitude of deformation: first the separation distance between the drops increases as the initial horizontal offset increases, and second, the magnitude of deformation

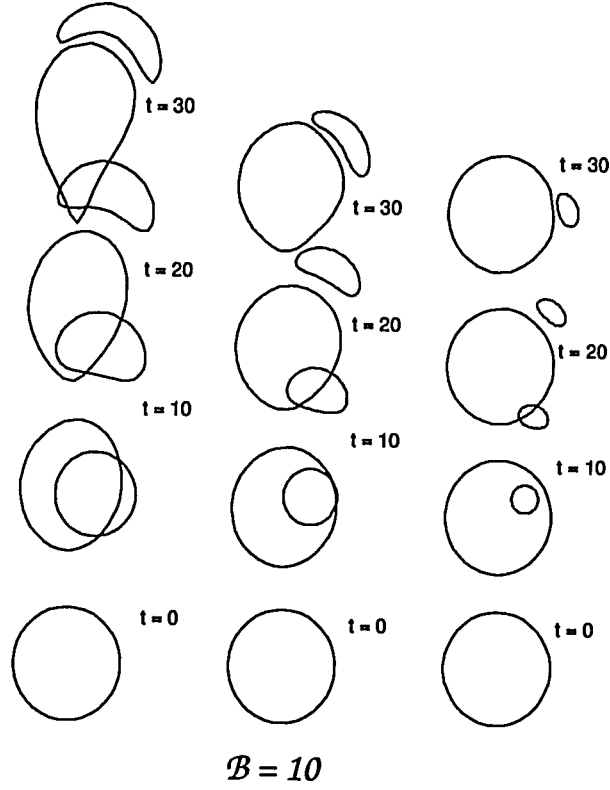


Figure 3.12: Three-dimensional boundary integral calculations illustrating the effect of relative size on the alignment of three-dimensional offset drops for size ratios (a_2/a_1) of 0.75, 0.5 and 0.25; $\mathcal{B} = 10$, $\lambda = 1$.

depends on the relative orientation of the drops. The magnitude of deformation is

$$\epsilon = O\left(a|\hat{\mathbf{d}} \cdot \hat{\mathbf{g}}|\mathcal{B}\frac{a^2}{d^2}\right), \quad (3.4)$$

where $\hat{\mathbf{d}}$ is a unit vector joining the centers of the two drops and $\hat{\mathbf{g}}$ is a unit vector in the vertical direction (see §4.3). In the figure showing drop trajectories, we also observe that as the initial horizontal offset increases the translation distance over which the large drop overtakes and passes the smaller drop decreases.

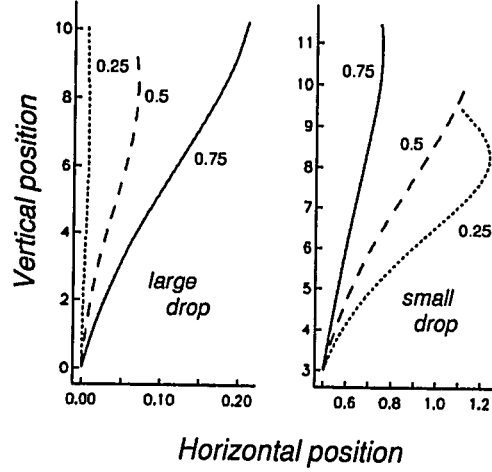


Figure 3.13: The effect of relative drop size on the trajectories of three-dimensional offset drops for size ratios (a_2/a_1) of 0.75, 0.5 and 0.25 corresponding to solid, dashed and dotted curves, respectively; $B = 10$, $\lambda = 1$. Trajectories correspond to the shapes presented in figure 3.12.

3.5.3 Effects of relative drop size

Finally, in figures 3.12-13 we consider the effect of the relative drop size on the alignment of drops. Results are presented for size ratios $a_2/a_1 = 0.75, 0.5$ and 0.25 ; $B = 10$ and $\lambda = 1$. The initial horizontal offset between the center-of-mass of the drops is identical in all three simulations. From the drop shapes, figure 3.12, we observe that as the relative drop size decreases, the likelihood of alignment decreases: for $a_2/a_1 = 0.75$ the small drop coats the larger drop whereas for $a_2/a_1 = 0.25$ the small drop is advected around the larger drop. We also note that, as in the previous results, the magnitude of deformation of the small drop is always greater than the larger drop, as expected from equation (3.1). From the figure showing drop trajectories we observe that the horizontal translation of the larger drop in the simulation with $a_2/a_1 = 0.25$ is small since the contribution of the first reflection to the rise speed of the larger drop is small.

3.6 Concluding remarks

We have shown experimentally that the interaction between initially horizontally offset deformable drops may result in the alignment and eventual coalescence of the drops, demonstrating that the axisymmetric two-drop problem studied in the previous chapter is a stable geometry. Thus, many of the features studied in chapter 2, namely the dynamics of the film drainage problem, are relevant to the interaction of deformable drops in suspensions since geometries similar to the axisymmetric problem will be produced as a result of drop alignment or entrainment. The importance of deformation on drop interactions and coalescence is highlighted by observing in the experimental results shown in figure 3.1*b* that bubbles separated by more than the sum of their radii may eventually coalesce. Deformation due interactions will result in a greatly enhanced rate of coalescence in suspensions of deformable drops and bubbles (chapter 5). In the following chapter we will demonstrate, using far-field approximations, that deformable drops migrate towards each other provided $\mathcal{B} > O(d/a)$, where d is the separation distance between the drops.

Although the spherical drop assumption, commonly employed in most investigations, allows for the development of many analytical results and approximations, in the limit of moderate to large Bond number, typically $\mathcal{B} > 1$, drops become highly deformed, and results based on spherical drops may become invalid. Some characteristics of drop interaction cannot be predicted by assuming spherical drop shapes, such as the alignment of drops owing to interaction-induced deformation and the coating of large drops by smaller drops. Although we have not included the effects of surfactants, we expect that the results presented in chapters 2 and 3 may qualitatively describe the behaviour of drops where the interfacial tension is greatly reduced by the presence of surfactants.

Chapter 4

Long range drop interactions

In this section we study analytically the lateral translation of two drops arising from their interaction-induced deformation. We demonstrate explicitly that the degree of deformation, controlled primarily by the Bond number and the separation distance between two drops, determines whether two drops will eventually coalesce.

There are three analytical features necessary to calculate the shape-induced migration. The method of reflections [*e.g.* Happel & Brenner 1965; Leal 1992] is used in §4.2 to determine the approximate velocity field in the neighbourhood of each drop. The local velocity gradient deforms the drop and the deformation is calculated in §4.3 using standard procedures for nearly spherical, distorted drops. The translational velocity induced by the nonspherical shape is then calculated in §4.4 using the Reciprocal theorem [*e.g.* Haj-Hariri et al. 1990]. We will assume for simplicity that both drops are composed of the same fluid.

4.1 Scaling analysis: An overview of drop alignment by flow-induced shape changes

Consider two widely separated drops, labeled 1 and 2, rising in an unbounded fluid at low Reynolds numbers (figure 4.1). The vector \mathbf{d} indicates the direction and magnitude of the separation between the centers of the two drops. We will always

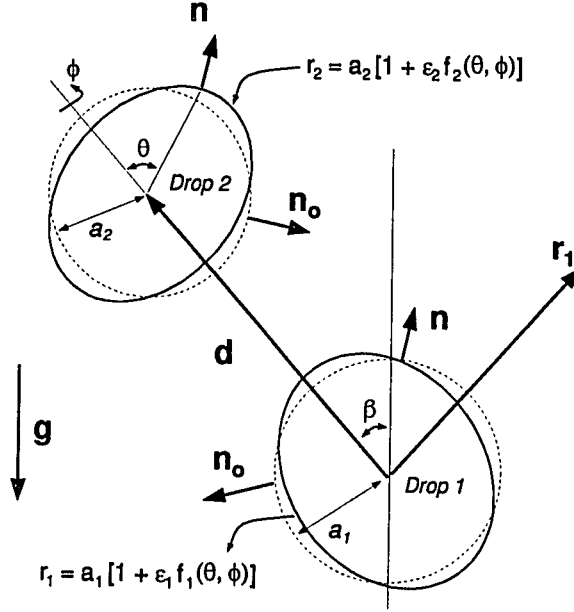


Figure 4.1: Geometry of the two drop problem and definition of the normals \mathbf{n} and \mathbf{n}_o and the spherical polar coordinate system. Drops 1 and 2 have radii a_1 and a_2 , respectively, and are separated by a distance d and are oriented at angle β with respect to gravity.

choose drop 1 to be the trailing drop, and define a Bond number based on the radius of drop 1

$$\mathcal{B} = \frac{\Delta \rho g a_1^2}{\sigma}. \quad (4.1)$$

4.1.1 Translation of a single drop in an unbounded fluid

Each drop will rise, to a first approximation, as though alone in an unbounded fluid. The rise speed as a function of the viscosity ratio λ is given by the Hadamard-Rybczyński result

$$\mathbf{U}_i^{(0)} = -\frac{2(1+\lambda)}{3(2+3\lambda)} \frac{\Delta \rho a_i^2}{\mu} \mathbf{g} \quad i = 1, 2, \quad (4.2)$$

where the subscript i is used to denote drops 1 or 2. In the limit that $\lambda \rightarrow 0$ (bubble), $U^{(0)} = -\Delta \rho g a^2 / 3\mu$ and in the limit $\lambda \rightarrow \infty$ (rigid sphere) $U^{(0)} = -2\Delta \rho g a^2 / 9\mu$.

4.1.2 Method of reflections

Drop 2 experiences an $O(U_1^{(0)}a_1/d)$ change to the Hadamard-Rybczyński velocity owing to the long-range interaction with drop 1. Physically, we can think of the first reflection of $O(Ua/d)$ as representing the additional translation speed of each drop due to the flow created by the other drop: drop 2 is “pushed” by drop 1, whereas drop 1 is “pulled” by drop 2. If the drops remain spherical, the next correction to the rise speed is $O(U_1^{(0)}a_1^3/d^3)$ [Kim & Karrila 1991]. However, when deformation occurs, we will show that there is a translational velocity component due to the nonspherical shape.

4.1.3 Shape distortion

Let ϵ_i measure the small distortion away from a spherical shape. The far-field velocity gradient generated by drop 1 in the vicinity of drop 2 is U_1a_1/d^2 . A balance of viscous stresses, $\mu U_1a_1/d^2$, by the interfacial tension stresses of drop 2, $\epsilon_2\sigma/a_2$, which tend to keep the drop nearly spherical, leads to a small shape distortion with magnitude

$$\epsilon_2 = \frac{a_1^3a_2\Delta\rho g}{\sigma d^2} = \mathcal{B} \left(\frac{a_1a_2}{d^2} \right). \quad (4.3)$$

A similar analysis for drop 1 gives

$$\epsilon_1 = \frac{a_1a_2^3\Delta\rho g}{\sigma d^2} = \mathcal{B} \left(\frac{a_2^3}{a_1d^2} \right). \quad (4.4)$$

We note that the small drop is always more deformed than the larger drop (see figures 2.3, 3.7, 3.8 and 3.12). Although restoring interfacial tension stresses are larger for small drops, scaling as $\epsilon_2\sigma/a_2$ for drop 2, the viscous stresses deforming drop 2 are proportional to a_1^3 . Thus, the size of the other drop controls the magnitude of drop distortion. The relative magnitude of distortion

$$\frac{\epsilon_1}{\epsilon_2} = \left(\frac{a_2}{a_1} \right)^2 \quad (4.5)$$

By contrast, for $\mathcal{B} \ll 1$, the larger drop becomes more deformed than the smaller drop [Yiantsios & Davis 1991].

The small distortions are oblate for the leading drop and prolate for the trailing drop, *e.g.*, figure 2.3. We will demonstrate that the $O(\epsilon)$ shape distortion leads to an $O(\epsilon U^{(0)})$ contribution to the drops' translational velocity, with particular importance assigned to the horizontal component of translation which may lead to alignment. Thus, drop alignment depends on the relative magnitudes of a/d and ϵ . We will show that drop deformation should lead to drop alignment in an on-axis configuration when

$$\mathcal{B} > O\left(\frac{d}{a}\right). \quad (4.6)$$

Nevertheless, there is an upper bound on the small deformation analysis we describe which requires $\mathcal{B} < O(d/a)^2$.

4.1.4 Quasi-steady assumption

Implicit in arriving at equations (4.3) and (4.4), a quasi-steady small distortion is assumed; the drop deforms in response to the viscous stresses created by the motion of the other drop on a timescale τ_d for deformation that is less than the timescale τ_a over which the separation distance d changes. Estimates of these timescales for drop 2 are

$$\tau_d \approx a_2(1 + \lambda)\mu/\sigma \quad \text{and} \quad \tau_a \approx d/|U_1 - U_2|, \quad (4.7)$$

where the factor of $1 + \lambda$ indicates that the largest fluid viscosity controls the rate of drop deformation. The quasi-steady assumption neglects explicit time-dependence in the free-boundary problem, and thus, requires that

$$\mathcal{B} < \frac{d}{(1 + \lambda)|1 - a_2^2/a_1^2|a_2}. \quad (4.8)$$

For nearly equal sized drops, large separation distances, and $\lambda < O(1)$ the right hand side of equation (4.8) is very large and the assumption of rapid shape adjustment to changes in the local flow is justified. For (4.3-4) and (4.8) to be consistent the drops must have similar radii so that the local flow near either drop changes slowly. For equal sized drops, $\tau_a \approx \epsilon U^{(0)}$ (see §4.4), and thus leads to the constraint

$$\mathcal{B}^2 < O\left(\frac{d^3}{a^3}\right) \quad (4.9)$$

which is less restrictive than (4.8). The quasi-steady assumption, though restrictive, is assumed in the analysis below.

4.2 Migration of spherical drops: Application of the method of reflections

As a first approximation we assume the drops are spherical. Let \mathbf{r}_i denote the position vector relative to the center of drop i (see figure 4.1). The velocity field due to the translation of drop i in an unbounded fluid is

$$\mathbf{u}_i^{(0)}(\mathbf{r}_i) = \frac{2\pi(2+3\lambda)}{(1+\lambda)} a_i \left[1 + \frac{\lambda a_i^2}{2(2+3\lambda)} \nabla^2 \right] \mathbf{J}_i \cdot \mathbf{U}_i^{(0)} \quad (4.10)$$

where

$$\mathbf{J}_i(\mathbf{r}_i) = \frac{1}{8\pi} \left(\frac{\mathbf{I}}{r_i} + \frac{\mathbf{r}_i \mathbf{r}_i}{r_i^3} \right). \quad (4.11)$$

$\mathbf{U}_i^{(0)}$ is the Hadamard-Rybczyński given by equation (4.2), and the superscript (0) is used to denote that this velocity is the first approximation to the detailed velocity field. There are a few interesting features of the flow field described by equation (4.10), as discussed in Hinch [1988].

1. The velocity field decays as $O(U^{(0)}a/r)$ for large r . The external flow field described by (4.10) includes a flow created by a point force, $2\pi(2+3\lambda)a \mathbf{J} \cdot \mathbf{U}^{(0)}/(1+\lambda)$, which decays as $U^{(0)}a/r$ and a contribution due to the finite size of the drop $\pi\lambda a^3 \nabla^2 \mathbf{J} \cdot \mathbf{U}^{(0)}/(1+\lambda)$ which decays as $U^{(0)}(a/r)^3$.
2. At large distances r away from the drop, the disturbance speed in front or behind the drop is twice as large as the disturbance speed at a distance r to the side of the drop.
3. Streamlines created by a translating drop diverge in front of the drop, and converge behind the drop, see figure 2.4.

Each drop will move faster owing to the interaction with the far-field flow produced by the other drop. The change in translational velocity is proportional to the speed of the other drop, with a magnitude that decays as $O(U^{(0)}a/d)$. The corrected rise speed of drop 1 is caused by drop 2 and has a value $\mathbf{u}_2^{(0)}(\mathbf{r}_2 = \mathbf{d})$; thus drop 1 translates with velocity

$$\begin{aligned}\mathbf{U}_1 &= \mathbf{U}_1^{(0)} + \left(\frac{a_2}{d}\right) \mathbf{U}_1^{(1)} + O(U_2^{(0)}a_2^3/d^3) \\ &= \mathbf{U}_1^{(0)} + \frac{(2+3\lambda)}{4(1+\lambda)} \frac{a_2}{d} [\mathbf{U}_2^{(0)} + \mathbf{U}_2^{(0)} \cdot \hat{\mathbf{d}}\hat{\mathbf{d}}] + O\left(U_2^{(0)} \frac{a_2^3}{d^3}\right)\end{aligned}\quad (4.12)$$

where $\hat{\mathbf{d}} = \mathbf{d}/|\mathbf{d}|$ is a unit vector in the direction of the line-of-centers of the two drops, directed from drop 1 to drop 2 (figure 4.1). Similarly, drop 2 rises with velocity

$$\mathbf{U}_2 = \mathbf{U}_2^{(0)} + \frac{(2+3\lambda)}{4(1+\lambda)} \frac{a_1}{d} [\mathbf{U}_1^{(0)} + \mathbf{U}_1^{(0)} \cdot \hat{\mathbf{d}}\hat{\mathbf{d}}] + O\left(U_1^{(0)} \frac{a_1^3}{d^3}\right). \quad (4.13)$$

The horizontal separation distance between the drops increases or decreases due to the difference in horizontal velocities, ΔU_H , given by

$$\Delta U_H = \frac{\Delta \rho g a_1^3}{6\mu d} \sin \beta \cos \beta \left[1 - \left(\frac{a_2}{a_1}\right)^3\right], \quad (4.14)$$

where we observe that equation (4.14) is independent of the viscosity ratio λ . We note that if drop 1 is larger than drop 2, the case of interest here, then the horizontal separation distance will increase for spherical drops ($\Delta U_H > 0$), whereas, if drop 2 is larger than drop 1 the separation distance will decrease ($\Delta U_H < 0$), in agreement with the illustration shown in figure 3.2. In the following section we consider the correction to the translational velocity arising from drop deformation with magnitude $\mathcal{B}(a/d)^2$, *e.g.* equation (4.3). For the horizontal separation distance to decrease (for the drops to align as in figures 3.1 and 3.3) we then require that $\mathcal{B} > O(d/a)$ to counteract the drifting described by equations (4.12-14).

Higher order reflections, to $O((a/d)^4)$, may be derived by considering the second derivative terms in Faxen's relations. The rise speed of two drops, accurate to $O((a/d)^6)$ is given in Kim & Karrila [1990].

4.3 Shape calculation

The contribution of the second reflection to the flow-field due to translating spherical drops produces corrections that are $O(U^{(0)}(a/d)^3)$ [Kim & Karrila 1991]. The corrections due to the second reflection are smaller than the high Bond number non-spherical shape corrections which we now describe.

In the vicinity of drop 2 the velocity field produced by drop 1 may be represented as a Taylor series

$$\mathbf{u}_1(\mathbf{r}_1 = \mathbf{d} + \mathbf{r}_2) = \mathbf{u}_1|_{\mathbf{r}_1=\mathbf{d}} + \mathbf{r}_2 \cdot \nabla \mathbf{u}_1|_{\mathbf{r}_1=\mathbf{d}} + \dots \quad (4.15)$$

The velocity gradient $\nabla \mathbf{u}_1|_{\mathbf{r}_1=\mathbf{d}}$ in the neighbourhood of drop 2 is responsible for drop deformation. Using the velocity field in equation (4.10) we find that

$$\nabla \mathbf{u}_1|_{\mathbf{r}_1=\mathbf{d}} = -\frac{(2+3\lambda)a_1}{4(1+\lambda)d^2} [\mathbf{I}\hat{\mathbf{d}} \cdot \mathbf{U}_1^{(0)} - 3\hat{\mathbf{d}}\hat{\mathbf{d}}\hat{\mathbf{d}} \cdot \mathbf{U}_1^{(0)} - \hat{\mathbf{d}}\mathbf{U}_1^{(0)} + \mathbf{U}_1^{(0)}\hat{\mathbf{d}}]. \quad (4.16)$$

We will assume that the deformed shape of drop 2 may be described in spherical coordinates (r, θ, ϕ) by

$$r_2 = a_2 [1 + \epsilon_2 f_2(\theta, \phi)], \quad (4.17)$$

where $\epsilon_2 \ll 1$. A drop immersed in a linear flow, $\mathbf{r}_2 \cdot (\nabla \mathbf{u}_1)$, is distorted into an ellipsoidal shape [Taylor 1932], described by

$$\epsilon_2 f_2(\theta, \phi) = \frac{\mu a_2 (16 + 19\lambda)}{8\sigma(1 + \lambda)} \mathbf{n}_o \cdot (\nabla \mathbf{u}_1) \cdot \mathbf{n}_o \quad (4.18)$$

where \mathbf{n}_o is a unit normal to a spherical drop. In the derivation of (4.18) the quasi-steady boundary condition $\mathbf{u} \cdot \mathbf{n}_o = 0$ is used. The quasi-steady approximation is justified provided the timescale for drop deformation by viscous stresses is shorter than the timescale for changes in the local flow producing the deformation, as discussed in §4.1.4. Thus, using equations (4.16)-(4.18) and definition of the Bond number given by equation (4.1), the steady deformed shape of each drop is an ellipsoid described by second degree Legendre polynomials as

$$r_2 = a_2 \left[1 + \mathcal{B} \left(\frac{a_2}{a_1} \right) \left(\frac{a_1}{d} \right)^2 \frac{(16 + 19\lambda)}{48(1 + \lambda)} [1 - 3(\hat{\mathbf{d}} \cdot \mathbf{n}_o)^2] \hat{\mathbf{d}} \cdot \hat{\mathbf{g}} \right] \quad (4.19)$$

and

$$r_1 = a_1 \left[1 - \mathcal{B} \left(\frac{a_2}{a_1} \right) \left(\frac{a_2}{d} \right)^2 \frac{(16 + 19\lambda)}{48(1 + \lambda)} [1 - 3(\hat{\mathbf{d}} \cdot \mathbf{n}_o)^2] \hat{\mathbf{d}} \cdot \hat{\mathbf{g}} \right] \quad (4.20)$$

where $\hat{\mathbf{g}}$ is a unit vector in the vertical direction (parallel to \mathbf{g}). The drop shapes in the experiments in figures 2.1 and 3.1 and the numerical calculations eventually lose the ellipsoidal symmetry as the separation distance a/d becomes small and ϵ becomes large.

In equations (4.19) and (4.20) the small parameter ϵ can be identified as $\mathcal{B}a_1a_2/d^2$ for drop 2 and $\mathcal{B}a_2^3/a_1d^2$ for drop 1 (as deduced in §4.1.3). For simplicity, in the discussion that follows we refer to the small deformation of either drop as having magnitude $O(\mathcal{B}a^2/d^2)$.

As expected on physical grounds, or from a sketch of the streamlines, the leading drop deforms into an oblate spheroid whereas the trailing drop is deformed into a prolate spheroid. We may expect by analogy to the motion of ellipsoidal rigid particles in low Reynolds number flows that the ellipsoid shapes will migrate in a manner tending to promote on-axis configurations (and possibly coalescence). We now calculate explicitly this translational velocity. Rather than solving for the flow field and then computing the translational velocity, we will use the Reciprocal theorem to provide a direct calculation of the velocity.

4.4 Translational velocity from the Reciprocal theorem

The above analysis suggests a small $O(\mathcal{B}a^2/d^2)$ correction to the local description of the flow field owing to the drop's deformation. Since a/d and \mathcal{B} are independent parameters we seek the next order correction to the velocity field, $\mathcal{B}(a/d)^2 \mathbf{u}^{(2)}(\mathbf{r})$, satisfying the Stokes equations both inside and outside the drop. This analysis corresponds to the translation of an isolated slightly deformed drop in an otherwise quiescent fluid. Thus, we seek solutions for the approximate translational velocity in

the form

$$\mathbf{U}(a/d, \mathcal{B}) = \mathbf{U}^{(0)} + \left(\frac{a}{d}\right) \mathbf{U}^{(1)} + \mathcal{B} \left(\frac{a}{d}\right)^2 \mathbf{U}^{(2)} + O\left(U^{(0)} \frac{a^3}{d^3}\right). \quad (4.21)$$

Provided $\mathcal{B} > O(d/a)$ the dominant correction to the migration velocity arises from the third term on the right hand side. Furthermore, so long as $\mathcal{B} > O(a/d)$, shape modifications are at least as important as the $O(a/d)^3$ corrections calculated using the method reflections for spherical drops.

The boundary conditions satisfied by $\mathbf{u}^{(2)}(\mathbf{r})$ are obtained by using standard domain perturbation techniques whereby all variables are expanded in the neighbourhood of a spherical shape and evaluated at $|\mathbf{r}_i| = a_i$. For this part of the analysis it is convenient to nondimensionalize the equations and boundary conditions. The dimensionless boundary value problem assumes the form (see Appendix D.1)

$$\begin{aligned} \nabla \cdot \mathbf{T}^{(2)} &= 0 & r > 1 & \quad \nabla \cdot \hat{\mathbf{T}}^{(2)} = 0 & r < 1 \\ \nabla \cdot \mathbf{u}^{(2)} &= 0 & & \quad \nabla \cdot \hat{\mathbf{u}}^{(2)} = 0 \end{aligned} \quad (4.22)$$

$$\mathbf{u}^{(2)} - \hat{\mathbf{u}}^{(2)} = \mathbf{A}(\mathbf{n}_o, f) \text{ on } r = 1 \quad (4.23)$$

$$\mathbf{u}^{(2)} \cdot \mathbf{n}_o = B(\mathbf{n}_o, f) + \frac{\mathbf{U}^{(2)} \cdot \mathbf{n}_o}{U^{(0)}} \text{ on } r = 1 \quad (4.24)$$

$$\mathbf{n}_o \cdot \mathbf{T}^{(2)} - \lambda \mathbf{n}_o \cdot \hat{\mathbf{T}}^{(2)} = \mathbf{C}(\mathbf{n}_o, f) \text{ on } r = 1 \quad (4.25)$$

where $\hat{}$ denotes variables inside the drop. The dimensionless functions \mathbf{A} , B and \mathbf{C} are derived in Appendix D.1, and depend on the detailed drop shape $f(\theta, \phi)$.

We can then use the Reciprocal theorem (equation (D34) in Appendix D.2) to obtain the second order velocity correction ¹

$$\begin{aligned} \mathbf{U}^{(2)} = & -\frac{U^{(0)}}{4\pi(2+3\lambda)} \int_S \{[(1+2\lambda)\mathbf{I} + \mathbf{n}_o \mathbf{n}_o] \cdot \mathbf{C}(\mathbf{n}_o, f) + 3\lambda [\mathbf{I} - 3\mathbf{n}_o \mathbf{n}_o] \cdot \mathbf{A}(\mathbf{n}_o, f) \\ & + 3(2+3\lambda)B(\mathbf{n}_o, f)\mathbf{n}_o\} dS, \end{aligned} \quad (4.28)$$

¹The following identities are very useful for integrating products of the unit normal over a spherical surface

$$\int_0^{2\pi} \int_0^\pi n_i n_j \sin \theta d\theta d\phi = \frac{4\pi}{3} \delta_{ij} \quad (4.26)$$

$$\int_0^{2\pi} \int_0^\pi n_i n_j n_k n_l \sin \theta d\theta d\phi = \frac{4\pi}{15} (\delta_{ij} \delta_{kl} + \delta_{ik} \delta_{jl} + \delta_{il} \delta_{jk}). \quad (4.27)$$

Integrals of odd products of the unit normal vector over a spherical surface are zero.

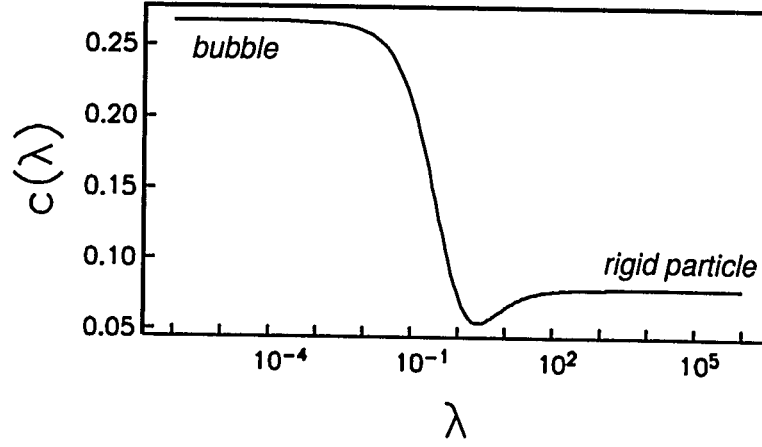


Figure 4.2: The function $c(\lambda)$ defined by equation (4.31).

where S denotes a spherical drop surface. Evaluating the integrals we find

$$\mathbf{U}_1^{(2)} = -c(\lambda)\mathbf{U}_1^{(0)} \cdot \hat{\mathbf{d}} (\mathbf{e}_z \cdot \hat{\mathbf{d}}) [\mathbf{e}_z - 3\mathbf{e}_z \cdot \hat{\mathbf{d}}\hat{\mathbf{d}}] \quad (4.29)$$

and

$$\mathbf{U}_2^{(2)} = c(\lambda)\mathbf{U}_2^{(0)} \cdot \hat{\mathbf{d}} (\mathbf{e}_z \cdot \hat{\mathbf{d}}) [\mathbf{e}_z - 3\mathbf{e}_z \cdot \hat{\mathbf{d}}\hat{\mathbf{d}}] \quad (4.30)$$

where $\mathbf{e}_z = -\hat{\mathbf{g}}$ is a unit vector in the vertical direction and

$$c(\lambda) = \frac{(16 + 19\lambda)(8 - \lambda + 3\lambda^2)}{240(1 + \lambda)^2(2 + 3\lambda)}. \quad (4.31)$$

Note that $c = 4/15$ for a bubble, $c = 19/240$ for a rigid particle, and c has a minimum value for $\lambda \approx 2.64$. The function $c(\lambda)$ is plotted in figure 4.2. The condition that the horizontal separation between the drops decreases (see equation (4.14)) is given by $\mathcal{B}(a_2^3/a_1 d^2)\Delta U_1^{(2)} \cdot \mathbf{e}_x - \mathcal{B}(a_1 a_2/d^2)\Delta U_2^{(2)} \cdot \mathbf{e}_x + \Delta U_H < 0$, *i.e.*,

$$\mathcal{B} > \left(\frac{d}{a_1}\right) \frac{2 + 3\lambda}{24(1 + \lambda)c(\lambda)\cos^2 \beta} \left[\left(\frac{a_1}{a_2}\right)^3 - 1\right]. \quad (4.32)$$

Using the above results we can integrate the drop velocities to determine the trajectory of a pair of drops, assuming a quasi-steady deformation given by the instantaneous separation distance. In figure 4.3 bubble trajectories ($\lambda = 0$) are shown for $\mathcal{B} = 0, 10$ and 50 , and radii ratios $a_2/a_1 = 1$ and 0.95 . The bubbles are separated

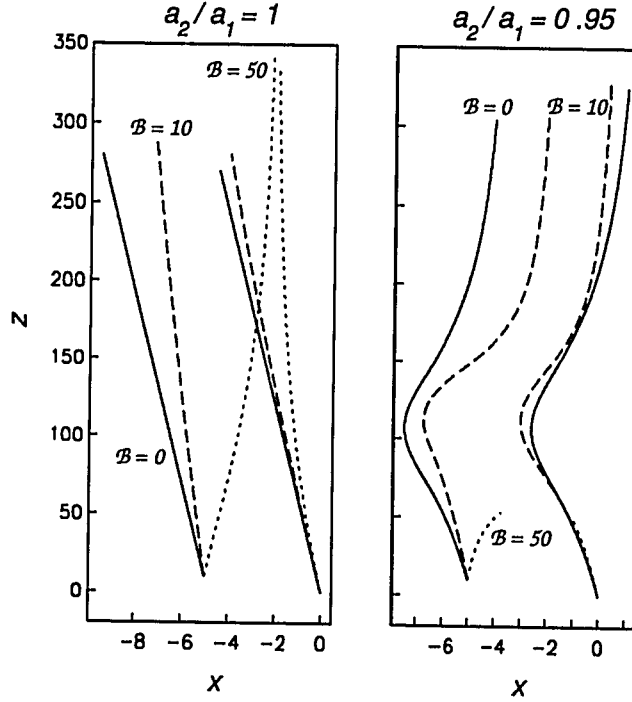


Figure 4.3: Trajectories of two bubbles ($\lambda = 0$) for different values of the Bond number and bubble sizes, in the limit of small deformation. The solid curves are for $B = 0$, the dashed curves for $B = 10$, and the dotted curves for $B = 50$. The curves for $a_2/a_1 = 0.95$ and $B = 10$ are stopped when the bubbles have aspect ratios greater than 2. The bubbles are initially separated by a horizontal distance of $5a_1$ and a vertical distance of $10a_1$.

initially by a horizontal (x) distance of 5 and a vertical (z) distance of 10, where the length scale is normalized to the radius of the larger bubble a_1 . The vertical length scale is compressed significantly. The calculations are stopped when the aspect ratio of one of the bubbles exceeds $3/2$.

For the equal-sized bubbles shown on the left, the $B = 50$ bubbles (trajectories shown with dotted curves) are aligned. For comparison, spherical bubbles ($B = 0$) drift horizontally maintaining the same orientation and separation distance. Even for the $B = 10$ simulation there is a noticeable difference in bubble translation compared

to the simulation for spherical bubbles. When the leading bubble is smaller than the trailing bubble ($a_2/a_1 = 0.95$), the small bubble is swept around the larger one for small Bond numbers, $\mathcal{B} = 0$ and 10. In the $\mathcal{B} = 50$ simulation, the bubbles are aligned and in real systems would be expected to coalesce eventually. The examples shown in figure 4.3 demonstrate explicitly the importance of deformation on drop and bubble interactions, particularly for large Bond numbers.

4.5 Concluding remarks

We have calculated the magnitude of deformation and the translation speed of two interacting drops in the limit that the separation distance between the drops is large, $d/a \gg 1$, the magnitude of the deformation is small so that the drops are near-spheres, $\mathcal{B}(a/d)^2 \ll 1$, so long as a quasi-steady approximation is valid (section 4.1.4). The results demonstrate explicitly that deformation due to interaction acts to align, or tend to align, deformable drops. Note that even equal-size drops will eventually coalesce since the leading drop becomes oblate and thus translates more slowly than the trailing drop which becomes prolate. In the following chapters we apply the two drop results to suspensions of many drops.

Finally, we note that although we have only considered the buoyancy-driven translation of drops in chapters 2-4, drop alignment should also be characteristic of drops driven by other mechanisms. For example, neutrally buoyant drops driven by thermocapillary forces² may also be aligned. For neutrally buoyant drops in a temperature gradient \mathbf{G} , in which the interfacial tension gradient $\nabla\sigma \propto \mathbf{G}$, the external flow is described by

$$\mathbf{u}(\mathbf{r}) \propto \mathbf{G} \cdot \left(\frac{\mathbf{I}}{|\mathbf{r}|^3} - 3 \frac{\mathbf{r} \mathbf{r}}{|\mathbf{r}|^5} \right). \quad (4.33)$$

Streamlines corresponding to (4.33) and flow due to a point force are shown in figure 4.4. Streamlines produced by a drop translating, as a consequence of interfacial

²Flows induced by interfacial tension gradients produced by temperature gradients are called thermocapillary motions.

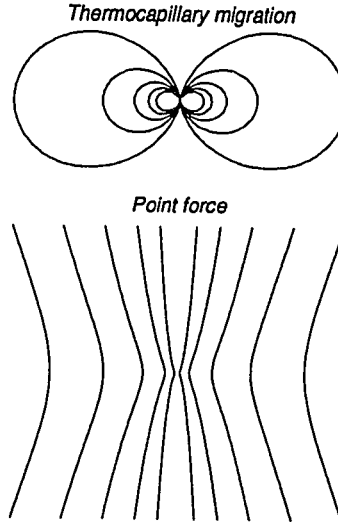


Figure 4.4: The flow produced by a small drop in thermocapillary motion, and the flow produced by a point force. Both flows produce drop deformation which may eventually lead to drop alignment.

tension variations, diverge in front of the drop and converge behind the drop. We expect deformable drops to interact similar to the interaction shown in figure 2.4 and 3.3 (provided the the trailing drop is in a region where the streamlines produced by the leading drop converge, and the leading drop is in a region where the streamlines produced by the trailing drop diverge). The magnitude of the deformation, however, will scale as $O(\mathcal{B}(a/d)^4)$ for thermocapillary flows (where the Bond number $\mathcal{B} = \mu U_c / \sigma$ is based on an average value of σ and the translational velocity U_c) compared to $O(\mathcal{B}(a/d)^2)$ for buoyancy-driven flows. Thus, for thermocapillary-driven motions the process of alignment will be slower than for buoyancy-driven motions since the velocity disturbance and associated deformations are weaker.

Chapter 5

Three drops, four drops, clouds of drops and suspensions

We demonstrate that the interactions which occur between three drops or four drops may be characterized qualitatively by the two drop interactions considered in the previous chapters. Thus the results of two drop studies should be applicable to suspensions of deformable drops. In a dilute monodisperse suspension (a suspension in which all particles have the same size), we calculate the rate of coalescence from the far-field analytical results derived in chapter 4. We determine the rate of coalescence in a dilute polydisperse suspension (a suspension in which particles have different sizes) of bubbles in corn syrup by performing a large number of laboratory experiments, for Bond numbers based on the larger bubble radius in the range $15 < \mathcal{B} < 120$. The rate of coalescence is greatly enhanced owing to the effects of deformation compared to the predictions of models for spherical bubbles which include hydrodynamic interactions among spherical bubbles. The rate of coalescence is even greater than the rate predicted by the Smoluchowski model which ignores *all* hydrodynamic interactions (hydrodynamic interactions result in the small bubble being advected around larger bubbles). The experimental results are used in conjunction with a standard population dynamics model to calculate the evolution of the bubble-size distribution in suspensions.

5.1 Introduction

We are interested in studying the rate of coalescence of particles in a suspension in order to calculate macrophysical properties of the suspension such as the particle-size distribution and the average sedimentation rate.¹ The typical approach to calculating macrophysical properties involves using population dynamics models, and is a standard procedure in the aerosol and hydrosol literature [*e.g.* Friedlander 1977]. Population dynamics models require an understanding of the interactions between the many particles in the suspension. The hydrodynamics of two interacting particles are microphysical properties of the suspension. Previous work for low Reynolds number interactions has considered the interactions between two spherical drops (generally including van der Waals forces) due to Brownian motion [*e.g.* Zhang & Davis 1991], gravitational settling [*e.g.* Zhang & Davis 1991], interfacial tension variations due to surfactant concentration variations or thermocapillary effects [*e.g.* Satrape 1992], or a combination of effects [*e.g.* Zhang et al. 1993].

In this chapter we consider the effects of particle deformation on the evolution of the particle-size distribution and concentration. Deformation is characterized by the

¹Characterizing quantitatively the behaviour of suspensions at low Reynolds number by accounting for all the hydrodynamic interactions has proven to be a challenging problem. Difficulties arise because of the long-range interaction of particles at low Reynolds number. Consider, for example, an attempt to calculate the settling speed of particles in a suspension at low Reynolds numbers. Since disturbance velocities decay as $1/r$ away from a translating particle, equation (4.10), the velocity of a particle \mathbf{U}_p due to the contribution $\Delta\mathbf{u}(\mathbf{r})$ from all other particles at position \mathbf{r} found by integrating over the surrounding fluid volume,

$$\mathbf{U}_p = \mathbf{U}_p^{(0)} + \int \Delta\mathbf{u}(\mathbf{r})p(\mathbf{r})d\mathbf{r}^3 \rightarrow \infty \quad (5.1)$$

where $p(\mathbf{r})$ is the probability of finding another particle at position \mathbf{r} , with $p \rightarrow 1$ as $\mathbf{r} \rightarrow \infty$. The integral (5.1) diverges. The resolution to the apparent paradox was first discussed by Batchelor [1972]. In real problems, boundary effects and back flow due to the presence of a bottom or top on the container containing the particles results in a decrease of the average settling velocity of particles – the presence of a lower boundary requires that the average fluid velocity $\langle \mathbf{u} \rangle$ be zero.

Bond number

$$\mathcal{B} = \frac{\Delta\rho g a^2}{\sigma}. \quad (5.2)$$

We will further assume that the Reynolds number is small, the Peclet number is very large (negligible Brownian motion and diffusion, negligible growth by Ostwald ripening), and interfacial tension variations are negligible. We begin in §5.2 by calculating the buoyancy-driven translation and deformation of drops in systems of either three drops or four drops, and demonstrate that the interaction of drops may be qualitatively described by the two drop interactions studied in chapters 2-4. In §5.3 we discuss the dynamics of particle clouds, discrete regions in space with a greater than average concentration of particles. We then calculate in §5.5 the effects of deformation due to long-range hydrodynamics on the rate of coalescence in a dilute monodisperse suspension. Next we determine experimentally in §5.6 the coalescence rate of bubbles in a dilute polydisperse suspension as a function of the Bond number and relative bubble size. Finally, in §5.7 we use a population dynamics model (following the methodology described in papers by Davis and coworkers) to calculate the bubble-size distribution in suspensions.

5.2 Three drops and four drops

As a preliminary we extend the study of two drop interactions considered in chapters 2-4. We present numerical calculations performed using a three-dimensional boundary integral method (see Appendix C) for the buoyancy-driven translation and deformation of drops in systems containing either three or four drops.

In dilute suspensions, it is commonly supposed that two particle interactions provide a good description of particle interactions in the suspension so that population dynamics models can be based on two particle hydrodynamics. We consider briefly the translation and deformation of three-dimensional buoyant drops with $\lambda = 1$, where λ is the ratio of drop to external fluid viscosity. We demonstrate qualitatively that two drop dynamics describe the interactions in systems with more than two drops.

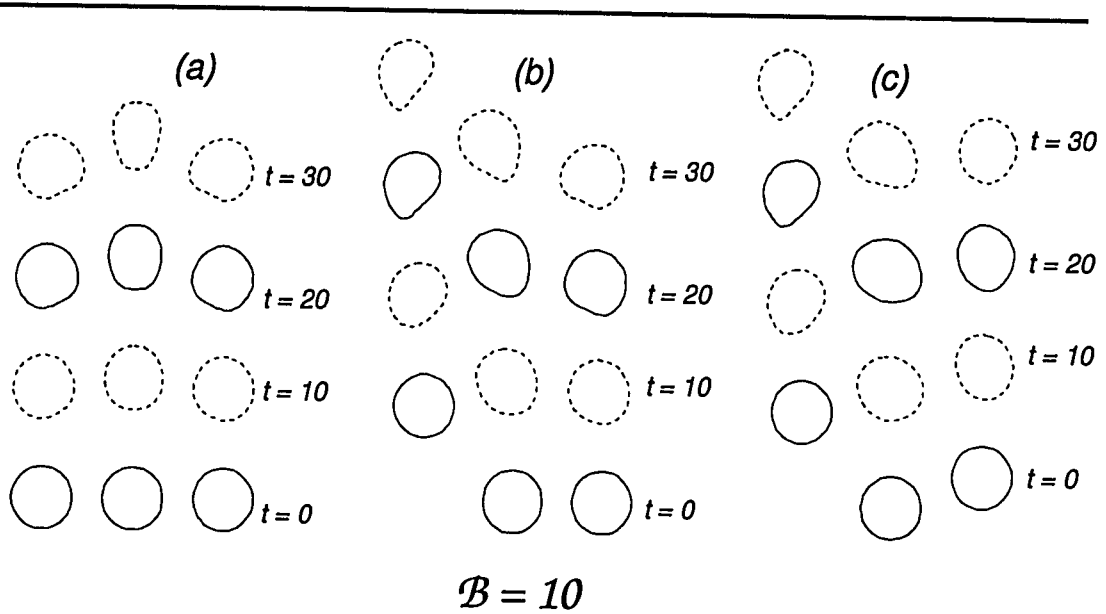


Figure 5.1: Shapes of three three-dimensional drops, for three equal-size drops with different initial vertical offsets but identical horizontal offsets; $\mathcal{B} = 10$, $\lambda = 1$. Cross-sections of drop shapes are shown. No symmetries are assumed in the calculations.

5.2.1 Three drops

In figure 5.1 we present calculated interface shapes for three different simulations of three drop interactions. As in chapter 3, we present cross-sections through the three-dimensional shapes. The initial configurations, *i.e.* the interface shapes at $t = 0$, are different for the three simulations; $\mathcal{B} = 10$, $\lambda = 1$. All the drops have the same undeformed radius. In figure 5.1a showing three initially equally-spaced horizontally aligned drops, the middle drop translates faster than the two outer drops. As with spherical drops, the rise speed of the middle drop is largest owing to the sum of the first reflections (§4.1.2) characteristic of drop interactions: the first reflection for the middle drop gives rise to an $5U^{(0)}a/4d$ correction to its rise speed, whereas the correction to the rise speed of the outer drops is $15U^{(0)}a/16d$, where d is the separation distance between the drops and $U^{(0)}$ is the Hadamard-Rybczyński rise speed (see §4.2). The deformed drop shapes are consistent with predictions based

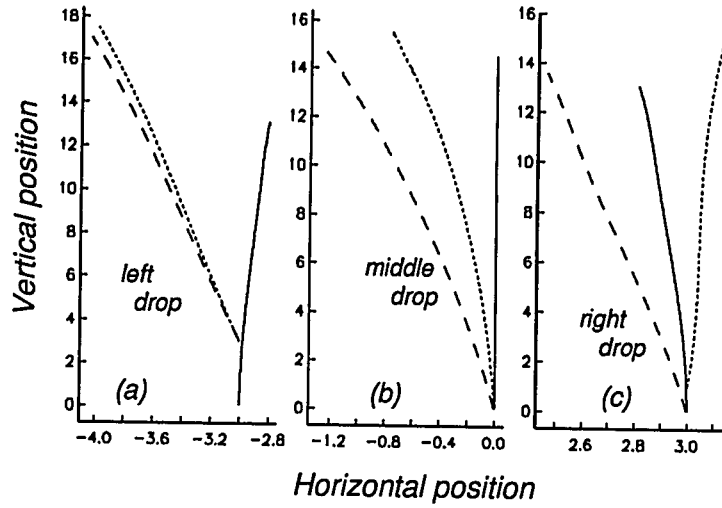


Figure 5.2: Trajectories of three three-dimensional drops, for three equal-size drops with different initial vertical offsets but identical horizontal offsets; $\mathcal{B} = 10$, $\lambda = 1$. Trajectories correspond to the simulations shown in figure 5.1. The solid curves correspond to 5.1a; the dashed curves correspond to 5.1b; the dotted curves correspond to 5.1c.

on figures 2.4 and 3.3: the middle drop is squeezed by the flow created by the outer two drops (so that it becomes elongated in the vertical direction and extended in a direction perpendicular to the page) whereas the outer drops are extended in a direction approximately aligned with a line joining the outer drops with the middle drop.

In chapter 4 we derived analytical expressions for the magnitude of drop deformation due to interactions. To leading order, the magnitude of drop deformation is $O(a\mathcal{B}a^2/d^2)$. However, the magnitude of deformation also depends on the relative orientation of the drops, described by equations (4.19-20), with vertically aligned drops having the largest degree of deformation and horizontally aligned drops exhibiting no deformation. To leading order the shape change, measured relative to a , has magnitude

$$\epsilon = O\left(\mathcal{B}\frac{a^2}{d^2}\hat{\mathbf{d}} \cdot \hat{\mathbf{g}}\right), \quad (5.3)$$

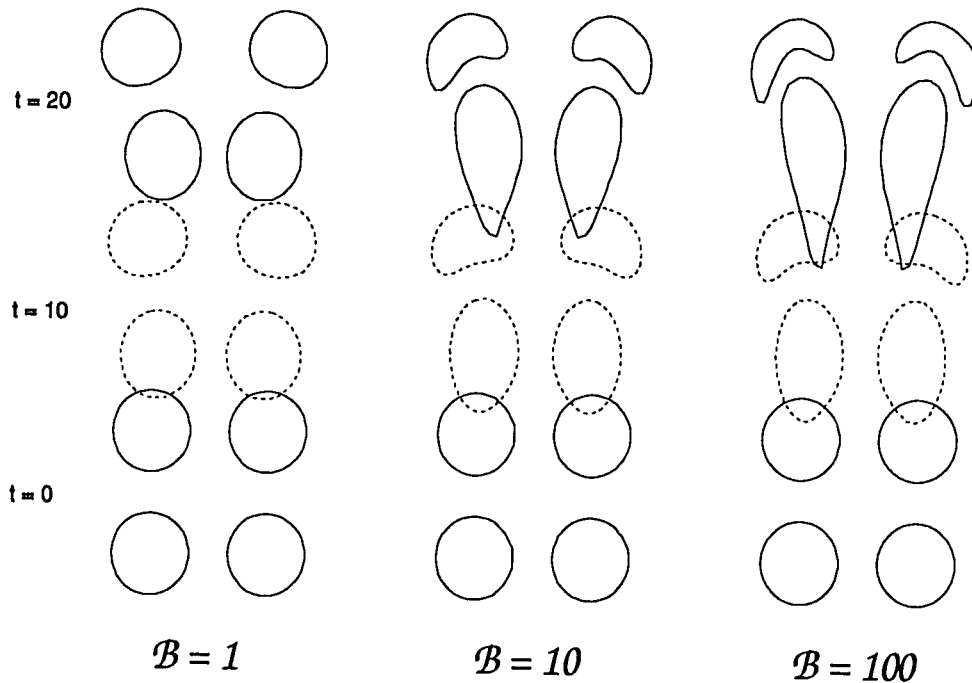


Figure 5.3: Interaction of four three-dimensional drops initially placed in the same plane and forming the sides of a square, for four equal-size drops with $\mathcal{B} = 1, 10$ and 100 ; $\lambda = 1$. Cross-sections of drop shapes are shown. No symmetries are assumed in the calculations.

where $\hat{\mathbf{d}}$ and $\hat{\mathbf{g}}$ are unit vectors in the direction of \mathbf{d} and \mathbf{g} , respectively (see figure 4.1). The effects of relative drop orientation are evident in the two simulations in figure 5.1 with initially vertically offset drops. In both simulations the middle drop is deformed primarily by the drop on the left even though the separation distance between the middle and right drop is less than the separation distance between the middle and left drop. We note that the deformed drop shapes for the middle and left drop are similar to the shapes in simulations with only two drops, such as in figure 5.6. The importance of relative drop orientation is highlighted in figure 5.2 which shows trajectories of the center-of-mass of each of the three drops for the three simulations shown in figure 5.1.

5.2.2 Four drops

In figure 5.3 we show three simulations of four drop interactions, for $\mathcal{B} = 1, 10$ and 100 ; $\lambda = 1$. Again we present cross-sections through the three-dimensional shapes. We first describe the interaction of rising spherical nondeformable drops. The evolution of the four drop system can be deduced by considering the first reflections: the two lower drops approach each other, the two upper drops move away from each other, and the two lower drops rise faster than the outer drops so that they rise and form a horizontal line with the upper drops; the two middle drops continue to rise faster than the outer drops and then move apart while the two outer drops approach each other; a configuration identical to the initial configuration will then arise, however, the lower drops will have replaced the upper drops. The evolution of the system will continue and the drop motion may be described as “leap-frogging” [*e.g.* Hocking 1964; Durlofsky et al. 1987]. If the drops are deformable, for example the simulations shown in figure 5.3, the drops will deform and may coalesce without “leap-frogging”. Again, the importance of the relative orientation of the drops on the shape and magnitude of deformation is apparent in figure 5.3. Qualitatively, the interaction between the right two drops is largely unaffected by the left drops (compare the simulations in figure 5.3 with the simulations presented later in figure 5.6).

5.3 Clouds of drops

If the suspended phase consists of spherical nondeformable buoyant particles uniformly distributed in a finite volume, we call the finite group of particles a particle cloud. The resulting evolution and deformation of the cloud of particles may be described by the motion of a drop with negligible interfacial tension [*e.g.* Hinch 1989]. A spherical cloud of uniformly distributed spherical drops (viscosity $\lambda\mu$ and density $\rho + \Delta\rho$), which remain uniformly distributed, translating in a fluid with viscosity μ and density ρ , far away from any boundaries, rises with speed

$$U_{cloud} = \frac{2(1 + \gamma)}{3(2 + 3\gamma)} \frac{\Delta\rho\phi g R^2}{\mu} \quad (5.4)$$

where R is the radius of the cloud, ϕ is the volume fraction of drops and $\gamma\mu$ is the effective viscosity of the cloud. To leading order, the effective viscosity of the cloud for small volume fractions ϕ is given by [Taylor 1932]²

$$\gamma\mu = \left(1 + \frac{1 + 5\lambda/2}{1 + \lambda}\phi\right)\mu. \quad (5.5)$$

Assuming the analogy between a cloud of particles and a drop of fluid is valid, then a spherical particle cloud will remain spherical provided the cloud is far away from any boundaries. However, if the cloud shape is non-spherical, the shape of the cloud will deform continuously, with an initially oblate cloud developing a cavity inside the cloud and will produce an annular tail following the cloud (figure 1.3). If the shape is initially prolate, the cloud will develop a nearly spherical shape followed by a cylindrical tail (figure 1.3). If the particle cloud is moving towards, through or away from a boundary or deformable interface, then the evolution of the cloud shape will be similar to the results presented later in chapter 8 for $\lambda = 1$.

If the particles are nonspherical, for example they might be ellipsoidal, then an instability is predicted to develop in which local variations of particle concentration will develop resulting in effective density variations [Koch & Shaqfeh 1989]. Similarly we expect that the effects of deformation will result in the coalescence of drops and bubbles and thus a bubble cloud will evolve such that the bubbles which coalesce and thus translate faster will separate from the smallest bubbles least likely to be involved in coalescence events.

5.4 Coalescence in suspensions

Below we provide an overview of a method for determining the evolution of particle size and concentration in dilute suspensions. The method involves first estimating the collision or coalescence rate of two particles, and then developing a population dynamics model to simulate a suspension. In §5.5 we consider the rate of coalescence

²In the limit $\lambda \rightarrow \infty$, $\gamma = 1 + 5\phi/2$, a result first derived by Einstein [1906] (translated version published in *On the theory of brownian motion*, Dover 1956).

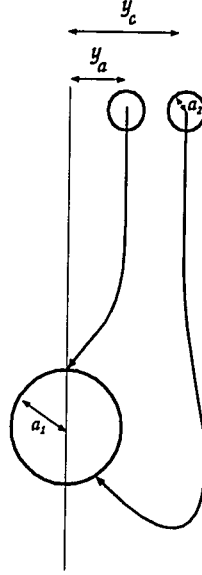


Figure 5.4: Schematic illustration of the collection radius or capture cross-section for interacting drops. The horizontal separation distance between the centers-of-mass of the drops at infinity which separates trajectories which result in alignment from trajectories which result in entrainment is defined as y_a ; the separation distance y_c separates trajectories which result in entrainment from trajectories of bubbles which miss each other.

in monodisperse suspensions, in §5.6 we study experimentally the rate of coalescence of bubbles in polydisperse suspensions of deformable bubbles, and in §5.7 we apply the results of §5.6 to suspensions of bubbles using a population dynamics model.

5.4.1 Collision-frequency function

For a dilute suspension we make the standard approximation that only two particle interactions need to be considered since the probability that a third particle will affect the dynamics is small. The rate at which particles with radius i collide with particles with radius j is given by the collision-frequency function [*e.g.* Davis 1984]

$$J_{ij} = n_i n_j \int_{r=a_i+a_j} p_{ij}(\mathbf{r})(\mathbf{v}_i - \mathbf{v}_j) \cdot \hat{\mathbf{r}} dS, \quad (5.6)$$

where n_i is the number of particles of size i per unit volume, $p_{ij}(\mathbf{r})$ is the pair-distribution function which represents the probability of finding a particle of size i at position \mathbf{r} with respect to the position of particle j , $\mathbf{v}_i - \mathbf{v}_j$ is the difference in velocities of particles of size a_i and a_j , and $\hat{\mathbf{r}}$ is a unit vector in the direction of \mathbf{r} . For notational convenience we will assume that a_i is the radius of the larger of the two drops.

The pair-distribution function p_{ij} satisfies a conservation equation

$$\frac{\partial p_{ij}}{\partial t} + \nabla \cdot (p_{ij}[\mathbf{v}_i - \mathbf{v}_j]) = 0. \quad (5.7)$$

In the limit that $r \rightarrow \infty$, the boundary conditions on the pair-distribution functions are

$$p(\mathbf{r})_{ij} \rightarrow 1 \text{ as } r \rightarrow \infty, \quad (5.8)$$

since the suspension has particles uniformly distributed at large distances r . At $r = a_i + a_j$ the drops are in contact, and thus coalesce, so that

$$p(\mathbf{r})_{ij} = 0 \text{ at } r = a_i + a_j. \quad (5.9)$$

If the particle size and number distribution remain nearly constant at a given position in the tank than we can make a quasi-steady approximation,

$$\nabla \cdot (p_{ij}[\mathbf{v}_i - \mathbf{v}_j]) = 0. \quad (5.10)$$

Applying the divergence theorem to the collision-frequency equation (5.6) we find

$$J_{ij} = n_i n_j \int_{r=a_i+a_j} \nabla \cdot (p(\mathbf{r})_{ij}[\mathbf{v}_i - \mathbf{v}_j]) dV + n_i n_j \int_{r=\infty} p(\mathbf{r})_{ij} (\mathbf{v}_i - \mathbf{v}_j) \cdot \hat{\mathbf{r}} dS \quad (5.11)$$

The first integral vanishes identically because of the quasi-steady assumption, equation (5.10), and the collision-frequency function simplifies to

$$J_{ij} = n_i n_j \int_{r=\infty} (\mathbf{v}_i - \mathbf{v}_j) \cdot \hat{\mathbf{r}} dS, \quad (5.12)$$

where we have applied the boundary condition on $p_{ij}(\mathbf{r})$ at infinity, equation (5.7).

5.4.2 The Smoluchowski model

The collision-frequency function determined from the integral (5.12) involves an integration over the surface at infinity, S_∞ . The surface S_∞ encloses all possible drop trajectories which result in coalescence. The surface S_∞ can be described as a circle or disc of radius y_c , such that all drops with horizontal separation distances less than y_c coalesce, and all drops with horizontal separation distances greater than y_c do not coalesce (see figure 5.4). Since $\mathbf{v}_i - \mathbf{v}_j = \mathbf{U}_i^{(0)} - \mathbf{U}_j^{(0)}$ as $r \rightarrow \infty$ (interactions do not affect the rise speed), the rate of coalescence is given by

$$J_{ij} = n_i n_j \pi (U_i^{(0)} - U_j^{(0)})^2 y_c^2 \quad (5.13)$$

where $U_i^{(0)}$ is the Hadamard-Rybczyński speed.

The Smoluchowski model (Smoluchowski [1917] as cited in Davis [1984]) assumes that there are no hydrodynamic interactions between particles so that the drops rise vertically, thus

$$J_{ij} = n_i n_j \pi (U_i^{(0)} - U_j^{(0)}) (a_i + a_j)^2. \quad (5.14)$$

Hydrodynamically interacting spheres, as shown by previous investigators, have a reduced collision rate compared to the Smoluchowski model (even if van der Waals forces are present and included in the analysis) since small drops will tend to follow streamlines around larger drops, *e.g.* figure 3.2. However we will demonstrate that *deformable* drops not only have an enhanced rate of coalescence due to the effects of deformation, but may also even have a collision rate greater than predicted by the Smoluchowski model (*e.g.* the experiments shown in figure 3.1).

5.5 Monodisperse suspensions

In chapter 4 we derived, in the limit of small deformation, an expression for the rise speed of two widely separated particles, separated by distance d , of the form

$$\mathbf{U} = \mathbf{U}^{(0)} + \frac{a}{d} \mathbf{U}^{(1)} + \mathcal{B} \left(\frac{a}{d} \right)^2 \mathbf{U}^{(2)} + O \left(U^{(0)} \frac{a^3}{d^3} \right) \quad (5.15)$$

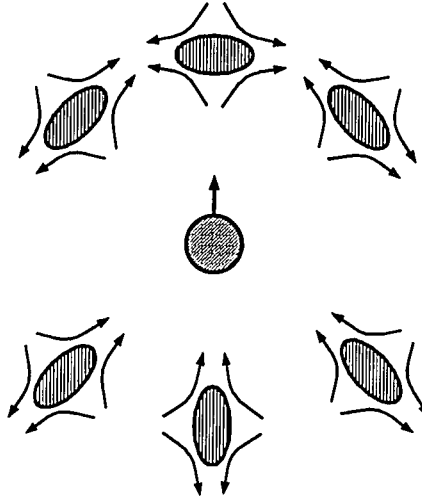
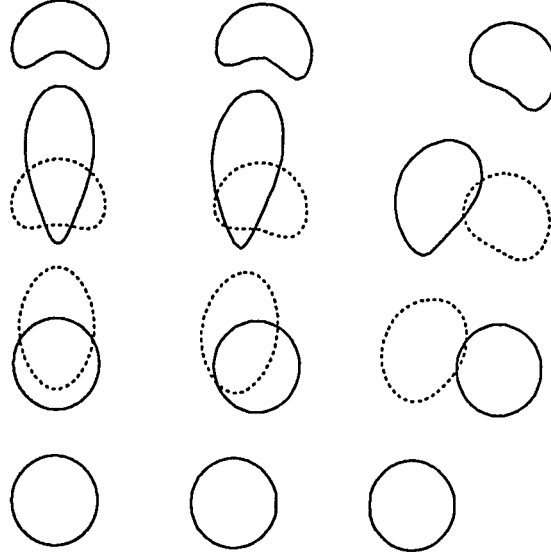


Figure 5.5: Schematic illustration of the interaction of two deformable drops in a suspension. The effects of hydrodynamic interactions result in deformation which will always lead to a component of translation which tends to align two drops.

The difference in rise speed of two equal-size drops is $O(U^{(0)}\mathcal{B}a^2/d^2)$. The derivation of equation (5.15) required a quasi-steady assumption for the drop shapes, *i.e.* that the time scale for the drops to deform is less than the time scale for the two drop geometry to change; *e.g.* see discussion in §4.1.4. Since two equal-size deformable drops will always be aligned owing to the effects of deformation, figure 5.5, then S_∞ is a spherical surface at infinity. Using the far-field analytical results derived in chapter 4, the collision-frequency function $J(a)$ for two drops with radius a in a monodisperse suspension with n drops per unit volume is given by

$$J(a) = 4\pi n^2 c(\lambda) a^2 \mathcal{B} U^{(0)}. \quad (5.16)$$

In deriving equation (5.16) we have neglected all short range phenomena such as van der Waals forces which are required for the eventual coalescence of particles and we have assumed that the magnitude of drop distortion is small so that the perturbation expansion (5.15) is valid.



$$\mathcal{B} = 10$$

Figure 5.6: Shapes of two three-dimensional drops, for equal-size drops with different initial horizontal offsets; $\mathcal{B} = 10$, $\lambda = 1$. Cross-sections of drop shapes are shown. No symmetries are assumed in the calculations.

In papers by Davis and coworkers the rate of coagulation of particles is characterized by a dimensionless collision efficiency function

$$E_{ij} = J_{ij}/J_{ij}^*, \quad (5.17)$$

where

$$J_{ij}^* = n_i n_j \pi (a_i + a_j)^2 (U_i^{(0)} - U_j^{(0)}) \quad (5.18)$$

is the Smoluchowski result. Note that the dimensionless collision efficiency E_{ij} is infinite for equal-size bubbles for all Bond numbers (since $J_{ij}^* \rightarrow 0$ as $a_i \rightarrow a_j$) although the actual collision rate J_{ij} will be finite.

In figure 5.6 we demonstrate numerically using a fully three-dimensional boundary integral calculation that the effects of interaction lead to deformed shapes which promote alignment, and thus the coalescence of drops, *even in monodisperse suspensions*.

5.6 Collision-frequency in polydisperse suspensions

In a polydisperse suspension, a suspension in which the drops may have different sizes, we need to determine the capture cross-section, y_c^2 , as a function of the Bond number, \mathcal{B}_i , the relative drop size, a_j/a_i , and the viscosity ratio between the drops and surrounding fluid, λ , *i.e.*

$$J_{ij} = n_i n_j \pi (U_i^{(0)} - U_j^{(0)}) y_c^2 \left(\mathcal{B}_i, \frac{a_j}{a_i}, \lambda \right) \quad (5.19)$$

The complexity of the interaction of deformable bubbles prohibits the use of analytical results and numerical studies (*e.g.* chapter 2-4) to quantitatively characterize the interaction of deformable bubbles. Numerical calculations are prohibitively time consuming since many hundreds of simulations are necessary to construct a model. In order to estimate the capture radius y_c , the initial vertical separation distance between the bubbles must be very large; the initial vertical offset in the numerical simulations must be very large and thus, computation times become especially long. In addition, numerical simulations are difficult for $\lambda \neq 1$ and for large interface distortions. The analytical results developed in chapter 4 are limited to small ellipsoidal drop distortions and thus large separation distances.

5.6.1 Experimental apparatus and procedure

In order to determine the collision frequency in a polydisperse suspension we performed a large number of laboratory experiments characterizing the interaction of air bubbles in corn syrup in order to develop a model for the coalescence of bubbles in dilute suspensions.³ In the experimental results presented here we consider only the limit in which large distortions occur so that the deformation, as observed in figure 3.1, results in the capture and coalescence of bubbles. Interfacial effects such as van

³We gratefully acknowledge the patience and devotion of Harvard undergraduate Joe Rice who performed more than 500 experiments to collect the data presented in this section.

der Waals forces or the presence of surfactants are important for the eventual coalescence of two bubbles; however, for the limit of large distortions considered here, such effects will only play a minor role in the rate of coagulation of bubbles. The experiments were performed in a large tank with dimensions 61 cm \times 61 cm \times 122 cm filled with commercial grade corn syrup (figure 5.7). Bubbles were injected into the bottom of the tank through a sequence of regularly spaced holes fitted with one-way valves. Bubble volume was measured by calibrating a series of syringes. The error in measuring bubble radius was less than 4%.⁴ In the experiments, a smaller bubble was injected first. In order to minimize the effects of not having an initially infinite vertical separation distance between the bubbles, the second larger bubble was injected once the small bubble has risen at least 25 cm. In order to minimize boundary effects, all interactions were required to occur at least 25 cm away from a boundary (side walls, the upper free-surface and the lower rigid boundary) in order

⁴The syringes used to inject the bubbles were calibrated so that the relative radius of the bubbles could be determined from the volumes of air injected into the tank. In the table below we list the syringe volume and associated rise speed of the bubble for typical experiments using different syringe volumes. Between eight and ten measurements of the rise speed are used to determine the uncertainties. Typically uncertainties of the bubble rise speed are about 1% so that typical uncertainties of the relative bubble radii will be less than 1%.

Syringe volume ml	Bubble rise speed cm/s
60	1.025 ± 0.008
30	0.635 ± 0.008
20	0.472 ± 0.006
10	0.336 ± 0.001
5	0.131 ± 0.002

Note that although the uncertainty of the relative bubble size is small, the uncertainty of the absolute bubble radius will be larger; in order to calculate the bubble radius we need a measure of the fluid viscosity, and the density contrast (since the radius is determined from a rise speed formula). The uncertainties of the fluid viscosity and density contrast are 2% and 1%, respectively. Thus the uncertainty of the bubble radius will be about 3-4%; however, the uncertainty of the relative bubble radii will be only about 1%.

to be included as acceptable data.

5.6.2 Experimental results

In figure 5.8, we present a series of experimental results which characterize the three different possible modes of bubble interactions for $\mathcal{B} = 120; 73, 30$ and 15 . For convenience we assume that the radius of the larger bubble is a_i and that the Bond number is based on the radius of the largest bubble, $\mathcal{B} = \Delta\rho g a_i^2 / \sigma$. The data illustrate that for a given horizontal separation distance, y , coalescence is more likely if the bubbles have a nearly equal size than a very large size difference. For a given relative size (fixed a_j/a_i , see figure 5.7), as the separation distance is increased, (i) the bubbles first interact such that the smaller bubble spreads over or “coats” the larger bubble (as in figure 3.1a), (ii) as the horizontal separation distance is gradually increased, the small bubble may be advected around the larger bubble and then entrained inside the larger bubble (as in figure 3.1b), and finally (iii) for still greater horizontal separation distances, the small bubble is advected around the larger bubble and coalescence does not occur.

In figure 5.9 we present experimental measurements for the capture radius y_c in equation (5.19) as a function of \mathcal{B} and the relative bubble radius a_j/a_i ; we use these results to construct an approximate quantitative model for bubble coalescence. Results are presented for $\mathcal{B} = 15, 30, 73$ and 120 . Data points separate interactions which result in coalescence (such as in figure 3.1) from interactions in which no coalescence occurs. Error bars are not shown. Typical errors on measurements of bubble radii are less than about 4%. Data presented in figure 5.9 is deemed acceptable if the initial vertical separation distance was sufficiently large; specifically, we required that the magnitude of bubble distortion based on the initial separation distance predicted by the far-field analysis presented in chapter 4 was less than 10% ($\epsilon < 0.1$ as defined by equations (4.3-4)). Despite the large volume of the tank, we could only accept experimental results for a limited number of horizontal bubble separation distances, Bond numbers and relative bubble sizes. A larger apparatus would be necessary to

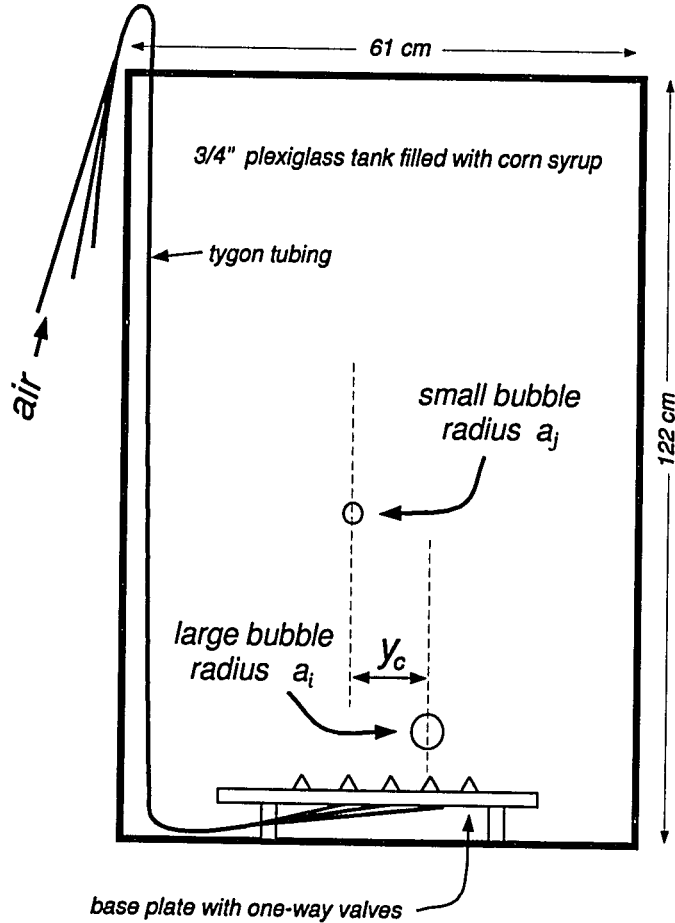


Figure 5.7: Schematic diagram of the tank used for the experiments presented in figures 5.8 and 5.9. The tank is made of 3/4" plexiglass. Bubbles are injected from calibrated syringes into the tank through tygon tubing connected to one-way valves. The radii of the larger and smaller bubbles are a_i and a_j , respectively, and the horizontal separation distance between the bubbles which separates interactions in which coalescence occurs from trajectories in which the bubbles do not coalesce is y_c .

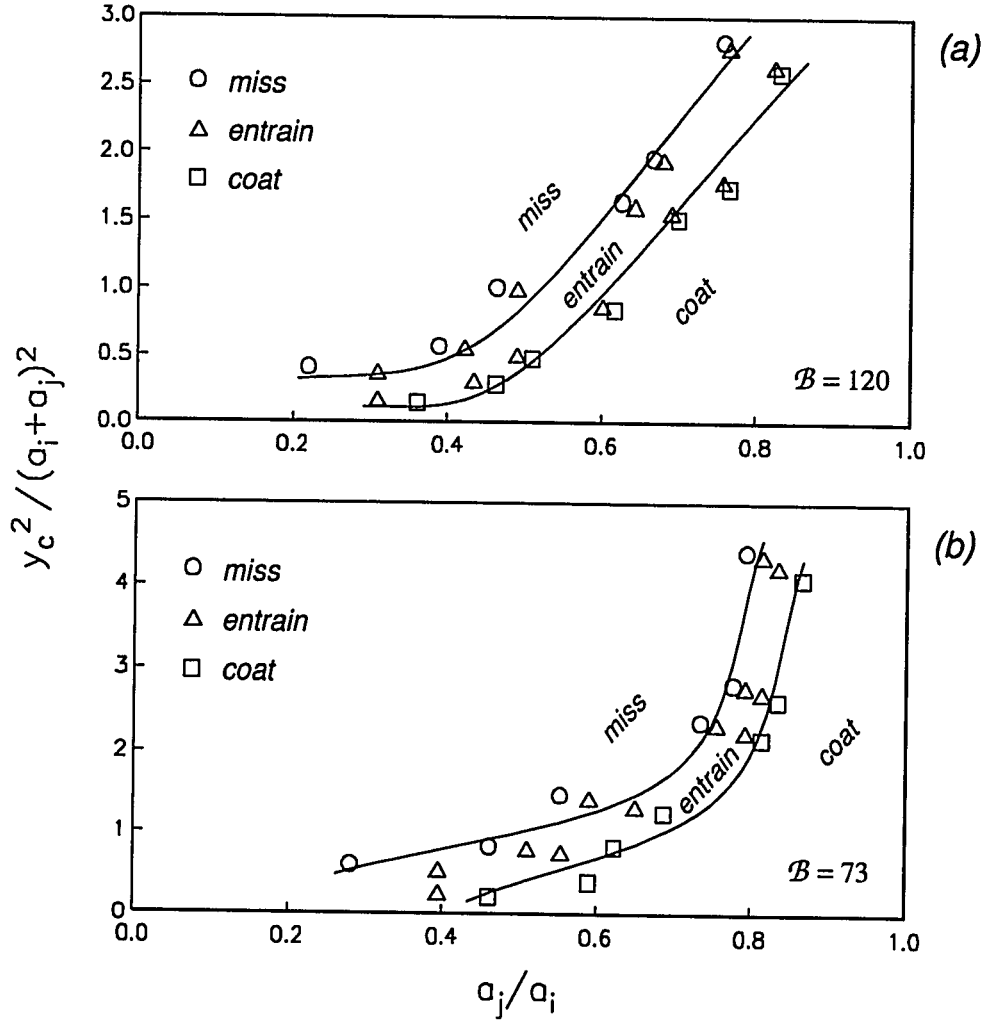


Figure 5.8: The mode of bubble interaction as a function of bubble offset, y_c , and relative bubble size, a_j/a_i for (a) $B = 120$ and (b) $B = 73$. “Coat” refers to interactions as in figure 3.1a (shown with the symbol \square), “entrain” refers to interactions as in figure 3.1b (shown with the symbol \triangle), and “miss” refers to interactions in which the bubbles do not coalesce (shown with the symbol \circ). The bubbles are initially separated vertically by at least $10a_i$.

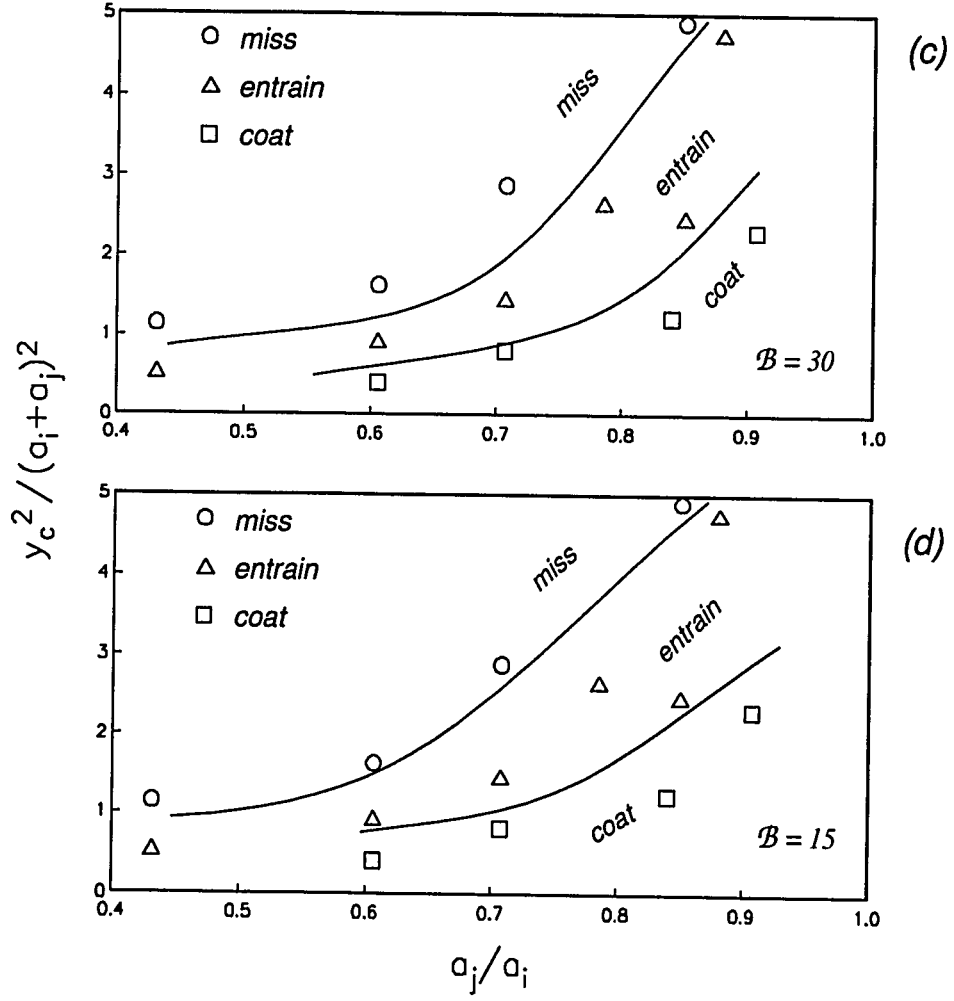


Figure 5.8: (continued) The mode of bubble interaction as a function of bubble offset, y_c , and relative bubble size, a_j/a_i for (c) $B = 30$ and (d) $B = 15$. "Coat" refers to interactions as in figure 3.1a (shown with the symbol \square), "entrain" refers to interactions as in figure 3.1b (shown with the symbol \triangle), and "miss" refers to interactions in which the bubbles do not coalesce (shown with the symbol \circ). The bubbles are initially separated vertically by at least $18a_i$.

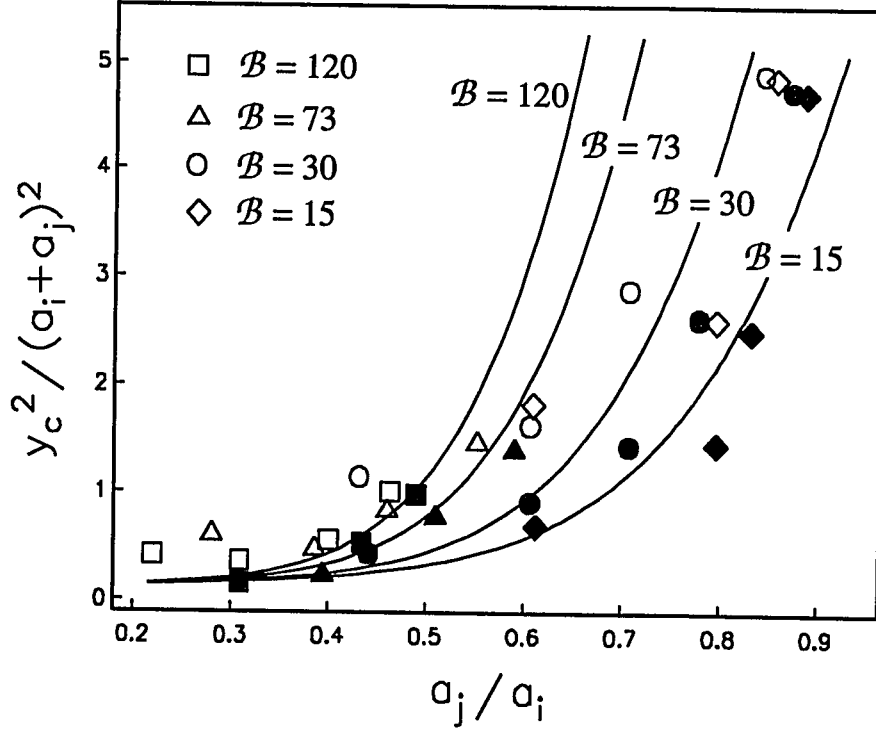


Figure 5.9: Experimental results used to derive an approximate quantitative model for the coalescence of deformable bubbles. Acceptable experimental results require that the initial condition is a good approximation to bubbles with an infinite vertical separation. Results are presented for $B = 120$ (\square), $B = 73$ (\triangle), $B = 30$ (\circ) and $B = 15$ (\diamond). Open symbols represent interactions in which the bubbles do not coalesce and solid symbols represent interactions in which the bubbles coalesce. Error bars are not shown. The solid curves represent predictions of a model of the form $y_c^2 / (a_j + a_i)^2 = 0.3(a_j/a_i)^{1/2} + 0.5B(a_j/a_i)^6$. We emphasize that the model is *not* based on analytical results or theory, but is only a useful functional relationship between the capture cross-section, y_c , the Bond number and the relative bubble size, which is approximately consistent with the limited amount of experimental data.

collect additional data for bubbles with large Bond numbers ($\mathcal{B} = 73$ and 120). For comparison, predictions from an empirical model of the form

$$\frac{y_c^2}{(a_i + a_j)^2} = 0.3 \left(\frac{a_j}{a_i} \right)^{1/2} + \frac{1}{2} \mathcal{B} \left(\frac{a_j}{a_i} \right)^6 \quad (5.20)$$

are shown with solid curves for the four values of the Bond numbers corresponding to the experimental measurements. From equation (5.20), in the limit that $\mathcal{B} \rightarrow 0$ we approximately recover the result of Zhang & Davis [1991] for spherical bubbles. Equation (5.20) is *not* based on analytical results or theory, but is only a useful functional relationship between the capture cross-section, y_c^2 , the Bond number, and the relative bubble size, which is approximately consistent with the limited amount of experimental data presented in figure 5.9.

From the results shown in figures 5.8 and 5.9, we note that the capture cross-section may even be larger than the sum of the bubble radii (see also the experiment shown in figure 3.1). A capture cross-section equal to the sum of the bubble radii, $y_c^2/(a_i + a_j)^2 = 1$, corresponds to the interaction between spherical bubbles moving vertically with no hydrodynamic interactions (so that smaller bubbles are not advected around larger bubbles).

The dimensionless rate of coalescence, J_{ij} , is shown in figure 5.10 for the model described by equation (5.19) and a capture cross-section defined by equation (5.20). For comparison, the analytical results for spherical bubbles (*i.e.* $\mathcal{B} = 0$) from Zinchenko [1982] are shown with small open circles. The rate of coalescence of deformable bubbles may be more than one order of magnitude greater than for spherical bubbles for a wide range of size ratios, *e.g.* $0.7 < a_j/a_i < 1$ for $\mathcal{B} = 10$. For small a_j/a_i , the effects of deformation are small (although the magnitude of deformation may be large, *e.g.* figure 3.12), and small bubbles tend to follow streamlines and are thus advected around larger bubbles. As $a_j/a_i \rightarrow 1$, equation (5.19) predicts no coalescence since the relative velocity of the bubbles $U_i - U_j \rightarrow 0$. However, as illustrated in figure 5.6 and discussed in §5.5, shape changes due to deformation will result in the eventual coalescence of equal-sized bubbles. Thus the model described by equations (5.19-20) *underestimates* the rate of coalescence as $a_j/a_i \rightarrow 1$.

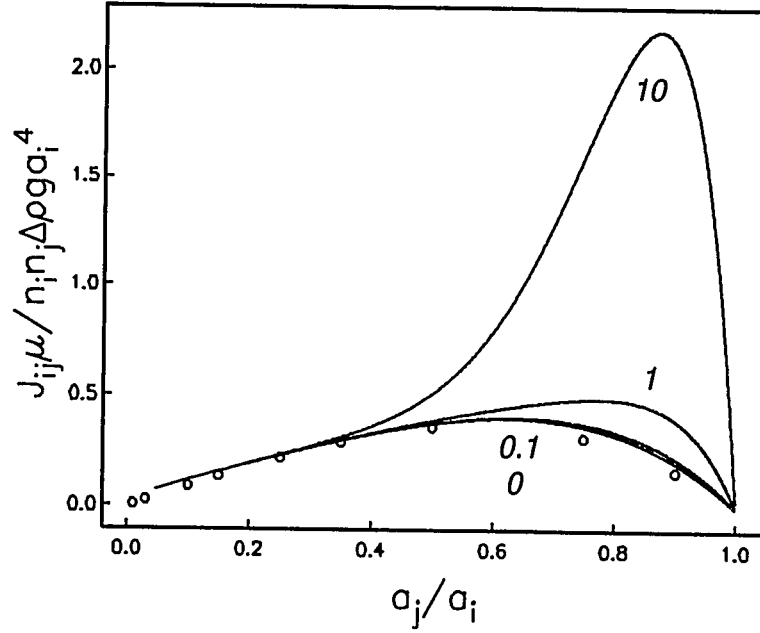


Figure 5.10: Dimensionless rate of coalescence of deformable air bubbles rising in corn syrup based on the model described by equations (5.19-20) for $B = 0, 0.1, 1$ and 10 . For comparison, the analytical results for spherical bubbles (*i.e.* $B=0$) from Zinchenko [1982] are shown with open circles. As illustrated in figure 5.6 and discussed in §5.4, shape changes due to deformation will result in the eventual coalescence of equal-sized bubbles, thus the model described by equations (5.19-20) and presented above underestimates the rate of coalescence as $a_j/a_i \rightarrow 1$.

5.7 Population dynamics simulations

In this section we calculate the size and concentration of buoyant deformable bubbles in dilute suspensions. We will consider two problems:

1. the bubble-size distribution of bubbles as a function of time in an isotropic and homogeneous suspension;
2. the evolution of the bubble-size distribution and concentration as a function of time and position in a tank of finite size.

Following the approach of Davis and coworkers [*e.g.* Zhang et al. 1993], we employ a population dynamics model based on two bubble interactions. In the simulations we ignore any boundary or wall effects and consider only the two particle interactions described above. Despite the limitations of the rate-of-coalescence equation (5.19) and the approximate nature of the model for the coalescence of deformable bubbles, equation (5.20), we will apply the experimentally derived model presented in §5.6 to the suspensions considered here. The problem of calculating dynamics in suspensions is a difficult problem and the results we present are at least based on experimental data and a theory valid for small volume fractions of bubbles, and hence capture qualitatively if not quantitatively several of the important and characteristic features of real systems.

5.7.1 The population dynamics model

In a homogeneous and isotropic suspension the discretized population dynamics equations which describe the rate of formation of particles of radius a_k (the bubble-size distribution is discretized into discrete intervals of bubble radii) are given by [*e.g.* Friedlander 1977]

$$\frac{dn_k}{dt} = \underbrace{\frac{1}{2} \sum_{i+j=k} J_{ij}}_{\text{creation of bubbles}} - \underbrace{\sum_{i=1}^{\infty} J_{ik}}_{\text{loss of bubbles}}, \quad (5.21)$$

where n_k is the number of bubbles with radius a_k per unit volume, and J_{ij} is the collision-frequency function given by (5.6). The first term on the right-hand side of (5.21) represents the creation of bubbles with radius a_k due to coalescence (the factor of 1/2 accounts for double counting) and the second term on the right-hand side of (5.21) represents the loss of bubbles with radius a_k due to coalescence.

We study the evolution of a given initial distribution of bubble sizes following the approach of previous investigators [*e.g.* Zhang et al. 1993]. Numerically, the bubble distribution is represented as a discrete spectrum of bubble sizes with N bins of bubble sizes equally spaced in the logarithm of the bubble volume. The initial size distribution is assumed to be a normal distribution of the volume fraction $\phi(a)$ about

an average bubble radius a_o . In all the results presented here the standard deviation characterizing the initial bubble distribution is $0.2a_o$ (*e.g.* the distribution at $t = 0$ in figure 5.11). The total volume fraction ϕ_o of bubbles is given by

$$\phi_o = \int_{\ln a=0}^{\infty} \phi(\ln a) d \ln a \quad (5.22)$$

The velocity characteristic of bubble interactions is

$$U_c = \frac{\Delta \rho g a_o^2}{\mu} \quad (5.23)$$

so that the characteristic time scale for interactions (based on the population dynamics equations) is

$$t_c = \frac{\mu}{\Delta \rho g a_o \phi_o}. \quad (5.24)$$

where $a\phi_o^{-1}$ is the typical distance between particles in a dilute suspension.

In solving equation (5.21) for homogeneous isotropic suspensions we choose a dimensionless time step of 0.0001 and discretize the bubble-size distribution so that the bubble volume doubles every 5 bins.

5.7.2 Isotropic polydisperse suspensions with a homogeneous concentration distribution

We first consider the evolution of the bubble-size distribution in a suspension in which the concentration and size distribution of bubbles are initially uniform throughout the suspension and which remain uniform at all times. We will refer to such a suspension as an isotropic homogeneous suspension. Such a suspension might be characteristic of local dynamics in suspensions for time intervals over which larger bubbles do not rise and separate from the rest of the bubbles in the suspension.

In figure 5.11 we show bubble concentration in an isotropic homogeneous suspension as a function of time for different Bond numbers. The distribution of bubble sizes is based on the population dynamics equations (5.21) with a collision frequency function defined by equations (5.19) and (5.20). The Bond number labeled on the curves and reported in the figure captions is based on the average initial bubble radius

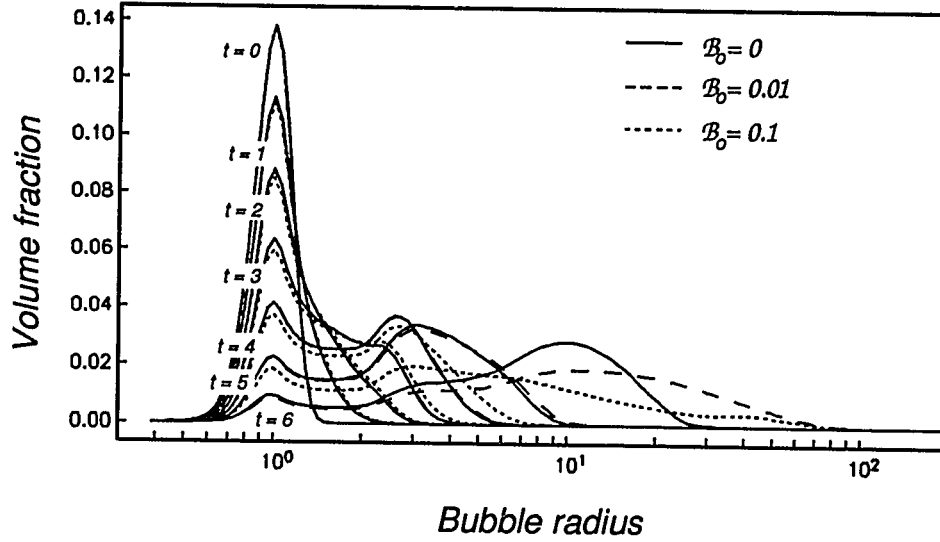


Figure 5.11: Bubble concentration in an isotropic homogeneous suspension determined by solving the population dynamics equations (5.21). The bubble distribution is shown at dimensionless times $t = 0, 1, 2, 3, 4, 5$ and 6 , where time is normalized by $\mu/\Delta\rho g a_o \phi_o$. The solid curves correspond to a simulation with $B_o = 0$, the dashed curves a simulation with $B_o = 0.01$, and the dotted curves a simulation with $B_o = 0.1$. The Bond number B_o is based on the average initial bubble radius a_o . The bubble distribution for the simulation with $B_o = 0.1$ is shown at times $t = 0, 1, 2, 3, 4$ and 5 .

a_o , i.e. $B_o = \Delta\rho g a_o^2/\sigma$. We use equation (5.19) with B_i based on the radius of bubble i to describe the capture cross-section so that *all* Bond numbers are included in the numerical simulations. As a result of coalescence the average bubble radius increases with time. The mean bubble volume as a function of time is shown in figure 5.12 for the simulations presented in figure 5.11. Notice in figure 5.11 that there is always a peak in the bubble size distribution around $a/a_o = 1$. Since the rate of coalescence of bubbles becomes very small as $a_j/a_i \rightarrow 0$ (figure 5.10), then as the average bubble size increases due to coalescence, the smaller bubbles with $a/a_o \approx 1$ are less likely to be involved in coalescence events. If the bubbles are deformable, a wider range of bubble sizes develops in the suspension (compare the solid curve for nondeformable

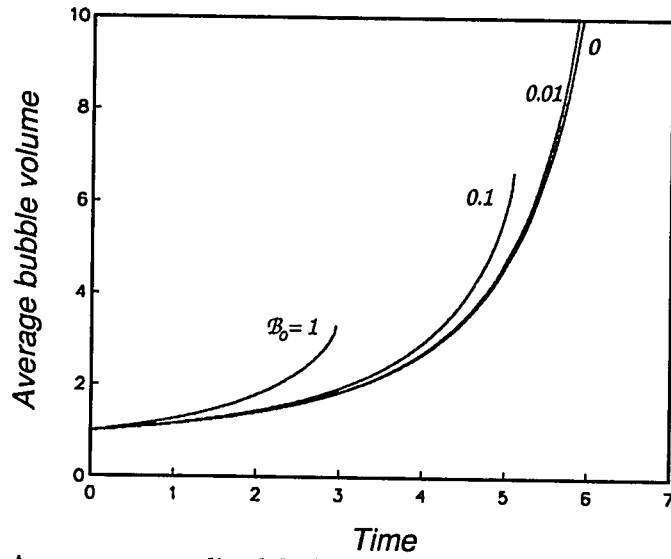


Figure 5.12: Average normalized bubble volume as a function of time in isotropic homogeneous suspension. Time is normalized by $\mu/\Delta\rho g a_o \phi_o$. Results are presented for $B_o = 0, 0.01, 0.1$ and 1 . The Bond number B_o is based on the average initial bubble radius a_o and curves terminate when the simulation is stopped.

bubbles with the dashed and dotted curves for deformable bubbles at times $t = 5$ and 6). As the average bubble size increases, the rate of coalescence increases; since deformation enhances the rate of coalescence, the mean bubble volume in suspensions containing deformable bubbles increases more rapidly than in suspensions of spherical bubbles, as illustrated in figure 5.12.

We note that the approximate model for the coalescence of deformable bubbles, equation (5.20), is based on experimental results for $15 < B < 120$. We might expect that the effect of deformation on the rate of coalescence becomes saturated for large Bond numbers. Thus, in the simulations presented in figures 5.11 and 5.12, we terminate the simulations once the Bond number of largest bubbles exceeds 150.

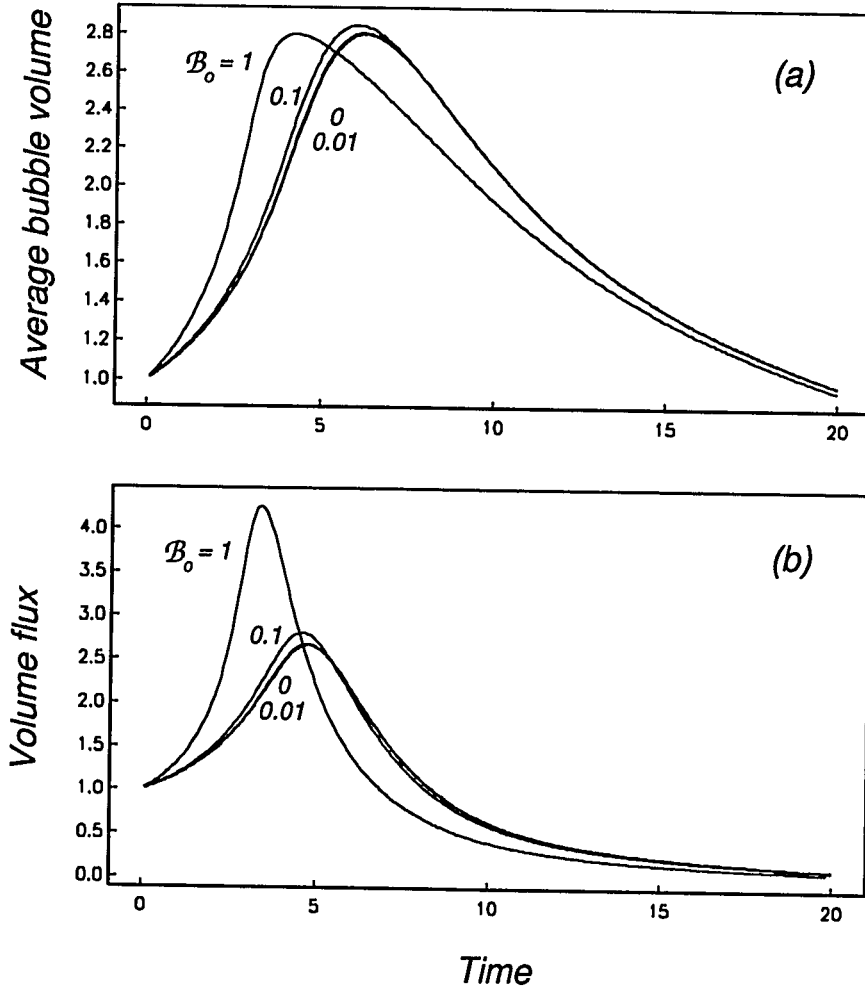


Figure 5.13: (a) Average normalized bubble volume of bubbles at the top of a tank as a function of time in an initially homogeneous suspension. Time is normalized by $\mu/\Delta\rho g a_o \phi_o$. The height of the tank is $50a_o/\phi_o$. (b) Volume flux of bubbles emerging from the tank. Results are presented for $\mathcal{B}_o = 0, 0.01, 0.1$ and 1 . The Bond number \mathcal{B}_o is based on the average initial bubble radius a_o . Both the average bubble volume and volume flux are normalized by their respective values at $t = 0$.

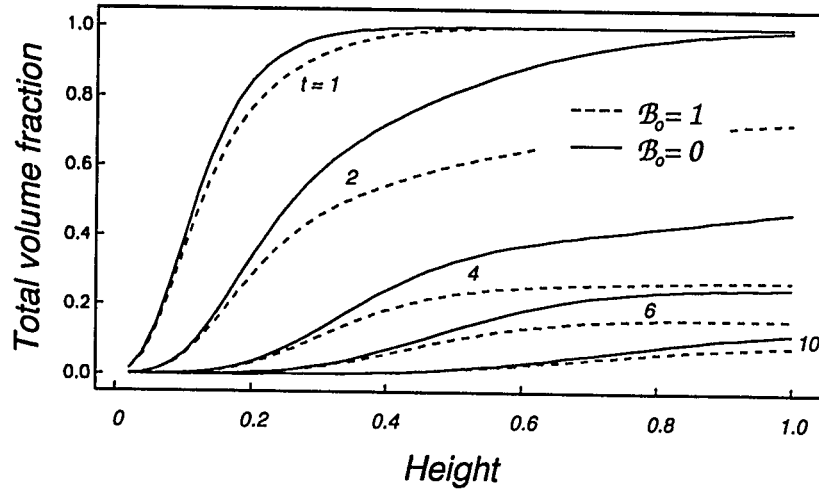


Figure 5.14: Total volume fraction of bubbles, normalized by the initial volume fraction ϕ_o , as a function of tank height (0=bottom, 1=top), at dimensionless times $t = 1, 2, 4, 6$ and 10 . Results are presented for $\mathcal{B}_o = 1$ (dashed lines) and $\mathcal{B}_o = 0$ (solid lines). Time is normalized by $\mu/\Delta\rho g a_o \phi_o$. The height of the tank is normalized by $50a_o/\phi_o$. The Bond number \mathcal{B}_o is based on the average initial bubble radius a_o .

5.7.3 “Sedimentation” and separation in a polydisperse suspension

In suspensions containing bubbles, the larger bubbles rise and separate from smaller bubbles, and bubbles may also leave the suspension when they reach the upper surface. Thus, we also performed a number of simulations in which we allow the bubble concentration to vary with vertical position within the suspension.

If bubbles may leave the suspension, as occurs for example in a tank filled with a bubbly fluid in which the bubbles are free to rise to an upper free-surface and escape from the tank, the volume fraction distribution $\phi(a)$ will also be a function of position. In the one-dimensional simulations presented below we model the dynamics by discretizing the tank height into L horizontal layers with thickness a_o/ϕ_o in which bubbles of a given size are uniformly distributed. Bubbles are assumed to rise with the Hadamard-Rybczyński speed $U^{(0)}$ based on the bubble radius, thus, we are assuming

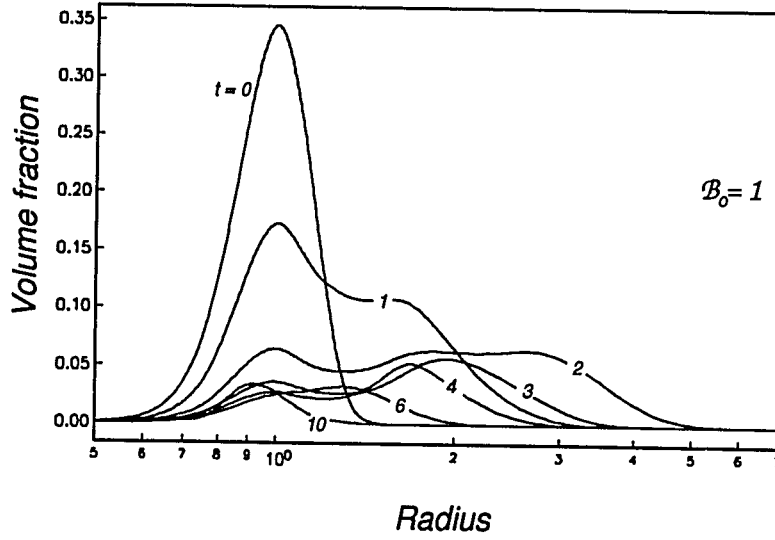


Figure 5.15: The size distribution of bubbles at the top of the tank, at dimensionless times $t = 0, 1, 2, 3, 4, 6$ and 10 ; $B_o = 1$. Time is normalized by $\mu/\Delta\rho g a_o \phi_o$. The height of the tank is $50a_o/\phi_o$. The Bond number B_o is based on the average initial bubble radius a_o .

there are no corrections due to interactions.⁵ Bubbles rise from one layer to the next layer, so that $n_i^{(l)}$ which denotes the number of bubbles of radius a_i in layer l per unit volume is given by

$$\begin{aligned} \frac{dn_i^{(l)}}{dt} = & \underbrace{\frac{\phi_o}{a_o} n_i^{(l-1)} U_i^{(0)}}_{\text{gain of bubbles by convection}} - \underbrace{\frac{\phi_o}{a_o} n_i^{(l)} U_i^{(0)}}_{\text{loss of bubbles by convection}} \\ & + \underbrace{\frac{1}{2} \sum_{i+j=k} J_{ij}}_{\text{creation of bubbles due to coalescence}} - \underbrace{\sum_{i=1}^{\infty} J_{ik}}_{\text{loss of bubbles due to coalescence}}. \end{aligned} \quad (5.25)$$

In figure 5.13 we demonstrate the effect of bubble deformation on the rate of separation of bubbles from the tank. The height of the tank is $50a_o/\phi_o$. Results are

⁵Batchelor [1972] has shown that the average translation speed in a dilute monodisperse suspension of rigid spheres is reduced to $U = U^{(0)} [1 - 6.55\phi_o + O(\phi_o^2)]$.

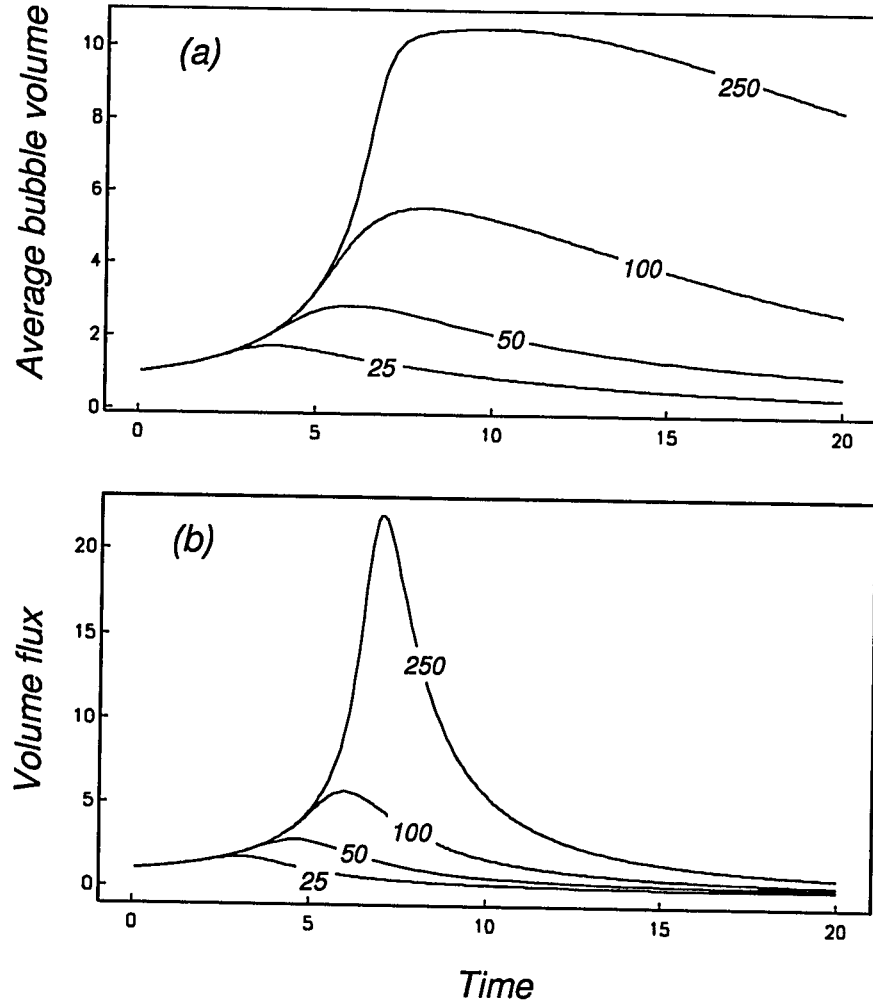


Figure 5.16: (a) Average normalized bubble volume of bubbles escaping from the top of a tank as a function of time in an initially homogeneous suspension. Results are presented for tank heights of $25a_o/\phi_o$, $50a_o/\phi_o$, $100a_o/\phi_o$ and $250a_o/\phi_o$; $\mathcal{B}_o = 0.1$. Time is normalized by $\mu/\Delta\rho ga_o\phi_o$. The Bond number \mathcal{B}_o is based on the average initial bubble radius a_o . (b) Volume flux of bubble emerging from the tank. Both the average bubble volume and volume flux are normalized by their respective values at $t = 0$.

presented for $\mathcal{B}_o = 0, 0.01, 0.1$ and 1 . The reported Bond number is based on the average initial bubble radius a_o . The rate of coalescence of bubbles is greatest for $\mathcal{B}_o = 1$. Thus, the average bubble volume increases fastest for the system with $\mathcal{B}_o = 1$. Since larger bubbles rise more rapidly, the volume flux of bubbles out of the tank will also increase most rapidly for the system with $\mathcal{B}_o = 1$. The maximum volume flux of bubble occurs at earlier times, and is greater in systems with deformable bubbles than nondeformable bubbles; thus, the rate of separation of the dispersed phase is increased by allowing the dispersed phase to deform. The importance of deformation on the rate of separation of the bubbles is highlighted in figure 5.14 which shows the volume fraction of bubbles as a function of height in the tank for systems with deformable ($\mathcal{B}_o = 1$) and nondeformable ($\mathcal{B}_o = 0$) bubbles.

In figure 5.15 we show the size distribution of bubbles at the top of the tank for the simulation with $\mathcal{B}_o = 1$. Initially the average bubble size increases as a result of coalescence, and the volume fraction of bubbles is large since the tank still contains a large number of bubbles (*e.g.* $t = 1$ and 2). As the larger bubbles rise and leave the tank, the total volume fraction of bubbles decreases, see figure 5.14, and the volume fraction and average size of bubbles decreases. For long times, (*e.g.* $t = 10$), the mean bubble size is small and the volume fraction is small.

Finally, in figure 5.16 we consider the effect of tank height on the average size and rate of separation of bubbles in the tank. In figure 5.16 we show results for tank heights of $25a_o/\phi_o$, $50a_o/\phi_o$, $100a_o/\phi_o$ and $250a_o/\phi_o$; $\mathcal{B}_o = 0.1$. The Bond number is based on the average initial bubble radius a_o . In larger tanks the total volume of bubbles (for a given volume fraction ϕ_o) is greater and the time available for interactions is greater so that larger bubbles will form. Thus, the maximum volume flux of bubbles out of the tank will be larger and the maximum average volume of bubbles will also be larger in taller tanks.

5.7.4 Limitations of the population dynamics simulations

Inherent in the simulations are a large number of approximations and assumptions that will limit the applicability and quantitative accuracy of the procedure described in §5.7.1 which is used to calculate the results presented in figure 5.11 - 5.16: *(i)* the collision-frequency function and population dynamics model is applicable only in dilute suspensions, for which two particle interactions are a useful model for describing the interactions in suspensions (although the simulations reported in §5.2 demonstrate that the interactions between many deformable drops may be characterized qualitatively by two drop interactions; thus, the dilute limit might be less restrictive for deformable drops than for rigid particles), *(ii)* the collision frequency model used in the simulations for deformable bubbles is based on a limited number of experimental data and underestimates the rate of coalescence as $a_j/a_i \rightarrow 1$, *(iii)* for the finite volume tank simulations we have assumed that bubbles are uniformly distributed in each layer at all times, and that the number of bubbles advected from one layer to the next layer depends on the concentration of bubbles in the layer, *(iv)* we have assumed a one-dimensional model for the bubble distribution, which assumes that the bubble concentration varies only with height in the tank, and *(v)* no wall or boundary effects are included. Nevertheless, we expect that the results presented in figures 5.11-16 are qualitatively representative of the evolution of bubble sizes and concentrations in dilute suspensions.

5.8 Concluding remarks

We have shown that the effects of deformation lead to an enhanced rate of coalescence of deformable drops and bubbles. The rate of coalescence may be more than one order of magnitude greater than the rate of coalescence of nondeformable particles.

We note that a suspension of deformable drops and bubbles may be unstable in the sense that distribution of particles may not remain homogeneous. As discussed in more detail in the following chapter [and by Koch & Shaqfeh 1989], regions of high

particle concentration will lead to greater fluid velocities than on average; the induced velocity gradients lead to particle deformation which will tend to move particles from a region of low to high particle concentration, and thus may lead to the generation of an instability, see §6.2.1.

Chapter 6

Interactions between bubbles in magmas and lavas: Effects of bubble deformation

We have demonstrated in previous chapters that deformation due to hydrodynamic interactions between bubbles leads to alignment of horizontally offset bubbles and thus an enhanced rate of coalescence in suspensions. In this chapter we discuss some of the implications of bubble dynamics on the evolution of volcanic and magmatic systems. Here we suggest that bubble alignment may produce spatial inhomogeneities in bubble concentrations in magmas which implies temporal variations in the concentration and size of bubbles in erupting magmas and spatial variations in solidified lavas. Based on the results presented in chapters 2-5, we conclude that the effects of deformation can be ignored if the largest bubbles have radii less than about 5 mm in silicate magmas.

6.1 Introduction

The dynamics of bubbles in magmas affect volcanic processes and the behaviour of related magmatic systems. For example, the interactions and coalescence of bubbles in ascending magmas and magma chambers may be important processes governing the style of volcanic eruptions [*e.g.* Wilson & Head 1981; Jaupart & Vergnolle 1988]. Bubble coalescence is also inferred to occur frequently in basaltic flows [*e.g.* Sahagian et al. 1989; Walker 1989; Herd & Pinkerton 1993] thus affecting the spatial and size distribution of bubbles in solidified lavas. The rate of coalescence and ascent of bubbles in molten rock is also of interest during the process of In Situ Vittrification, which is a treatment method for contaminated soils. The contaminated region is melted and later allowed to resolidify; organic and volatile components in the soil are pyrolyzed and vapourized, respectively, and the gases rise in the form of bubbles to the surface of the molten region where combustion occurs [Jacobs et al. 1988].

Owing to the large viscosities of silicate magmas, which range from $30 \text{ Pa} \cdot \text{s}$ for some basalts to $10^7 \text{ Pa} \cdot \text{s}$ for some rhyolites [Bottinga & Weill 1972], bubble dynamics in magmas are typically characterized by small Reynolds numbers,

$$\mathcal{R} = \rho U a / \mu < 1, \quad (6.1)$$

where μ is the magma viscosity, ρ is the magma density, a is the bubble radius, and U is the bubble rise speed. Bubbles are predicted to reach diameters of 0.1 to 5 cm in basalts due to growth by diffusion and depressurization as they rise [Sparks 1978; Proussevitch et al. 1993a], although the observed size of bubbles preserved in basalts is often less than 1 cm [Sarda & Graham 1990; Mangan et al. 1993]. The degree of deformation is governed by the Bond number,

$$\mathcal{B} = \Delta \rho g a^2 / \sigma, \quad (6.2)$$

which represents the ratio of buoyancy forces relative to the surface tension forces that resist deformation (σ is the surface tension, g is gravitational acceleration, and $\Delta \rho$ is the density difference between the magma and gas in the bubble). The surface

tension between silicate magmas and gases at atmospheric pressure is 0.35-0.37 N/m [Walker & Mullins 1981], thus for bubbles with radii of 1 cm, $\mathcal{B} \approx 10$. At higher pressures, the surface tension between water vapour and melts may be significantly reduced with a magnitude about 0.1 N/m at pressures of 300 MPa [Khitarov et al. 1979].

We have shown in the preceding four chapters that for $\mathcal{R} \ll 1$ and $\mathcal{B} > O(1)$ bubble interactions lead to significant shape distortions, which affect the translation, coalescence and spatial distribution of bubbles. Bubble deformation and coalescence will be important processes provided sufficient time exists for bubble interactions to influence coalescence, as expected in magma chambers [Vergnolle & Jaupart 1986, 1990] and during eruptions with slow ascent rates [Toramoru 1988]. Interactions and coalescence should also affect the resulting distribution of bubbles in cooling and solidifying magmas [Sahagian 1985; Sahagian et al. 1989].

Owing to the complexity of bubble dynamics and coalescence, bubble hydrodynamics are generally ignored or parameterized in studies of eruption processes [Wilson & Head 1981; Vergnolle & Jaupart 1986], bubble migration in cooling lavas [Sahagian 1985; Sahagian et al. 1989], and studies interpreting bubble size distributions [Toramoru 1990; Sarda & Graham 1990]. The dynamics considered in this thesis should be applicable to bubbles in magmas provided the concentration of bubbles is low enough that the bubbles are able to rise and interact. At bubble concentrations greater than 74% [Proussevitch et al. 1993b], when all the bubbles are in near contact, the two-phase system is best described as a foam and will have different dynamics.

6.2 Applications to bubbles in magmas and lavas

Below we consider some volcanological problems involving basaltic magmas and lavas in which bubble interactions may occur. The processes illustrated in figure 3.1, which are characteristic of two bubble interactions for large Bond numbers, may not be the dominant processes governing the style of basaltic eruptions and the behaviour of

bubbles in lavas. Nevertheless, the two bubble coalescence experiments highlight some of the consequences of bubble interactions which will occur between the larger bubbles in magmas (radii greater than about 0.5 cm), and may play a previously unrecognized role in the dynamics of volcanic and magmatic systems. In the experimental results shown in figure 3.1, bubbles typically interact and deform over a translational distance of a few bubble diameters: in some volcanic systems, magma chambers and lava flows, magma velocities are sufficiently small that time will exist for interactions and coalescence of bubbles to occur.

6.2.1 The formation of instabilities of bubble concentration

The alignment and coalescence of bubbles may give rise to spatial inhomogeneities of bubble concentrations which lead to temporal variations in the amount of gases erupted with magmas. Bubble migration due to the deformed bubble shapes will lead to spatial inhomogeneities analogous to those which develop in suspensions of ellipsoidal particles [Koch & Shaqfeh 1989]. By analogy to the suspension of rigid ellipsoids studied by Koch & Shaqfeh, in an initially homogeneous and monodisperse suspension of bubbles the lengthscale of the instability

$$\lambda \approx \frac{1}{\sqrt{na}}, \quad (6.3)$$

where n is the number of bubbles per unit volume and a is a typical radius of the bubbles. The instability arises since variations of bubble concentration lead to velocity gradients in the magma which deform bubbles. Deformed bubbles migrate from a region of low to high bubble concentration, as schematically illustrated in figure 6.1. The growth rate of the instability will depend on the magnitude of bubble deformation and thus on the Bond number, and therefore we expect that the larger bubbles in a magma will set the lengthscale of the instability. In a magma with a volume fraction of 0.1% vesicles with radius 1 cm, the length scale of the instability is predicted to be on the order of half a meter and might be observed in solidified lavas.

We also note that, based on the study of Koch & Shaqfeh [1989], spatial inho-

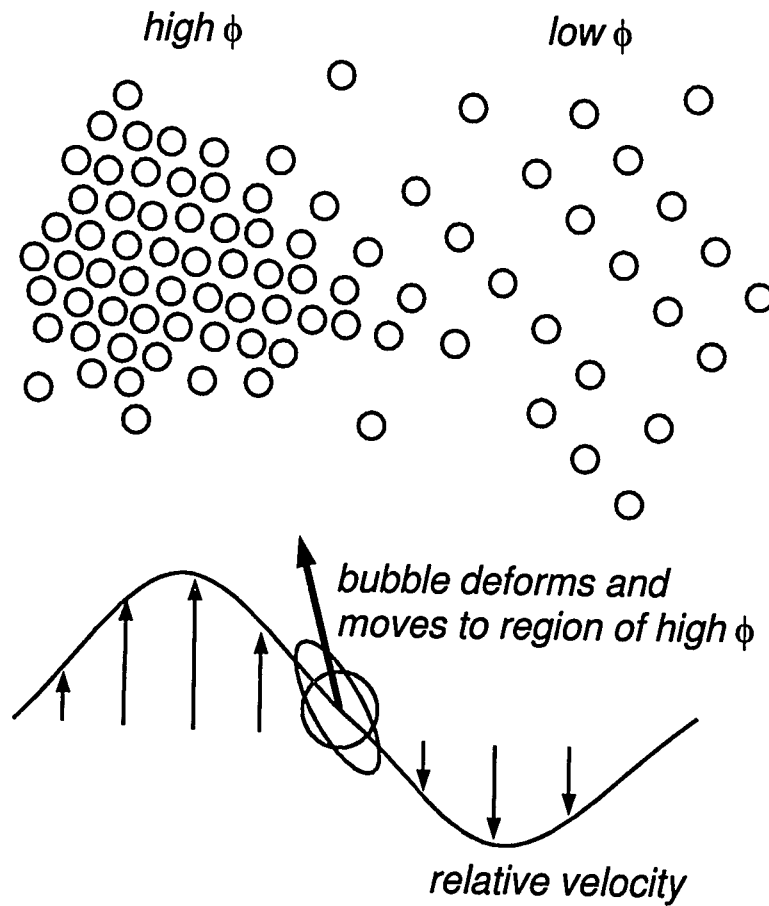


Figure 6.1: Schematic illustration of the development of spatial variations of bubble concentration [after Koch & Shaqfeh 1989]. Variations of bubble concentration lead to variations of fluid rise speeds and thus local velocity gradients. Velocity gradients deform bubbles which will then migrate from a region of lower to higher bubble concentration.

mogeneities in the concentration of sedimenting olivine crystals will develop. The occurrence of aggregates of olivine crystals in some Hawaiian basalts [Schwindinger & Anderson 1989] may be due to such an instability.

6.2.2 Applications to volcanic systems

Spatial variations of bubble concentration have been proposed to explain the temporal variations in eruptive style in Kilauea [Jaupart & Vergnolle 1990], with periods of high gas flow resulting in fire-fountaining, whereas magmas with low bubble concentrations are extruded smoothly (figure 6.2). If sufficient bubble coalescence occurs, a conduit filling gas plug or cluster of bubbles may develop resulting in strombolian eruptions [Blackburn et al. 1976]. Previous calculations suggest that for magma rise speeds in the conduit $U_{magma} > 1$ m/s fire-fountaining will occur, whereas for $U_{magma} < 0.1$ m/s sufficient time exists for coalescence to produce conduit-filling gas plugs which result in discrete strombolian eruptions [Wilson & Head 1981]. Image processing of eruptions at Stromboli suggests that individual eruptions consist of single impulses (thus, a single large bubble) and more frequently successive pulses with time intervals of about 1 second (thus, a sequence of closely spaced bubbles) [Ripepe et al. 1993].

The long duration of fire-fountaining events, typically one day, is greater than the residence time of the magma in the rift zone which is typically a few hours [Head & Wilson 1981]. The models by Jaupart & Vergnolle [1988, 1990] thus require that bubble accumulation occurs at the top of a magma chamber in order to account for the extended duration of fire-fountaining. However, degassing at Kilauea is thought to be a two-stage process, with gases in the magma chamber vented through fumaroles, whereas carbon depleted gases, which form at depths less than a few hundred meters, are vented through eruptions in the rift zones [Greenland et al. 1985; Gerlach & Graeber 1985]. We note that the enhancement of bubble coalescence by bubble alignment is an additional mechanism which allows spatial variations in bubble concentrations to develop in the conduit and in magma chambers, without necessarily involving the accumulation of a bubbly or foam layer at the top of a magma chamber.

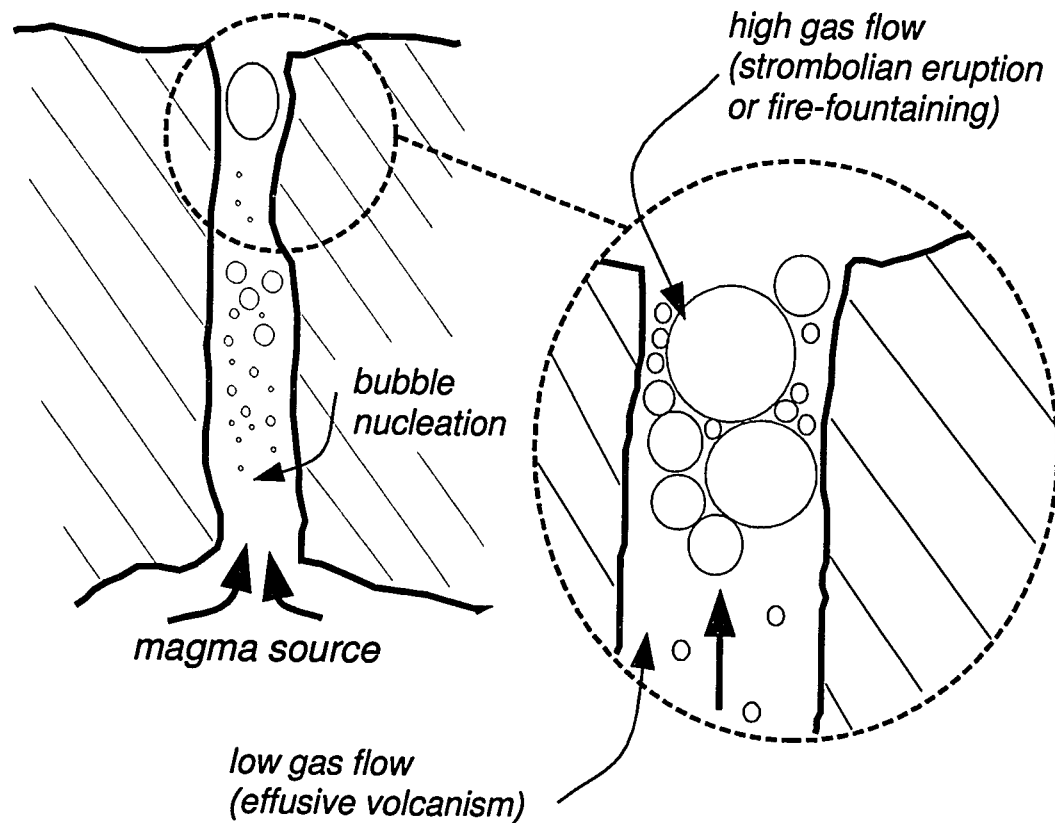


Figure 6.2: Illustration of possible processes involving bubble interactions in basaltic magmas. Bubble nucleation occurs in the conduit. As the bubbles rise they interact and tend to produce regions with varying concentrations of bubbles owing to bubble alignment and coalescence. As the magma reaches the surface, regions with high bubble concentrations may result in fire-fountaining (or strombolian eruptions if there is sufficient accumulation of gas) whereas the regions with low bubble concentrations result in effusive volcanism. The resulting flow in the conduit would be similar to the the flows produced in the experiments by Jaupart & Vergnolle [1990] in which bubble interactions occur in a foam layer at the top of a magma chamber.

The physics of bubble interactions shown in figures 3.1 is also relevant to the interaction between clouds of bubbles (discrete regions in the magma with a much larger bubble concentration than the surrounding magma characterized by very large Bond numbers) which may form following the breakup of the foam at the roof of a magma chamber [Jaupart & Vergnolle 1988]. The interactions of bubbles and bubble clouds in the conduit may also help account for the significant variations of eruption heights (fountain heights vary from 10 to 400 m) which change over periods of a few hours [Head & Wilson 1987]. The final coalescence of bubbles into larger bubbles may involve the coalescence of bubbles in a foam rather than by the processes illustrated in figure 3.1 depending on the concentration and size of bubbles. We note that the bubbles preserved in lavas and contained in effusive magmas may not be representative of those in erupting magmas. The largest bubbles responsible for fire-fountaining and explosive events will be destroyed during eruption – small bubbles (*i.e.* small Bond numbers, hence small deformations) are swept around larger bubbles and will generally still be present in the effusive volcanic lavas.

6.2.3 Application to bubbles in lava flows

Bubble coalescence is thought to be an important process causing changes of bubble-size distribution in some quiescent lava flows [Sahagian et al. 1989; McMillan et al. 1987] and flowing lavas [Walker 1989]. In systems containing very small bubbles (thus small Bond numbers) such as the mid-ocean ridge basalts studied by Sarda & Graham [1990] and the Kilauean basalts studied by Mangan et al. [1993] coalescence is inferred to not occur frequently. The final distribution of bubbles in solidified lavas may be used to infer atmospheric pressure at the time the lavas were erupted and thus may be used to infer paleobathymetry, paleoelevation, and uplift or subsidence histories [Sahagian et al. 1989].

An example of a lava flow in which bubbles may have large Bond numbers and bubble coalescence was probably an important process governing the final size distribution of bubbles is the Cohasset flow of the Grande Ronde Basalt [McMillan et

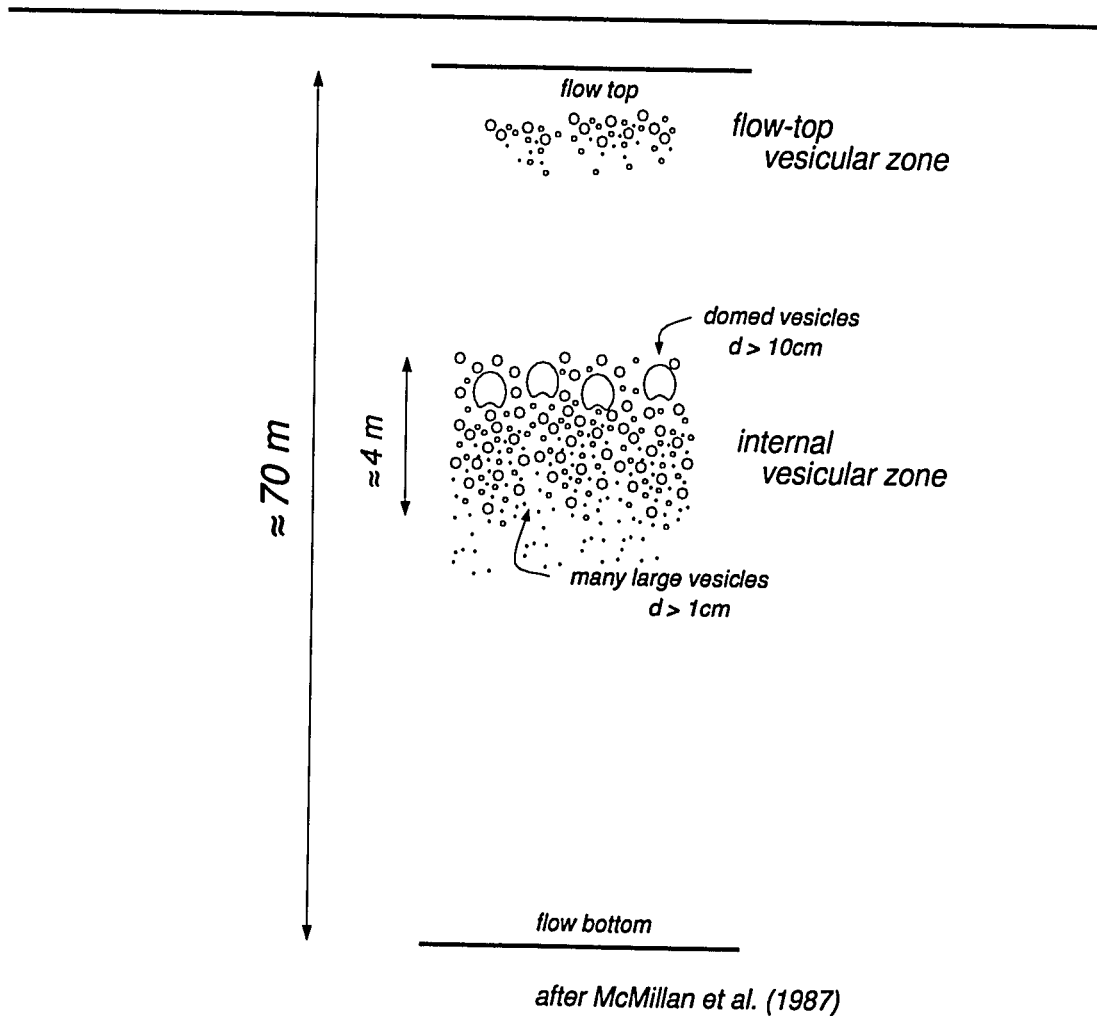


Figure 6.3: Schematic cross-section of the Cohasset flow of the Columbia River basalts (after McMillan et al. [1987] figure 2). The flow-top vesicular region forms shortly after the emplacement of the flow and consists of bubbles initially contained in the erupted magma. It is believed that the internal vesicular zone contains bubbles nucleated at the lower solidification front which have risen and coalesced to create a number of large vesicles, with diameters d greater than 1 cm, and very large domed vesicles with d greater than 10 cm.

al. 1987]. The flow is typically 70 m thick and contains two distinct layers with high vesicularities, an upper layer near the top of the flow, and an internal vesicular layer about 4 m thick at a depth of about 40 % of the flow thickness (see figure 6.3 which has been adapted from McMillan et al. [1987] figure 2). The flow-top vesicular region forms soon after the emplacement of the flow and consists of bubbles initially contained in the erupted magma. The internal vesicular zone contains bubbles nucleated at the lower solidification front which have risen and coalesced to create a number of large vesicles, with diameters d greater than 1 cm, and very large domed vesicles with d greater than 10 cm. Lava flows with thickness less than 10 m show no internal vesicular zone and little evidence for coalescence except for the presence of a small number of vesicles with radii a greater than 1 cm [Aubele et al. 1989].

Larger bubbles formed as a result of coalescence will rise and separate more rapidly [Wilson & Head 1981] resulting in spatial variations of bubble size and concentration and thus producing the observed gradation of bubbles sizes in the internal vesicular zone, with larger bubbles near the top and smaller bubbles near the bottom. The calculations of Sahagian [1985] demonstrate the separation of bubble sizes due to differential ascent rates. However, the quantitative details of the bubble distribution in solidified lavas may differ from the predictions of Sahagian owing to the effects of deformation, which will result in a rate of coalescence greater for deformable bubbles ($a > 5$ mm) than for spherical bubbles, as discussed in chapter 5.

Many lava flows contain vertically aligned structures called pipe vesicles and vesicle cylinders [*e.g.* Aubele et al. 1989; Sahagian et al. 1989; Walker 1987; Goff 1977]. We make the distinction, following Philpotts & Lewis [1987], between pipe vesicles which are elongated tubes with typical diameters of 5 mm and lengths greater than 10 cm and vesicle cylinders which are composed of highly vesicular basalt with typical diameters of several centimeters, lengths up to several meters, and often regular spacing between cylinders with separations of tens of centimeters [Goff 1977]. Vesicles cylinders commonly contain large vesicles with radii greater than a few millimeters and are generally located in the interior of a flow [Aubele et al. 1989; Goff 1977]. The

coalescence of pipes vesicles observed by Walker [1987] may be due to the mechanisms of coalescence discussed in this thesis if the bubbles rise due to buoyancy forces. Goff [1977] proposes that vesicle cylinders form as a result of a Rayleigh-Taylor instability of a highly vesicular layer in basalts with high concentrations of dissolved water. The instability discussed in §6.2.1 may be an additional mechanism leading to the formation of vesicles cylinders; further experimental and analytical work is necessary to predict the implications of bubble alignment on the formation of vesicular structures in lava flows.

6.3 Concluding remarks

The results discussed here are strictly applicable only for sufficiently dilute systems of bubbles in magmas that buoyancy-driven interactions occur. A simple consequence of bubble interactions is that the capture cross-section for coalescence of comparable-sized bubbles may much larger than the sum of the bubble radii (see chapter 5). Previous investigations have assumed a capture cross-section proportional to the square of the radius of the smaller bubble [Wilson & Head 1981] or have ignored the important hydrodynamic effects associated with deformation [Sahagian 1985, Sahagian et al. 1989]. For sufficiently deformable bubbles, $B > O(1)$, and bubbles with comparable sizes, the effects of deformation will promote the coalescence of bubbles – thus, the physics of deformable bubbles and consequences of deformation for multiple bubble interactions at low Reynolds numbers are fundamentally different from spherical bubbles. The experimental results presented in chapter 5 demonstrate that results which neglect the effects of deformation underestimate the rate of coalescence of bubbles, perhaps by more than an order of magnitude in a system with a greater than 0.5 cm. The effects of deformation can be neglected if the largest bubbles have Bond numbers less than $O(1)$, which corresponds to bubbles with radii less than a few millimeters in silicate magmas.

The enhancement of coalescence of bubbles will have a few possibly important

effects: (i) larger bubbles will form and rise quickly resulting in the separation of larger bubbles from smaller bubbles (the rise speed in Stokes flow is proportional to the square of the radius), (ii) the ratio of surface area to volume decreases as bubble size increases, so that the total surface area over which reactions, diffusion and absorption of various chemical species can occur decreases as coalescence occurs, (iii) an instability may occur so that spatial variations of bubble concentration develop. We expect that a better understanding of bubble dynamics in magmas combined with measurements of bubble size distributions may provide additional constraints on the depth of bubble nucleation, bubble growth rates, and magma dynamics in conduits and magma chambers.

Chapter 7

The low Reynolds number motion of drops, bubbles and rigid particles through fluid-fluid interfaces

In this chapter we study the time-dependent buoyancy-driven translation of a deformable drop towards and through a fluid-fluid interface in the low Reynolds number flow limit. The Bond numbers characteristic of both the drop and initially flat fluid-fluid interface (referred to hereafter as the interface) are sufficiently large that the drop and interface become highly deformed. Boundary integral calculations are presented for Bond numbers $\mathcal{B} = \Delta\rho g a^2 / \sigma$ in the range $5 \leq \mathcal{B} < \infty$ (where $\Delta\rho$ is the density contrast across either interface and a is the undeformed drop radius) and viscosity ratios λ in the range $0.01 \leq \lambda \leq 10$. Drops passing from a higher to lower viscosity fluid are extended vertically as they pass through the interface; drops passing from a lower to higher viscosity fluid become flattened as they approach the interface. For sufficiently large Bond numbers characterizing the drop distortion, the degree of deformation produced as a result of the drop-interface interaction is sufficiently large that the drop may deform continuously, developing either an ever-elongating tail or

ever-enlarging cavity at the back of the drop, analogous to the deformation characteristic of single deformable drop in an unbounded fluid. The viscosity ratio between the drop and the external fluids, and the viscosity ratio across the initially planar fluid-fluid interface have significant effects on the rate of film drainage: the film of fluid between the drop and fluid-fluid interface thins most rapidly for the case that the drop enters a more viscous fluid, or the case that the drop has a viscosity lower than the surrounding fluids.

Experimental results are presented for the motion of bubbles, rigid spheres and rigid slender bodies through fluid-fluid interfaces. Bubbles entering a less viscous fluid are extended vertically, in agreement with the numerical calculations, and may break into smaller bubbles. The column of fluid entrained by either a single or multiple particles passing through an interface may also break into drops. Experiments with two or more spherical particles indicate that the spatial distribution of particles may change as the particles pass through interfaces: particles tend to form clumps. Slender bodies passing through a fluid-fluid interface into a lower viscosity fluid become oriented parallel to gravity. Slender bodies entering a more viscous fluid do not become oriented perpendicular to gravity.

7.1 Introduction

The motion of drops, bubbles and rigid particles passing through fluid-fluid interfaces at low Reynolds number occurs in a variety of industrial separation systems and naturally occurring stratified fluid systems. A model problem, consisting of a single deformable drop approaching and passing through a deformable interface, is considered in this chapter. We also present experimental results for the motion of rigid slender bodies through fluid-fluid interfaces. Hereafter, we will refer the initially planar fluid-fluid interface as the interface. Features of the model problem which are of interest include

1. the rate at which a drop passes through an interface,
2. whether a drop remains intact and connected or breaks into a sequence of smaller drops,
3. the amount of fluid entrained by a drop as it passes through an interface,
4. the thickness of the film of fluid coating a drop as it passes through an interface.

Previous numerical work has been limited to the motion of a *rigid* sphere through an interface for moderate interface distortions [Lee & Leal 1982; Geller et al. 1986]. The motion of deformable drops approaching their homophase (a drop approaching a fluid layer with the same chemical composition as the drop) was studied by Chi & Leal [1989]. Published experimental research on the low Reynolds number motion of drops through interfaces has also been limited to drops and bubbles approaching their homophase and rigid spheres approaching interfaces (see summaries in Chi & Leal [1989] and Geller et al. [1986]). Approximate analytical results for a sphere translating normal and parallel to a deformable interface were developed by Lee & Leal [1980] using domain perturbation techniques and the Lorentz reciprocal theorem (similar to the methods employed in chapter 4 to study the interaction and translation of two deformable drops). A combination of lubrication theory and boundary integral methods was used by Yiantsios & Davis [1990] to study the close approach of a nearly spherical deformable drop to a nearly flat deformable interface.

In the present study we are concerned with the limit in which large interface distortions occur to the drop, to the interface, or to both fluid-fluid interfaces. Large distortions occur when the Bond number is large,

$$\mathcal{B} = \frac{\Delta\rho g a^2}{\sigma} > O(1), \quad (7.1)$$

where $\Delta\rho$ is the density contrast across either interface, a is the undeformed drop radius, σ is the interfacial tension, and g is the gravitational acceleration. Typically, in most engineering systems, large Bond numbers correspond to large drop and particle radii. However, large Bond numbers are also characteristic of systems with miscible

fluids or low values of interfacial tensions such as the interfacial tension between different oils.

In figure 7.1 we present photographs of experiments which illustrate several features characteristic of the problem we study. Photographs from two different sequences of photographs are presented in order to illustrate some of the features (items 2-4 listed in this introduction) of the model problem. In the experiments shown in figures 7.1*a* and 7.1*b*, an air bubble translates through very viscous corn syrup ($\mathcal{R} \approx 10^{-3}$) towards a lower viscosity layer of polybutene (viscosity contrast between polybutene and corn syrup is 0.15). In figure 7.1*a* we observe that the initially spherical bubble is extended vertically as it passes through the interface. In figure 7.1*b* we show a photograph, taken from the same experiment as (*a*) but at a later time, in which the large bubble breaks into three smaller bubbles. In the experiments shown in figures 7.1*c* and 7.1*d*, an air bubble translates through glycerin ($\mathcal{R} \approx 1$) towards a higher viscosity layer of polybutene (viscosity contrast between polybutene and glycerin is 40). In figure 7.1*c* we notice that a very small layer of glycerin coats the air bubble as it passes through the interface. In figure 7.1*d* we show a photograph, taken from the same experiment as figure 7.1*c*, in which the column of glycerin entrained by the bubble as it passes through the interface has broken into a sequence of smaller drops by a capillary (Rayleigh) instability.

The four photographs presented in figure 7.1 illustrate several of the features of the flow problem we consider. Boundary integral numerical simulations presented in §7.3 allow us to consider limits which are not readily studied by means of laboratory experiments and we are also able to obtain quantitative details of the flow. The experimental results presented in §7.4 allow us to consider the breakup of drops and interfaces (*e.g.* figure 7.1*b,d*), geometries which are difficult to simulate numerically (such as very thin films), and the motion of several particles through fluid-fluid interfaces.

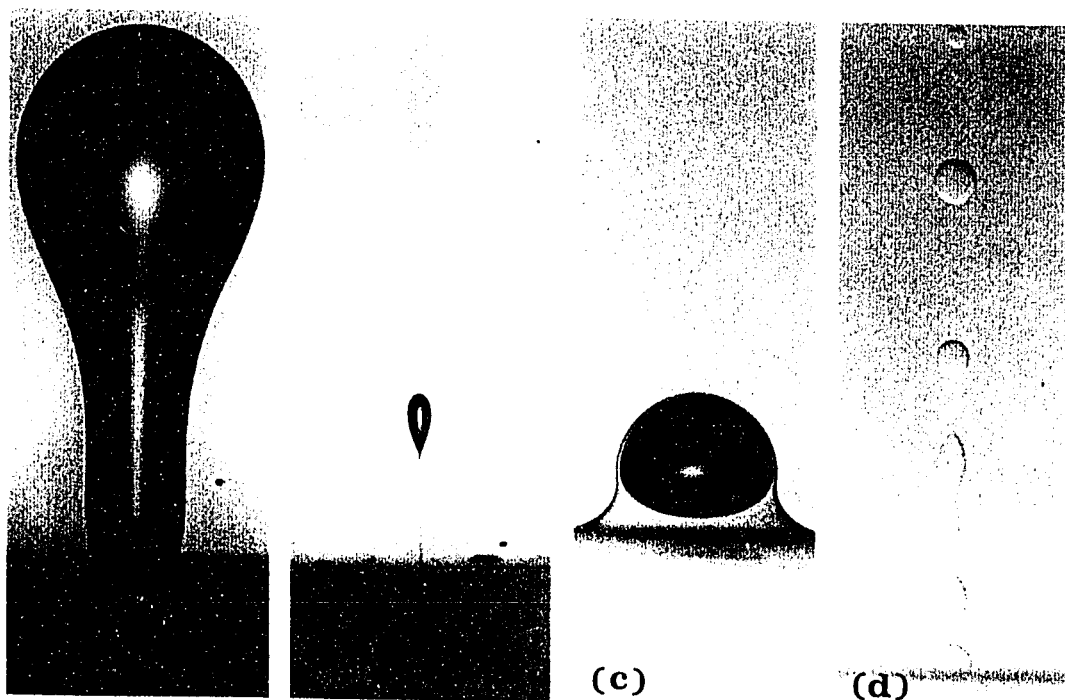


Figure 7.1: Different features characteristic of the motion of bubbles through fluid-fluid interfaces. The experimental results illustrate features 2-4 listed in the introduction. In (a) and (b), an air bubble translates through very viscous corn syrup towards a lower viscosity layer of polybutene (viscosity contrast between polybutene and corn syrup is 0.15). In (c) and (d), an air bubble translates through glycerin ($\mathcal{R} \approx 1$) towards a higher viscosity layer of polybutene (viscosity contrast between polybutene and glycerin is 40). The four photographs presented in figure 7.1 illustrate several of the features of the flow problem we consider. Complete sequences of photographs corresponding to *a-b* and *c-d* are shown in §7.4.

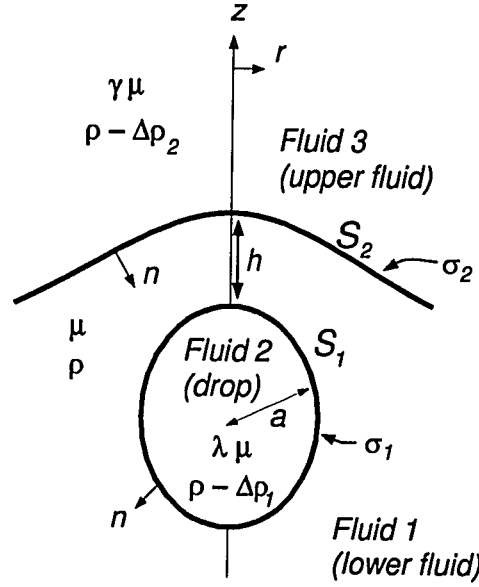


Figure 7.2: Geometry of the drop-interface problem. In this chapter, the initially planar fluid-fluid interface is referred to as the interface. The unit normal vector \mathbf{n} is directed outward from the drop and into the lower fluid away from the interface. The drop has undeformed radius a , viscosity $\lambda\mu$ and density $\rho - \Delta\rho_1$; the lower fluid has viscosity μ and density ρ ; the upper fluid has viscosity $\gamma\mu$ and density $\rho - \Delta\rho_2$. The interfacial tension is denoted by σ_1 on S_1 and σ_2 on S_2 . In all the calculations the initial position of the drop is $h = 4a$ below the initially flat interface, S_2 .

7.2 Problem formulation

The motion of a drop passing through a stably stratified fluid-fluid interface is modeled by considering three fluid domains: the drop, a lower fluid, and an upper fluid, as shown in figure 7.2. The boundary integral method is used to numerically study the flow problem. We denote the three fluid domains with subscripts 1, 2 and 3 for the lower fluid, the drop, and the upper fluid, respectively. The initially planar fluid-fluid interface will be referred to hereafter as the interface.

We require that the velocity decays to zero far from the drops,

$$\mathbf{u}_1 \rightarrow \mathbf{0} \text{ as } |\mathbf{x}| \rightarrow \infty \quad (7.2)$$

$$\mathbf{u}_3 \rightarrow \mathbf{0} \text{ as } |\mathbf{x}| \rightarrow \infty \quad (7.3)$$

and that the velocity is continuous across all interfaces,

$$\mathbf{u}_2 = \mathbf{u}_1 \text{ on } S_1 \text{ and } \mathbf{u}_3 = \mathbf{u}_1 \text{ on } S_2, \quad (7.4)$$

where S_1 is the surface bounding the drop and S_2 is the interface. The stress jump $[\![\mathbf{n} \cdot \mathbf{T}]\!]_i$ across a interface S_i is balanced by the pressure jump arising from density contrasts and interfacial tension stresses, which depend on the local curvature $\nabla_s \cdot \mathbf{n}$ of the interface:

$$[\![\mathbf{n} \cdot \mathbf{T}]\!]_1 = \mathbf{n} \cdot \mathbf{T}_1 - \mathbf{n} \cdot \mathbf{T}_2 = \sigma_1 (\nabla_s \cdot \mathbf{n})\mathbf{n} + \mathbf{n}\Delta\rho_1\mathbf{g} \cdot \mathbf{x} \quad \mathbf{x} \in S_1 \quad (7.5)$$

$$[\![\mathbf{n} \cdot \mathbf{T}]\!]_2 = \mathbf{n} \cdot \mathbf{T}_1 - \mathbf{n} \cdot \mathbf{T}_3 = \sigma_2 (\nabla_s \cdot \mathbf{n})\mathbf{n} + \mathbf{n}\Delta\rho_2\mathbf{g} \cdot \mathbf{x} \quad \mathbf{x} \in S_2, \quad (7.6)$$

where σ_i denotes the constant interfacial tension, \mathbf{n} is the unit normal directed into the lower fluid, and $\nabla_s = (\mathbf{I} - \mathbf{nn}) \cdot \nabla$ is the gradient operator tangent to the interface. Additionally there is a kinematic constraint, expressed with the Lagrangian description

$$\frac{d\mathbf{x}}{dt} = \mathbf{u}(\mathbf{x}) \quad \mathbf{x} \in S_1 \text{ and } S_2. \quad (7.7)$$

The equations are made dimensionless by choosing the characteristic length as the undeformed radius a of the drop, the velocity scale as $\Delta\rho_1ga^2/\mu$ and an advective timescale as $\mu/\Delta\rho_1ga$. For a given initial configuration (dimensionless separation distance h/a in figure 7.2), five dimensionless parameters characterize the flow: the viscosity ratios,

$$\lambda = \frac{\mu_{drop}}{\mu_{lower}} \text{ and } \gamma = \frac{\mu_{upper}}{\mu_{lower}}, \quad (7.8)$$

two Bond numbers

$$\mathcal{B}_1 = \frac{\Delta\rho_1ga^2}{\sigma_1} \text{ and } \mathcal{B}_2 = \frac{\Delta\rho_2ga^2}{\sigma_2}, \quad (7.9)$$

and a buoyancy parameter, defined as

$$\beta = \frac{\Delta\rho_2}{\Delta\rho_1}. \quad (7.10)$$

The frequently studied problem of a drop approaching its homophase corresponds to $\lambda = \gamma$, $\mathcal{B}_1 = \mathcal{B}_2$ and $\beta = 1$.

The mathematical problem as posed is axisymmetric so we seek axisymmetric solutions. We use the boundary integral formulation as described in appendices A and B and in chapter 2 to numerically study the problem illustrated in figure 7.2. Both fluid-fluid interfaces are represented numerically by 100 collocation points. In the numerical solution of the boundary integral equations, the initially planar interface, S_2 , is truncated at a distance of 15 drop radii from the axis of symmetry. Results computed for an interface that extends to distances between 10 and 50 drop radii show very little variation. A more detailed discussion of the effects of interface truncation are discussed in Lee & Leal [1982], Geller et al. [1986] and Stoos & Leal [1990].

7.3 Results

Below we present numerically calculated results for the buoyancy-driven motion of a deformable drop through a fluid-fluid interface. We begin in §7.3.1 by presenting interface shapes at different times during the simulations, with the dimensionless times labeled next to the corresponding drop shapes. Time is normalized by $\mu/\Delta\rho_1ga$. We then discuss four specific features characteristic of the dynamics: mode of drop deformation (§7.3.2), drop rise speed (§7.3.3), drop surface area (§7.3.4), and the rate of drainage of fluid between the drop and interface (§7.3.5).

7.3.1 Drop and interface deformation

There are five dimensionless parameters governing the translation and deformation of drops passing through interfaces, λ , γ , β , \mathcal{B}_1 and \mathcal{B}_2 as defined in §7.2.

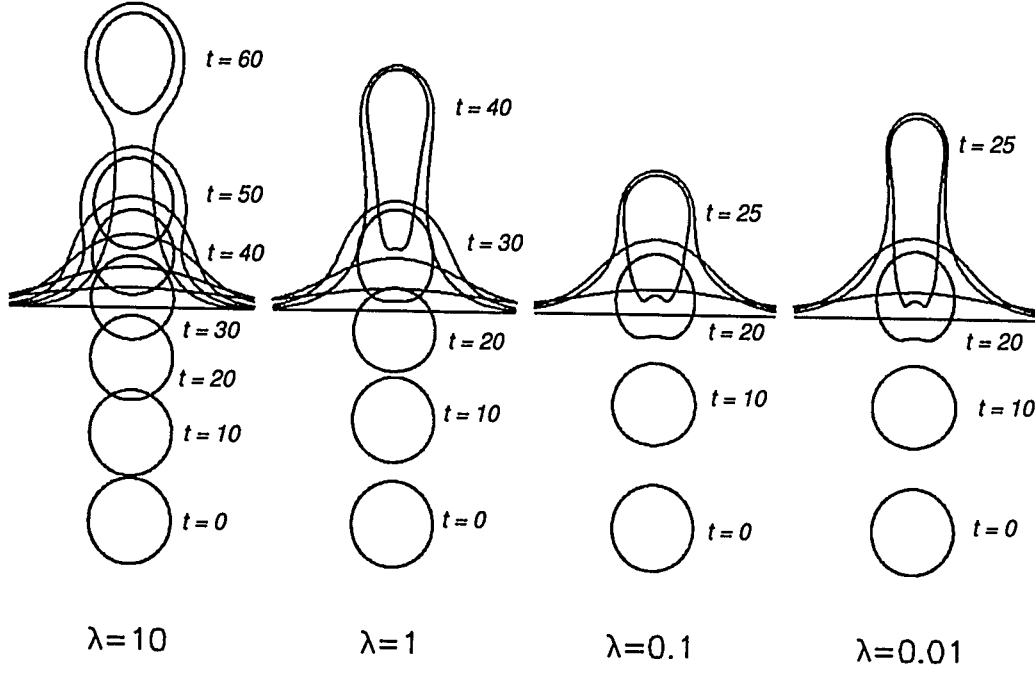


Figure 7.3: Effect of changing the ratio of drop to lower fluid viscosity for $\lambda = 10, 1, 0.1$ and 0.01 ; $\gamma = 0.1, \beta = 0.2, \mathcal{B}_1 = 20$ and $\mathcal{B}_2 = \infty$ for all simulations. Times are labeled next to the corresponding interface shapes.

(a) *Changing the ratio of drop to lower fluid viscosity; effects of changing λ*

In figure 7.3 we consider the effect of changing the viscosity ratio λ , the ratio of drop to lower fluid viscosity, on the translation of a drop through an interface. We present simulations for $\lambda = 10, 1, 0.1$ and 0.01 ; $\gamma = 0.1, \beta = 0.2, \mathcal{B}_1 = 20$ and $\mathcal{B}_2 = \infty$ for all simulations. As the viscosity ratio λ decreases, we observe that the magnitude of drop deformation at a given height above the interface increases. The rate at which the drop passes through the interface increases with decreasing λ . We further observe that the viscosity ratio λ affects the rate of drainage of the film of fluid which surrounds the drop as it passes through the interface. For $\lambda = 10$, the drop entrains a thick and nearly spherical layer of the lower fluid through the interface, whereas for $\lambda < O(1)$ the drops entrain only a thin layer of the lower fluid through the interface.

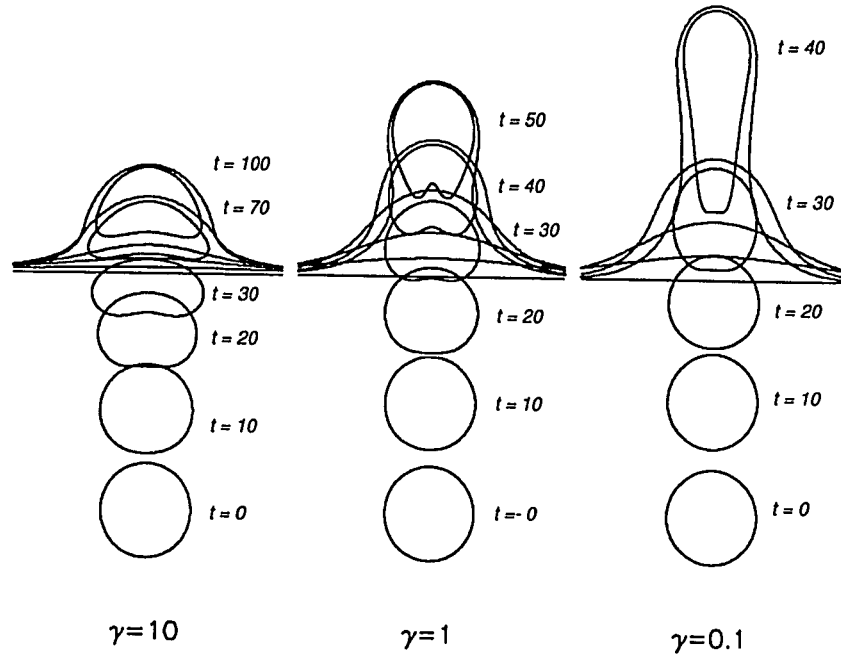


Figure 7.4: Effect of changing the ratio of upper to lower fluid viscosity for $\gamma = 10$, 1 and 0.1; $\lambda = 1$, $\beta = 0.2$, $\mathcal{B}_1 = 20$ and $\mathcal{B}_2 = \infty$. Times are labeled next to the corresponding interface shapes.

If the drops are sufficiently deformable, simulations with $\lambda = 1$, 0.1 and 0.01, the drop becomes extended as it enters the upper lower-viscosity fluid since the rise speed of the drop in the upper fluid is larger than the rise speed in the lower fluid. The time scale for deformation scales approximately as $1/(1 + \lambda)$ [Rallison 1984; Kojima et al. 1984] so that the $\lambda = 10$ high viscosity drop experiences significantly less distortion than the drops in the other simulations.

(b) Changing the ratio of upper to lower fluid viscosity; effect of changing γ

In figure 7.4 we consider the effect of changing the viscosity ratio γ , the ratio of upper to lower fluid viscosity, on the translation of a drop through a fluid interface. We present simulations for $\gamma = 10$, 1 and 0.1; $\lambda = 1$, $\beta = 0.2$, $\mathcal{B}_1 = 20$ and

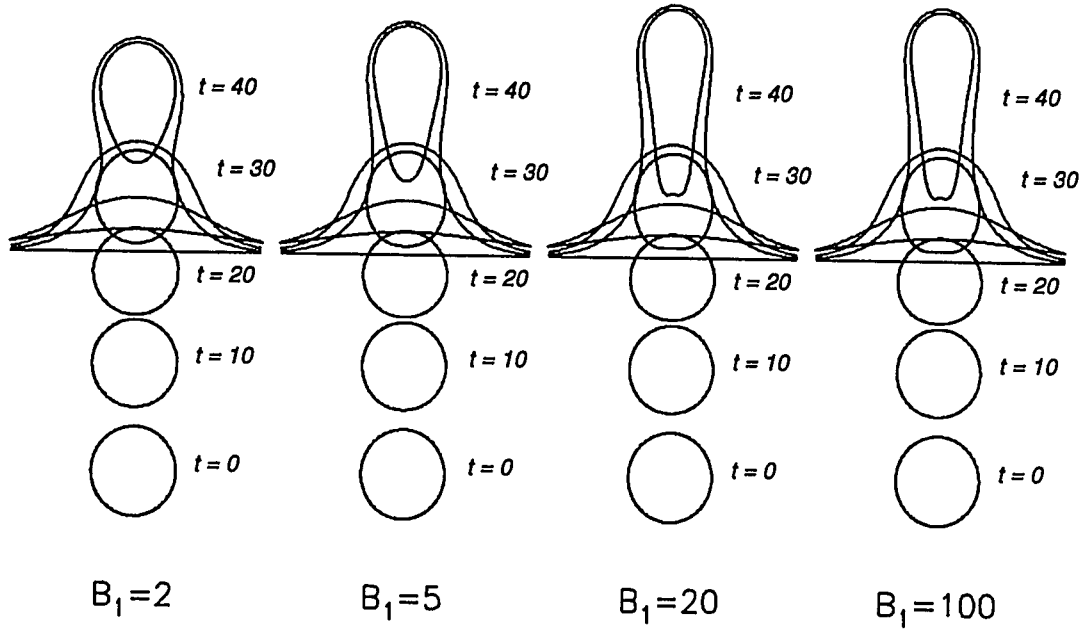


Figure 7.5: Effect of changing \mathcal{B}_1 for $\mathcal{B}_1 = 2, 5, 20$ and 100 ; $\lambda = 1$, $\gamma = 0.1$, $\beta = 0.2$, and $\mathcal{B}_2 = \infty$. Times are labeled next to the corresponding interface shapes.

$\mathcal{B}_2 = \infty$ for all simulations. Drops entering the low viscosity upper fluid are extended and translate more rapidly (accelerate), while drops entering a higher viscosity upper fluid develop a dimple or small cavity at the back of the drop and translate more slowly (decelerate). The vertical extension of drops entering a lower viscosity upper fluid occurs since the rise speed of the drop is greater in the upper fluid than the lower fluid (the Hadamard-Rybczyński rise speed is inversely proportional to the external fluid viscosity).

(c) *Changing the ratio of buoyancy forces to interfacial tension forces*

In figure 7.5 and 7.6 we consider the effect of changing the importance of interfacial tension forces relative to buoyancy forces, corresponding to varying the parameters \mathcal{B}_1 and \mathcal{B}_2 . Increasing the importance of interfacial tension, decreasing \mathcal{B} , decreases the magnitude of interface deformation. In figure 7.5 we change the Bond number of

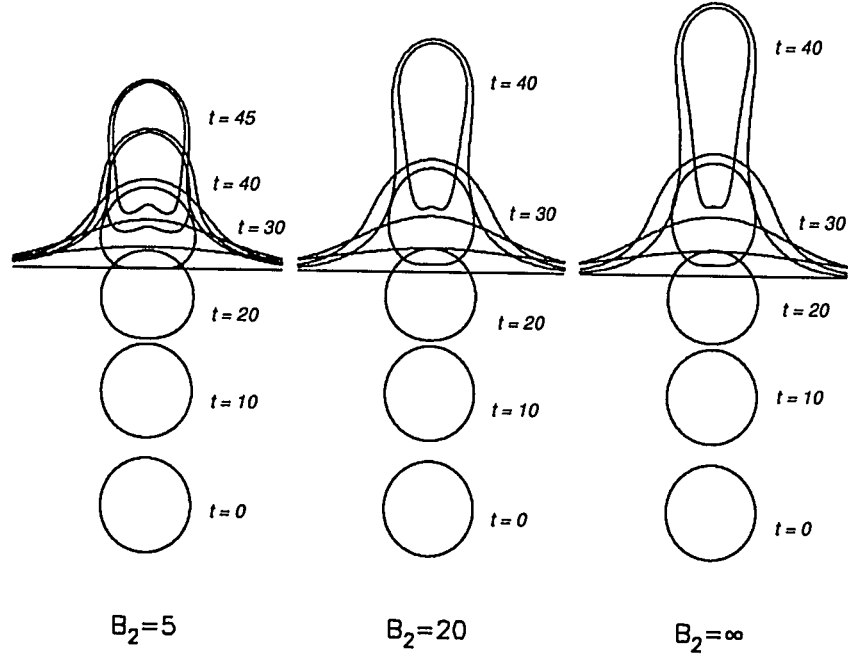
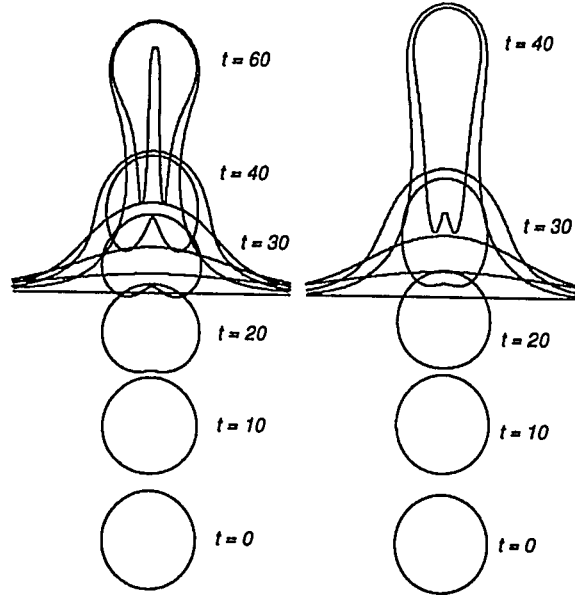


Figure 7.6: Effect of changing B_2 for $B_2 = 5, 20$ and 100 ; $\lambda = 1$, $\gamma = 0.1$, $\beta = 0.2$, and $B_1 = 20$. Times are labeled next to the corresponding interface shapes.

the drop, for $B_1 = 2, 5, 20$ and 100 ; $\lambda = 1$, $\gamma = 0.1$, $\beta = 0.2$, and $B_2 = \infty$. For the large values of the Bond number considered here, as the Bond number decreases the magnitude of drop distortion decreases, however the rate at which the drop passes through the interface changes very little. In figure 7.6 we change the Bond number of the interface, for $B_2 = 5, 20$ and 100 ; $\lambda = 1$, $\gamma = 0.1$, $\beta = 0.2$, and $B_1 = 20$. Increasing the interfacial tension on the interface decreases the rate at which the drop passes through the interface. For the $B_2 = 5$ simulation, a dimple or indentation develops at the back of the drop.

7.3.2 Mode of drop deformation

Previous studies by Koh & Leal [1989, 1990] and Pozrikidis [1990] have demonstrated that nonspherical drops are unstable if the interfacial tension stresses are not suffi-



$$\lambda=\gamma=1$$

$$\lambda=1, \gamma=0.1$$

Figure 7.7: Mode of deformation: (a) cavity formation for $\lambda = \gamma = 1$ and (b) drop elongation for $\lambda = 1$ and $\gamma = 0.1$. For both simulations $\mathcal{B}_1 = \mathcal{B}_2 = \infty$ and $\beta = 0.2$.

ciently large to return the drop to a spherical shape. The shape is unstable in the sense that it will deform and change shape continuously with the only stable shape being a sphere [Kojima et al. 1984]. Two distinct modes of deformation for unstable shapes are observed (as demonstrated in figure 1.3).

1. Initially prolate drops become elongated, the front of the drop develops a nearly spherical shape, and the back of the drop forms an ever-elongating tail which may eventually break into a series of smaller droplets due to a capillary instability.
2. Initially oblate drops become indented at the back and a cavity develops inside the drop. For large Bond numbers, an ever-elongating annular tail forms at the back of the drop surrounding the cavity inside the drop.

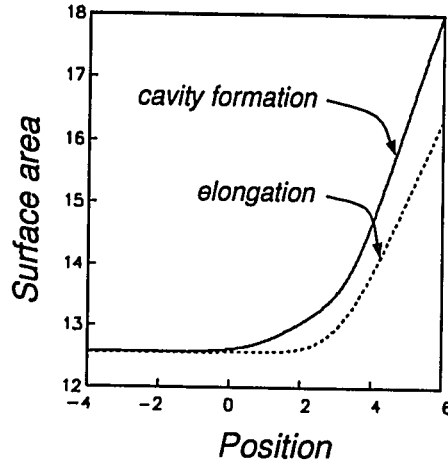


Figure 7.8: Drop surface area for the simulations shown in figure 7.7. Surface area increases most rapidly (rapidly is defined in terms of the vertical distance traveled through the interface) when a cavity forms.

Drops passing through interfaces also exhibit modes of deformation analogous to the two modes of deformation of a single drop in a unbounded fluid. In figure 7.7 we present two examples of simulations illustrating both modes of deformation, referred to hereafter as “cavity formation” and “elongation”. All fluid properties in both simulations are the same except the viscosity ratio of the upper to lower fluids. For the simulation with $\gamma = 1$ a cavity develops inside the drop and an annular tail forms; for the simulation with $\gamma = 0.1$ the drop becomes elongated. All drops initially develop a dimple at the back as they approach the fluid interface since all drops slow down as they approach an interface. The distorted drop shape, produced as a result of the interaction with the fluid interface, may be unstable in a manner analogous to a single drop in an unbounded fluid; the drop may then develop a cavity and possibly an annular tail if interfacial tension stresses are not sufficiently large to return the drop to, or retain, a nearly spherical shape. If the drop enters a lower viscosity fluid, where it translates faster, the drop may become elongated. For the simulation with $\gamma = 0.1$ the effects of the elongation dominate over the effects of the initial indentation at the back of the drop. Notice that a small dimple persists at the

back of the elongated drop.

In figure 7.8 we consider one feature of very deformable drops passing through an interface. For the two simulations presented in figure 7.7 we compute the surface area of the drop as a function of the distance the drop has translated through the interface. At a given height above the interface, the surface area of the drop with a cavity is larger due to the additional surface area of the cavity.

7.3.3 Rise speed

In figure 7.9 we present drop rise speeds as a function of position. The rise speed is defined as the velocity of the front of the drop along the axis of symmetry. The position is defined by the height of the front of the drop relative to the initial position of the flat fluid-fluid interface. The four set of curves, figures 7.9a-d, correspond to the simulations presented in figures 7.3-7.6.

As the viscosity of the drop decreases, the rise speed increases, both as the drop approaches the interface (with variations largely determined by the Hadamard-Rybczyński speed), and as the drop passes through the interface. As the viscosity ratio of the upper fluid increases, the rise speed of the drop decreases, since rise speed is proportional to the external fluid viscosity.

Changing the interfacial tension on the drop for large Bond numbers ($\mathcal{B} > 5$) does not significantly affect the rise speed of the drop. As the interfacial tension of the interface is increased, *i.e.* as \mathcal{B}_2 is decreased, the rise speed of the drop decreases. In particular, the minimum rise speed decreases as \mathcal{B}_2 decreases. However, as the drop moves away from the interface, larger interfacial tension stresses will result in faster rise speeds due to an enhanced constriction of the interface around the extended drop (compare the curve for $\mathcal{B} = 5$ with the curve for $\mathcal{B} = 100$ for positions $h > 4a$).

All drops reach a minimum rise speed when the front of the drop is at a distance of about 0.5 to 2.5 drop radii above the initial position of the fluid-fluid interface, as a result of the negative buoyancy or restoring forces associated the more dense lower fluid displaced vertically and entrained by the rising drop. Low viscosity ratio

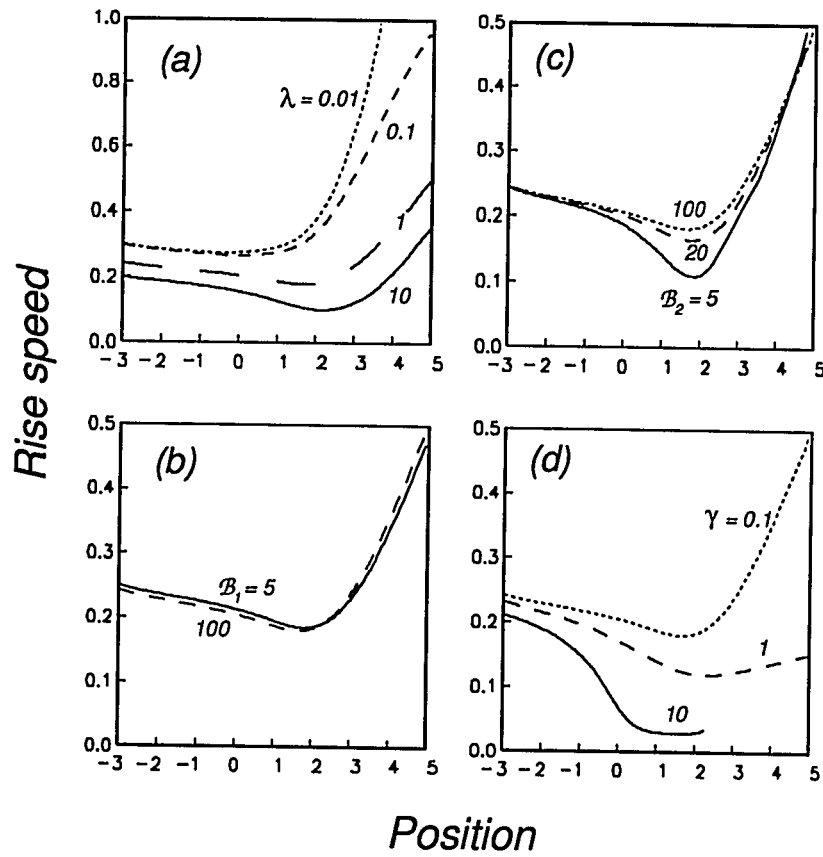


Figure 7.9: Rise speed of the top of the drop as a function of the position of the top of the drop: (a) $\lambda = 10, 1, 0.1$ and 0.01 with $\gamma = 0.1, \beta = 0.2, B_1 = 20, B_1 = \infty$, (b) $B_1 = 5, 20$ and 100 with $\lambda = 1, \gamma = 0.1, \beta = 0.2, B_2 = \infty$, (c) $B_2 = 5, 20$ and 100 with $\lambda = 1, \gamma = 0.1, \beta = 0.2, B_1 = 10$, and (d) $\gamma = 10, 1$ and 0.1 with $\lambda = 1, \beta = 0.2, B_1 = 20, B_1 = \infty$.

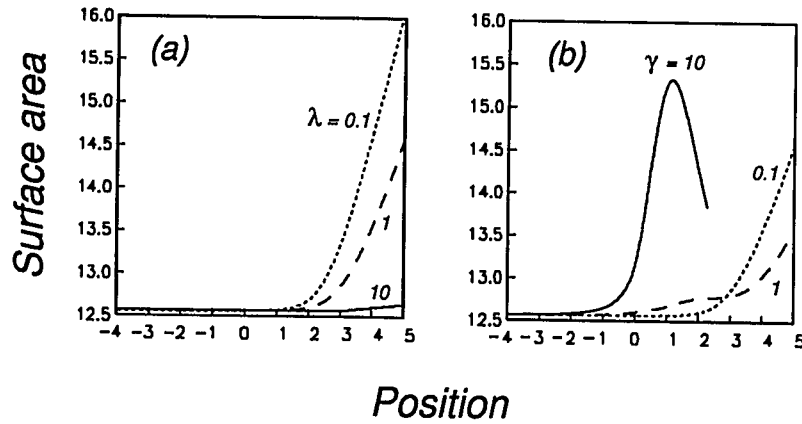


Figure 7.10: Surface area of drop as a function of the height of the top of the drop: (a) $\lambda = 10, 1$ and 0.1 with $\gamma = 0.1$, $\beta = 0.2$, $B_1 = 20$, $B_1 = \infty$, and (b) $\gamma = 10, 1$ and 0.1 with $\lambda = 1$, $\beta = 0.2$, $B_1 = 20$, $B_1 = \infty$.

drops reach their minimum rise speed at a smaller distance past the initial interface position than high viscosity ratio drops.

7.3.4 Drop surface area

In figure 7.10 we present calculated surface areas of drops for the simulations presented in figure 7.3 and 7.4. For the case of drops entering a lower viscosity upper fluid, figure 7.10a, at a given height above the interface the surface area is larger for drops with low viscosity ratios λ . Since the rate of deformation scales approximately as $1/(1+\lambda)$, drops with a low viscosity ratio deform faster than drops with a high viscosity ratio.

The calculated surface areas of the drops presented in 7.10b illustrate a few interesting features (in figure 7.10b the ratio of the upper to lower fluid viscosity is changed). As discussed in §7.3.3, the flattening of the drop beneath a higher viscosity upper fluid for the simulation with $\gamma = 10$ leads to a greater surface area as the drop approaches the interface. The drop for $\gamma = 1$ develops a cavity (whereas the drop for $\gamma = 0.1$ is elongated) thus resulting in a larger increase in surface area for a given

translation distance for positions less than about $3a$. As the drops continue to rise through the interface, the effect of elongation for $\gamma = 0.1$ results in a greater increase in surface area than the simulation with $\gamma = 1$. In the simulation with $\gamma = 10$, the drop's surface increases as the drop approaches the interface and then decreases as the drop passes through the interface. The initial increase in surface area is the result of the drop spreading and flattening beneath the high viscosity upper fluid. The decrease of surface area occurs since the interfacial tension stresses become large compared to the stresses which result in deformation and thus the drop tends to return to a spherical shape. The timescale for deformation due to interfacial tension stresses changes very little however the timescale for deformation due to translation of a nonspherical shape is greatly reduced due to the higher viscosity of the upper fluid (although the buoyancy forces do not change).

7.3.5 Gap thickness

In figure 7.11 we present the computed gap thickness for the simulations presented in figures 7.3-7.6. Gap thickness provides an indication of the rate of which the film surrounding the drop thins. The results presented in chapter 2 [Manga & Stone 1993a] demonstrate the importance of the viscosity ratio λ and interfacial tension (characterized by the Bond number) on the manner in which the film drains. However, for the range of parameters considered here, namely large Bond numbers $\mathcal{B} > 5$, no dimple is observed to form, at least for the range of gap thicknesses computed and the parameter range examined in the numerical simulations. A previous study by Chi & Leal [1989] for drops approaching their homophase with $1 < \mathcal{B} < 10$ (the drop is the same fluid as the upper fluid) developed a dimpled mode of film drainage under similar conditions to those required for two drops (chapter 2). We suggest that since the drops studied here are passing through the interface, the motion of the drops prevents the formation of a dimple, with only uniform and rapid modes of drainage occurring. Yiantsios & Davis [1991] found that dimples always form for $\mathcal{B} \ll 1$.

The results presented in figure 7.11 indicate that for a drop at a given height

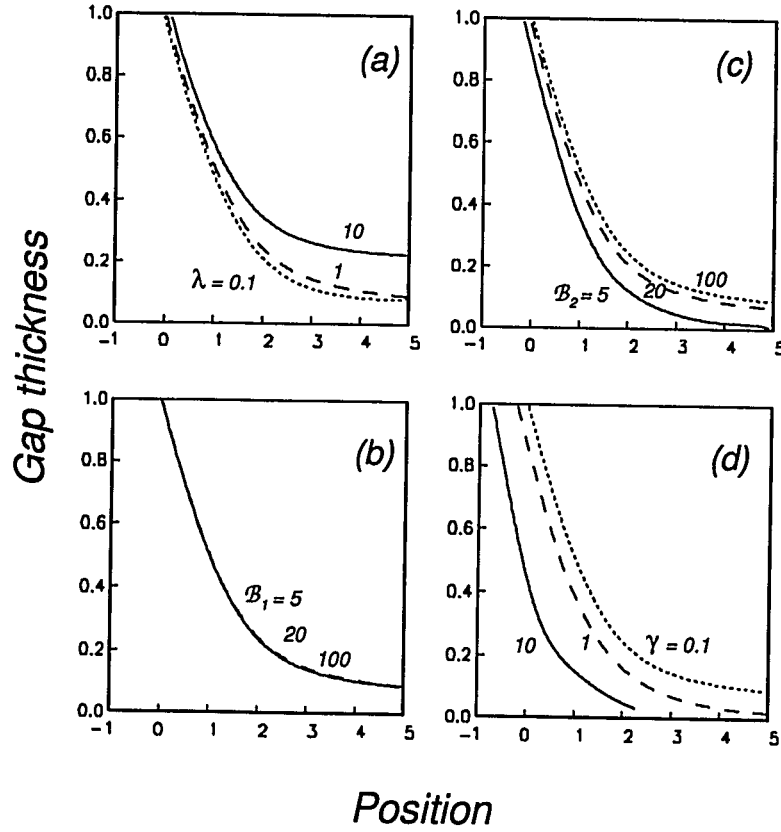


Figure 7.11: Gap thickness h/a between the top of the drop and the interface along the axis of symmetry: (a) $\lambda = 10, 1$ and 0.1 with $\gamma = 0.1$, $\beta = 0.2$, $B_1 = 20$, $B_1 = \infty$, (b) $B_1 = 5, 20$ and 100 with $\lambda = 1$, $\gamma = 0.1$, $\beta = 0.2$, $B_2 = \infty$, (c) $B_2 = 5, 20$ and 100 with $\lambda = 1$, $\gamma = 0.1$, $\beta = 0.2$, $B_1 = 10$, and (d) $\gamma = 10, 1$ and 0.1 with $\lambda = 1$, $\beta = 0.2$, $B_1 = 20$, $B_1 = \infty$.

above the interface, the film of fluid coating the drop is thinnest for drops with a low viscosity ratio λ . Drops with a high viscosity ratio λ entering a lower viscosity fluid become coated with a thick layer of the lower fluid (figure 7.11*a*; see also the simulation with $\lambda = 10$ in figure 7.3) since the high viscosity drop acts to retard drainage of the film fluid whereas low viscosity drops provide little resistance to film drainage. Increasing the viscosity of the upper fluid (increasing γ) results in a thinner gap for drops which have translated the same distance through the interface (figure 7.11*d*). Increasing the interfacial tension of the interface results in a thinner gap for drops which have translated the same distance through the interface (figure 7.11*c*). The Bond number of the drop has little effect on film drainage for moderate to large Bond numbers, $B > 2$ (figure 7.11*b*).

7.4 Experimental results

In section 7.3 we considered the motion and deformation of a single drop translating through an interface. Due to limitations of the numerical approach employed in §7.3 (the separation distance between the two fluid-fluid interfaces could not become too small during the computations nor could we model drop and interface breakup) there are a number of features of the problem we could not consider, for example, *(i)* the break-off of the drop from the interface which requires the interfacial-tension-driven constriction of the thin column of fluid entrained by the rising drop, *(ii)* the breakup of the drop as it is extended when passing from a higher to lower viscosity fluid, and *(iii)* multiple particle interactions. In this section we consider experimentally the long-time evolution of the different fluid phases as bubbles and rigid spheres pass through fluid-fluid interfaces. We also discuss the implications of the experimental and numerical results on separation and extraction processes (which involve many sedimenting particles or rising bubbles) which might occur in both some industrial multiphase flows as well as naturally occurring stratified fluid systems.

Table 7.1: Tank geometries used in laboratory experiments. Dimensions are *length* \times *width* \times *height*.

Tank number	Tank size (cm)	Upper fluid	Lower fluid	Corresponding experiments
1	$19 \times 19 \times 36$	Polybutene	Corn syrup	figure 7.22
2	$31 \times 15 \times 19$	Polybutene	Corn syrup	figures 7.1 <i>ab</i> , 7.12, 7.18
3	$31 \times 15 \times 19$	Polybutene	Glycerin	figures 7.1 <i>cd</i> 7.13, 7.14 figures 7.16, 7.17, 7.19, 7.21

7.4.1 Experimental apparatus

The experiments are performed in either a rectangular tank with a height of 36 cm, and a base 19 cm by 19 cm, referred to hereafter as tank 1, or in one of two smaller rectangular tanks with heights 19 cm, and a base 15 cm by 31 cm, referred to hereafter as tanks 2 and 3 (see table 7.1). Tanks 1 and 2 are filled with corn syrup (bottom) and polybutene (top). Tank 3 is filled with glycerin (bottom) and polybutene (top). The corn syrup in tank 2 is coloured with red food colouring in order to enhance the visual contrast between the two fluid layers. The Reynolds number \mathcal{R} of bubbles and particles presented here is small in corn syrup, $\mathcal{R} < O(0.001)$ and polybutene, $\mathcal{R} < O(0.1)$, but may be large in glycerin, $\mathcal{R} = O(1)$.¹

¹An estimate of the interfacial tension between corn syrup and polybutene and between glycerin and polybutene was determined using the pendant drop technique [Fordham 1948]. We found $\sigma = 0.028 \pm 0.006$ N/m for corn syrup and polybutene and $\sigma = 0.022 \pm 0.04$ N/m for glycerin and polybutene. The error estimates are based on measurement uncertainties. The relaxing drop method [Tjahjadi et al. 1994] was also used to confirm the pendant drop results. The relaxing drop method provided similar results, but with larger experimental uncertainties. Since we are using the experimental results to present and describe qualitative features of the motion of bubbles and particles through fluid interfaces, we can justify the large uncertainty in the estimates of interfacial tension.

Typical bubble and particle lengthscales (radii for bubbles and rigid spheres and length for slender bodies) are 0.5-2 cm. Thus in the experiments wall and boundary effects should be small so that boundary effects should have little qualitative effect on the experimental results presented below.

7.4.2 A single bubble passing through an interface

In figure 7.1*a,b* we presented two photographs of the translation of an air bubble through an interface into a less viscous fluid. In figure 7.12 we present the complete sequence of photographs from which the photographs in figure 7.1 were taken, and focus on the deformation of the air bubble. As the bubble approaches the interface, it initially becomes slightly oblate or flattened. As the bubble passes through the fluid interface the bubble becomes extended and a long tail forms behind the bubble. The long tail then breaks off from the bubble and eventually breaks again to form two smaller bubbles. Notice that the two small bubbles are moving down in the final photographs. The downwards motion is the result of the relaxation of the deformed interface due to the negative (restoring) buoyancy forces exerted by the deformed interface. The general features of the experimental results at earlier times are similar to the numerical results shown in figure 7.3 for the simulation with $\lambda = 0.01$; in particular note the shape of the bubble and the distinctive shape of the back of the bubble. In the numerical calculations the film of fluid between the drop and interface eventually becomes too thin to allow us to compare the experimental and numerical results for times longer than those shown in figure 7.3.

In figure 7.1*c,d* we presented two photographs of the motion of an air bubble through an interface into a more viscous fluid. In figure 7.13 we present the complete sequence of photographs from which the photographs in figure 7.1 were taken, and focus on the thin column of the lower fluid entrained through the interface. The Reynolds number based on the lower fluid viscosity (glycerin) characteristic of the motion of the bubble towards the interface is large, $\mathcal{R} \approx 1$. Notice that the air bubble in the lower fluid is not spherical, but slightly oblate which is characteristic of

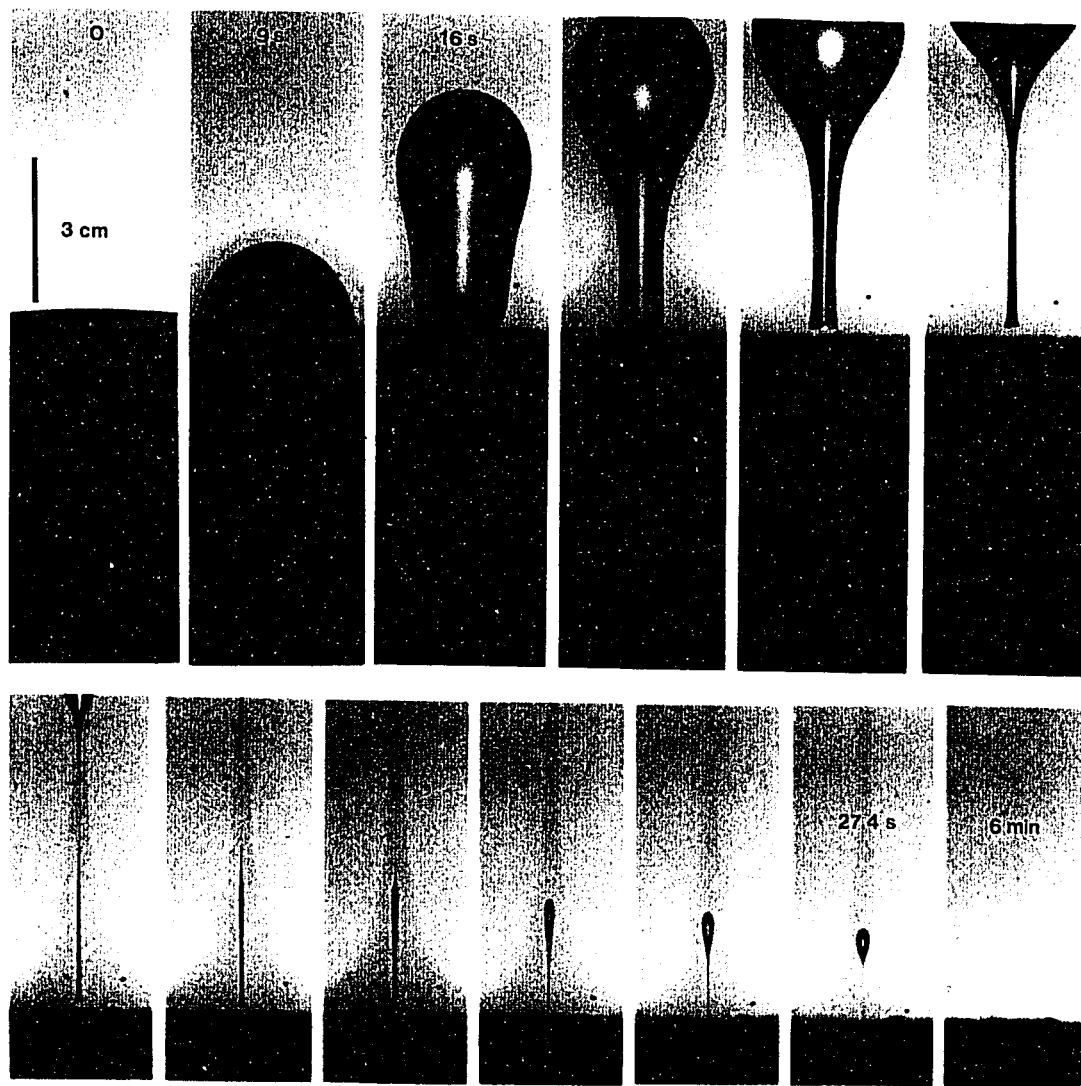


Figure 7.12: Photographs of an air bubble passing from a higher to lower viscosity fluid. Times and a scale bar are shown on the photographs. The upper fluid is polybutene, the lower fluid is corn syrup; $\lambda = 0$, $\gamma = 0.15$, $B_1 \approx 45$, $B_2 \approx 40$ and $\beta = 0.37$. The Reynolds number is < 0.001 in the lower fluid and < 0.05 in the upper fluid.

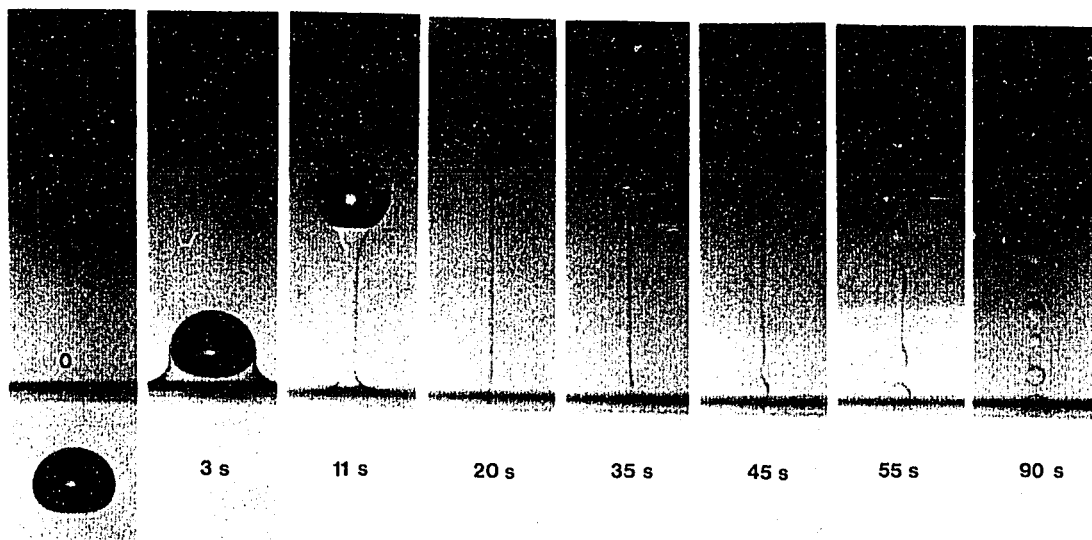


Figure 7.13: Photographs of an air bubble passing from a lower to higher viscosity fluid. Times and a scale bar are shown on the photographs. The upper fluid is polybutene, the lower fluid is glycerin; $\lambda = 0$, $\gamma = 0.02$, $B_1 \approx 4$, $B_2 \approx 3.4$ and $\beta = 0.27$. The Reynolds number is ≈ 1 in the lower fluid and < 0.01 in the upper fluid.

translating bubbles at high Reynolds numbers. The Reynolds number based on the upper fluid viscosity (polybutene) characteristic of the motion of the bubble through and past the interface is smaller, $\mathcal{R} < 0.01$. As the bubble continues to rise, a long column of the lower fluid is entrained across the interface. At a height of about 10 radii above the interface, the bubble breaks off from the lower fluid. The column of the lower fluid entrained by the bubble undergoes a Rayleigh or capillary instability and breaks up into smaller drops. The droplets consisting of the lower fluid then sediment and eventually coalesce with the lower fluid.

In figure 7.3 we observed that drops with a large viscosity ratio λ entrain a thick layer of fluid around the drop as they pass through an interface into a lower viscosity fluid. In figure 7.14 we present a sequence of photographs of a rigid teflon sphere passing through an interface into a lower viscosity fluid (from polybutene into glycerin).

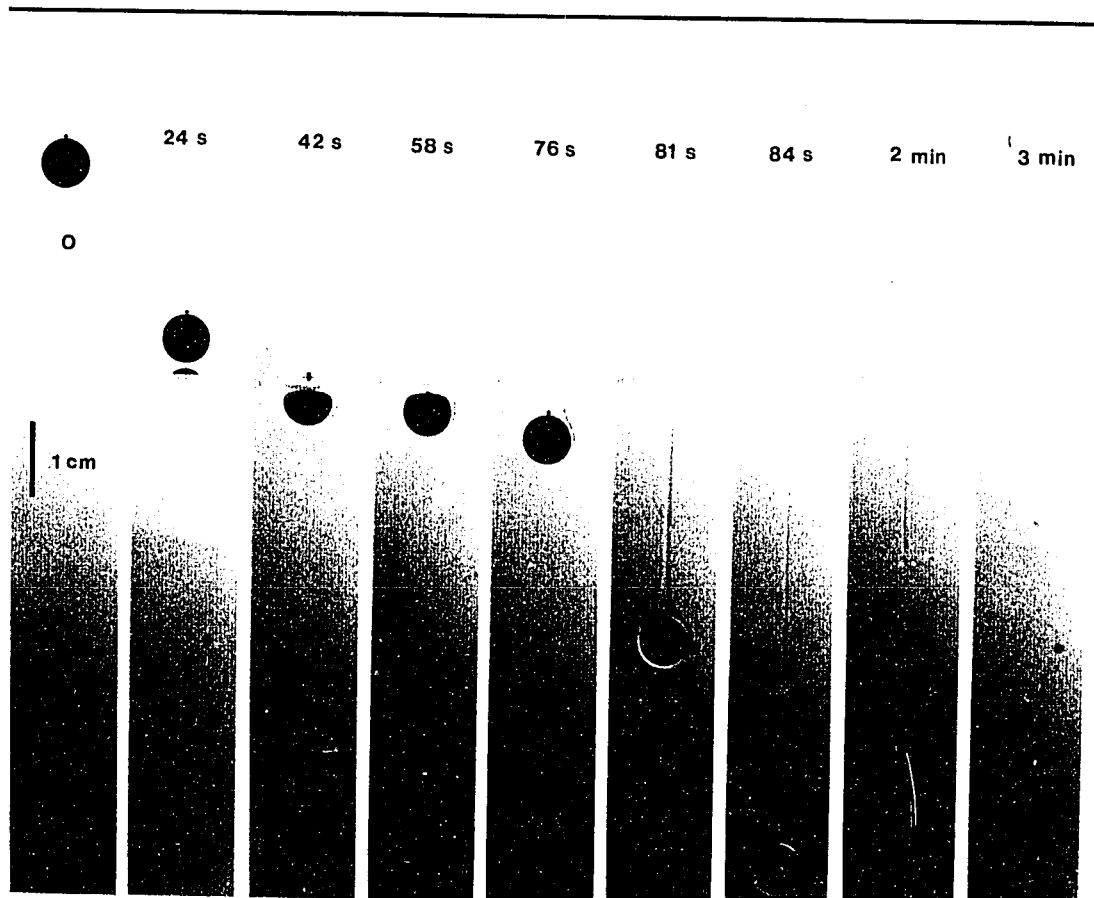


Figure 7.14: Photographs of a teflon sphere passing from a higher to lower viscosity fluid. Times and a scale bar are shown on the photographs. The upper fluid is polybutene, the lower fluid is glycerin; $\lambda = \infty$, $\gamma = 40$, $\mathcal{B}_2 \approx 1.4$ and $\beta = 0.23$. The Reynolds number is < 0.0001 in the upper fluid and < 0.1 in the lower fluid.

The sphere remains coated with a thick layer of polybutene as it passes through the interface. By contrast, the bubbles in figures 7.12 and 7.13 do not remain coated as they pass through the interface. The coated sphere sinks to the bottom of the tank. Since the layer of fluid entrained by the sphere (polybutene) is buoyant relative to the lower fluid (glycerin) the entrained fluid eventually separates from the sphere and forms a drop; the drop then rises through the lower fluid, and coalesces with the upper fluid.

In order to understand some of the features of the results presented in figures 7.12-14, we show numerically calculated streamlines for a drop passing through an interface in figure 7.15. Streamlines are shown for drops at different stages as they pass through the interface. Streamlines for a rising drop approaching an interface converge behind the drop and diverge in front of the drop. Note that there is a stagnation point in the flow in 7.15*a* above the interface due to the relaxation of the interface at large radial distances away from the drop; as the drop approaches the interface, the wavelength of the surface deformation decreases (and the amplitude increases) so that the longest wavelengths of the surface distortion are always relaxing. Once the drop has passed through the interface and the fluid interface is relaxing, a stagnation point develops in the flow field behind the drop. The flow induced by the relaxing interface in figure 7.15*c* explains the downwards motion of the small bubbles in figure 7.12.

7.4.3 Multiple particles passing through interfaces

In this section we present experimental results for the motion of two or more rigid spheres through fluid-fluid interfaces.

In figure 7.16 we present a sequence of photographs of two rigid spheres passing through an interface into a lower viscosity fluid. The spheres are initially offset in the horizontal direction. As the spheres pass through the interface, they approach each other and translate through the interface together and sediment as a “doublet”. As discussed in §7.3.3, the first sphere slows down as it approaches the interface. The second sphere is then able to “catch up” to the first sphere.

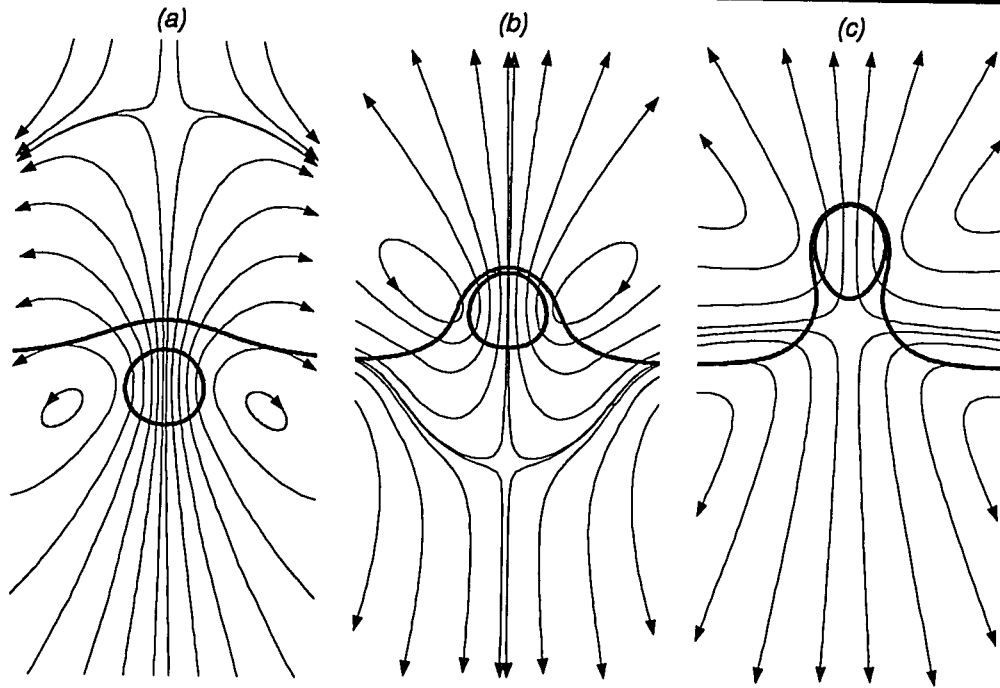


Figure 7.15: Streamlines due to a translating drop passing through an interface: (a) a drop approaching the interface, (b) a drop passing through the interface and (c) a drop which has passed through the interface. Streamlines are calculated for a simulation with $\lambda = \gamma = 1$, $B_1 = 5$, $B_2 = \infty$ and $\beta = 0.2$. In (c), since the interface is relaxing due to negative buoyancy (restoring) forces associated with the deflected interface, there is a stagnation point in the flow beneath the drop.

The clustering or coagulation of the two spheres in this experiment is the result of interfacial tension effects associated with the deformed interface. A region of large curvature develops on the interface between the two spheres which relaxes and pulls the two spheres together. The lateral motion of the spheres is possible since the lower fluid offers very little resistance because of its relatively low viscosity. Physically, we may expect that since the interface “tries” to minimize its surface area, particles tend to cluster together at the interface.

The coagulation or clustering of particles is demonstrated more clearly in figure 7.17. In the experiment presented in figure 7.17 a large number of spheres are released

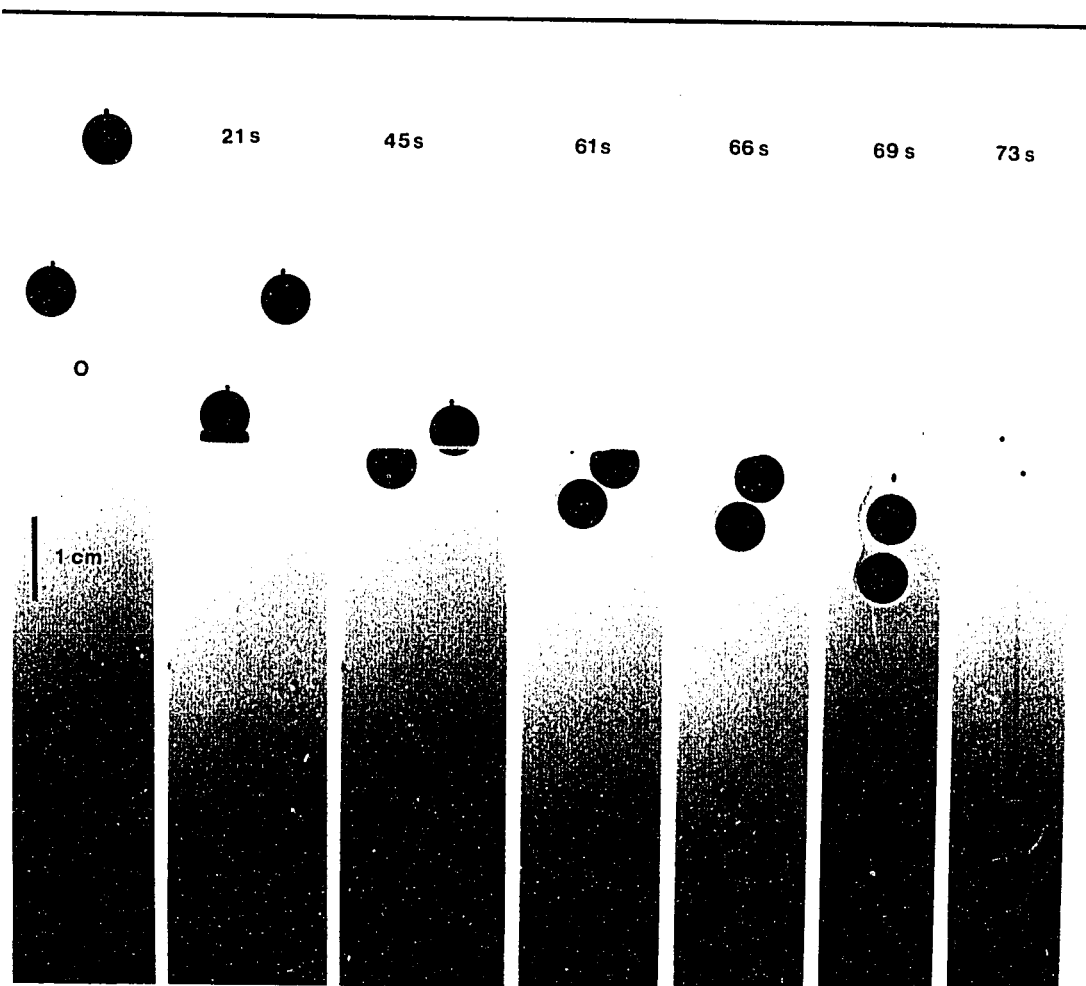


Figure 7.16: Photographs of two tefflon spheres passing from a higher to lower viscosity fluid. Times and a length scale are shown on the photographs. The upper fluid is polybutene, the lower fluid is glycerin; $\lambda = \infty$, $\gamma = 40$, $\mathcal{B}_2 \approx 1.4$ and $\beta = 0.23$. The Reynolds number is < 0.0001 in the upper fluid and < 0.1 in the lower fluid.

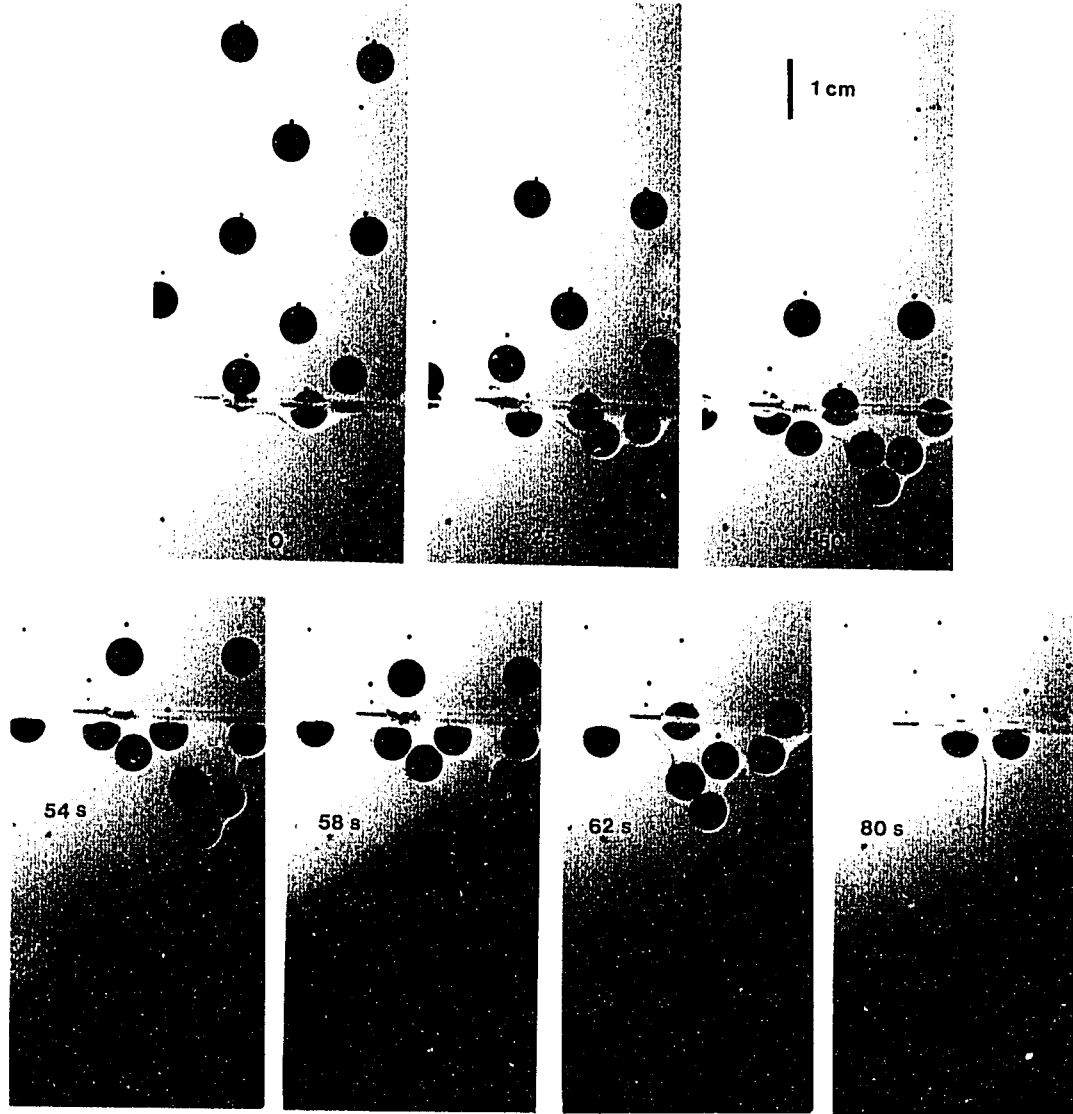


Figure 7.17: Photographs of several tefton spheres passing from a higher to lower viscosity fluid. Times and a length scale are shown on the photographs. The upper fluid is polybutene, the lower fluid is glycerin; $\lambda = \infty$, $\gamma = 40$, $B_2 \approx 1.4$ and $\beta = 0.23$. The Reynolds number is < 0.0001 in the upper fluid and < 0.1 in the lower fluid.

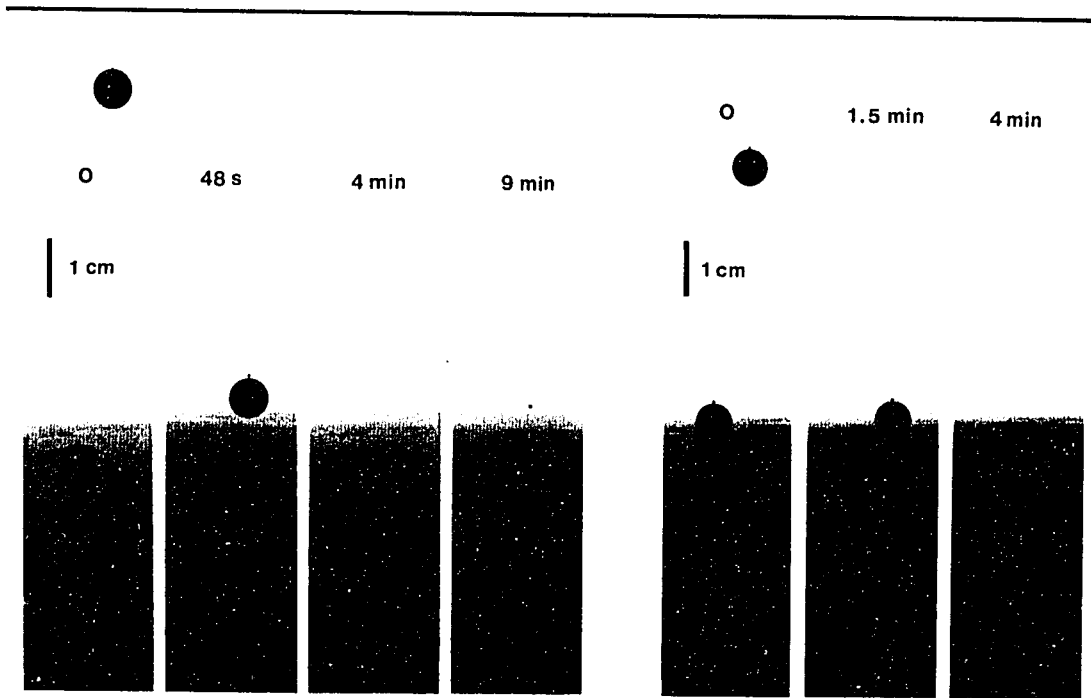


Figure 7.18: Photographs of two teflon spheres passing from a lower to higher viscosity fluid. Times and a length scale are shown on the photographs. The upper fluid is polybutene, the lower fluid is corn syrup; $\lambda = \infty$, $\gamma = 7$, $B_2 \approx 1.1$ and $\beta = 0.37$. The Reynolds number is < 0.0001 in the both fluids.

into the upper fluid. The spheres are initially well distributed in the upper fluid. Since the spheres slow down as they pass through the interface they tend to accumulate at the interface. At the interface, spheres tend to cluster before they pass through the interface. Note that groups of spheres (compare figure 7.16 and 7.17 with figure 7.14) entrain more fluid than single spheres.

If particles instead move from a lower to higher viscosity fluid, a thin column of low viscosity fluid is entrained through the interface. The low viscosity channel offers a path of lowered resistance and we might expect that a trailing and offset particle may follow the path of lower resistance, and thus follow the leading particle, leading to the formation of vertically aligned structures. However, the rigid spheres shown in 7.18 passing into a higher viscosity fluid do not become vertically aligned. One

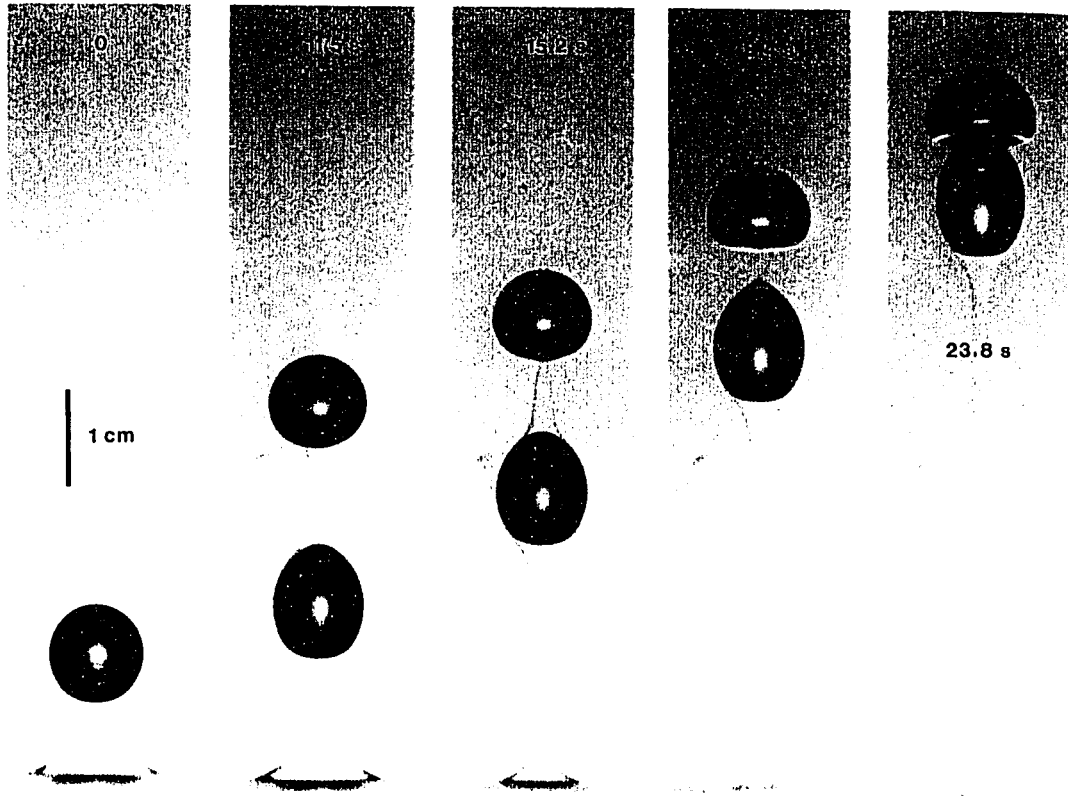


Figure 7.19: Photographs of two vertically aligned bubbles passing from a lower to higher viscosity fluid. Times and a length scale are shown on the photographs. The upper fluid is polybutene, the lower fluid is glycerin; $\lambda = \infty$, $\gamma = 0.02$, $B_1 \approx 3.4$, $B_2 \approx 2.7$, and $\beta = 0.27$. The Reynolds number is ≈ 1 in the lower fluid and < 0.01 in the upper fluid.

possible explanation for the lack of alignment might be that the spheres were too far apart horizontally. However, we recall that once the first sphere has passed through the interface, the interface relaxes, driving a flow which would tend to push the second sphere away from the column of entrained fluid.

7.4.4 The motion of two vertically aligned bubbles through a fluid-fluid interface

In figure 7.19 we show a sequence of photographs of two vertically aligned bubbles passing from a lower to higher viscosity fluid. The first bubble entrains a column of the lower viscosity fluid across the interface. The second bubble experiences less viscous resistance as it follows the first bubble through the column. The second bubble develops a slightly elongated shape. In the limit of vanishing interfacial tension, the effect of such conduits of low viscosity fluid has been studied experimentally by Olson & Singer [1985]. The second bubble, in both the experiment shown here and the results of Olson & Singer for two miscible fluids, translates faster than the first bubble.

7.5 The motion of slender bodies through a fluid-fluid interface

Many separation processes involve the buoyancy-driven settling of long slender particles. A number of biological organisms and many crystals have shapes which may be approximated as slender bodies. Typically, slender body analyses assume that the length l of the particle is much greater than the width a (see figure 7.20). The translation of a single slender body was first discussed by G.I. Taylor and the problem of the translation of a slender body in an unbounded fluid at zero Reynolds number was studied in more detail by Cox [1970] and Batchelor [1970]. The effects of boundaries on the translation and rotation of slender bodies in Stokes flows have been studied

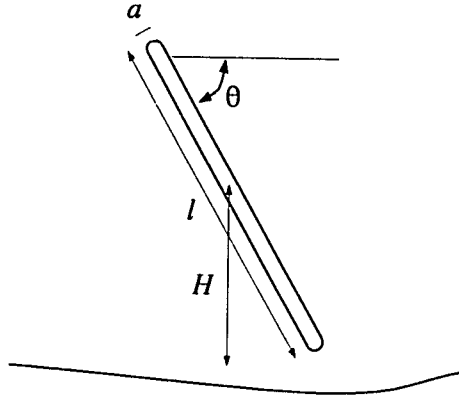


Figure 7.20: Geometry for the motion of the slender-body through a fluid interface. The aspect ratio of the slender body is a/l . The height of the center of the slender body is H . The orientation of the slender body is characterized by the angle θ .

by Yang & Leal [1983] and the effects of inertia have been studied by Khayat & Cox [1989].

Here we investigate experimentally the motion of inclined slender bodies through a fluid-fluid interface and provide a qualitative explanation for the observations. The slender bodies were straight pieces of cylindrical wire, 2 cm long with an aspect ratio of $l/a = 15$, made from paperclips.

7.5.1 The motion of a slender body passing into a less viscous fluid

In figure 7.21 we present of a sequence of photographs of the motion of a slender body though polybutene into less viscous glycerin. As the rod approaches the interface it rotates such that the angle between the vertical and the rod axis increases, or the angle θ defined in figure 7.19 decreases. As the rod passes through the interface it rotates and becomes oriented nearly parallel to gravity. The angle θ increases since the front of the rod is able to translate faster as it enters the lower viscosity fluid. The Reynolds number of the rod (based on the rod length) in the upper fluid (polybutene)

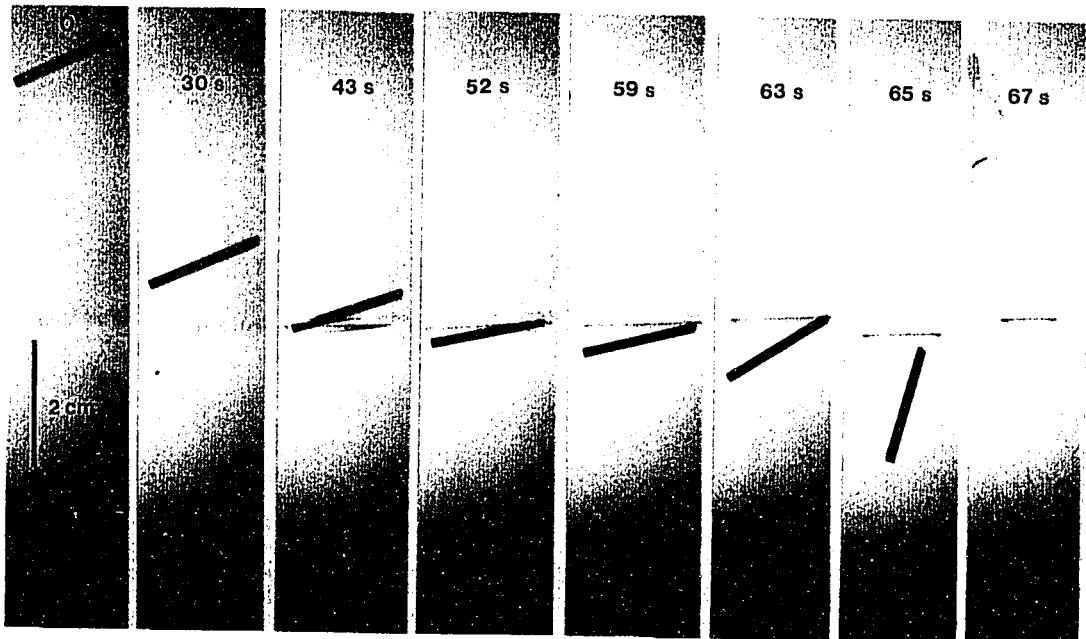


Figure 7.21: Photographs of a rigid rod passing from a higher to lower viscosity fluid. Times and a length scale are shown on the photographs. The upper fluid is polybutene, the lower fluid is glycerin; $\gamma = 0.02$. The Reynolds number is < 0.001 in the upper fluid and < 0.5 in the lower fluid.

is small, $\mathcal{R} < 0.01$ but in the lower fluid (glycerin) is moderate, $\mathcal{R} \approx 0.5$. However, the reorientation of the rod as it enters the lower fluid is not due to inertial effects since inertial effects would favour the rod sedimenting with an orientation perpendicular to gravity [Khayat & Cox 1989].

7.5.2 The motion of a slender body passing into a more viscous fluid

In figure 7.22 we present of a sequence of photographs of the motion of a slender body though polybutene into more viscous corn syrup. As the rod approaches the interface it again rotates such that the angle θ decreases and the rod becomes nearly horizontal. As the rod passes through the interface and then moves away from the interface, the

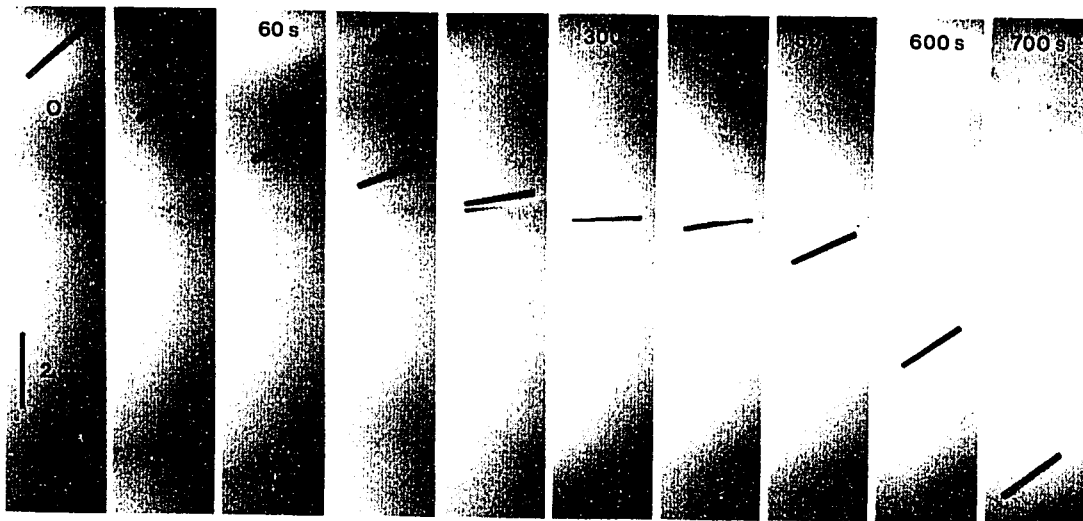


Figure 7.22: Photographs of a rigid rod passing from a lower to higher viscosity fluid. Times and a length scale are shown on the photographs. The upper fluid is polybutene, the lower fluid is corn syrup; $\gamma = 7$. The Reynolds number is < 0.01 in the both fluids.

rod rotates, and the angle θ increases. In our experiments the rod did not obtain a vertical orientation but instead adopted an inclined orientation. The Reynolds number of the rod (based on the rod length) in both fluids is small, $\mathcal{R} < 0.01$.

7.6 Concluding remarks

As drops approach and pass through fluid-fluid interfaces, significant deformation of both the drop and interface may occur for large Bond numbers (typically characteristic of particles with radii greater than a few mm). A significant amount of fluid may be entrained by particles passing through fluid interfaces resulting in mixing across the initially stably-stratified interface and thus the disruption of the interface. The amount of fluid entrained across the interface increases as the viscosity ratio of the particle increases, and increases if the particle enters a lower viscosity fluid.

Based on the experimental results presented in figures 7.12-7.19, we note that

the spatial distribution of particles may change as particles pass through fluid-fluid interfaces. For example, rigid spheres entering a lower viscosity fluid, such as the experimental results shown in figure 7.17, may form small clumps of particles. Particles passing from a lower to higher viscosity fluid entrain columns of lower viscosity fluid through the interface. We might expect that a second particle would tend to rise through the lower viscosity column of fluid, thus leading to the formation of vertically aligned structures or particles. The experimental results presented in figure 7.18, however, do not show the vertical alignment of rigid spheres entering a higher viscosity fluid.

The reorientation of long slender particles as they pass through a fluid-fluid interface may lead to the formation of structure in sedimenting suspensions of slender particles and the development of preferred particle orientations. Particles passing through an interface into a lower viscosity fluid become oriented parallel to gravity and thus settle faster. We have not been able to determine from a literature review whether a suspension of sedimenting slender bodies will also develop preferred particle orientations. However, suspensions of spheroids are expected to develop spatial inhomogeneities of particle concentrations due to long-range particle interactions as discussed in §6.2.1. Further work is required to determine whether sedimenting suspensions of slender bodies oriented parallel to gravity are stable so that the slender bodies do not become reoriented. Particles passing through an interface into a higher viscosity fluid do not become oriented perpendicular to gravity.

The formation of structures in suspensions of particles passing through fluid-fluid interfaces may have some relevance to separation processes in stratified magma chambers. Some magma chambers are thought to be stratified, with the lighter, more silicic and more viscous magmas on top and the denser, more basaltic and less viscous magmas on the bottom [*e.g.* Hildreth 1981]. The experimental results presented here suggest that long slender bodies, characteristic of some crystal shapes, may become oriented as they settle in magma chambers (some mineral crystals, such as plagioclase, are lighter than the magma from which they crystallize and will rise). Bubbles

rising through a magma chamber might form vertically aligned structures as they pass from the lower viscosity basaltic melt to the higher viscosity more silicic melt. Bubbles may also accumulate beneath the high viscosity upper layer in a magma chamber and form a layer; the layer of bubbles may then become unstable by means of a Rayleigh-Taylor instability forming “plumes” of bubbles [Thomas et al. 1993].

Chapter 8

The Interaction of Plume Heads With Compositional Discontinuities in the Earth's Mantle

The effects of compositional discontinuities of density and viscosity in the Earth's mantle on the ascent of mantle plume heads are studied using a boundary integral numerical technique. Three specific problems are considered:

1. a plume head rising away from a deformable interface,
2. a plume head passing through an interface, and
3. a plume head approaching the surface of the Earth.

For the case of a plume attached to a free-surface, the calculated time-dependent plume shapes are compared with experimental results. Two principal modes of plume head deformation are observed: plume head elongation or the formation of a cavity inside the plume head. The inferred structure of mantle plumes, namely, a large plume head with a long tail, is characteristic of plumes attached to their source

region, and also of buoyant material moving away from an interface and of buoyant material moving through an interface from a high to low viscosity region. As a rising plume head approaches the upper mantle, most of the lower mantle will quickly drain from the gap between the plume head and the upper mantle if the plume head enters the upper mantle. If the plume head moves from a high to low viscosity region, the plume head becomes significantly elongated and, for the viscosity contrasts thought to exist in the Earth, could extend from the 670 km discontinuity to the surface. Plume heads that are extended owing to a viscosity decrease in the upper mantle have a cylindrical geometry. The dynamic surface topography induced by plume heads is bell-shaped when the top of the plume head is at depths greater than about 0.1 plume head radii. As the plume head approaches the surface and spreads, the dynamic topography becomes plateau-shaped. The largest stresses are produced in the early stages of plume spreading when the plume head is still nearly spherical, and the surface expression of these stresses is likely to be dominated by radial extension. As the plume spreads, compressional stresses on the surface are produced beyond the edges of the plume; consequently, extensional features will be produced above the plume head and may be surrounded by a ring of compressional features. This chapter represents a modified version of Manga et al. [1993]

8.1 Introduction

The behavior of mantle plumes has received considerable attention since their existence was first proposed [Morgan 1971]. Research has been focused on the possible relation between mantle plume heads and continental flood basalts [*e.g.* Richards et al. 1989], mass extinctions [*e.g.* Renne & Basu 1991], continental rifting and extension [*e.g.* Hooper 1990], and geomagnetic field reversals [Larson & Olson 1991]. Mantle plumes are generally thought to be high-temperature, low-viscosity, buoyancy-driven instabilities arising from the D'' layer just above the core-mantle boundary [*e.g.* Loper & Stacey 1983; Olson et al. 1987; Whitehead & Luther 1975], although they may also

have relatively shallow source regions such as the upper mantle-lower mantle seismic discontinuity [*e.g.* McKenzie & O’Nions 1983].

The “standard model” for plume structure consists of a nearly spherical plume head connected to the plume source region by a thin cylindrical conduit or tail through which material flows to the plume head [*e.g.* Olson & Singer 1985; Griffiths & Campbell 1990; Whitehead & Luther 1975]. This model is based on observations of the large volume of material extruded in continental flood basalts (from the plume head) and the comparatively small amounts of material and heat flux generated by hotspots (from the plume tail) [*e.g.* Richards et al. 1989]. In this paper we study the dynamics of buoyant volumes of fluid in order to understand the possible behavior of mantle plume heads. This paper considers the limit of constant volume plumes which may be a reasonable approximation to thermals produced in a high Rayleigh number time-dependent convecting system [Stewart 1993]. There are a number of possible circumstances in which detached plumes or diapirs may be produced. For example, such dynamical cases include thermals in the hard turbulence regime which might be characteristic of Venus or the Archean Earth [*e.g.* Hansen et al. 1990], diapiric structures in the upper mantle due to phase changes [Liu et al. 1991] or changes in rheological laws [van Keken et al. 1992], and disconnected plumes produced by a shear flow [*e.g.* Stilbeck & Whitehead 1978]. In each of these cases we believe that the constant volume plume approximation may be appropriate.

Numerical studies of mantle plumes have generally been considered in the context of global thermal mantle convection models (see Gable & O’Connell [1991] and Schubert [1992] for a review of numerical work). In this study, we are interested in the effects of compositional discontinuities, represented by changes of viscosity and/or density, which are likely to be present in the Earth. These effects have previously been studied numerically by means of a two-dimensional axisymmetric constant viscosity thermal convection model [Kellogg 1991]. The method we apply here allows us to extend these previous results to the limit of zero chemical diffusion and to consider the effects of both radial and lateral viscosity variations.

Numerous low Reynolds number experimental studies of both thermal plumes [*e.g.* Griffiths & Campbell 1990] and compositional plumes [*e.g.* Olson & Singer 1985; Whitehead & Luther 1975] arising from a constant flux source or a Rayleigh-Taylor instability have been performed and have focused on the behavior of plumes far from boundaries. In the later stages of plume ascent, plumes approach the surface of the Earth. The effects of the impenetrable upper surface of the Earth on the ascent of plume heads, as well as the surface expression of rising plume heads, have been studied both experimentally [*e.g.* Griffiths & Campbell 1991; Griffiths et al. 1989; Olson & Nam 1986] and numerically [Koch 1993].

The purpose of this study is to examine the effect of possible compositional and viscosity discontinuities on the deformation and ascent of plume heads. The numerical problem considered in this paper is formulated as a viscous blob representing the plume head moving normal to a deformable fluid-fluid interface. The use of a simple model, such as the one investigated here, allows us to understand some of the essential physical features and dynamical consequences of buoyant plume heads.

8.2 Problem Formulation

We assume that the plume head has a constant volume and that the tail or conduit that trails the plume head is a passive feature and we ignore the conduit in the calculations reported here. These approximations are reasonable for starting plumes since the buoyancy forces associated with the plume head will be much larger than the buoyancy forces associated with the trailing conduit.

In order to model the interaction between a rising plume head and mantle interfaces, a three-fluid system is considered, with fluid properties denoted by the subscripts 1, 2, and 3, respectively (see figure 8.1). The word “plume head” refers to a buoyant volume of fluid of arbitrary shape (fluid 2). As an initial condition, the buoyant volume is assumed to be a sphere or hemisphere. Again, the flow in all fluid domains is assumed to be governed by the Stokes equations. For a given initial geom-

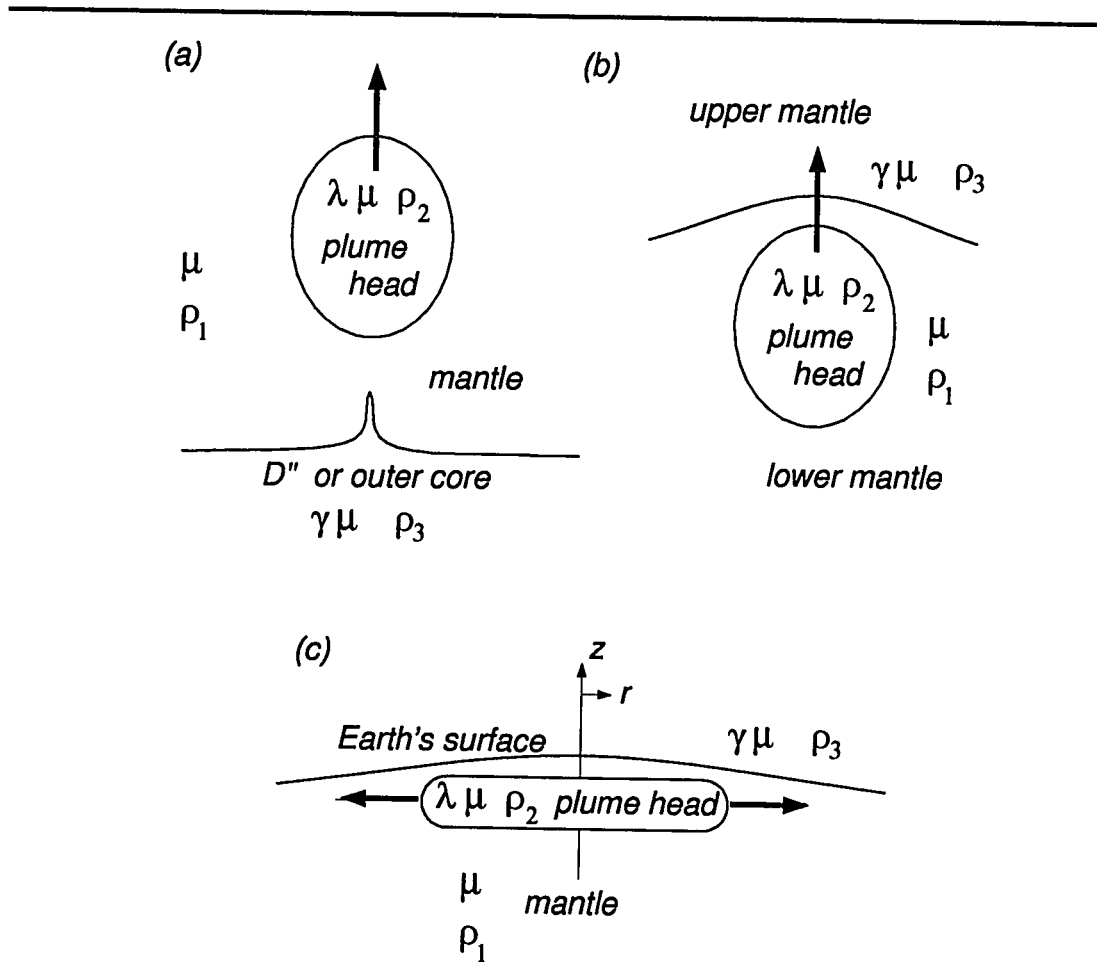


Figure 8.1: Geometry of the model used to study the ascent of mantle plume heads. An axisymmetric geometry is assumed. The horizontal interface is infinite in radial extent. (a) Plume head rising away from the CMB or D''. (b) Plume head passing through a composition discontinuity in the mantle. (c) Plume head spreading beneath the surface of the Earth. The initially spherical plume head radius is a .

etry, the numerical problem may be characterized by three dimensionless parameters, the two viscosity ratios

$$\lambda = \mu_2/\mu_1 \quad (8.1)$$

$$\gamma = \mu_3/\mu_1,$$

and a buoyancy parameter defined as

$$\beta = \left| \frac{\rho_3 - \rho_1}{\rho_2 - \rho_1} \right|. \quad (8.2)$$

For the application of the Stokes equations (1.4-5) to rising plume heads, we have assumed that the fluid viscosity and density are constant in each fluid domain. In the context of thermal plumes, this constant material property assumption requires a large Peclet number

$$Pe = \frac{Ua}{\kappa} \gg 1, \quad (8.3)$$

where U is a typical velocity, a is a typical length scale, and κ is the thermal diffusivity. Rather conservatively, for a plume head with radius of 100 km and a rise speed of 10 cm/yr, $Pe \approx 300$. The Peclet number based on chemical diffusion is much larger, typically $O(10^{13} - 10^{15})$. For such large Peclet numbers, it is appropriate to study compositional plumes, as has been done in a number of previous studies [*e.g.* Olson & Singer 1985], in order to investigate the main features of both thermal and compositional plumes. We note, however, that for long times the effect of including effects due to thermal diffusion may be important owing to the formation of a thin thermal boundary layer around the plume head which will lead to external fluid being entrained inside the rising plume [*e.g.* Griffiths & Campbell 1990].

In the numerical calculations, the initially flat fluid-fluid interface is truncated at a distance of $15a$. Both fluid-fluid interfaces are represented by 100 collocation points.

8.3 Results

In this section we study the effects of mantle and plume head densities, described by β , and viscosity contrasts λ and γ on the deformation of a rising buoyant plume head. We compare a sequence of numerically computed shapes with experimental results for plumes attached to a free-surface, in order to demonstrate the reliability of the numerical method for large interface distortions. The results presented for a plume head passing through a compositional discontinuity are similar to the results for a drop passing through a fluid-fluid interface presented in chapter 7, however the limit of zero interfacial tension is considered in this chapter. Numerical results are presented as a series of computed shapes at different times. The length scale is normalized to the initially spherical plume head radius a , and time is normalized to the advective time scale $\mu_1/(\rho_2 - \rho_1)ag$.

8.3.1 Plume head moving away from a deformable interface

In figure 8.2, we show the evolution of a buoyant plume attached to a nondeformable free-surface (representing, for example, the core-mantle boundary). Both numerical and laboratory results are presented; the laboratory results verify the reliability of the numerical method for large deformations. The experiments were performed using a drop of colored corn syrup in colorless glycerin (these are miscible fluids). The air-syrup and air-glycerin interfaces are approximated as free-slip surfaces. Since the free-surface remains flat because of the large density contrast across the air-fluid interface compared to the density contrast between the glycerin and syrup ($\beta \approx 6.7$), the effects of interfacial tension will be negligible (the coefficient of interfacial tension between air and corn syrup is about 0.07 N/m). In the experiment and numerical simulations, the plume head is followed by a long, narrow tail-like structure attached to the free-surface. The numerical results differ from the experimental results by 5-13% (the error estimate is based on differences in tail width, plume length, and plume head diameter). This discrepancy is within the uncertainty of the experimental

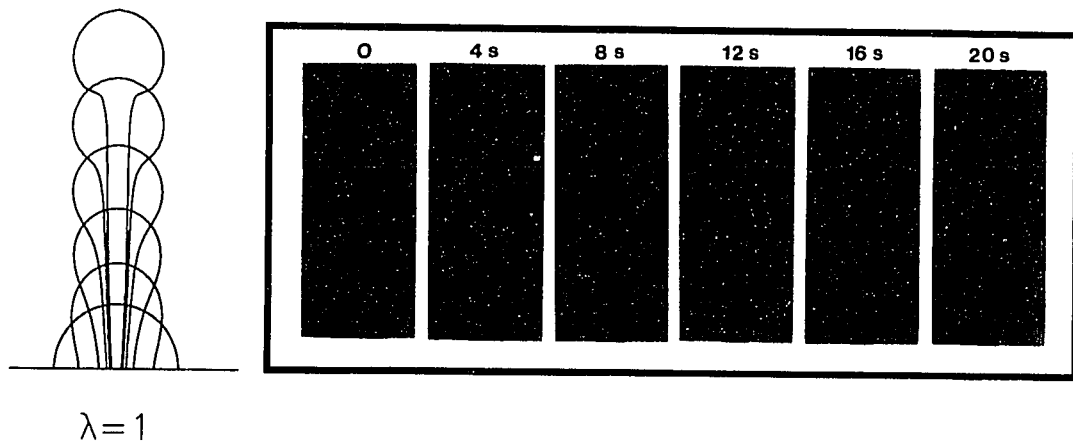


Figure 8.2: The rise of a plume with $\lambda = 1$ away from a free-slip surface. Numerical results, for a nondeformable free-slip surface, are shown on the left and experimental results on the right. The experiments were performed with colored corn syrup in colorless glycerin, and are shown upside down. The free-surface is a liquid-air interface. Both fluids have the same viscosity and are miscible (negligible interfacial tension). The Reynolds number $Re = \rho Ua/\mu \approx 0.01$. Interface shapes are shown at 4 second time intervals (from left to right).

parameters. Using a wide range of half-ellipsoids as initial shapes, the final plume shapes shown in figure 8.2 are found to be insensitive to the initial shape. Unlike plumes with a constant flux source [*e.g.* Olson & Singer 1985; Griffiths & Campbell 1990], the plume heads of constant volume plumes reach a maximum rise speed, owing to the decreased buoyancy force of the plume head as fluid is incorporated into an ever enlarging tail.

In figure 8.3 we show interface shapes for an initially spherical blob or plume head moving away from a deformable boundary such as the core-mantle boundary, for $\lambda = 10, 1$, and 0.1 and $\gamma = 1000$ and 0.001 . Physically, the high and low γ calculations correspond to rigid and free-slip lower boundaries, respectively. The high-viscosity ratio simulations ($\gamma = 1000$) may be appropriate if the D'' layer is a compositionally

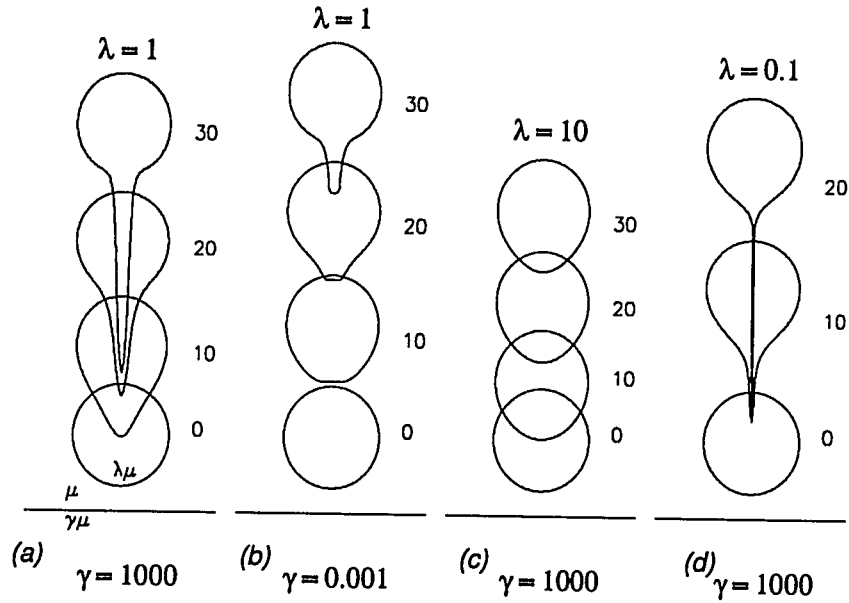


Figure 8.3: Initially spherical plume head moving away from a deformable interface showing the effect of the viscosity of the lower fluid, for (a) $\gamma = 1000$ and $\lambda = 1$, (b) $\gamma = 0.001$ and $\lambda = 1$, (c) $\gamma = 1000$ and $\lambda = 10$, and (d) $\gamma = 1000$ and $\lambda = 0.1$. The buoyancy parameter $\beta = 100$ for the simulations with $\gamma = 0.001$, and $\beta = 1$ for the simulation with $\gamma = 1000$. Interface shapes are shown at the times labelled next to the corresponding plume head. Time is normalized by $\mu_1/(\rho_2 - \rho_1)ag$.

distinct layer with a higher viscosity than the lower mantle (although this is unlikely); thus, the lower interface would represent the top of the D'' layer. The low-viscosity ratio simulation ($\gamma = 0.001$) may be appropriate if there is no viscosity increase in the D'' layer; thus, the lower interface would represent the core-mantle boundary. Corresponding to these two possible physical situations, the density contrast across the lower interface for the simulations with $\gamma = 0.001$ is very large, with $\beta = 100$, whereas for the simulations with $\gamma = 1000$, the density contrast is small, with $\beta = 1$. In both cases the deformation of the lower interface is small because of either the large stable density contrast or the high viscosity of the lower fluid.

As the plume head rises, the deformation appears as a growing tail from the back of the plume head. The effect of increasing the lower fluid viscosity (which resists deformation of the lower boundary) is to increase the rate and magnitude of deformation at the rear of the plume head. Once a tail develops, it will continue to grow, as has been shown by other experimental and numerical stability studies [Koh & Leal 1989 1990; Pozrikidis 1990; chapter 1 of this thesis]. For tail-like instabilities such as shown in figure 8.3, the end of the tail remains essentially stationary while the plume head continues to rise (figure 8.3*d*): the thin tail has a much smaller buoyancy force than the plume head and thus rises much more slowly. Many calculations, in addition to those shown here, demonstrate that the effect of changing the viscosity of the plume head on the deformation of the lower interface is negligible. Provided that $\beta > O(1)$, changing the density contrast across the lower interface does not noticeably affect the deformation of the rising plume head.

8.3.2 Plume head passing through an interface

In this section we study the effects of plume and mantle viscosity on plume heads passing through compositional interfaces. For the sake of discussion we assume that the interface represents the lower mantle-upper mantle discontinuity, although other compositional discontinuities, not necessarily seismically detectable, may exist at other depths within the mantle.

We begin by considering the effect of changing the ratio of upper to lower mantle viscosities, which corresponds to changing γ . Joint geoid and seismic tomography studies [*e.g.* Hager & Clayton 1989] suggest a viscosity increase by a factor of 10 to 30 from the upper to the lower mantle. As shown in figure 8.4, by decreasing γ , the mode of deformation at the back of the rising plume head changes from indentation to elongation. Moreover, the mode of deformation is related to the rise speed in the upper mantle relative to the rise speed in the lower mantle. If the plume head travels faster in the upper mantle, it will become elongated; the cylindrical geometry of the plume head in figure 8.4*c* resembles the geometry often inferred for plumes.

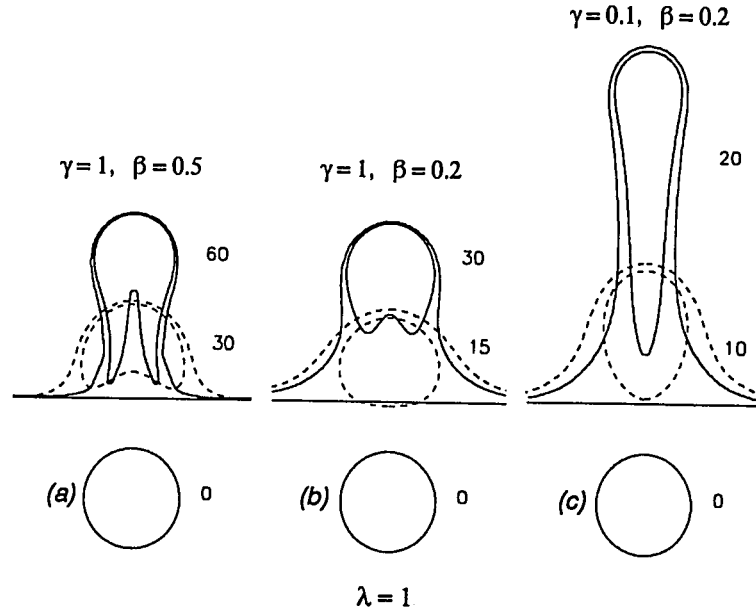


Figure 8.4: The effect of changing the ratio of upper to lower mantle viscosity, γ , and plume head buoyancy, β , for (a) $\gamma = 1$ and $\beta = 0.5$, (b) $\gamma = 1$ and $\beta = 0.2$, and (c) $\gamma = 0.1$ and $\beta = 0.2$. For all cases $\lambda = 1$. Interface shapes are shown at the times labelled next to the corresponding plume head. Time is normalized by $\mu_1/(\rho_2 - \rho_1)ag$.

Conversely, if the plume travels more slowly, the lower surface of the plume head will become indented; the indented plume head develops a cavity at the lower surface of the plume head, and lower fluid is entrained into the cavity.

The effect of changing plume viscosity is shown in figure 8.5 for $\lambda = 10, 1$, and 0.5 , $\gamma = 0.1$, and $\beta = 0.2$. These parameters correspond to a layered Earth with weak density stratification and strong viscosity stratification. Plume viscosity plays an important role in the rate of plume head deformation and the rate of drainage of the region between the leading edge of the plume head and the upper mantle. As the viscosity of the plume head increases, the thickness of the layer of lower mantle surrounding the plume head increases; for less deformable plume heads ($\lambda = 10$ here) this layer is thick and nearly spherical. When $\lambda \ll 1$, the gap between the plume head

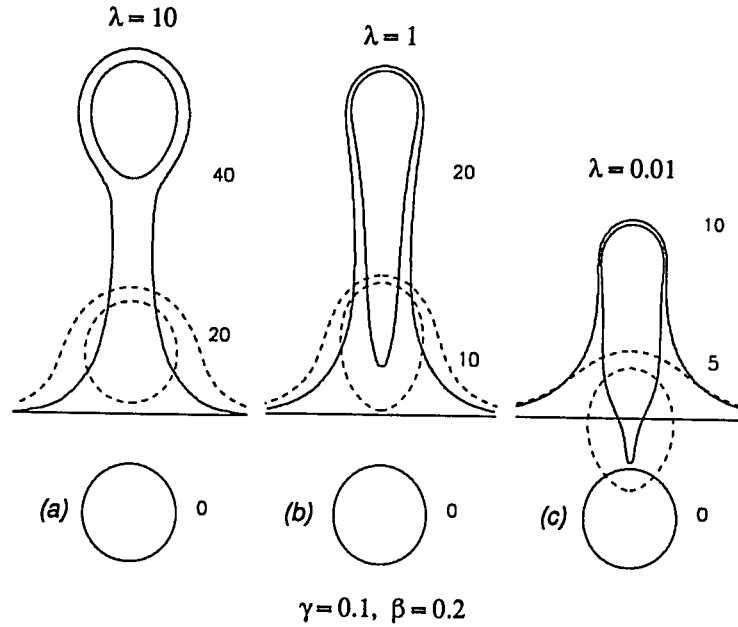


Figure 8.5: The effect of changing the ratio of plume to lower mantle viscosity, λ , for (a) $\lambda = 100$, (b) $\lambda = 1$, and (c) $\lambda = 0.01$. For all cases, $\gamma = 0.1$ and $\beta = 0.2$. Interface shapes are shown at the times labelled next to the corresponding plume head. Time is normalized by $\mu_1/(\rho_2 - \rho_1)ag$.

and the upper fluid thins very quickly, and the boundary integral numerical method eventually breaks down since the interfaces become closer than the separation distance between collocation points used in the numerical integration. The viscosity ratio λ between the plume and the lower mantle also has an effect on the rate at which the plume head passes through the interface: as λ increases the velocity decreases.

8.3.3 Plume head approaching the surface of the Earth

The final stage of plume head ascent involves the interaction of the rising plume head with the lithosphere and surface of the Earth. Since neither plumes nor plume heads have been seismically detected, all direct observations and inferences of plume dynamics are based on this interaction. Figures 8.6-9 document a number of dynamical

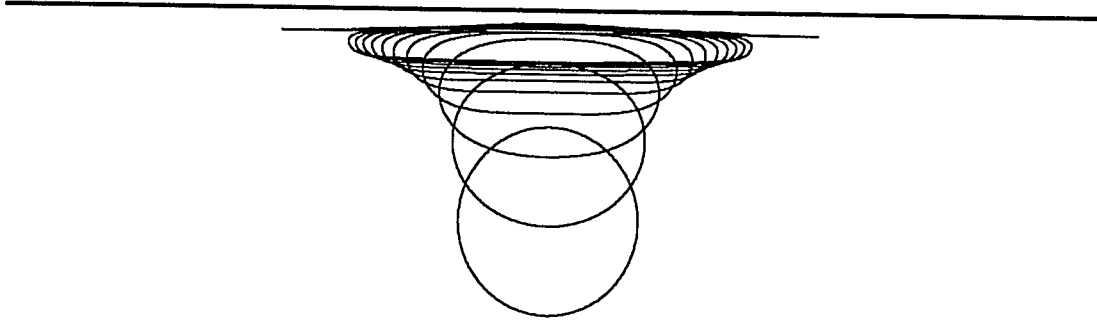


Figure 8.6: Plume approaching the surface of the Earth; $\lambda = 1$, $\gamma = 0$ and $\beta = 10$. Interface shapes shown at times $t = 0, 5, 10, 15, 20, 25, 30, 35, 40, 45$ and 50 . Time is normalized by $\mu_1/(\rho_2 - \rho_1)ag$.

features of the interaction of a plume head and a deformable free-surface. In figure 8.6 we show the spreading of a plume head beneath a deformable free-surface. Numerical and analytical solutions to the similar problem of a drop spreading on or beneath a nondeformable free-surface have previously been studied [Koch 1993]. As the plume head spreads it becomes flattened. The plume radius R is found numerically to increase as $R(t) \propto t^{0.25}$. This is only slightly larger than the experimentally inferred spreading of low-viscosity plumes in which $R(t) \propto t^{0.22 \pm 0.02}$ [Griffiths & Campbell 1991] and the lubrication theory result of $R(t) \propto t^{0.2}$ [Koch 1993]. For plumes heads that are as flat as the final shapes shown in figure 8.6, the Peclet number decreases from $Pe \approx 300$ in the mid-mantle to $Pe \approx 1$ (where the length scale is chosen to be the thickness of the layer between the plume and the upper surface), and the effects of thermal diffusion may become important.

One of the characteristic surface effects associated with plumes and plume heads is the formation of swells and plateaus. In figure 8.7 we show the surface elevation for the plume head shapes shown in figure 8.6. The maximum axial height corresponds to a plume head at a moderate distance beneath the surface, before significant spreading occurs. As the plume head approaches the surface and spreads, the topography changes from a bell-shape to a plateau-shape. Note that the plateau edge corresponds

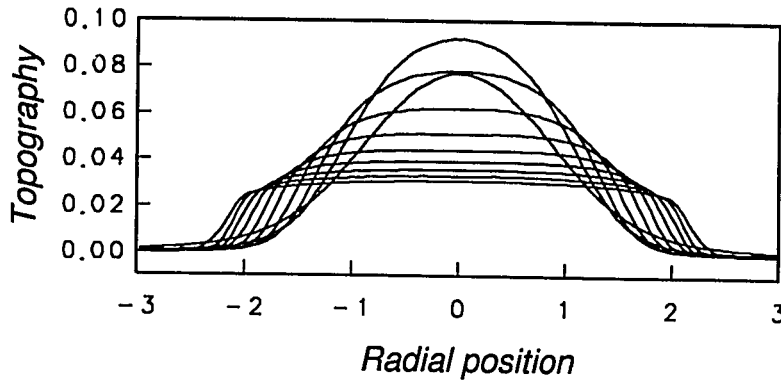


Figure 8.7: Topography of the surface of the Earth for the shapes shown in 8.6; $\lambda = 1$, $\gamma = 0$ and $\beta = 10$. The edges of the plateaus correspond to the edges of the plume. Topography is proportional to the normal stress on the upper surface. The radial position is normalized by the initial plume head radius, a .

to the edge of the plume head. Also, as illustrated in figure 8.8, the rapid initial uplift is followed by a slow relaxation and flattening, in agreement with experiments [*e.g.* Olson & Nam 1986]. For the results presented in figure 8.8, the plume head was started at a depth of $10a$. The maximum axial topography with amplitude $0.09a$ occurs at time $t = 44.2$ when the top of the plume head is $0.15a$ below the surface.

By differentiating the axial topography shown in figure 8.8 we can calculate the rate of dynamic surface uplift and subsidence. The maximum rate of axial surface uplift is 0.0078 at time $t = 38.2$ when the top of the plume head is about $0.5a$ below the surface; the maximum rate of axial surface subsidence is 0.0035 at time $t = 49.9$ when the top of the plume head is $0.04a$ below the surface. For a plume head with a radius of 300 km, a density contrast with the upper mantle of 1% , and a mantle viscosity of 10^{21} Pa s, the maximum dimensional rate of dynamic uplift corresponds to 0.5 km/m.y. and the maximum rate of dynamic subsidence corresponds to 0.25 km/m.y. The maximum axial height occurs about 5 m.y. after noticeable surface uplift begins. For comparison, Crough [1983] estimated a rate of uplift of 0.2 km/m.y. for the

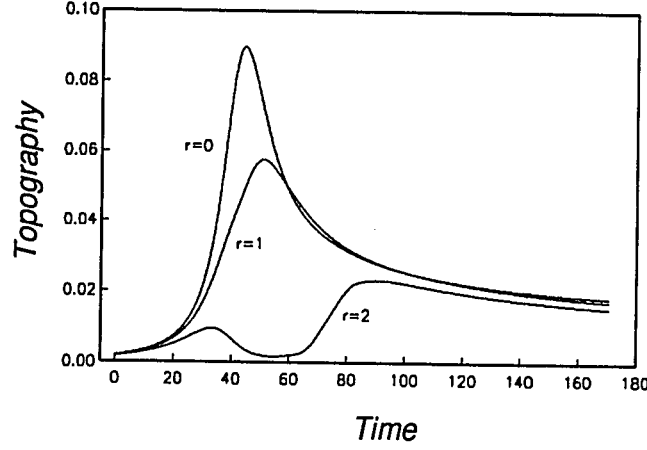


Figure 8.8: Surface uplift along the axis of symmetry versus dimensionless time, at radial positions $r = 0, 1$ and 2 ; $\lambda = 1$, $\gamma = 0$ and $\beta = 10$. The plume head is initially at a depth of $10a$ beneath the free-surface. The radial position normalized by the initial plume head radius, a . Time is normalized by $\mu_1/(\rho_2 - \rho_1)ag$.

Hawaiian swell, and for Wrangellia, Richards et al. [1991] estimated uplift rates of 5 km/m.y. and initial subsidence rates of 50 m/m.y. (which quickly diminishes to 10 m/m.y.). Dynamic effects will be most important during the initial uplift, however thermal effects will have an important effect on actual subsidence rates.

In figure 8.8 we also show the surface topography at different radial positions as a function of time. At a radius $r = 2a$ the surface topography versus time curve has two maxima: the first peak is produced owing to the longer wavelength of the surface topography when the plume head is far from the surface, and the second peak is produced by the spreading plume head. For the plume head parameters assumed above, the time difference between these two maxima would be about 25 m.y.

Finally, the deviatoric normal stress $-\sigma_{zz} = -2\mu_1\partial u_z/\partial z$, radial stress $\sigma_{rr} = 2\mu_1\partial u_r/\partial r$ and hoop stress $\sigma_{\theta\theta} = 2\mu_1 u_r/r$ on the free-surface are shown in figure 9 at $t = 10$ when the plume head is still nearly spherical and at time $t = 50$ when the plume head is significantly flattened (calculations correspond to those shown in figure 8.6).

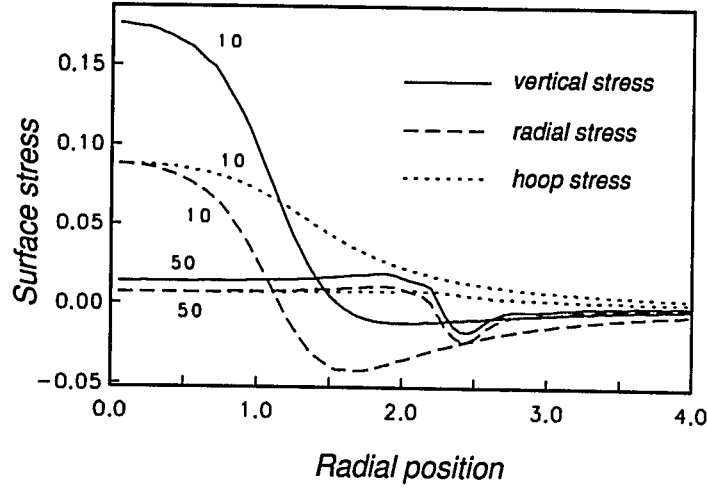


Figure 8.9: Deviatoric stresses on the surface at $t = 10$ and 50 , for the results shown in figure 8.6; $\lambda = 1$, $\gamma = 0$ and $\beta = 10$. These stresses are defined by $-\sigma_{zz} = -2\mu_1\partial u_z/\partial z$ (negative normal stress), $\sigma_{rr} = 2\mu_1\partial u_r/\partial r$ (radial stress), and $\sigma_{\theta\theta} = 2\mu_1 u_r/r$ (hoop stress), and are shown by solid, dashed, and dotted lines, respectively. Stresses are normalized by $2ag(\rho_2 - \rho_1)$. Length scales are normalized by the initial plume head radius, a . Time is normalized by $\mu_1/(\rho_2 - \rho_1)ag$. At time $t = 50$, the plume head is significantly flattened (with an aspect ratio, the ratio of width to thickness, of 16 to 1).

While the plume head is still nearly spherical, the largest stresses are extensional, and radial extension occurs above the plume head, surrounded by horizontal shear. As the plume head spreads and become flattened, the normal stress becomes larger than the hoop stress beyond the edge of the plume, and we expect a change from concentric extension above the plume head to concentric compression surrounding the spreading plume. A more detailed treatment of the stresses and surface signature of spreading plume heads is presented by Koch [1993].

In order to minimize numerical error in our calculations we have presented results for the case $\lambda = 1$ in figures 8.6-9. Analytic solutions describing the motion of a rising sphere beneath a free-surface have shown that the effect of decreasing the plume

head viscosity on surface observables is small [Koch & Ribe 1989], and numerical calculations have shown that the surface observables for a spreading plume head are qualitatively the same as those shown in figure 8.7-9 for all viscosity ratios [Koch 1993].

8.4 Discussion

As a plume head passes from a high viscosity region to one with a lower viscosity, the plume extends vertically. This mode of deformation occurs because of the higher velocity of the plume in the low viscosity fluid. If the plume head slows down as it passes through an interface, by moving into a lower density or higher viscosity fluid, a cavity may develop inside the plume head, and lower mantle material might be entrained in the cavity and into the plume head. Identifying source material from continental flood basalts, however, cannot distinguish between these two modes of deformation, since lower mantle material will also be incorporated into the plume head by entrainment as the mantle surrounding the plume head heats up by thermal diffusion [*e.g.* Griffiths 1986]. Because the viscosity of plumes is probably much less than the viscosity of the mantle, and the lower mantle is thought to be more viscous than the upper mantle, the thickness of the layer of lower mantle material between the plume and upper mantle should decrease rapidly (see figures 8.4-5). Thus, although the entrained material above the top of the plume head may be the first to melt and to be extruded at the Earth's surface, its signature in the earliest melts will probably be small. While on the basis of our numerical results we might expect a small amount of entrainment by low viscosity plumes, we expect a more significant amount of entrainment by high viscosity sinking lithospheric slabs (suggested by the calculations presented in figure 8.5).

One of the characteristics of continental flood basalts is their rapid emplacement rates, determined from stratigraphy and radiometric dating. Emplacement times are estimated to be less than 2 m.y. for the Columbia plateau [Hooper 1982], less than 1

m.y. for the Deccan traps [Duncan & Pyle 1988; Courtillot et al. 1988], from 2 to 4 m.y. in the North Atlantic [White and McKenzie 1989] and from 1 to a few m.y. in Parana [Bellieni et al. 1984]. Such rapid and voluminous eruptions rates, typically 10^5 – 10^6 km³ of basalt, would appear to be inconsistent with the extension of plume heads by a decrease in viscosity at 670 km, since elongated plume heads should lead to a prolonged period of volcanism. However, if the rise time of plume heads is very fast, or plume heads become flattened and spread beneath the surface of the Earth before volcanism begins, then plume heads may still be extended as they pass from the lower mantle to the upper mantle and the emplacement time for flood basalts may still be short. Since the process of lithospheric erosion is slow [*e.g.* Olson et al. 1988] even extended plume heads may rise and flatten before melting and extrusion occurs. Alternatively, if plume heads are as large as some researchers have suggested, with a diameter of 1000 km [Griffiths & Campbell 1990], then the effect of a viscosity decrease at 670 km will be small (such as the intermediate shapes shown in figure 8.4).

While plume heads are thought to form continental flood basalts and some oceanic plateaus [Richards et al. 1989], hotspots are often attributed to plumes [Morgan 1971] (a tail or conduit that follows the plume head). Many previous numerical studies have modeled plumes as constant flux pipes or upwellings [*e.g.* Sleep 1987; Richards et al. 1988]. In this study we have shown that buoyant volumes of fluid moving away from a boundary will develop tails. We also note that buoyant volumes of fluid moving from a high viscosity region, such as the lower mantle, to a lower viscosity region, such as the upper mantle, may be extended. Qualitatively, it appears that a constant flux source for plumes is not required. However, the volume flux in the tail of the plume head shown in figure 8.3*d* at $t = 20$ is more than 10^{-3} times smaller than the volume flux in the plume head, where the volume flux is a measure of the amount of material transported vertically per unit time in the plume head or tail. The volume flux of material transported by plume heads, inferred from the volumes of continental flood basalts, is not more than 100 times the volume flux of plumes, inferred from active

hotspots [*e.g.* Sleep 1990; Richards et al. 1989]. Thus the volume of fluid in the tails shown in figure 8.3 does not appear to be sufficient to maintain continuous and vigorous hotspot activity. However, extended plume heads, such as the ones shown in figures 8.4-5, will have a much higher ratio of volume flux in the tail compared to the volume flux by the plume head. In fact plume heads passing from a high to low viscosity region develop a cylindrical shape and have a structure similar to those suggested for plumes that feed hotspots. Even for a uniform mantle in which plume heads are not extended, the absence of a tail large enough to account for extended hotspot activity in our model does not invalidate the results presented here since the buoyancy forces associated with the plume head will be larger than the buoyancy forces associated with the tail, and the tail may be regarded as a passive feature.

Although we have studied only plume heads passing through compositional discontinuities, we should expect similar results for material property changes (density and viscosity) due to phase changes. The elongation of plume heads when passing from a high to low viscosity fluid, however, should be enhanced due to the absence of a restoring force related to the uplift of the interface. The effect of the phase change of perovskite and magnesiowüstite to spinel (with a negative Clapeyron slope) on hot plumes would be to retard plume head extension, whereas the spinel to olivine change (with a positive Clapeyron slope) would act to further enhance plume head elongation (see Liu et al. [1991] for a more detailed discussion).

A stability analysis by Kojima et al. [1984] of the translation of an isolated drop in an infinite Newtonian fluid predicts that the rate of drop deformation scales as $1/(1 + \lambda)$, where λ is the ratio of drop or plume viscosity to exterior fluid viscosity, as previously defined. Such a deformation-rate scaling is suggested by the form of the integral equations for Stokes flows (*e.g.* equation (1.24) in chapter 1), and simply indicates that the larger of the two fluid viscosities controls the timescale for interface deformation. From numerical studies of finite drop deformation accompanying buoyancy-driven motion, this scaling has been shown to be reasonably accurate, particularly for small to moderate deformations [Koh & Leal 1990]. In the present study,

numerical problems prevented us from investigating the interesting geophysical limit of very low viscosity plumes, with $\lambda < 0.001$. Since the deformation rate scales as $1/(1 + \lambda)$, for $\lambda \ll 1$ we should not expect significantly more deformed plumes than the shapes shown for $\lambda = 0.01$ in figure 8.5, and we suggest that the results based on iso-viscous models may adequately describe the behavior of low viscosity plume heads, with the maximum deformation rate only twice the deformation rate for $\lambda = 1$. However, in applying the scaling of the deformation rate to the plume heads shown in figure 8.5, we note that the appropriate viscosity ratio might be approximately λ/γ since the geometry of the problem resembles a plume head with viscosity $\lambda\mu$ in a mantle with viscosity $\gamma\mu$. This may explain why the plume heads have shapes characteristic of diapiric plumes rather than cavity plumes [Olson & Singer 1985]. On timescales for which the diffusion of heat from the plume head does not significantly reduce the viscosity of the lower mantle entrained above and around the plume head, the deformation rate of the plume head will still be dominated by the viscosity of the lower mantle, and the deformation rate will scale as $1/(1 + \lambda)$.

As plumes spread beneath the surface of the Earth, the largest stresses will occur above the center of the plume when the plume head is still nearly spherical and at some distance beneath the surface (topography in figure 8.7 is proportional to the vertical stress). For a plume head with a radius of 300 km and a density contrast of 1%, the maximum stresses for the spreading plume head are about 50 MPa, and the maximum surface uplift is about 2 km, when the top of the plume head is at a depth of 50 km (note that we do not include a high viscosity lithosphere in these calculations). If these same plume head parameters are used, the calculated surface elevations shown in figure 8.8 are comparable to the dynamic uplift required for rapid extension [Houseman & England 1986, figure 6], both in the early stages of uplift when the lithosphere is cold and the uplift is large and in the later stages of spreading when the lithosphere has been heated and the uplift is small. Diffusion of heat from the plume head as it spreads will decrease the stresses needed for extension [Houseman & England 1986], and thus faulting and extension may be more likely to occur above a

spreading plume head than during the early approach of the plume head to the surface even though the stresses are significantly smaller. This may explain why volcanism associated with mantle plume heads often precedes rifting events [Hooper 1990], or in some cases, such as the Siberian Traps [Renne & Basu 1991], rifting may not occur at all. Even if stresses at the surface are insufficient to cause continental breakup, they are large enough to affect the dynamics of surface plate motions [Hill 1991] since stresses induced by plume heads are comparable to stresses due to convection. Further work is required to understand the effects of the interaction of a spreading plume with the lithosphere: thermal effects and nonlinear rheologies should be included to study the generation of melts, surface deformation, and surface tectonics. We also note that the topography and stresses shown in figures 8.6 and 8.9, produced by a plume spreading beneath a free-surface, will differ if a high viscosity lithosphere or elastic lithosphere is included [*e.g.* Bott & Kusznir 1979]. The effect of a high viscosity lithosphere is to decrease the wavelength and increase the amplitude of the surface topography [Morgan 1965].

Previous studies have related rising plume heads or diapirs to Venusian coronae [*e.g.* Stofan et al. 1991; Squyres et al. 1992] and Venusian highlands [*e.g.* Herrick & Phillips 1990]. Coronae are elevated regions with radii of 100-1000 km and are often associated with volcanic features. Highlands have diameters of 1000 to 3000 km, and elevations of 1 to 5 km. Highland topography varies from high dome-shaped rises (*e.g.* Beta Regio, Atla Regio) to lower, broader, plateau-like structures (*e.g.* western Aphrodite Terra, Alpha Regio). As discussed by Koch [1994], the results shown in figures 9.6-9 may be more relevant to Venus where the assumption of a uniform viscosity mantle without a high-viscosity lithosphere may be appropriate. The pattern of deviatoric stresses shown in figure 8.9 would result in the formation of extensional features above the spreading plume head surrounded by compressional features. This evolution of the topography and surface stresses shown in figures 8.7-9 corresponds to an evolutionary sequence of features associated with novae, then arachnoids, and finally coronae on Venus [Koch 1994]. While the plateau-shaped uplift predicted by the

spreading plume model may be typical of the observed topography of many Venusian coronae, the simple model investigated here, with a uniform and Newtonian mantle, cannot account for the rim and moat that surround many coronae. This model is, however, consistent with the gross features of many coronae, as discussed by Stofan et al. [1991] and Koch [1994].

8.5 Concluding remarks

One of the most notable characteristics of rising plume heads is that trailing tails may develop as the plume head moves away from a boundary and that plume heads may be significantly elongated as they pass from a high to a low viscosity region. Thus, it appears that the inferred structure of mantle plumes (both the large plume head and trailing tail) may be characteristic of plumes attached to their source region, buoyant material moving away from an interface, and buoyant material moving from a high to a low viscosity region. However, the tails formed when a buoyant volume of fluid moves away from a boundary are probably not large enough to maintain continued hotspot activity. A plume head passing from the high viscosity lower mantle to the lower viscosity upper mantle will be extended vertically and will develop a cylindrical shape, and could conceivably account for hotspot activity.

We also note that the interaction of a plume head with the surface of the Earth may be successfully modeled by a spreading buoyant blob and that such a model can describe many features of Venusian highlands and coronae (see Koch [1994] for a more detailed discussion).

Chapter 9

Deformation of continental roots, the formation of Venusian highlands and “dregs” at the base of the mantle

In this chapter we consider a few problems which might be representative of commonly arising geometries and dynamics in mantles of the terrestrial planets. In particular we focus on some of the consequences of lateral viscosity variations, the spatial distribution of buoyancy forces, and the interaction of large scale mantle flow with compositionally distinct regions of the mantle. Specifically we will consider three problems:

1. the rate of deformation of continental roots,
2. the formation of the Venusian highlands,
3. the dynamics of mantle “dregs” at the base of the mantle.

9.1 Introduction

A large number of numerical investigations of mantle convection have been presented over the last 30 years; recent summaries may be found in Gable & O’Connell [1991] and Schubert [1992]. The significant increase in computational speed and resources has recently permitted a number of very sophisticated computations approaching Earth-like Rayleigh numbers¹ including three-dimensional simulations of temperature-dependent and stress-dependent convection [Tackley 1993] and studies which include the effects of phase changes [Tackley et al. 1993]. The aim of convection studies is to perform a number of forward models are compare calculated observables with geophysical observations (such as postglacial rebound data, surface heat flux, surface divergence, density variations inferred from seismic tomography) in order to gain some insight into the properties, structure and evolution of the mantle.

In this chapter we consider a number of idealized models of features in a convecting mantle. Specifically we will assume that different regions of the mantle can be represented as distinct homogeneous Newtonian fluids. Thus, in addition to simplifying the numerical problem of computing fluid flows, we are able to isolate and treat separately different parameters and aspects of mantle convection. Our aim is not to simulate a convecting mantle, but to understand some of the consequences of possible properties of the mantle on surface observables.

We consider the effects of buoyancy, geometry, mantle flow and viscosity contrasts on the evolution of compositionally distinct volumes of crust or mantle at a planet’s surface or the core-mantle boundary: possible applications include understanding the evolution or estimating the properties of the continental tectosphere (continental roots, §9.3), evaluating proposed upwelling and downwelling models for

¹The Rayleigh number, Ra , in a fluid with density variations owing to temperature or compositional variations, can be interpreted as the ratio of the timescale for diffusion (thermal or chemical diffusion) to the timescale for advection due to density contrasts. At Rayleigh numbers greater than some critical Rayleigh number, typically $Ra > O(1000)$, the fluid will begin to convect. “Earth-like” Rayleigh numbers are $O(10^7)$.

elevated plateaus on Venus, §9.4, and relating the seismically observed structure of D” to mantle flows, §9.5.

9.2 Problem formulation

We consider the time-dependent evolution of a buoyant volume of fluid (representing a thickened crust, a compositionally distinct continental root, or a mantle “dreg” at the base of the mantle), referred to hereafter as the “blob”, see figure 9.1: both the blob and mantle are assumed to be Newtonian fluids. Over the long timescales characteristic of mantle convection, we expect that deformation of the lithosphere will be described by the equations of fluid mechanics rather than solid mechanics. Although we are assuming that all fluids are Newtonian fluids, we can imagine that the viscosities of each fluid domain are “effective” viscosities which are qualitatively representative of fluids with a more complicated rheology. Numerical calculations are performed using a boundary integral method.

The externally imposed flow, representing a mantle flow, is assumed to be a biaxial extensional flow, described by

$$\begin{aligned} \mathbf{u}^{external} &= \mathbf{E} \cdot \mathbf{x} \\ &= \gamma \begin{bmatrix} 1 & 0 & 0 \\ 0 & 1 & 0 \\ 0 & 0 & -2 \end{bmatrix} \cdot \mathbf{x} \end{aligned} \quad (9.1)$$

where \mathbf{x} is a position vector, and γ is a strain-rate.

Time is normalized by

$$\tau = \mu / \Delta \rho g a \quad (9.2)$$

where $\Delta \rho$ is the density contrast between the blob and the mantle, μ is the viscosity of the mantle, g is gravity and a is the initial thickness of the blob. The ratio of viscous forces associated with the mantle flow to buoyancy forces is characterized by the parameter Λ ,

$$\Lambda = \tau \gamma = \gamma \mu / \Delta \rho g a, \quad (9.3)$$

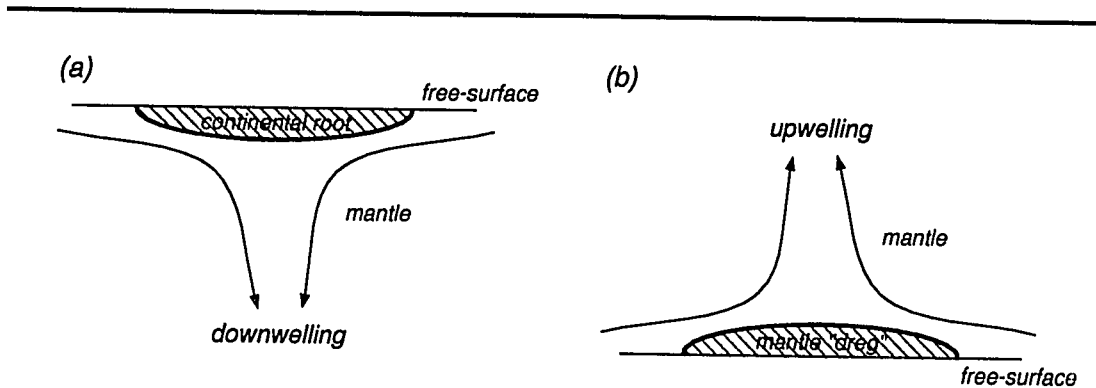


Figure 9.1: The “blob” has viscosity $\lambda\mu$ and density $\rho - \Delta\rho$; the mantle has viscosity μ and density ρ . The initial thickness of the blob is a .

where τ is the timescale over which the blob sinks or rises and γ^{-1} is the timescale over which the blob deforms due to the external flow.

We demonstrate here that buoyant crust (or mantle) which accumulates and thickens above downwellings (or mantle “dregs” at the base of the mantle which thicken beneath upwellings) thickens to the point that the buoyancy forces are balanced by viscous forces and thus a nearly-steady geometry is achieved. Small amounts of the blob may be entrained by the flow, as demonstrated in Lenardic et al. [1993].

9.3 Continental roots

In this section we consider the rate of deformation of a buoyant region in the mantle. Specifically, we will consider the effect of the viscosity ratio λ (defined in figure 9.1) on the rate of deformation of a blob attached to a free-surface for the case of $\gamma = 0$ (no externally imposed flow).

9.3.1 The tectosphere hypothesis

Regions of anomalously fast mantle beneath continents, extending to depths of up to 400 km, figure 9.2, have been interpreted as being compositionally distinct material

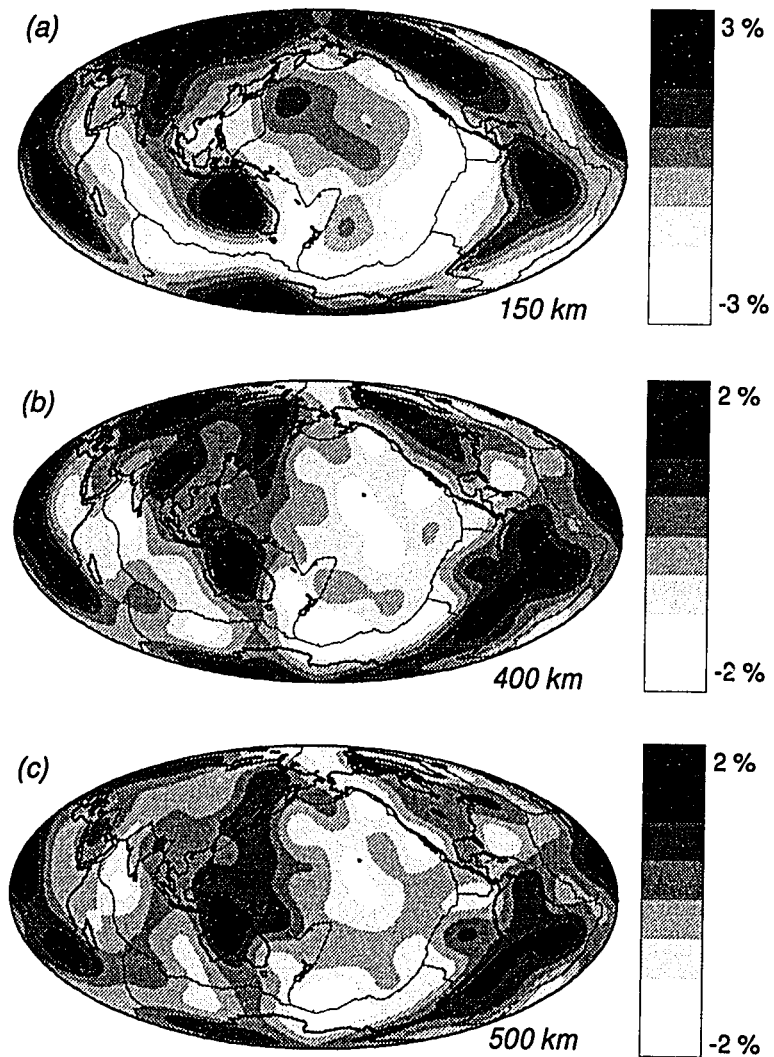


Figure 9.2: Tomographic images of the Earth's upper mantle (courtesy of Wei-jia Su, based on the model of Su et al. [1994]) at a depth of (a) 150 km, (b) 400 km and (c) 500 km. The scale bar indicates the percent variation of S wave speed in the heterogeneous Earth compared to a radially symmetric model.

which form stable (*i.e.* persistent and old) continental roots which translate coherently with moving plates [Jordan 1975]. The model proposed by Jordan involves a “delicately balanced tectosphere” [Jordan 1978] produced by dynamic and magmatic processes associated with the Wilson cycle; specifically, the persistence of the tectosphere beneath Archean cratons for 3 b.y. requires that the tectosphere is chemically buoyant relative to the mantle, possibly as a result of the extraction of basaltic and komatiitic melt leaving behind an iron and calcium depleted residuum [Jordan 1978; 1979].

An alternative explanation for the seismically fast regions beneath continents is that they represent downwellings of cold mantle. One consequence of the second hypothesis, is that continents are currently depressed owing to the negative dynamic topography produced above downwellings [Forte et al. 1993].

At smaller length scales, the detachment and delamination of a thickened lithosphere (associated with, for example, continent-continent collisions) or the lower crust with horizontal length scales of only a few hundred km has been proposed beneath the Alps [Austreim 1991], beneath California [Zandt & Carrigan 1993] and beneath the Himalayas [Molnar et al. 1993].

9.3.2 Effect of viscosity ratio

Here we consider some of the dynamic consequences of the model proposed by Jordan. The model consists of either a positively or negatively buoyant continental root with an initial aspect ratio of 10:1 (ratio of diameter to thickness) with an ellipsoidal shape. We assume the continental root is a fluid volume with viscosity $\lambda\mu$ and density $\rho - \Delta\rho$ above a mantle with viscosity μ and density ρ and that there is no external flow. The time for the continental root to thicken or thin by a factor of two is presented in figure 9.3a. The rate of deformation is predicted to scale as $1/(1 + \lambda)$ from the form of the integral equations (1.24), in agreement with the calculations presented in figure 9.3. A continental root with a density contrast of 1%, a thickness of 100 km, a mantle viscosity of 10^{21} Pa s and a viscosity contrast of 1000 will take more than 1 b.y. to

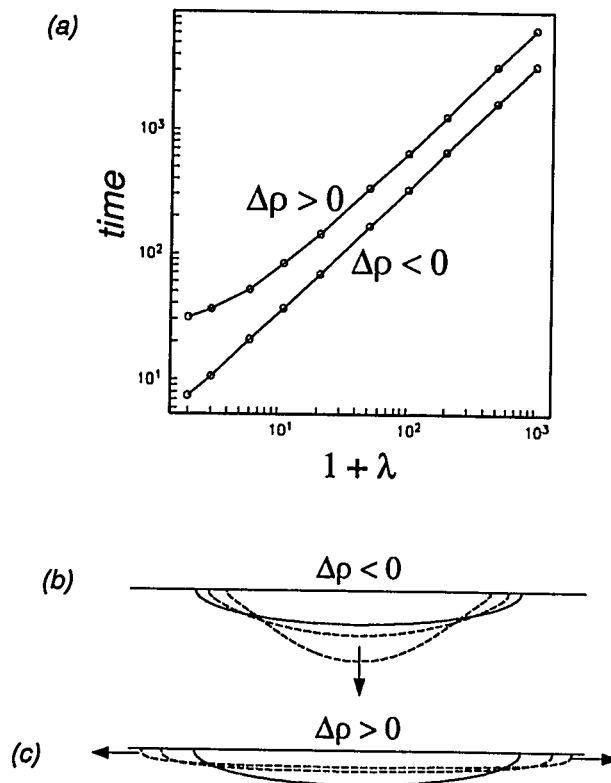


Figure 9.3: (a) The time for a buoyant blob to thicken ($\Delta\rho < 0$) on thin ($\Delta\rho > 0$) by a factor of two as a function of the viscosity contrast λ . Deformation rate scales approximately as $1/(1 + \lambda)$. Examples of numerically computed shapes are shown for (b) a sinking blob and (c) a spreading blob.

thicken or thin by a factor of two.

In appendix E we consider the effects of lateral viscosity variations associated with ocean-continent boundaries on geophysical surface observables.

9.3.3 Remarks

We can use the estimates of the timescale for continental roots to deform to infer several features of the mantle (assuming continental roots exist). Since continental roots appear to exist beneath most continents and appear to have comparable thick-

nesses we will further assume that they have deformed very little. If the roots are not neutrally buoyant, based on the results present in figure 9.3a for $\Delta\rho > 0$, we require

$$20\epsilon(1 + \lambda)\frac{\mu}{\Delta\rho ga} > O(3 \text{ b.y.}). \quad (9.4)$$

where ϵ is a measure of the deformation or strain of the continental root. Choosing $a = 400 \text{ km}$, $\mu = 10^{21} \text{ Pa s}$, and $\epsilon = 0.4$, we find $\lambda > O(1000\Delta\rho)$ where $\Delta\rho$ is measured in kg/m^3 .

The strain-rate of a neutrally buoyant blob scales as $1/(1 + \lambda)$ the mantle strain-rate [Rallison 1984]. If continental roots are neutrally buoyant or deform very slowly due to buoyancy forces so that the dominant source of deformation is viscous stress applied by a convecting mantle, then the timescale over which convective patterns in the mantle change, T , must be less than the characteristic timescale over which continental roots deform,

$$T < O\left(\frac{\epsilon(1 + \lambda)}{\gamma}\right) \quad (9.5)$$

where γ is the strain-rate in the mantle, and ϵ is the magnitude of deformation of the continental root. Observations of changes of plate motion suggest the time scale over which flow in the mantle changes may be $O(100\text{m.y.})$. Assuming that the large scale flow in mantle may change even more slowly than plate motions, we choose $T = 1 \text{ b.y.}$ For upper mantle strain-rates of 10^{-15} s^{-1} , and assuming $\epsilon < 0.2$, we require $\lambda > O(200)$.

Since it is unlikely that $\Delta\rho$ is less than 0.2 kg/m^3 (the density contrast required for external flows to deform roots more rapidly than flow due to density contrasts), an estimate of the effective viscosity contrast based on (9.4) is probably more appropriate than (9.5). Thus, if continental roots exist and are persistent features in the mantle, they are likely to be very viscous, with an effective viscosity more than 10^4 times the viscosity of the upper mantle, assuming a density contrast of 10 kg/m^3 (a small value). Jordan [1978] proposes that the continental tectosphere beneath stable cratons is between 300 and 500°C colder than the mantle beneath the oceans. The density increase due to the colder temperatures is “delicately balanced” by a density decrease

due to the extration of basaltic components from the mantle beneath continents. The cold temperatures of such a tectosphere may lead to effective viscosity contrasts on the order of $10^3 - 10^6$.

9.4 Highlands and coronae on Venus

While coronae, arachnoids and novae (elevated regions with radii of 100-1000 km often associated with volcanic features) are thought to be related to the ascent of plumes or diapirs [*e.g.* Janes et al. 1993; Koch 1994], the dynamical processes associated with the formation of larger features, called highlands, is more controversial. Venusian highlands are concentrated in a loosely connected band of rises that occurs in the vicinity of the equator. Highlands have diameters of 1000 to 3000 km, and elevations of 1 to 5 km. The shape of the topography varies from high dome-shaped rises (*e.g.* Beta Regio, Atla Regio) to lower, broader, plateau-like structures (*e.g.* western Aphrodite Terra, Alpha Regio). Proposed models for the formation of highlands include both upwellings [*e.g.* Kiefer & Hager 1991] and downwellings [*e.g.* Bindscadler & Parmentier 1990]. Bindscadler et al. [1992] suggest Alpha, Ovda, Tellus, Thetis and Phoebe Regio and Western Ishtar Terra are surface expressions of downwellings. Tackley & Stevenson [1991] have proposed that highlands and coronae are related: large highlands may form from large scale upwellings whereas smaller features may form from Rayleigh-Taylor instabilities in partially molten regions produced in the upwellings. Other models involve a modified form of subduction occurring around the edges of coronae and highlands [*e.g.* Sandwell & Schubert 1992].

9.4.1 Crustal thickening above a downwelling

Here we present a few calculations, consistent with earlier work by Bindscadler & Parmentier [1990], to demonstrate that downwelling models for the formation of highlands are not inconsistent with observations and then draw a few general conclusions regarding the consequences of highlands being the result of downwellings.

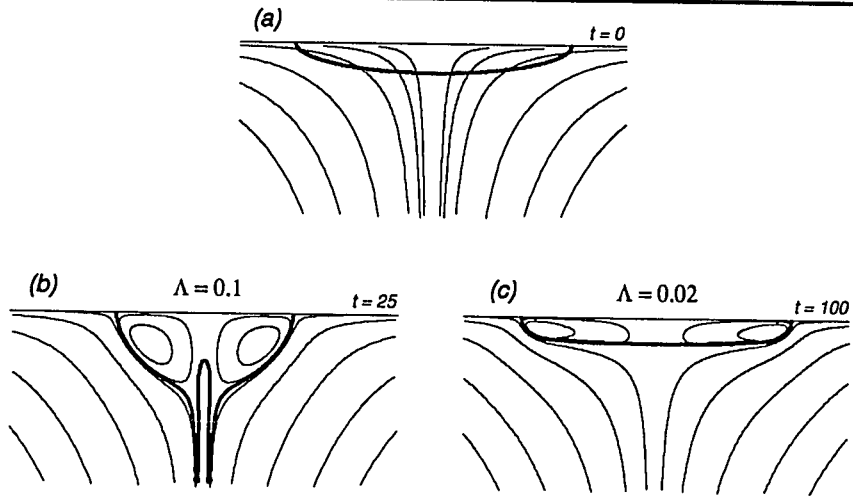


Figure 9.4: Computed streamlines for flow due to a downwelling beneath a buoyant and thickening crust for $\lambda = 1$; (a) the initial conditions at $t = 0$ showing the initial shape of the crust and the externally imposed flow; (b) flow at time $t = 25$ for $\Lambda = 0.1$ and (c) flow at time $t = 100$ for $\Lambda = 0.02$. A nearly-steady shape is reached in (b) and (c), although small amounts of crust are entrained by the downwelling into the mantle for $\Lambda = 0.1$. Time normalized by $\mu/\Delta\rho ga$.

In figure 9.4 we present calculated flow fields at different times during the thickening of a buoyant layer above an axisymmetric downwelling. Initially, at $t = 0$ the surface layer is advected downwards by the downwelling (figure 9.4a). We present results at later times for two different models with $\lambda = 1$: $\Lambda = 0.1$ (figure 9.4b) and $\Lambda = 0.02$ (figure 9.4c). For the results presented in figures 9.4bc, the surface layer has thickened so that a nearly-steady shape is reached (streamlines do not intersect the surface layer). However, for $\Lambda = 0.1$ small amounts of the surface layer are entrained by the downwelling, similar to the crustal entrainment which occurred in the two-dimensional calculations of Lenardic et al. [1993].

The computed surface stresses and expected patterns of deformation corresponding to the results presented in figure 9.4 are shown in figure 9.5-6. The three deviatoric stresses shown are the vertical stress, $\sigma_{zz} = 2\mu\partial u_z/\partial z$, the radial stress,

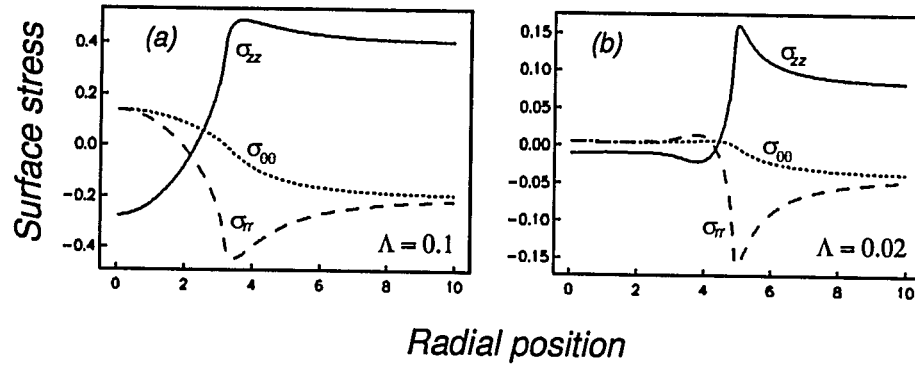


Figure 9.5: Computed deviatoric surface stresses for flow due to a downwelling beneath a buoyant and thickening crust for $\lambda = 1$. (a) Stresses for $\Lambda = 0.1$ at $t = 25$ and (b) stresses for $\Lambda = 0.02$ at $t = 100$. Stresses correspond to the results presented in figures 9.4bc. Radial position is normalized by the initial thickness of the layer, a . Stresses and time normalized by $ag\Delta\rho$ and $\mu/\Delta\rho ga$, respectively.

$\sigma_{rr} = 2\mu\partial u_r/\partial r$, and the hoop stress $\sigma_{\theta\theta} = 2\mu u_r/r$. The pattern of surface stresses shown in figure 9.6 illustrates schematically the spatial distribution and style of deformation consistent with the stresses shown in figure 9.5. Deformation patterns are indicated by small symbols; the longest line in each symbol indicates the predicted strike of faults and the arrows indicate the direction of relative motion across the faults. The actual pattern of deformation will be complicated by a number factors:

1. The numerical model does not include a brittle surface layer and surface stresses are not released by faulting. Thus, the results presented in figure 9.6 are only qualitatively useful.
2. Regional stresses due to other dynamics affect the pattern of surface stresses.
3. The patterns illustrated in figure 9.6 does not take into account the magnitude of stresses (and thus, whether the magnitudes of the stresses are sufficient to result in faulting or folding).
4. During the evolution of crustal thickening, the pattern of stresses changes so that

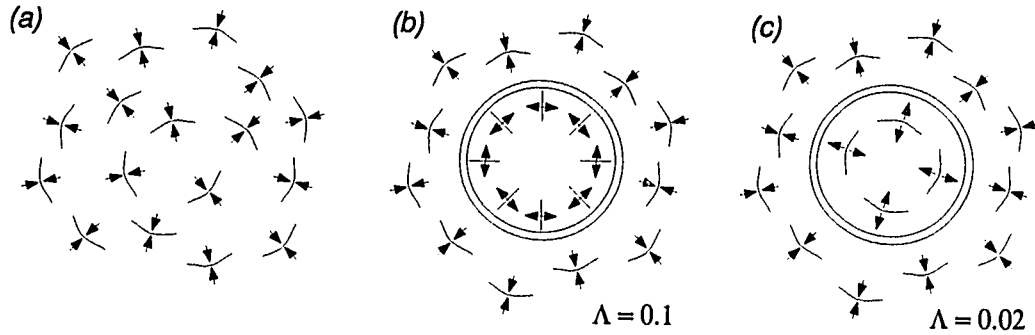


Figure 9.6: The pattern of surface stresses and expected deformation due to the flows shown in figure 9.4; (a) deformation due to a downwelling characterized by concentric compression, (b) deformation for $\Lambda = 0.1$ at $t = 25$ characterized by concentric compression around the thickened crust and radial extension above the thickened crust, and (c) deformation for $\Lambda = 0.02$ at $t = 100$ characterized by concentric compression around the thickened crust and concentric extension above the thickened crust. The patterns illustrate schematically the spatial distribution and style of deformation consistent with the stresses shown in figure 9.5. Deformation patterns are indicated by small symbols; the longest line in each symbol indicates the predicted strike of faults and the arrows indicate the direction of relative motion across the faults.

a complicated set of deformation features may arise since folding and faulting which occur throughout the evolution are preserved.

During the early stages of crustal thickening the pattern of surface deformation is expected to be dominated by compressional features. As the crust thickens, we expect extensional features to develop above the thickened crust.

Finally, in figure 9.7 we show the surface topography corresponding to the results presented in figure 9.4*bc*. The surface topography is dome-shaped for $\Lambda = 0.1$ and is plateau-shaped for $\Lambda = 0.02$.

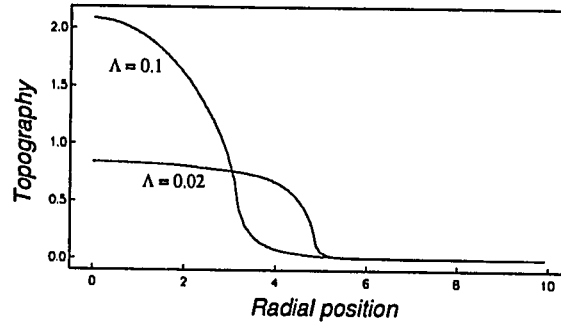


Figure 9.7: Computed surface topographic anomaly corresponding to the flows in figure 9.4bc; (a) $\Lambda = 0.1$ at $t = 25$, and (b) $\Lambda = 0.02$ at $t = 100$. Topography normalized by $a\Delta\rho/\rho$.

9.4.2 Comparison with ascending plume models

Most previous studies have proposed that highlands form above upwellings. In figure 9.8 we reproduce numerically the results of the model proposed by Koch [1994] for the formation of highlands and coronae which involves the ascent and spreading of a plume head. In figure 9.8 we also present calculated surface stresses and in figure 9.9 we illustrate schematically the expected surface deformation (which are subject to the same limitations as the results discussed in the previous section). During the earliest stages of deformation, when the plume head is a several radii beneath the surface, radial extension is expected above the plume head. As the plume head spreads beneath the surface we expect the pattern of deformation to change so that concentric extension occurs above the plume head. The inferred pattern of deformation from the model presented in figure 9.8 is consistent with the features of coronae, arachnoids and novae [Koch 1994].

9.4.3 Remarks

Several models have been proposed for the origin of Venusian highlands. The model proposed by Koch [1994] involving the ascent and spreading of a plume head predicts an evolutionary timescale for the formation of highlands of only 20 m.y. and 200 m.y.

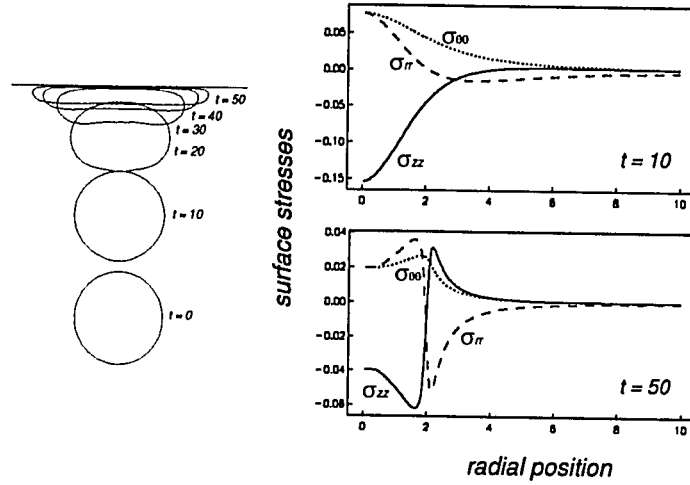


Figure 9.8: Computed deviatoric surface stresses for flow due to a rising plume head at times $t = 10$ and 50 . The shape of the plume head is shown on the left at times $t = 0, 10, 20, 30, 40$ and 50 ; $\lambda = 1$. Stresses and time normalized by $ag\Delta\rho$ and $\mu/\Delta\rho ga$, respectively. Calculations based on the model proposed by Koch [1994] for the formation of Venusian highlands.

for coronae. Although such rates are not unreasonable for coronae-sized features, the rates of highland construction are short compared to the highland age estimates based on crater population and deformation [*e.g.* Schaber et al. 1992]. The timescale for the formation of plateaus is longer than the timescale over which a plume head rises and spreads beneath the surface of Venus. The timescale for crustal thickening (and relaxation of thickened crust) will scale approximately $1/(1 + \lambda)$ the timescale for the uniform viscosity results presented here (see §9.3). The old apparent age of many of the Venusian highlands and the lack of deformation of craters on some highlands suggests that the viscosity of the lithosphere must be sufficiently large that the deformation rate is slow.

The shape of the surface topography calculated here for $\Lambda = 0.02$ is characterized by a plateau-like shape, similar to topographic profiles across several highlands such as Phoebe, Tellus, Ovda and Thetis [Smrekar & Phillips 1991]. The dome-shaped highlands such as Beta, Atla, Western Eistla and Bell were successfully modeled by

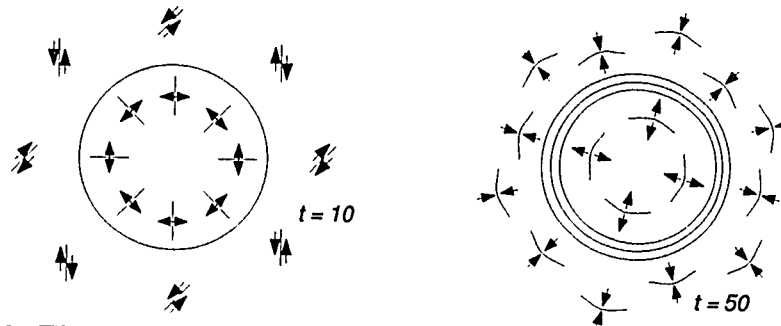


Figure 9.9: The pattern of surface stresses and expected deformation due to a rising and spreading plume head; (a) deformation at $t = 10$ characterized by radial extension above the plume head and strike-slip faulting at larger radial distances, and (b) deformation at $t = 50$ characterized by concentric extension above the spreading plume head surrounded by concentric compression. Figure based on Koch [1994].

steady-state cylindrical upwellings by Kiefer & Hager [1991, 1992]. The upwelling models of Kiefer & Hager reproduce the large geoid-topography ratio of the dome-shaped highlands, but not the lower geoid-topography ratio of the plateau-shaped highlands. Koch [1994] proposes that the low geoid-topography ratios and topographies characteristic of the plateau-shaped highlands are formed by plume heads which have spread beneath the surface of Venus. Since we have parameterized the downwelling responsible for crustal thickening, we did not calculate the geoid, and thus only a limited comparison between the calculations presented here and observations is possible.

The results presented in this section suggest that if surface stresses could be inferred from structural features, then upwelling and downwelling models can be distinguished. Specifically, both radial and concentric extensional features may form above downwellings and concentric extensional features may form above upwellings. Highlands formed above downwellings may thus have a combination of compressional features (remaining from early stages of crustal thickening) as well as extensional features, whereas, highlands formed above upwellings will have only extensional features above the upwelling. Ovda, Alpha and Thetis (plateau-shaped highlands) are

characterized by compressional features whereas Atla, Beta and Eistla (dome-shaped highlands) are characterized by extensional features [Solomon et al. 1992]. We note that the inferred surface deformation in figure 9.6 and 9.9 is highly idealized and involves a number of approximations and assumptions. In order to compare model predictions with observations we must also be able to distinguish pre-existing deformation from features related to the upwelling or thickening of the crust.

Simons et al. [1994] suggest two possible dynamical regimes consistent with geoid-topography ratios on Venus: (*i*) Venus may be in a steady-state convective regime in which plateau-shaped highlands with compressional features are the result of crustal thickening above current downwellings and dome-shaped volcanic rises are the results of current upwellings; (*ii*) plateau-shaped highlands with compressional features remain from earlier stages of deformation and dome-shaped highlands and lowlands occur above upwellings and downwellings, respectively. The model presented here would be characteristic of the plateau-shaped highlands formed in regime (*i*) and the results discussed in §9.3 would apply to the evolution and relaxation of plateau-shaped highlands formed in regime (*ii*).

9.5 “Dregs” at the base of the mantle

Early seismic investigations of the mantle above the core-mantle boundary found evidence for a global layer about 200 km thick, named the D” layer, with a seismic velocity about 2% greater than the overlying lower mantle. More recent studies involving ScS-S travel-time data have found evidence that the D” layer does not have a uniform thickness and does not even appear to exist in some locations [*e.g.* Young & Lay 1990]. The correct interpretation of velocity variations in D” is not obvious or simple. Small-scale topography at the core-mantle boundary and a limited knowledge of high pressure elastic properties of lower mantle minerals provide limitations on possible geophysical interpretations of the seismological observations. The best evidence for a chemical change across D” (and the presence of a compositionally distinct layer)

comes from observations of reflections off D" [*e.g.* Lay & Helmberger 1983].

Proposals for the origin and composition of D" include (i) primordial differentiation products from a magma ocean and core formation, (ii) a thermal boundary layer, (iii) components frozen out of a saturated core, (iv) the products of core-mantle reactions [Knittle & Jeanloz 1989], (v) "dead" slabs [*e.g.* Hoffman & White 1982], and (vi) ponded cold material from "flushing" events (periodic convective events which are observed to occur in numerical simulations of mantle convection [*e.g.* Tackley et al. 1993] which allow for phase changes).

Here we assume that the D" layer consists of compositionally distinct dense material and consider some of the dynamics associated with the D" layer. Specifically we will consider the entrainment and spreading of D" in the presence of mantle flow. The geometry of the numerical problem is illustrated in figure 9.1*b*. The model is not totally inappropriate to the actual physical problem since numerical simulations of mantle convection have demonstrated that a mantle heated primarily from within by radiogenic elements is characterized by broad large-scale upwellings and narrow sheet-like downwellings, whereas narrow axisymmetric "plume-like" structures occur in a mantle heated at the core-mantle boundary.

9.5.1 Dynamics of mantle "dregs"

The numerical problem considered here consists of a negatively buoyant region, referred to hereafter as D" or a mantle "dreg",² above the core-mantle boundary and beneath an axisymmetric upwelling. The upwelling will tend to entrain the material in D" whereas buoyancy-forces will tend to cause D" to spread over the core-mantle boundary. We might expect that in certain limits, buoyancy forces will balance viscous forces exerted by the upwelling so that D" will develop a steady or nearly-steady shape.

²The expression "mantle dreg" is used to describe material above the core-mantle boundary which is too dense to be entrained into the overlying mantle. Mantle dregs are analogous to continents, which are too light to be entrained into the mantle.

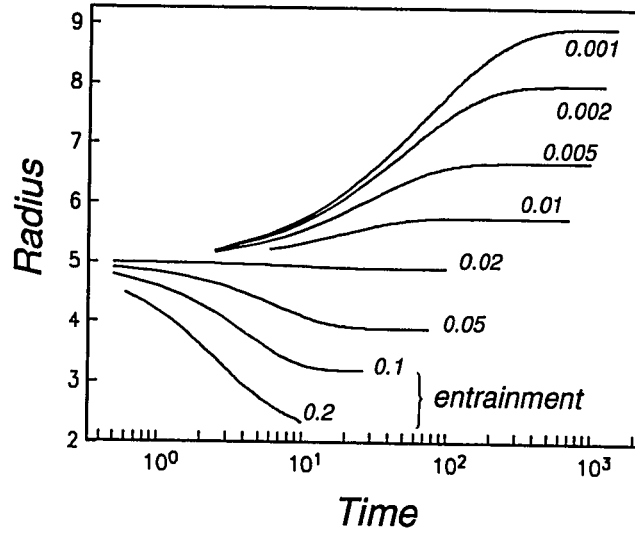


Figure 9.10: Radius of the mantle “dreg” as a function of time for different strain rates, characterized by different values of Λ labeled on the corresponding curves. For $\Lambda = 0.2$ a nearly-steady shape is not achieved. The initial shape of the dreg is a half-ellipsoidal shape with a thickness a and radius $5a$. The radius is normalized to the initial dreg thickness a . Time is normalized by $\mu/\Delta\rho ga$.

In figure 9.10 we show the calculated radius of D'' as a function of time for $\lambda = 1$ and for different values of the entrainment parameter Λ . The initial shape of the dreg is a half-ellipsoidal shape with a thickness a and radius $5a$. For low values of the entrainment parameter, a steady shape develops (the radius does not change with time). For the simulations with $\Lambda = 0.2$ most of the dreg and for $\Lambda = 0.1$ some of the dreg is entrained into the upwelling. Examples of numerically computed streamlines and shapes are shown for different values of Λ in figure 9.11.

Note that since the simulations reported here are numerical simulations, we might not be resolving numerically the interface and some of the mantle dreg may be entrained for all values of Λ . Numerical studies by Lenardic & Kaula [1993] and Lister [1989] and analytical results by Sleep [1988] suggest that thin tendrils will always

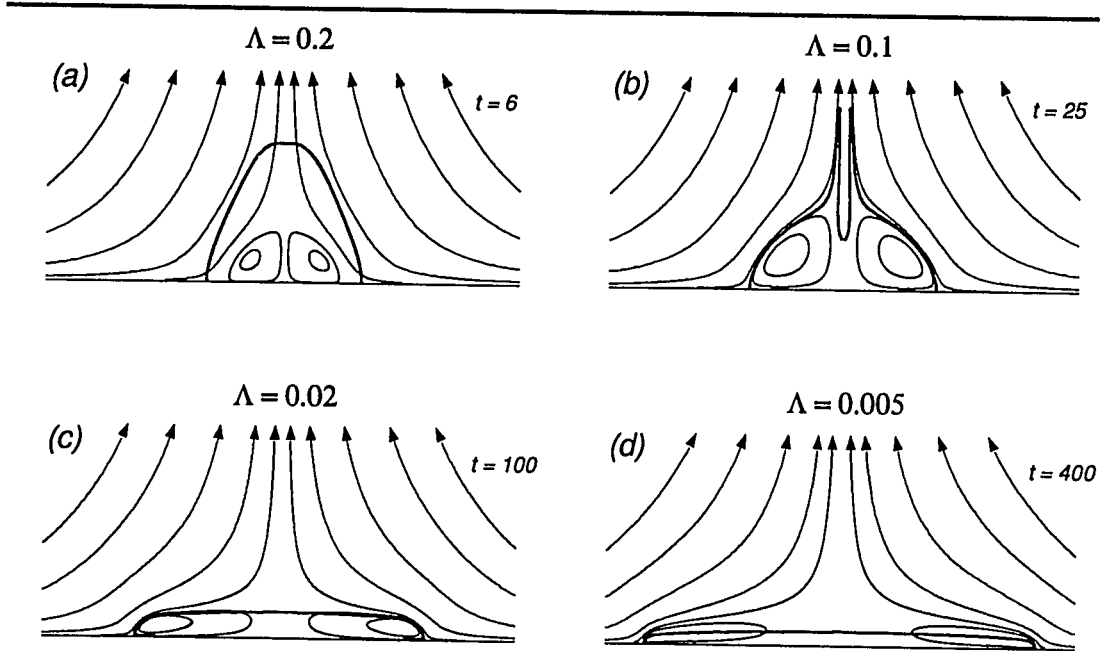


Figure 9.11: Streamlines in the mantle and mantle dreg due to an upwelling for different values of the entrainment parameter; (a) $\Lambda = 0.2$ at $t = 6$, (b) $\Lambda = 0.1$ at $t = 25$, (c) $\Lambda = 0.02$ at $t = 100$, (d) $\Lambda = 0.005$ at $t = 400$. For all simulations $\lambda = 1$. Most of the mantle dreg is entrained for $\Lambda = 0.2$, a small amount is entrained for $\Lambda = 0.1$, and for $\Lambda = 0.02$ and 0.005 none of the dreg is entrained during the simulations. The shape of the mantle dreg is shown with a heavy curve.

be entrained. However, in the problem considered here we recall that the external flow has a constant (in space) strain-rate; the flow due to a sink considered by Lister [1989] has a strain-rate which increases as the distance from the sink decreases, thus entrainment is more likely to occur.

9.5.2 Scaling analysis for the steady-state radius of dregs

In figure 9.12 we show the steady-state radius of D'' as a function of the entrainment parameter for a viscosity ratio $\lambda = 1$. Note that the point for $\Lambda = 0.1$ is only the nearly-steady radius since a small amount of the dreg is entrained into the upwelling (see figure 9.11b). When the mantle dreg has reached a nearly-steady shape, we expect

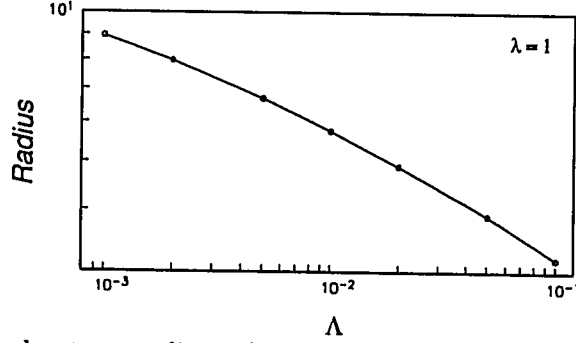


Figure 9.12: Steady-state radius of the mantle dreg as a function of the mantle strain-rate, characterized by Λ (from the results presented in figure 9.10). Results are presented for $\lambda = 1$. For $\Lambda = 0.1$ a small amount of the dreg is entrained.

that the viscous forces exerted by the upwelling will be balanced by the buoyancy forces of the dreg. We now present a scaling analysis which provides an estimate for the steady-state radius.

The radial component of the Stokes equations in fluid i is

$$\frac{\partial p_i}{\partial r} = \mu_i \nabla^2 u_{r_i}. \quad (9.6)$$

Let R and h be the radius and thickness of the dreg characterizing the steady-state shape. An estimate of the pressure gradient due to buoyancy forces in the dreg is

$$\frac{\partial p}{\partial r} \approx \frac{\Delta \rho g h}{R} \quad (9.7)$$

and an estimate of the right-hand side of (9.8) which is due to viscous forces in the dreg exerted by the external flow is

$$\mu \nabla^2 u_r \approx \frac{\mu \gamma}{h}. \quad (9.8)$$

For a steady shape, the flow inside the dreg will be predominantly in the radial direction (see, for example, the streamlines in figure 9.11) provided $R \gg h$. Thus, the radial velocity, u_r , in the dreg will be $\approx \gamma h$.

Conservation of volume requires that $hR^2 \propto V$, where V is the volume. Thus, we find

$$R \propto \Lambda^{-1/5}. \quad (9.9)$$

For comparison, the numerical results in figure 9.8 for $\lambda = 1$ (using the four points furthest on the left of figure 9.12) give

$$R \approx 2.41\Lambda^{-0.19}. \quad (9.10)$$

9.5.3 Remarks

The results of the simulations presented here are consistent with suggestions that Ocean Island Basalts (OIB) are enriched in incompatible elements compared to mid-ocean ridge basalts (MORB) due to the entrainment of recycled crust (assuming D" is a "graveyard" for subducted slabs) by upwelling plumes [*e.g.* Hoffman & White 1982; Campbell & Griffiths 1992].³ The convecting mantle is unable to entrain material from D" whereas plumes which originate as thermal instabilities in D" are able to entrain material from D".

Previous numerical studies [*e.g.* Davies & Gurnis 1986; Hansen & Yuen 1988] and experimental studies [Olson & Kincaid 1991] suggest that D" must be 2-3 % more dense than the lower mantle in order to not be entrained. Specifically, for a layer to be stable for long periods of time, the compositional buoyancy must be greater than thermal buoyancy,

$$\Delta\rho > \alpha\Delta T\rho \quad (9.11)$$

where α is the coefficient of thermal expansion and ΔT is the temperature difference across D". In order for a thermal plume to form in D" we thus require that $\Delta\rho/\rho\alpha\Delta T < 1$ so that D" may become thermally unstable. Choosing ΔT as 1000°C (the temperature difference across the lower thermal boundary layer), $\alpha = 3 \times 10^{-5}\text{°C}^{-1}$ we find that $\Delta\rho < 3\%$. However, for D" not to be entrained

³Alternatively, we could say that MORB is depleted in incompatible elements relative to OIB, suggesting a different interpretation. However, the enrichment of OIB (relative to MORB) is only characteristic of (most) basalts younger than about 2 billion years [Campbell & Griffiths 1992]. Campbell & Griffiths have proposed that the enrichment of post-Archean OIB occurs only once subducted crust is able to sink and spread over the core-mantle boundary to form D" and a source of enriched mantle.

into the convecting mantle we require $\Lambda < O(0.1)$. Assuming $a = 100$ km, $\mu = 10^{23}$ Pa s, $\gamma = 10^{-16}$ s $^{-1}$, we require $\Delta\rho > 2\%$. Thus, for density contrasts of approximately 2-3%, the convecting mantle will entrain only small amounts of D'' yet D'' is not sufficiently dense that it may still become unstable and be entrained by thermal plumes which originate at the core-mantle boundary. For D'' not to be entrained by the convecting mantle and not to become unstable and form a plume, we require

$$\Delta\rho > O(\alpha\Delta T\rho + 10\gamma\mu/ga). \quad (9.12)$$

Finally, we note that the time scale for a layer of cold material such as subducted slabs to heat up by diffusion and become unstable is approximately 1 b.y. for a layer 200 km thick.

Appendix A

The Boundary integral method (BIM)

Low Reynolds number flows are characterized by small velocities, small length scales and/or high fluid viscosities. In this limit the inertia terms in the Navier-Stokes equations are neglected; the fluid motion is governed by the linear (quasi-steady) Stokes equations. Integral equation formulations are a natural choice for certain classes of Stokes flow problems. The methods may be applied to flows involving only rigid boundaries (*e.g.*, a suspension of rigid particles) and flows involving at least one fluid-fluid interface, hereafter referred to as *free-boundary* problems.¹ The former subject has been discussed and developed by Kim and coworkers [*e.g.* Kim & Karrila 1991]. This appendix presents a brief survey of the application of boundary integral methods to free-boundary problems for flows at low Reynolds numbers, modified from a contribution by Tanzosh, Manga & Stone [1992].

¹Boundary integral methods have also been used to study high Reynolds number free-boundary problems. This is a separate subject and the interested reader can refer to [Baker et al. 1984; Lundgren & Mansour 1988; Oguz & Prosperetti 1990].

A.1 Introduction

The dynamics of interface deformation in low Reynolds number flows is of interest in a wide variety of fields including chemical and petroleum engineering, solid-earth geophysics, hydrology, and biology. Typical applications span an immense range of length scales from microns to hundreds of kilometers: biological studies of cell deformation; chemical engineering studies of coalescence, flotation, coating flows and the dynamics of thin films; and geophysical studies of mantle plumes, lithospheric slabs and magma chambers.

The principal difficulty with solving free-boundary problems is that the position of the interface is unknown *a priori* and must be determined as part of the solution. Thus, the problem of determining the time-dependent interface shape is inherently non-linear.

The boundary integral method relates velocities at points within the fluid to the velocity and stress on the bounding surfaces. It is an ideal method for studying free-boundary problems. Advantages of the technique include the reduction of problem dimensionality, the direct calculation of the interfacial velocity, the ability to track large surface deformations, and the potential for easily incorporating interfacial tension as well as other surface effects (*e.g.*, electric field-induced stresses, elastic membrane stresses).

The boundary integral formulation for Stokes flows was theoretically described by Ladyzhenskaya [1963] within the framework of hydrodynamic potentials. The integral equation method was developed and implemented numerically by Youngren & Acrivos [1975] in a study of the translation of arbitrarily-shaped rigid particles. Shortly thereafter, the method was extended to the study of deformation of fluid-fluid interfaces: the deformation of bubbles and drops in extensional flows [Youngren & Acrivos 1976; Rallison & Acrivos 1978] and the motion of a rigid sphere moving normal to a deformable interface [Lee & Leal 1982]. In recent years the number of applications has increased enormously.

Applications of boundary integral methods have ranged from the classical study

of a rising drop in an otherwise quiescent fluid [Koh & Leal 1989, 1990; Pozrikidis 1990a], to more complex situations such as drop breakup in extensional flows [*e.g.* Stone & Leal 1989b] the deformation of a blood cell [*e.g.* Li et al. 1988; Pozrikidis 1990c], and the deformation of small drops in electric and magnetic fields. The integral equation approach has also been applied to study the growth of two-dimensional Rayleigh-Taylor instabilities [Yiatsios & Higgins 1989; Newhouse & Pozrikidis 1990] and the selective withdrawal of fluid from a stratified layer [Lister 1989]. Although most work has been concerned with axisymmetric or two-dimensional interface deformations, which only require numerical treatment of line integrals, several studies have considered the more difficult case of three-dimensional surface distortion [Rallison 1981; deBruijn 1989; Kennedy et al. 1994]. Recent studies have combined boundary integral methods with lubrication theory to characterize the fluid motion in thin regions between two fluid layers [Barnocky & Davis 1989; Davis et al. 1990; Lister & Kerr 1989; Yiatsios & Davis 1990, 1991]. Many aspects related to integral equation methods for free-boundary problems are described in a recent book by Pozrikidis [1992]. Figure 1 summarizes applications of integral equation methods to free-boundary problems. The studies have been classified according to whether the geometry is axisymmetric, two-dimensional, or three-dimensional. Drop problems are further subdivided according to application.

We proceed by considering some of the details of the boundary integral formulation. In §A.2 we provide a derivation of the basic integral equations, along with the modifications necessary for the study of more complicated problems. In §A.3, we outline the numerical techniques typically applied in the treatment of free-boundary problems.

A.2 Analytic formulation

In this section we present the basic equations necessary for studying free-boundary Stokes flow problems using integral equation methods. A variety of free-boundary

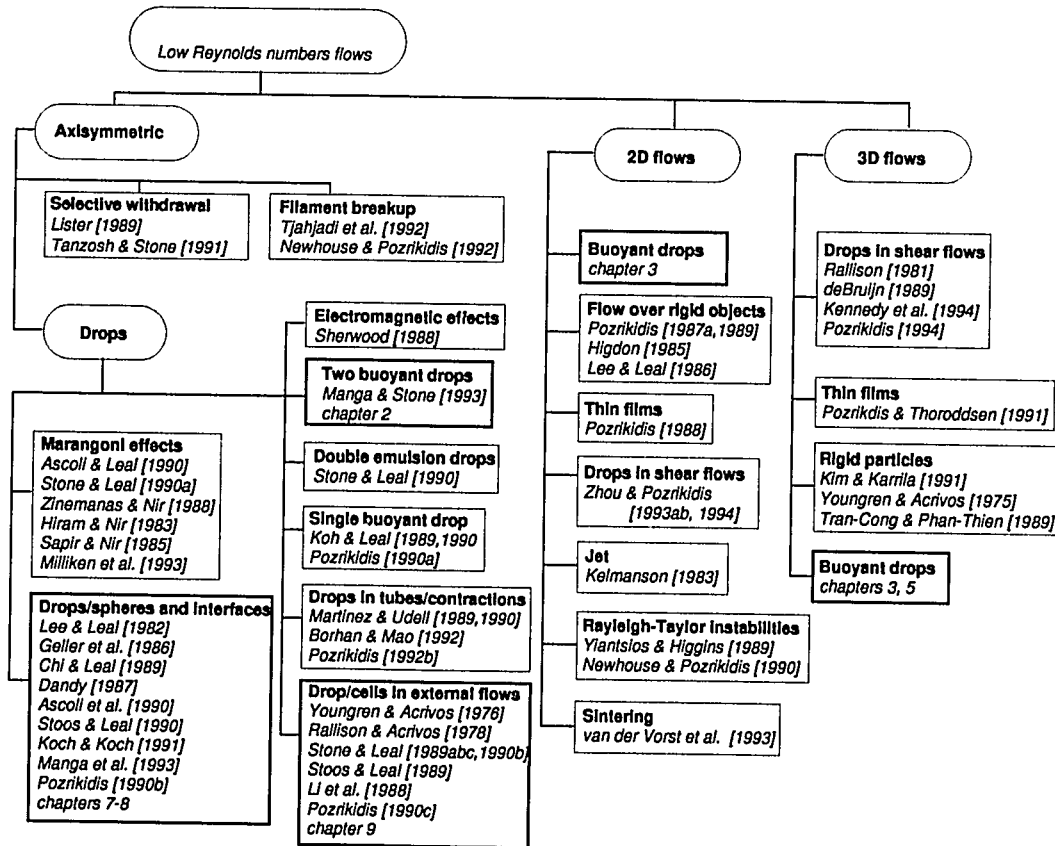


Figure A.1: Summary of many free-boundary problems studied numerically using the boundary integral formulation for low Reynolds numbers flows. Geometries and problems considered in this thesis are shown in bold boxes. Selected studies involving flow over rigid surfaces are included (dashed boxes). New problems considered in this thesis are contained in bold boxes.

problems can be posed, each involving different combinations of fluid-fluid interfaces, rigid boundaries and external flows. A generic treatment covering all possibilities is rather difficult, so details of the method are discussed within the framework of several prototypical problems:

1. a drop in an unbounded fluid, including the presence of an external flow, §A.2.4
2. a rigid particle translating normal to a deformable interface, §A.2.5
3. a drop translating normal to a deformable interface, §A.2.6.

The three free-boundary problems mentioned above illustrate the basic elements necessary for treatment of, respectively, (i) unbounded and external flows, (ii) rigid boundaries, and (iii) multiple fluid-fluid interfaces. In principle, generalization to other geometries is straightforward.

A.2.1 Equations and boundary conditions

In the low Reynolds number limit, incompressible fluid motion is governed by the Stokes and continuity equations

$$\nabla \cdot \mathbf{T} = -\nabla p + \mu \nabla^2 \mathbf{u} + \rho \mathbf{g} = 0 \quad (\text{A.1})$$

$$\nabla \cdot \mathbf{u} = 0, \quad (\text{A.2})$$

where \mathbf{u} is the velocity, p is the pressure, μ and ρ are the fluid viscosity and density, respectively, and \mathbf{g} is the gravitational acceleration. Here the stress tensor \mathbf{T} is defined to include the hydrostatic body force,

$$\mathbf{T} = -(p - \rho \mathbf{g} \cdot \mathbf{x}) \mathbf{I} + \mu [\nabla \mathbf{u} + (\nabla \mathbf{u})^T], \quad (\text{A.3})$$

in order to define a divergence-free field. The body force will appear explicitly in the boundary conditions if there are density contrasts across fluid-fluid interfaces. The low Reynolds number assumption requires

$$\mathcal{R} = \rho U a / \mu \ll 1 \quad (\text{A.4})$$

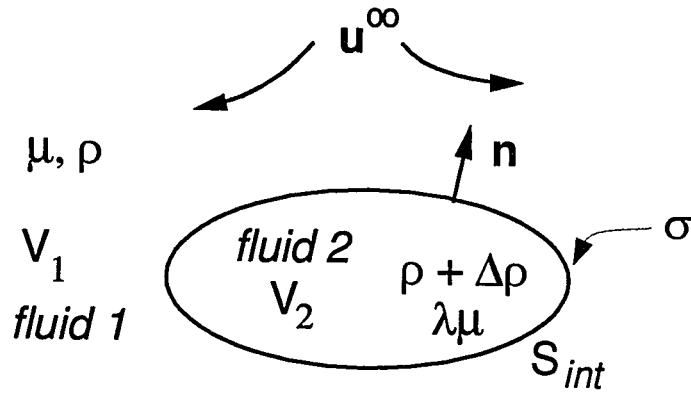


Figure A.2: A translating and deforming drop in an unbounded fluid. As the drop translates, its shape in general will change and it is one of the goals of the boundary integral analysis to predict this deformation.

where U and a are characteristic velocity and length scales of the fluid motion.

For illustrative purposes, consider the case of a drop of viscosity $\lambda\mu$ immersed in a second immiscible fluid of viscosity μ with an externally-imposed velocity field $\mathbf{u}^\infty(\mathbf{x})$, figure A.2, where \mathbf{x} is a position vector. The boundary conditions at a fluid-fluid interface S_{int} require a continuous velocity and a balance between the net surface traction and interfacial tension forces. Hence,

$$\mathbf{u}_1(\mathbf{x}) \rightarrow \mathbf{u}^\infty(\mathbf{x}) \quad \text{as } |\mathbf{x}| \rightarrow \infty \quad (\text{A.5})$$

$$\mathbf{u}_1(\mathbf{x}) = \mathbf{u}_2(\mathbf{x}) \quad \text{for } \mathbf{x} = \mathbf{x}_s \in S_{int} \quad (\text{A.6})$$

and the stress jump $[\mathbf{n} \cdot \mathbf{T}]$, accounting for a density difference across the interface, is given by (the normal \mathbf{n} points *into* fluid 1)

$$[\mathbf{n} \cdot \mathbf{T}] \equiv \mathbf{n} \cdot \mathbf{T}_1 - \mathbf{n} \cdot \mathbf{T}_2 = \sigma (\nabla_s \cdot \mathbf{n})\mathbf{n} - \nabla_s \sigma - \Delta\rho(\mathbf{g} \cdot \mathbf{x})\mathbf{n} \quad \text{for } \mathbf{x}_s \in S_{int}. \quad (\text{A.7})$$

Here \mathbf{u}_i is the velocity in fluid i , σ denotes the interfacial tension, $\Delta\rho$ is the density difference, $\nabla_s = (\mathbf{I} - \mathbf{n}\mathbf{n}) \cdot \nabla$ is the gradient operator tangent to the interface, $\nabla_s \cdot \mathbf{n}$ is the mean curvature of the interface and \mathbf{x}_s denotes a point on the interface. The stress balance (A.7) includes both a normal stress jump, proportional to the product of

interfacial tension and the local curvature, and a tangential stress jump, $-\nabla_s \sigma$, owing to variations in interfacial tension along the surface. Interfacial tension variations may result from either temperature gradients or the presence of surfactants in the fluid. In such instances, additional field equations (such as an advective-diffusion or Laplace equation) determine the temperature profile or the distribution of surfactants along the interface. Other stresses may be included in the stress jump boundary condition. For example, in studies of drop deformation, Sherwood [1988] examined the effect of electric or magnetic field-induced stresses and Li *et al.* [1988] studied the role of elastic stresses generated in a thin membrane surrounding a drop.

A kinematic constraint relates changes in the interface position to the local velocity. For example, the interface evolution may be described with a Lagrangian representation

$$\frac{d\mathbf{x}_s}{dt} = \mathbf{u}(\mathbf{x}_s). \quad (\text{A.8})$$

Although time-dependence does not appear explicitly in Stokes equations, it is consistent to study time-dependent interface distortions; the *quasi-static* assumption requires that

$$l^2/\nu \ll \tau \quad (\text{A.9})$$

where ν is the kinematic viscosity, and τ is a typical time for a change of the flow or geometry. Generally, $\tau = \min [O(l/u^\infty), O(l\mu/\sigma)]$, where the former is a time scale for an externally-driven flow, and the latter is the time scale of an interfacial-tension-driven motion. In most situations, the larger of the two fluid viscosities should be used for these estimates. Physically, the quasi-static approximation means that the fluid immediately adjusts to changes in the boundary location owing to rapid vorticity diffusion.

A.2.2 Green's functions

In order to derive an integral representation for Stokes flows, the fundamental singular solutions for Stokes equations are needed. These singular solutions correspond to the velocity and stress fields at a point \mathbf{x} produced by a point force \mathbf{F} located at \mathbf{y} (figure

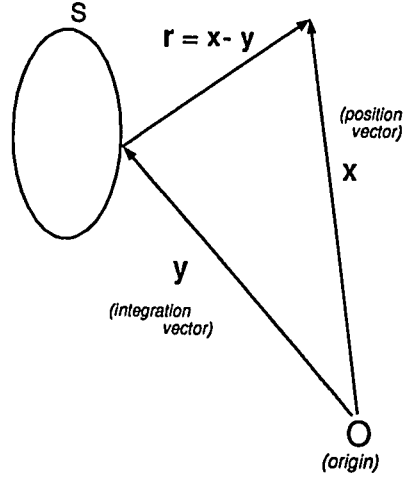


Figure A.3: illustrating the definition of the position vector \mathbf{x} and the integration vector \mathbf{y} used to define the fundamental singular solutions to the Stokes equations and the corresponding Green's functions.

A.3) and may be derived, for example, using Fourier transforms [Kim & Karrila 1991]. Denoting the singular solution by $\hat{\mathbf{u}}$ and solving

$$\nabla \cdot \hat{\mathbf{T}} + \mathbf{F} \delta(\mathbf{x} - \mathbf{y}) = 0 \quad \text{and} \quad \nabla \cdot \hat{\mathbf{u}} = 0 \quad (\text{A.10})$$

with $|\hat{\mathbf{u}}| \rightarrow 0$ and $|\hat{\mathbf{T}}| \rightarrow 0$ as $|\mathbf{x}| \rightarrow \infty$ yields

$$\hat{\mathbf{u}}(\mathbf{x}) = \frac{1}{\mu} \mathbf{J}(\mathbf{r}) \cdot \mathbf{F} \quad (\text{A.11})$$

and

$$\hat{\mathbf{T}}(\mathbf{x}) = \mathbf{K}(\mathbf{r}) \cdot \mathbf{F}, \quad (\text{A.12})$$

where the kernels, or Green's functions, are denoted \mathbf{J} and \mathbf{K} , and $\mathbf{r} = \mathbf{x} - \mathbf{y}$.

The free-field Green's functions mapping a force at \mathbf{y} to the field at \mathbf{x} in an unbounded three-dimensional domain are

$$\mathbf{J}(\mathbf{r}) = \frac{1}{8\pi} \left(\frac{\mathbf{I}}{r} + \frac{\mathbf{r}\mathbf{r}}{r^3} \right) \quad (\text{A.13})$$

and

$$\mathbf{K}(\mathbf{r}) = -\frac{3}{4\pi} \frac{\mathbf{r}\mathbf{r}\mathbf{r}}{r^5} \quad (\text{A.14})$$

Table A.1: Selected Green's functions for Stokes flow.

<i>Geometry</i>	<i>Reference</i>
Rigid plane wall	Blake [1971]
Semi-infinite plate	Hasimoto et al. [1983]
Solid sphere	Oseen (as cited in Kim & Karrila [1991])
Two intersecting planes	Sano & Hasimoto [1978]
Inside a circular cylinder	Liron & Shahar [1978]
Solid planar wall with a hole	Davis [1983], Miyazaki & Hasimoto [1984]
Between two parallel plates	Liron & Mochon [1976]
2-D Periodic: Symmetric with respect to a point or plane	Pozrikidis [1987ab]
2-D near a planar boundary	Liron & Blake [1981]

and in an unbounded two-dimensional domain are

$$\mathbf{J}(\mathbf{r}) = \frac{1}{4\pi} \left(\mathbf{I} \log r - \frac{\mathbf{r}\mathbf{r}}{r^2} \right) \quad (\text{A.15})$$

and

$$\mathbf{K}(\mathbf{r}) = \frac{1}{\pi} \frac{\mathbf{r}\mathbf{r}\mathbf{r}}{r^4}. \quad (\text{A.16})$$

Green functions for other geometries have also been derived. In practice, modified Green's functions reduce the number of boundary conditions which must be imposed in boundary integral applications, thereby simplifying the problems. Examples are listed in Table A.1.

A.2.3 Integral representation of Stokes equations

For two solenoidal velocity fields (\mathbf{u}, \mathbf{T}) and $(\hat{\mathbf{u}}, \hat{\mathbf{T}})$ it is straightforward to derive the Reciprocal theorem (a Green's theorem), which states

$$\int_V [\mathbf{u}(\mathbf{x}) \cdot (\nabla \cdot \hat{\mathbf{T}}) - \hat{\mathbf{u}} \cdot (\nabla \cdot \mathbf{T})] dV_x = \int_S \mathbf{n}(\mathbf{x}) \cdot [\hat{\mathbf{T}} \cdot \mathbf{u} - \mathbf{T} \cdot \hat{\mathbf{u}}] dS_x, \quad (\text{A.17})$$

where \mathbf{n} is the unit outward normal to the fluid volume V , S represents all surfaces bounding the domain (including a possible surface at infinity S_∞) and integration occurs with respect to \mathbf{x} .

Substituting the fundamental singular solutions (A.11 – A.12) into the Reciprocal theorem, applying the continuity equation (A.2), removing the arbitrary vector \mathbf{F} , and, for convenience, interchanging the labels \mathbf{x} and \mathbf{y} yields the integral equation

$$\frac{1}{\mu} \int_S \mathbf{n} \cdot \mathbf{T} \cdot \mathbf{J}(\mathbf{r}) dS_y + \int_S \mathbf{n} \cdot \mathbf{K}(\mathbf{r}) \cdot \mathbf{u} dS_y = \begin{cases} \mathbf{u}(\mathbf{x}) & \mathbf{x} \in V \\ \frac{1}{2} \mathbf{u}(\mathbf{x}_s) & \mathbf{x}_s \in S. \\ 0 & \mathbf{x} \notin V \end{cases} \quad (\text{A.18})$$

The reader is warned that other sign/nomenclature conventions are in use and reminded that \mathbf{J} and \mathbf{K} are, respectively, symmetric and antisymmetric tensors with respect to $\mathbf{r} = \mathbf{x} - \mathbf{y}$. The factor of 1/2 arises from the jump in the value of the \mathbf{K} integral as the surface is crossed. The surface is assumed to be Lyapunov smooth, which requires that a local tangent to the interface exist everywhere; sharp corners, cusps or edges violate this assumption and must be treated separately.

Equation (A.18) relates the velocity field $\mathbf{u}(\mathbf{x})$ at any point inside, outside, or on the boundary of a fluid volume to the velocity $\mathbf{u}(\mathbf{x}_s)$ and traction $\mathbf{n} \cdot \mathbf{T}(\mathbf{x}_s)$ on the bounding surface. For points on the boundary S , equation (A.18) is an integral equation of the *second kind* for the velocity $\mathbf{u}(\mathbf{x}_s)$ if the traction is known, and of the *first kind* for the traction $\mathbf{n} \cdot \mathbf{T}(\mathbf{x}_s)$ if the velocity is known. Finally, equation (A.18c) is a useful identity for developing integral equations with a minimum number of unknowns (see §A.2.5-6).

There are alternative procedures for producing integral representations for Stokes flow problems. Rather than using the primary variables $\mathbf{u}(\mathbf{x}_s)$ and $\mathbf{n} \cdot \mathbf{T}(\mathbf{x}_s)$ as in (A.18), an integral representation can be developed in terms of non-physical single-layer or double-layer distributions. For example, the single-layer distribution is $\mathbf{u}(\mathbf{x}) = \int_S \mathbf{J} \cdot \mathbf{q} dS_y$, with a similar expression for the associated stress field. Unlike (A.18) which yields an integral equation of the first kind for the stress distribution $\mathbf{n} \cdot \mathbf{T}$ if \mathbf{u} is known on all surface, the alternative formulation yields an integral equation

tion of the second kind. For problems involving rigid particles, the reader is referred to Kim & Karrila [1991] and Karrila & Kim [1989]. The approach has also been applied to free-boundary problems by Newhouse & Pozrikidis [1990] and Pozrikidis [1990a].

A.2.4 Integral equation for a fluid-fluid interface

Consider the case of a fluid drop, volume V_2 , in an unbounded fluid, volume V_1 , as shown in figure A.2. The viscosity ratio is denoted by λ . If there is an imposed flow $\mathbf{u}^\infty(\mathbf{x})$, the basic equations are developed in terms of ‘disturbance variables’. Define for both fluids 1 and 2 the disturbance velocities

$$\mathbf{u}'_i(\mathbf{x}) = \mathbf{u}_i(\mathbf{x}) - \mathbf{u}^\infty(\mathbf{x}) \quad i = 1, 2 \quad (\text{A.19})$$

and disturbance stresses

$$\mathbf{T}'_i(\mathbf{x}) = \mathbf{T}_i(\mathbf{x}) - \mathbf{T}_i^\infty(\mathbf{x}) \quad i = 1, 2. \quad (\text{A.20})$$

Equation (A.18) holds for \mathbf{u}' in both fluids and only the fluid-fluid interface S_{int} need be considered. The enclosing boundary at large distances S_∞ may be neglected because of the $1/r$ and $1/r^2$ decay of the velocity and stress fields characteristic of disturbance Stokes flows. Therefore, remembering that \mathbf{n} is directed from fluid 2 to fluid 1, we can write the two equations

$$-\frac{1}{\mu} \int_S \mathbf{n} \cdot \mathbf{T}'_1 \cdot \mathbf{J} \, dS_y - \int_S \mathbf{n} \cdot \mathbf{K} \cdot \mathbf{u}'_1 \, dS_y = \begin{cases} \mathbf{u}_1(\mathbf{x}) & \mathbf{x} \in V_1, \\ \frac{1}{2} \mathbf{u}_1(\mathbf{x}_s) & \mathbf{x}_s \in S_{int}, \\ 0 & \mathbf{x} \in V_2, \end{cases} \quad (\text{A.21})$$

and

$$\frac{1}{\lambda\mu} \int_S \mathbf{n} \cdot \mathbf{T}'_2 \cdot \mathbf{J} \, dS_y + \int_S \mathbf{n} \cdot \mathbf{K} \cdot \mathbf{u}'_2 \, dS_y = \begin{cases} 0 & \mathbf{x} \in V_1, \\ \frac{1}{2} \mathbf{u}_2(\mathbf{x}_s) & \mathbf{x}_s \in S_{int}, \\ \mathbf{u}_2(\mathbf{x}) & \mathbf{x} \in V_2. \end{cases} \quad (\text{A.22})$$

Multiplying equation (A.22) by λ , adding to (A.21), and using boundary conditions (A.6-A.7) yields

$$-\frac{1}{\mu} \int_{S_{int}} [\mathbf{n} \cdot \mathbf{T}'] \cdot \mathbf{J} \, dS_y - (1-\lambda) \int_{S_{int}} \mathbf{n} \cdot \mathbf{K} \cdot \mathbf{u}'_1 \, dS_y = \begin{cases} \mathbf{u}_1(\mathbf{x}) & \mathbf{x} \in V_1, \\ \frac{1+\lambda}{2} \mathbf{u}_1(\mathbf{x}_s), & \mathbf{x}_s \in S_{int} \\ \lambda \mathbf{u}_2(\mathbf{x}) & \mathbf{x} \in V_2, \end{cases} \quad (\text{A.23})$$

where the disturbance stress jump $[\mathbf{n} \cdot \mathbf{T}'] = [\mathbf{n} \cdot \mathbf{T}] - [\mathbf{n} \cdot \mathbf{T}^\infty]$. Alternatively, for problems with externally-imposed flows, it is more common to recast (A.23) in terms of the actual interfacial velocity and $\mathbf{u}^\infty(\mathbf{x})$. Using the identity

$$\int_{V_2} \nabla \cdot (\mathbf{T}^\infty \cdot \mathbf{J} + \mathbf{K} \cdot \mathbf{u}^\infty) \, dV = 0, \quad (\text{A.24})$$

one obtains the widely applied integral equation

$$\mathbf{u}^\infty(\mathbf{x}_s) - \frac{1}{\mu} \int_{S_{int}} [\mathbf{n} \cdot \mathbf{T}] \cdot \mathbf{J}(\mathbf{r}) \, dS_y - (1-\lambda) \int_{S_{int}} \mathbf{n} \cdot \mathbf{K}(\mathbf{r}) \cdot \mathbf{u}_1 \, dS_y = \begin{cases} \mathbf{u}_1(\mathbf{x}) & \mathbf{x} \in V_1 \\ \frac{1+\lambda}{2} \mathbf{u}_1(\mathbf{x}_s), & \mathbf{x}_s \in S_{int}, \\ \lambda \mathbf{u}_2(\mathbf{x}) & \mathbf{x} \in V_2. \end{cases} \quad (\text{A.25})$$

Rallison & Acrivos [1978] first presented (A.25b) for the interfacial velocity and Pozrikidis [1990b] presented the complete form of (A.25) for the general case of points off the fluid-fluid interface. Power [1987] showed that the integral equation (A.25) has real eigenvalues corresponding to $\lambda = 0$ or ∞ , and that a unique and continuous solution exists for $0 < \lambda < \infty$.

We can derive integral equations for the pressure field similar to the equations for the velocity field. The analogous equation to (A.18) is given by,

$$\frac{1}{4\pi} \int_S \mathbf{n} \cdot \mathbf{T} \cdot \frac{\mathbf{r}}{|\mathbf{r}|^3} \, dS_y + \frac{\mu}{2\pi} \int_S \mathbf{n} \cdot \nabla \left(\frac{\mathbf{r}}{|\mathbf{r}|^3} \right) \cdot \mathbf{u} \, dS_y = \begin{cases} p(\mathbf{x}) & \mathbf{x} \in V_1, \\ \frac{1}{2} p(\mathbf{x}) & \mathbf{x} = \mathbf{x}_s \in S_{int}, \\ 0 & \mathbf{x} \in V_2. \end{cases} \quad (\text{A.26})$$

Equations (A.18) and (A.26) for the velocity and pressure, respectively, represent formal integral equation solutions for the velocity and pressure fields \mathbf{u} and p of the generic Stokes flow problem.

For a given external flow and a known interface shape S_{int} , equation (A.23b) (or A.25b) is an integral equation of the second kind for the unknown disturbance velocity $u'(\mathbf{x}_s)$ (or the actual velocity $\mathbf{u}(\mathbf{x}_s)$), which depends on the stress jump $[[\mathbf{n} \cdot \mathbf{T}]]$ across the deformable surface. The stress jump is a function of the interface shape, with dependence on the position, normal and curvature as given by equation (A.7). The above equations can be the starting point for numerical investigation of numerous free-boundary problems. In addition, for a known interfacial velocity and interface shape, equations (A.23) or (A.25) determine the velocity at points off the surface and thus are useful for obtaining a detailed picture of the entire flow field.

The majority of studies assume that the interface shape is axisymmetric. The azimuthal integration can be performed analytically, thereby reducing the surface integral to a line integral. The resulting kernels involve elliptic functions (*e.g.* Lee & Leal [1982], see Appendix B). For the case of equal fluid viscosities ($\lambda = 1$), equations (A.23) and (A.25) simplify to an explicit expression for the interfacial velocity. If the problem sketched in figure A.3 is bounded, for example, by a rigid planar boundary, a modified Green's function may be used to account for the rigid surface; only integration along the deformable interface S_{int} is required.

In principle, either (A.23) or (A.25) and the kinematic condition are solved numerically in order to follow changes in the interface shape. However, before discussing details of the numerical solution, two additional applications are described for common free-boundary problems.

A.2.5 Application to a rigid particle near a fluid-fluid interface

Consider the slightly more complicated problem of a rigid buoyant sphere translating with unknown velocity \mathbf{U}_P normal to a deformable fluid-fluid interface in an otherwise quiescent fluid (figure A.4a). Label the fluids 1 and 3 to be consistent with the related problems shown in figures A.3 and A.4b.

For fluid 1, apply the integral representation of Stokes equations (A.18) and write

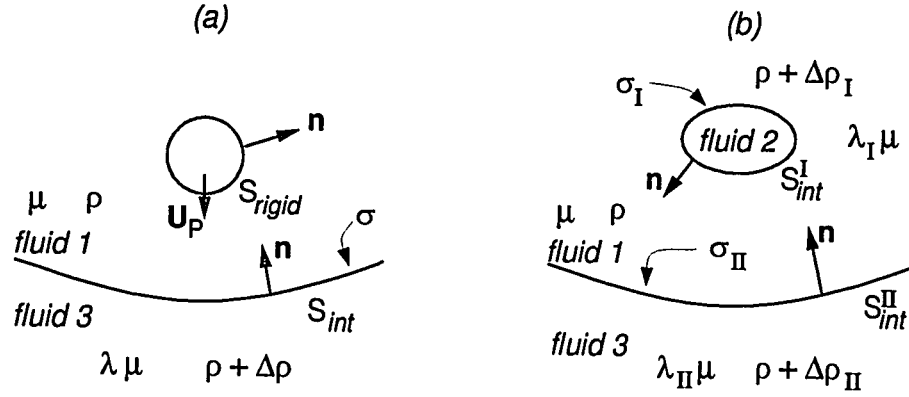


Figure A.4: (a) Rigid sphere and (b) drop approaching an interface.

four integral identities, two for field points on either of the bounding surfaces and two for points in either of the fluid volumes:

$$\begin{aligned}
 & -\frac{1}{\mu} \int_{S_{int}} \mathbf{n} \cdot \mathbf{T}_1 \cdot \mathbf{J} \, dS_y - \int_{S_{int}} \mathbf{n} \cdot \mathbf{K} \cdot \mathbf{u}_1 \, dS_y \\
 & - \frac{1}{\mu} \int_{S_{rigid}} \mathbf{n} \cdot \mathbf{T}_1 \cdot \mathbf{J} \, dS_y = \begin{cases} \mathbf{u}_1(\mathbf{x}) & \mathbf{x} \in V_1, \\ \mathbf{U}_P & \mathbf{x}_s \in S_{rigid}, \\ \frac{1}{2} \mathbf{u}_1(\mathbf{x}) & \mathbf{x}_s \in S_{int}, \\ 0 & \mathbf{x} \in V_3. \end{cases} \quad (A.27)
 \end{aligned}$$

The identity

$$\int_{S_{rigid}} \mathbf{n} \cdot \mathbf{K} \, dS = -\frac{1}{2} \mathbf{I}, \quad (A.28)$$

which follows from the Divergence Theorem and $\nabla \cdot \mathbf{K} + \mathbf{I} \delta(\mathbf{r}) = 0$, has been used to simplify the integral over S_{rigid} .

In a similar manner, for fluid 3 write the four equations

$$\frac{1}{\lambda \mu} \int_{S_{int}} \mathbf{n} \cdot \mathbf{T}_3 \cdot \mathbf{J} \, dS_y + \int_{S_{int}} \mathbf{n} \cdot \mathbf{K} \cdot \mathbf{u}_3 \, dS_y = \begin{cases} 0 & \mathbf{x} \in V_1, \\ 0 & \mathbf{x}_s \in S_{rigid}, \\ \frac{1}{2} \mathbf{u}_3(\mathbf{x}) & \mathbf{x}_s \in S_{int}, \\ \mathbf{u}_3(\mathbf{x}) & \mathbf{x} \in V_3. \end{cases} \quad (A.29)$$

Multiplying (A.27) by λ , adding to (A.29), and again using the boundary conditions

(A.6-A.7) of continuous velocity and the stress jump $[\mathbf{n} \cdot \mathbf{T}]$ yields

$$-\frac{1}{\mu} \int_{S_{int}} [\mathbf{n} \cdot \mathbf{T}] \cdot \mathbf{J} \, dS_y - (1 - \lambda) \int_{S_{int}} \mathbf{n} \cdot \mathbf{K} \cdot \mathbf{u}_1 \, dS_y \quad (\text{A.30})$$

$$- \frac{1}{\mu} \int_{S_{rigid}} \mathbf{n} \cdot \mathbf{T}_1 \cdot \mathbf{J} \, dS_y = \begin{cases} \mathbf{u}_1(\mathbf{x}) & \mathbf{x} \in V_1, \\ \mathbf{U}_P(\mathbf{x}) & \mathbf{x}_s \in S_{rigid}, \\ \frac{1 + \lambda}{2} \mathbf{u}_1(\mathbf{x}) & \mathbf{x}_s \in S_{int}, \\ \lambda \mathbf{u}_3(\mathbf{x}) & \mathbf{x} \in V_3. \end{cases}$$

The problem statement is completed by imposing the integral force constraint on the buoyantly rising particle,

$$\int_{S_{rigid}} \mathbf{n} \cdot \mathbf{T}_1 \, dS = \text{constant}, \quad (\text{A.31})$$

where the spherical particle is assumed not to rotate.

Equation (A.30) and the kinematic condition represent coupled equations for the unknowns $\mathbf{u}_1(\mathbf{x}_s \in S_{int})$ and $\mathbf{n} \cdot \mathbf{T}_1(\mathbf{x}_s \in S_{rigid})$, the rise speed of the particle \mathbf{U}_P , and the interface shape. If the particle translation velocity is specified, the force constraint is not applied. Also, following determination of the unknowns, the velocity field off the interface can be calculated. The formulation in (A.30) involves fewer unknowns than previous studies, which required solving for the actual stress distribution along the interface *e.g.*, Lee & Leal [1982], Geller et al. [1986] and Stoos & Leal [1989, 1990].

The problem formulation as an integral equation may be generalized easily to allow for an arbitrarily-shaped rigid particle by introducing an unknown particle rotation rate and imposing a torque-free constraint.

A.2.6 Generalization to multiple fluid-fluid interfaces

We now extend the discussion given in §A.2.4-5 to examine free-boundary problems involving multiple fluid-fluid interfaces. Consider the motion of a deformable drop moving normal to a deformable interface, sketched in Fig. A.4b. Numerical results for this problem are presented in §A.4.

In many previous applications of boundary integral methods to problems with multiple deformable interfaces, both the interfacial velocity and interfacial stresses remained as unknowns in the final equations, *e.g.* Stone [1990b]. However, by making full use of the integral relation defined by equation (A.18), integrals involving the *actual stress* can be replaced by integrals involving only velocities and *stress jumps* at each of the deformable interfaces, and thus we avoid solving an integral equation of the first kind for the stress.

The fluid velocities \mathbf{u}_1 , \mathbf{u}_2 and \mathbf{u}_3 (figure A.4b) can be written as integrals over all bounding surfaces using equation (A.18). Using a superscript I or II to distinguish the interfaces, the derivation presented in §A.2.5 can be generalized [*e.g.* Manga & Stone 1993; Manga et al. 1993] to show that the velocity field at any point along either of the two interfaces, S_{int}^I and S_{int}^{II} , or in either of the three fluid volumes is given concisely by

$$\begin{aligned}
& -\frac{1}{\mu} \int_{S_{int}^I} [\mathbf{n} \cdot \mathbf{T}^I] \cdot \mathbf{J} dS_y - (1 - \lambda_I) \int_{S_{int}^I} \mathbf{n} \cdot \mathbf{K} \cdot \mathbf{u}_1^I dS_y - \frac{1}{\mu} \int_{S_{int}^{II}} [\mathbf{n} \cdot \mathbf{T}^{II}] \cdot \mathbf{J} dS_y \\
& - (1 - \lambda_{II}) \int_{S_{int}^{II}} \mathbf{n} \cdot \mathbf{K} \cdot \mathbf{u}_1^{II} dS_y = \begin{cases} \mathbf{u}_1(\mathbf{x}) & \mathbf{x} \in V_1, \\ \lambda_I \mathbf{u}_2(\mathbf{x}) & \mathbf{x} \in V_2, \\ \lambda_{II} \mathbf{u}_3(\mathbf{x}) & \mathbf{x} \in V_3, \\ \frac{1 + \lambda_I}{2} \mathbf{u}_1^I(\mathbf{x}_s) & \mathbf{x}_s \in S_{int}^I, \\ \frac{1 + \lambda_{II}}{2} \mathbf{u}_1^{II}(\mathbf{x}_s) & \mathbf{x}_s \in S_{int}^{II}, \end{cases} \quad (\text{A.32})
\end{aligned}$$

where $[\mathbf{n} \cdot \mathbf{T}^I]$ and $[\mathbf{n} \cdot \mathbf{T}^{II}]$ denote the stress jumps across the two fluid-fluid interfaces. Equations (A.32d) and (A.32e) represent two coupled integral equations for the unknown interfacial velocities \mathbf{u}_1^I and \mathbf{u}_1^{II} and involve only the two stress jumps. Power (1993) has shown that a unique and continuous solution to equations (A.32d) and (A.32e) exists for viscosity ratios $0 < \lambda, \gamma < \infty$.

A.3 Numerical implementation

This section summarizes standard numerical solution procedures for treating the free-boundary problem. The discussion refers to the simplest case of deformation of a single interface (§A.2.4), but can be easily extended to multiple interfaces.

In many problems, the interface is continually deforming and the rate and degree of deformation (*e.g.*, drops breaking into smaller drops) are common topics of study. Numerical approaches for these transient problems will be addressed here; other approaches for determining steady shapes are discussed in Youngren & Acrivos [1976] and Pozrikidis [1988].

The integral equations derived in §A.2 are linear equations in the interfacial velocity $\mathbf{u}(\mathbf{x}_s)$, but are non-linear when the unknown shape is included. The interface evolves according to $d\mathbf{x}_s/dt = \mathbf{u}(\mathbf{x}_s)$. Representing the interface at N discrete points \mathbf{x}_s^i , the numerical problem is to determine the evolution of \mathbf{x}_s^i according to the system of equations

$$\frac{d\mathbf{x}_s^i(t)}{dt} = \mathbf{u}(\mathbf{x}_s^i) = \mathcal{F}\left\{\mathbf{x}_s^i, \frac{d\mathbf{x}_s^i(t)}{dt}\right\}, \quad i = 1, \dots, N \quad (\text{A.33})$$

where the non-linear functional \mathcal{F} depends on the unknown interface shape (hence involves knowledge of the surface normal and curvature) and the unknown interfacial velocity.

Almost all solutions of this problem *linearize* (A.33) by relaxing the kinematic condition so that the velocity calculation *decouples* from the determination of the unknown shape. There are three primary steps in the *iterated* solution procedure:

1. describe the deformed interface
2. calculate the surface velocity for a given shape by solving the second kind integral equation (A.23b) or (A.25b)
3. march the interface shape forward in time using the kinematic condition.

These three items are now discussed.

A.3.1 Interface description

Free-boundary problems, which involve interfacial tension, must accurately determine the position, normal and *curvature* of the interface. Thus the deforming interface shape ideally should have a twice continuously differentiable representation.

Axisymmetric or two-dimensional interface shapes have been studied extensively. In such cases it is common to represent the surface at N discrete nodal points. The position, normal, and curvature may be evaluated either directly at the nodes using a finite difference scheme, or at inter-nodal locations using interpolation. Examples of the latter use either a local interpolating function over a boundary element (piecewise polynomial interpolation, local circular arc approximation), or a global interpolation involving all nodes. Potential difficulties with highly distorted shapes, such as multi-valued representations and/or infinite derivatives, may be eliminated using an arclength parameterization scheme. A suitable method of representing the boundary must be chosen; here, the boundary shape is parametrized by the arc length parameter, s , such that on the boundary

$$H(r(s), z(s); t) = z - f(r, t) = 0. \quad (\text{A.34})$$

The unit normal vector in terms of this parametrization is given by

$$\mathbf{n} = \frac{\nabla H}{|\nabla H|}. \quad (\text{A.35})$$

The components of the normal and the divergence of the normal are evaluated by

$$n_r(s') = \frac{\dot{z}_s}{(\dot{r}_s^2 + \dot{z}_s^2)^{1/2}} \quad (\text{A.36})$$

$$n_z(s') = -\frac{\dot{r}_s}{(\dot{r}_s^2 + \dot{z}_s^2)^{1/2}} \quad (\text{A.37})$$

$$\nabla \cdot \mathbf{n}(s') = \frac{\dot{z}_s}{r_s(\dot{r}_s^2 + \dot{z}_s^2)^{1/2}} + \frac{\dot{r}_s \ddot{z}_s - \ddot{r}_s \dot{z}_s}{(\dot{r}_s^2 + \dot{z}_s^2)^{3/2}} \quad (\text{A.38})$$

with $r_s = r(s')$, $z_s = z(s')$, and the dot denoting differentiation with respect to s' .

Investigations of three-dimensional surface deformation are still in their early stages and only modest distortions have been computed, primarily in the context

of drop deformation in simple shear flow [Rallison 1981; deBruijn 1988; Kennedy et al. 1993; Pozrikidis 1994]. In chapters 3 and 5 we present calculations for buoyancy-driven drops in which large interfacial distortions occur – details of the interfacial description and numerical solution are described in Appendix C.

A.3.2 Calculation of the interfacial velocity (solution of the integral equation)

Given a description of the interface, the integral equation is reduced to a system of linear algebraic equations for the interfacial velocities $u(\mathbf{x}_s^i)$, following one of several possible numerical techniques. The most commonly used is a collocation technique, whereby the unknown velocity is typically discretized and approximated using a local polynomial interpolation, a quadrature scheme is introduced and the integral equation is enforced at the discrete points. For the two-dimensional and axisymmetric problems considered here, we assume that the unknown velocity is constant over each boundary element.

The resulting system of equations produces a dense matrix which may be solved by a direct method such as Gaussian elimination. Pozrikidis has shown that for Stokes flows iterative methods may be more efficient because a good initial guess for the value of the unknown is available from the previous time step. The potential time-savings may be important as larger and more complex problems are studied.

For problems involving multiple fluid interfaces, or problems with two or more unknown velocities, solutions to the discretized equations for the interfacial velocities must be iterated in order to solve for both velocities at each time step.

A.3.3 Interface evolution

The interface shape is updated using the kinematic condition. For example, the marker points may be marched forward using the actual surface velocity (a Lagrangian

representation),

$$\frac{d\mathbf{x}_s}{dt} = \mathbf{u}(\mathbf{x}_s). \quad (\text{A.39})$$

However, collocation points tend to be swept tangent to fluid interfaces even if only small shape changes actually occur. Consequently, frequent redistribution of points is necessary. For this case it is straightforward to implement a multi-step integrator.

Alternatively, an Eulerian view point can be taken. In practice, points on the interface are moved in a direction normal to the interface using the normal projection of the surface velocity,

$$\frac{d\mathbf{x}_s}{dt} = [\mathbf{n} \cdot \mathbf{u}(\mathbf{x}_s)] \mathbf{n}. \quad (\text{A.40})$$

with the advantage that marker points tend to remain evenly distributed. Typically, based on the numerical studies presented in this thesis, the Lagrangian approach (A.39) is best suited for buoyancy-driven motions whereas the Eulerian approach (A.40) is more successful when deformation is the result of an externally-driven flow.

A simple explicit Euler method is generally used because it is unclear how best to implement higher order integrators, although Kennedy et al. [1993] has employed a second order Runge-Kutta method to find the steady shape of drops in shear flows.

A.3.4 Miscellaneous remarks

The kernels \mathbf{J} and \mathbf{K} have integrable singularities (at $\mathbf{y} = \mathbf{x}_s$) and some care is needed in the numerical integration. Common procedures either cut out a region surrounding the singularity and perform the local integration analytically Rallison [1978] or subtract the singularity directly in the numerical approximation of the integral.

If the interface extends to infinity (*e.g.* figure A.4), a simple approximation to solve the integral equation is to truncate the interface at a finite distance and verify that the truncation distance is adequate [Lee & Leal 1982, Geller et al. 1986]. Alternatively, the interface may be extrapolated with an approximate curve, and the integration to infinity treated using an appropriate quadrature scheme [Lister 1989a].

In most studies of drop deformation, the constant volume of the drop is not imposed, but rather volume changes are used as a measure of the accuracy of the numeri-

cal method. For $\lambda = 1$, the volume changes typically are insignificant. However, most researchers report noticeable volume changes for low viscosity ratios, $\lambda < O(0.1)$, and may resort to a shape rescaling in order to continue the simulations for long times.

There have been a few preliminary attempts, *e.g.* Yiantsios & Higgins [1989] to solve (A.33) using a fully implicit (Newton) scheme. In addition, parallel processing has been applied to boundary element calculations of suspensions of rigid spheres in Stokes flows [Karrila et al. 1989].

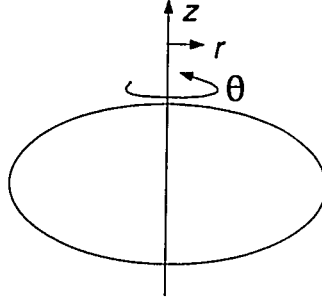
A.4 Summary

Integral equations of the second kind for the velocity along a fluid-fluid interface in low Reynolds number flows have been discussed. The development is extended in a straightforward manner to problems with multiple interfaces. In all cases, only the interfacial velocities and stress jumps across fluid-fluid interfaces, and the stress distributions and velocities along rigid surfaces, appear as unknowns.

Appendix B

Axisymmetric problems

If the problem being considered is axis-symmetric, the azimuthal integration of the kernels **J** and **K**, integration over θ from 0 to 2π ,



can be performed analytically by expanding the kernels (A.13) and (A.14) in polar coordinates and integrating term by term:

$$\mathbf{B}(\mathbf{x} - \mathbf{y}) = \int_0^{2\pi} \left(\frac{\mathbf{I}}{|\mathbf{x} - \mathbf{y}|} + \frac{(\mathbf{x} - \mathbf{y})(\mathbf{x} - \mathbf{y})}{|\mathbf{x} - \mathbf{y}|^3} \right) d\theta \quad (\text{B.1})$$

and

$$\mathbf{A}(\mathbf{x} - \mathbf{y}) = - \int_0^{2\pi} \frac{(\mathbf{x} - \mathbf{y})(\mathbf{x} - \mathbf{y})(\mathbf{x} - \mathbf{y})}{|\mathbf{x} - \mathbf{y}|^5} d\theta. \quad (\text{B.2})$$

with components

$$\begin{aligned} A_{rr} = & -E^{35}n_r r^2 r_s + E^{25}[n_r r^3 + 2n_r r_s^2 r - n_z r_s r(z - z_s)] + \\ & E^{15}[n_z r_s^2(z - z_s) + n_z r^2(z - z_s) - 2n_r r_s r^2 - n_r r_s^3] + \\ & E^{05}[n_r r_s^2 r - n_z r_s r(z - z_s)] \end{aligned} \quad (\text{B.3})$$

$$A_{rz} = -E^{25}n_r r_s r(z - z_s) + E^{15}[n_r(r^2 + r_s^2)(z - z_s) - (z - z_s)^2 r_s n_z] - E^{05}[n_r r r_s(z - z_s) - n_z r(z - z_s)^2] \quad (\text{B.4})$$

$$A_{zr} = E^{25}n_r r^2(z - z_s) + E^{15}[n_z r(z - z_s)^2 - 2n_r r r_s(z - z_s)] + E^{05}[n_r r_s^2(z - z_s) - n_z(z - z_s)^2 r_s] \quad (\text{B.5})$$

$$A_{zz} = E^{15}n_r(z - z_s)^2 r + E^{05}[n_z(z - z_s)^3 - n_r r_s(z - z_s)^2] \quad (\text{B.6})$$

$$B_{rr} = E^{11} + E^{13}(r_s^2 + r^2) - E^{23}r_s r - E^{03}r_s r \quad (\text{B.7})$$

$$B_{rz} = E^{03}r(z - z_s) - E^{13}r_s(z - z_s) \quad (\text{B.8})$$

$$B_{zr} = E^{13}r(z - z_s) - E^{03}r_s(z - z_s) \quad (\text{B.9})$$

$$B_{zz} = E^{01} + E^{03}(z - z_s)^2 \quad (\text{B.10})$$

where $\mathbf{x} = (r, z)$ is the point at which the function is desired and hence, is a fixed point with respect to the integration, and $\mathbf{y} = (r_s = r(s'), z_s = z(s'))$ is the coordinate of the integration variable. The functions E^{01} , E^{03} , E^{05} , E^{11} , E^{13} , E^{15} , E^{23} , E^{25} and E^{35} are complete elliptic integrals defined in Lee and Leal [1982] and have the form

$$E^{nm} = \int_0^{2\pi} \frac{\cos^n \theta}{(A^2 - B^2 \cos \theta)^{m/2}} d\theta \quad (\text{B.11})$$

with

$$A^2 = (z - z_s)^2 + r^2 + r_s^2 \quad (\text{B.12})$$

$$B^2 = 2rr_s. \quad (\text{B.13})$$

The elliptic integrals E^{nm} are evaluated using a polynomial approximation [Abramowitz & Stegun 1972, pages 591-592].

Appendix C

Three-dimensional problems

Many free-boundary problems of interest, for example the deformation of a drop in a shear flow, are fully three-dimensional. It is common to approximate many three-dimensional problems with two-dimensional or axisymmetric geometries which greatly reduces numerical computation time. A number of studies have considered three-dimensional problems using the boundary integral approach. Rallison [1978], deBruijn [1989], Kennedy et al. [1994] and Pozrikidis [1994] all considered the deformation of a neutrally buoyant drop in a shear flow while Pozrikidis & Thoroddsen [1991] considered the deformation of the free-surface of a thin film flowing above a planar boundary containing an imbedded particle.

Several numerical difficulties arise when considering three-dimensional free-boundary problems:

1. for finite Bond numbers and capillary numbers the interfacial curvature must be calculated which involves calculating second derivatives of the interface shape which thus requires accurate numerical description of the interface shape,
2. computational time is significant
3. all previous three-dimensional studies has been limited to modest interfacial distortions.

Below we describe details of the numerical procedures employed in this thesis to study

three-dimensional problems. The calculations presented in chapters 3 and 5 are the first three-dimensional boundary integral calculations for buoyancy-driven drops (at low Reynolds numbers) and the first to consider multiple fluid-fluid interfaces.

C.1 Numerical solution of the integral equations

The integral equations are solved numerically using a collocation approach. The surface normal, local curvature, and the stress jump (1.10) are assumed to vary linearly over each surface element. For $\lambda = 1$ (as defined in figures 1.1 and 1.2), the velocity can be determined by a direct integration. An Euler time step is used to update the interface shape – once the interfacial velocities are calculated the position of the interface is advected with the local velocity field.

C.1.1 Numerical mesh

Fluid-fluid interfaces are represented numerically by a grid of $2N \times M$ triangular surface elements and the interfacial velocities are calculated on a grid of $n \times m$ collocation points, where $n < N$ and $m < M$ (see figure C.1). In effect, two separate numerical meshes are employed: a high resolution mesh to describe the surface and perform integration (composed of 3200 triangular elements in the simulations presented in this thesis), and a second mesh at which velocities are calculated (consisting of 382 collocation points). The use of two meshes was found to be the most computationally efficient method to achieve a given accuracy. Interfacial velocities are interpolated linearly between collocation points.

Since the initial interface shapes are always spheres, we distribute collocation points along lines of latitude and longitude. Thus, the concentration of collocation points is greater near the poles. During the evolution of the interface shape the collocation points are redistributed since they tend to accumulate near stagnation points.

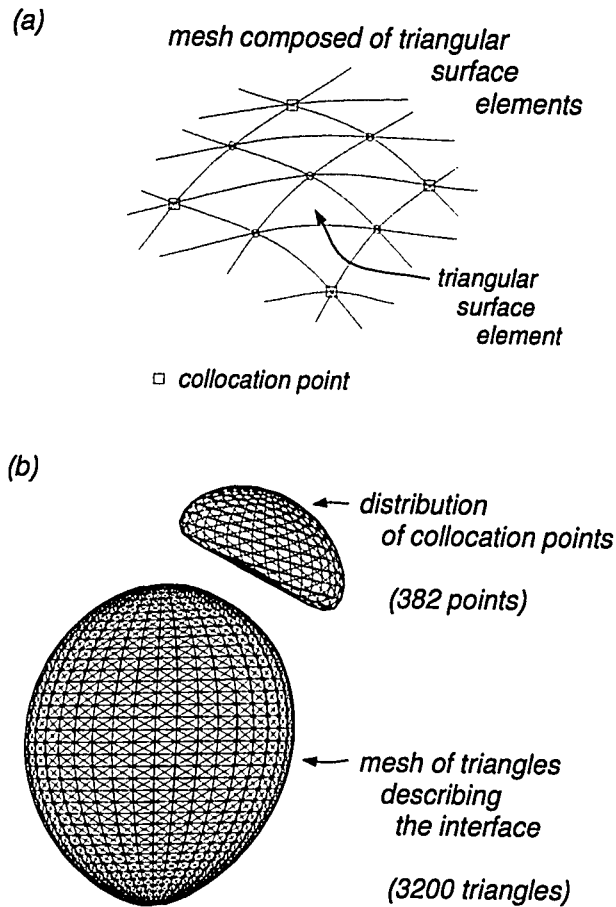
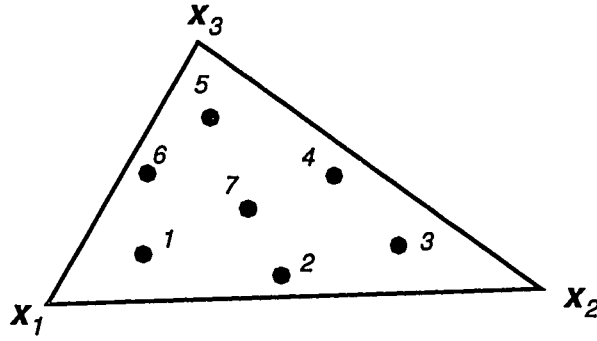


Figure C.1: (a) The interface shape is described by a mesh of triangles, with vertices shown by open circles. Collocation points at which interfacial velocities are evaluated describe a coarser mesh, shown with open squares. Interfacial velocities are interpolated between collocation points. (b) Example of the numerical mesh used to perform the three-dimensional boundary integral calculations for the two drop problem. The surface consists of 382 collocation points (vertices of the triangles in top drop) and 3200 triangular surface elements (bottom drop). The mesh shown is from a typical two drop calculation after 250 time steps, in which the large drop has translated more than 7 drop radii and the small drop has translated more than 10 drop radii. Notice that the collocation points (top drop) and triangular surface elements (bottom drop) remain well-distributed (we redistribute collocation points and triangles every 3 time steps) even after large translation distances.

Table C.1: Gaussian weights and abscissas for 7-point integration

Point (see figure)	Barycentric coordinate			Weights w
	λ_1	λ_2	λ_3	
1	0.79743	0.10129	0.10129	0.12592
2	0.47014	0.47014	0.05971	0.13238
3	0.10129	0.79743	0.10129	0.12592
4	0.05971	0.47014	0.47014	0.13238
5	0.10129	0.10129	0.79743	0.12592
6	0.47014	0.05971	0.47014	0.13238
7	0.33333	0.33333	0.33333	0.22500



C.1.2 Integration method

Numerical integration is performed using 7-point Gaussian integration,

$$\int_{S=\text{triangle}} f(\mathbf{x}) dS \approx \sum_{i=1}^7 w_i f(\mathbf{x}_i) \quad (\text{C.1})$$

where w_i are Gaussian weights, and

$$\mathbf{x}_i = \lambda_1 \mathbf{x}_1 + \lambda_2 \mathbf{x}_2 + \lambda_3 \mathbf{x}_3. \quad (\text{C.2})$$

where \mathbf{x}_i are the corners of the triangles, λ_i are abscissas, see table C.1. The 7-point integration used here is accurate to $O(h^6)$. For comparison a 1-point method is accurate to $O(h^2)$, Rallison [1981] and deBruijn [1989] use a trapezoidal rule accurate to $O(h^3)$ and the 7-point method used by Kennedy et al. [1993] is accurate to $O(h^4)$

[Abramowitz & Stegun 1972]. Since the Green's functions or Kernels for Stokes flow (A.11 and A.12) are singular, triangular surface elements containing a singularity are integrated analytically using expressions given by Rallison [1981] for the **J** kernel and deBruijn [1989] for the **K** kernel (assuming linear elements).

For a spherical drop, interfacial velocities differ by less than 0.15% from the Hadamard-Rybczyński result. In figure C.2, we present a test of the numerical procedures employed in the simulations by comparing cross-sections through interface shapes at different time for an axisymmetric calculation and a three-dimensional calculation for the same initial condition. The volume of the drops in the three-dimensional simulation decreased by 1.5 %. No volume rescaling was implemented for the simulations presented in figure C.2, though as mentioned earlier, drop sizes were rescaled for simulations presented in chapters 3 and 5.

C.1.3 Calculating curvature and normal vectors

We have considered two different approaches to calculate the surface normal and evaluate the local curvature.

(a) Quadratic surface representation

In the first method, suitable for problems in which interfacial tension stresses limit drop shapes to small distortions, $\mathcal{B} \approx 1$, we describe the interface *locally* by a quadratic

$$ax^2 + by^2 + cz^2 + dxy + eyz + fzx + gx + hy + iz = Q = \text{constant}. \quad (\text{C.3})$$

Nine surface points are used to determine the 9 coefficients ($a-i$) in the local quadratic expression (figure C.3a). The surface normal is then given by $\mathbf{n} = \nabla Q / |\nabla Q|$ and the curvature can be found by calculating $\nabla_s \cdot \mathbf{n}$. deBruijn [1989] employed a similar approach, however, because of the symmetry of the problem considered (a drop in a shear flow) only 6 unknowns described the quadratic surface.

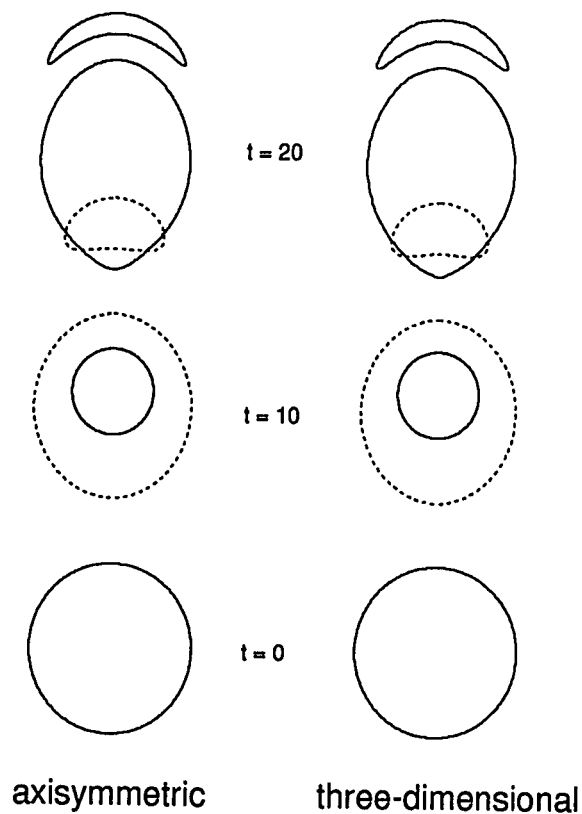


Figure C.2: Interaction and deformation of two vertically aligned drops for $\mathcal{B} = \infty$; $\lambda = 1$. Interface shapes from an axisymmetric calculation are shown on the left and cross-sections through the fully three-dimensional calculation are shown on the right. In the three-dimensional calculations, velocities are calculated at 382 collocation points and the interface is described by a mesh with 3200 surface elements.

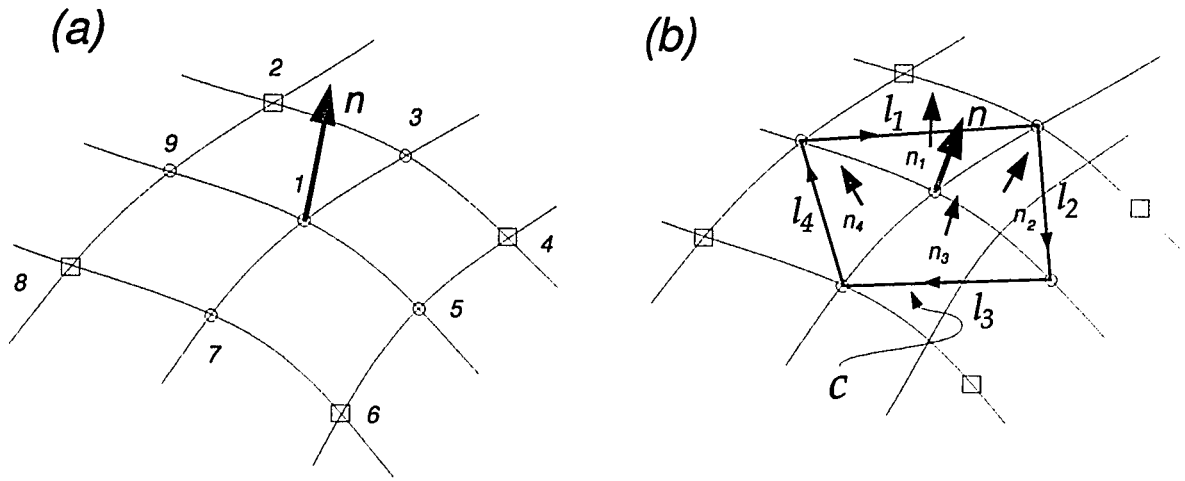


Figure C.3: (a) The normal and curvature at point 1 is calculated by fitting the points 1–9 with a local quadratic function, $Q = f(x, y, z)$, so that $\mathbf{n} = \nabla Q / |\nabla Q|$. (b) Calculating interfacial tension stresses by contour integration. The unit normal vectors to the four triangular surfaces \mathbf{n}_i surrounding the point of interest are calculated and then averaged to calculate \mathbf{n} . The interfacial tension stresses are then calculated by integrating the unit tangent vector $\mathbf{t} = \mathbf{l} \wedge \mathbf{n}$ times the interfacial tension around the closed contour C composed of the segments $l_1 + l_2 + l_3 + l_4$ [Pozrikidis 1994].

(b) Contour integration

For problems in which interfacial tension is negligible or significant interface distortion occurs we estimate the normal at all vertices of the triangular surface elements by averaging the normals to all the triangular surface elements adjacent to the vertex. The interfacial tension stresses can then be evaluated by performing a contour integral around the point of interest [following Pozrikidis 1994]

$$\int_C \sigma \mathbf{t} dl = \int_S \nabla_s \sigma dS - \int_S \sigma \mathbf{n} (\nabla_s \cdot \mathbf{n}) dS \quad (\text{C.4})$$

where $\mathbf{t} = \mathbf{l} \wedge \mathbf{n}$ is a unit vector tangent to the surface S which is perpendicular to the counterclockwise contour C (see figure C.3b). The contour integration is performed

Table C.2: Comparison of our numerical results with previous results for the steady deformed drop shape in a shear flow for $\lambda = 1$. Deformation is characterized by the parameter $D = (L - M)/(L + M)$ where L and M are the largest and smallest distances from the center of the drop to the drop surface. Results are presented for Capillary numbers $C = \mu Ga/\sigma = 0.1, 0.2$ and 0.3 , where G is the shear rate.

C	Kennedy et al. [1994]	DeBruijn [1989]	Quadratic surface	Contour integration
	D	D	§C.1.3a D	§C.1.3b D
0.1	0.11	0.11	0.11	0.11
0.2	0.24	0.21	0.22	0.23
0.3	0.35	0.32	0.33	0.35

using a trapezoidal rule. The curvature could be calculated to machine precision for a spheres and to within 2 % for ellipsoids with aspect ratios 3:1. Typically this second approach to calculating the curvature underestimates the curvature in regions of high curvature due largely to approximation of describing the surface with linear elements. Quadratic surface elements might improve the calculation of the local curvature.

We note that the second method of calculating interfacial tension stresses, the contour integration approach, is a much more powerful method since interfacial tension variations which lead to stresses characterized by the first integral on the right-hand side of (C.4) are more readily included.

(c) Tests

In figure C.4 we calculate the time-dependent relaxation of a prolate ellipsoid (aspect ratio 3:1). Cross-sections of axisymmetric calculations are shown with solid curves and a cross-sections through the three-dimensional calculations are shown with

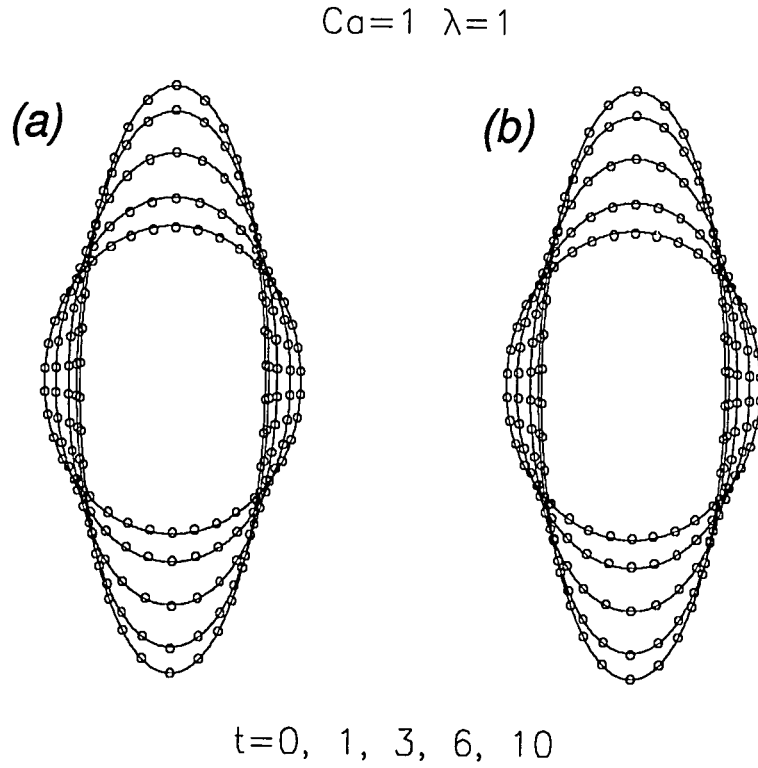


Figure C.4: Relaxation of an initially prolate ellipsoid (aspect ratio 3:1) for $C = 1$; (a) the interface is described locally by a quadratic, see §C.1.3a, and (b) the curvature is calculated from equation (C.4), see §C.1.3b. Interface shapes are shown at times $t = 0, 1, 3, 6$ and 10 . The axisymmetric calculated shapes are shown with solid curves and collocation points from a cross-section through a fully three-dimensional calculation are shown with open circles. The three-dimensional interface has 382 collocation points and the surface is discretized into 3200 surface elements.

open circles denoting positions of the collocation points. In the simulation presented in figure C.4a the interface is described locally by a quadratic, §C.1.3a, and in the simulation presented in figure C.4b the curvature is calculated from equation (C.4), §C.1.3b. The aspect ratio of the three-dimensional drops differs from the axisymmetric drops by less than 0.5% at all times during the simulations.

We also performed an additional test of the numerical routines by comparing calculated results for the steady deformed shape of a drop in a shear flow with previously determined results [deBruijn 1989; Kennedy et al. 1994]. Results are summarized in table C.2 Deformation is characterized by the parameter $D = (L - M)/(L + M)$ where L and M are the largest and smallest distances from the center of the drop to the drop surface. The magnitude of deformation D is characterized by the Capillary number

$$\mathcal{C} = \frac{\mu G a}{\sigma} \quad (\text{C.5})$$

where G is a shear rate defined so that the external flow is described by $\mathbf{u} = (Gz, 0, 0)$. The capillary number represents the ratio of external viscous forces to interfacial tension forces. Results in table C.2 are presented for $\mathcal{C} = 0.1, 0.2$ and 0.3 . Both methods of calculating interfacial curvature yield results in reasonable agreement with previous calculations.

Appendix D

The reciprocal theorem applied to the translation of nonspherical drops

Below we apply standard domain perturbation techniques to formulate a boundary-value problem for the translation of a slightly deformed drop (magnitude of distortion $\epsilon \ll 1$) with viscosity $\lambda\mu$ and density $\rho + \Delta\rho$ in an ambient fluid with density ρ and viscosity μ . We then derive an expression for the rise speed of the deformed drop using the Lorentz reciprocal theorem [Lorentz 1896 as cited in Leal 1992] without solving for the detailed flow in the drop and surrounding fluid. The Reciprocal theorem relates two Stokes flow boundary value problems in the same fluid domain with different boundary conditions.

D.1 Perturbation solution for the translation of a non-spherical drop

The dimensionless Stokes flow boundary value problem for the deformed drop with radius

$$r = 1 + \epsilon f(\theta, \phi)$$

has the form

$$\begin{aligned} \nabla \cdot \mathbf{T} &= 0 & r > 1 + \epsilon f(\theta, \phi) & \quad \nabla \cdot \hat{\mathbf{T}} = 0 & r < 1 + \epsilon f(\theta, \phi) \\ \nabla \cdot \mathbf{u} &= 0 & & \quad \nabla \cdot \hat{\mathbf{u}} = 0 \end{aligned} \quad (\text{D.1})$$

with boundary conditions

$$\mathbf{u} - \hat{\mathbf{u}} = 0 \quad \text{on } S \quad (\text{D.2})$$

$$\mathbf{u} \cdot \mathbf{n} = \mathbf{U} \cdot \mathbf{n} \quad \text{on } S \quad (\text{D.3})$$

$$\mathbf{n} \cdot \mathbf{T} - \lambda \mathbf{n} \cdot \hat{\mathbf{T}} = \frac{3(2+3\lambda)}{2\mathcal{B}(1+\lambda)} \mathbf{n} \nabla_s \cdot \mathbf{n} + \frac{3(2+3\lambda)}{2(1+\lambda)} \hat{\mathbf{g}} \cdot \mathbf{x} \mathbf{n} \quad \text{on } S \quad (\text{D.4})$$

where S is the deformed drop shape, and \mathbf{U} is the steady translational velocity of the drop, and $\hat{\mathbf{g}}$ is unit vector in the direction of the gravitational acceleration. Velocities are normalized by the Hadamard-Rybczyński velocity $U^{(0)}$ given by equation (4.2). Lengths are normalized by the drop radius a , and the stress and pressure are normalized by $\mu U/a$ and $\lambda \mu U/a$ outside and inside the drop, respectively. The normal and the curvature for nearly spherical surfaces, may be expanded as

$$\mathbf{n} = \mathbf{n}_o - \epsilon \nabla_e f + O(\epsilon^2) \quad (\text{D.5})$$

and

$$\nabla_s \cdot \mathbf{n} = 2 - \epsilon [\nabla_e^2 f + 2f] + O(\epsilon^2) \quad (\text{D.6})$$

where \mathbf{n}_o is a unit normal to the spherical surface and $\nabla_e = (\mathbf{I} - \mathbf{n}\mathbf{n}) \cdot \nabla$ is the surface gradient operator measuring variations along the spherical surface. The shape function $f(\theta, \phi)$ in spherical polar coordinates (defined in figure 4.1 and calculated in §4.3) has the form

$$f(r=1) = \frac{(2+3\lambda)(16+19\lambda)}{48(1+\lambda)^2} \cos \beta (1 - 3 \cos^2 \theta). \quad (\text{D.7})$$

It follows that

$$\nabla_e f(r=1) = \frac{(2+3\lambda)(16+19\lambda)}{8(1+\lambda)^2} \cos \beta \cos \theta \sin \theta \mathbf{e}_\theta \quad (\text{D.8})$$

where \mathbf{e}_θ is a unit vector in the θ direction, and

$$\nabla_e^2 f(r=1) = \frac{(2+3\lambda)(16+19\lambda)}{8(1+\lambda)^2} \cos \beta (3 \cos^2 \theta - 1). \quad (\text{D.9})$$

To use the Reciprocal theorem we need to apply the boundary conditions (D.2-D.4) on a spherical surface. First, expand \mathbf{u} in a Taylor series in the neighbourhood of a spherical surface

$$\begin{aligned} \mathbf{u}(r = 1 + \epsilon f) &= \mathbf{u}|_{r=1} + \epsilon f \frac{\partial \mathbf{u}}{\partial r}|_{r=1} + \frac{1}{2}(\epsilon f)^2 \frac{\partial^2 \mathbf{u}}{\partial r^2}|_{r=1} \\ &= \mathbf{u}^{(0)}|_{r=1} + \mathcal{B} \left(\frac{a}{d} \right)^2 \left[\mathbf{u}^{(2)} + f \frac{\partial \mathbf{u}^{(0)}}{\partial r} \right]_{r=1} + \dots \end{aligned} \quad (\text{D.10})$$

The continuity of velocity boundary condition (D.2) for the $O(\epsilon)$ terms leads to

$$\mathbf{u}^{(2)} - \hat{\mathbf{u}}^{(2)} = -f \left[\frac{\partial \mathbf{u}^{(0)}}{\partial r} - \frac{\partial \hat{\mathbf{u}}^{(0)}}{\partial r} \right] \quad (\text{D.11})$$

$$= f \frac{3(\lambda - 1)\mathbf{U}^{(0)}}{2(1 + \lambda)} \cdot [\mathbf{I} - \mathbf{n}_o \mathbf{n}_o] \text{ at } r = 1. \quad (\text{D.12})$$

The $O(\epsilon)$ contribution to the normal velocity boundary condition (D.3) gives

$$\mathbf{u}^{(2)} \cdot \mathbf{n}_o = \mathbf{u}^{(0)} \cdot \nabla_e f - f \mathbf{n}_o \cdot \frac{\partial \mathbf{u}^{(0)}}{\partial r} - \mathbf{U}^{(0)} \cdot \nabla_e f + \mathbf{U}^{(2)} \cdot \mathbf{n}_o \quad (\text{D.13})$$

$$= f \frac{\mathbf{U}^{(0)} \cdot \mathbf{n}_o}{1 + \lambda} - \frac{\mathbf{U}^{(0)} \cdot \nabla_e f}{2(1 + \lambda)} + \mathbf{U}^{(2)} \cdot \mathbf{n}_o \text{ at } r = 1. \quad (\text{D.14})$$

Similarly, we expand the stress in a Taylor series

$$\begin{aligned} \mathbf{T}(r = 1 + \epsilon f) &= \mathbf{T}|_{r=1} + \epsilon f \frac{\partial \mathbf{T}}{\partial r}|_{r=1} + \frac{1}{2}(\epsilon f)^2 \frac{\partial^2 \mathbf{T}}{\partial r^2}|_{r=1} + \dots \\ &= \mathbf{T}^{(0)}|_{r=1} + \mathcal{B} \left(\frac{a}{d} \right)^2 \left[\mathbf{T}^{(2)} + f \frac{\partial \mathbf{T}^{(0)}}{\partial r} \right]_{r=1} + \dots \end{aligned} \quad (\text{D.15})$$

On the spherical surface, the $O(\epsilon)$ stress boundary condition (D.4) becomes

$$\begin{aligned} \mathbf{n}_o \cdot \mathbf{T}^{(2)} - \lambda \mathbf{n}_o \cdot \hat{\mathbf{T}}^{(2)} &= -f \frac{\partial}{\partial r} [\mathbf{n}_o \cdot \mathbf{T}^{(0)} - \lambda \mathbf{n}_o \cdot \hat{\mathbf{T}}^{(0)}] + \nabla_e f \cdot (\mathbf{T}^{(0)} - \lambda \hat{\mathbf{T}}^{(0)}) \\ &\quad - \frac{3(2 + 3\lambda)}{2\mathcal{B}(1 + \lambda)} [2\nabla_e f + \mathbf{n}_o (\nabla_e^2 f + 2f)] \\ &\quad + \frac{3(2 + 3\lambda)}{2(1 + \lambda)} [f(\hat{\mathbf{g}} \cdot \mathbf{n}_o)\mathbf{n}_o - (\mathbf{g} \cdot \mathbf{n}_o)\nabla_e f] \end{aligned} \quad (\text{D.16})$$

$$\begin{aligned} &= -f \frac{3\mathbf{U}^{(0)}}{2(1 + \lambda)} \cdot (5\lambda\mathbf{I} + (4 - 9\lambda)\mathbf{n}_o \mathbf{n}_o) - 15 \frac{\mathbf{U}^{(0)} \cdot \mathbf{n}_o}{2(1 + \lambda)} \nabla_e f \\ &\quad - \frac{3(2 + 3\lambda)}{2\mathcal{B}(1 + \lambda)} \mathbf{n}_o [\nabla_e^2 f + 2\mathbf{n}_o f] \\ &\quad + \frac{3(2 + 3\lambda)}{2(1 + \lambda)} [f(\hat{\mathbf{g}} \cdot \mathbf{n}_o)\mathbf{n}_o - (\mathbf{g} \cdot \mathbf{n}_o)\nabla_e f] \text{ at } r = 1. \end{aligned} \quad (\text{D.17})$$

The boundary value problem for $\mathbf{u}^{(2)}$ may now be set up for a spherical geometry

$$\begin{aligned}\nabla \cdot \mathbf{T}^{(2)} &= 0 & r > 1 & \quad \nabla \cdot \hat{\mathbf{T}}^{(2)} = 0 & r < 1 \\ \nabla \cdot \mathbf{u}^{(2)} &= 0 & & \quad \nabla \cdot \hat{\mathbf{u}}^{(2)} = 0\end{aligned}\tag{D.18}$$

$$\mathbf{u}^{(2)} - \hat{\mathbf{u}}^{(2)} = \mathbf{A}(\mathbf{n}_o, f) \text{ on } r = 1\tag{D.19}$$

$$\mathbf{u}^{(2)} \cdot \mathbf{n}_o = B(\mathbf{n}_o, f) + \mathbf{U}^{(2)} \cdot \mathbf{n}_o \text{ on } r = 1\tag{D.20}$$

$$\mathbf{n}_o \cdot \mathbf{T}^{(2)} - \lambda \mathbf{n}_o \cdot \hat{\mathbf{T}}^{(2)} = C(\mathbf{n}_o, f) \text{ on } r = 1\tag{D.21}$$

where the vector and scalar functions \mathbf{A} , C and B are given in equations (D.12), (D.17) and (D.14). \mathbf{A} , C and B are functions of position defined on a spherical surface S involving the Hadamard-Rybczyński velocity field and the first approximation to the drop shape $f(\theta, \phi)$. Using the Reciprocal theorem, as outlined in Haj-Hariri et al. [1990], we can determine the second order correction to the rise speed of the deformed drop $\mathbf{U}^{(2)}$ without solving for the detailed flow field $\mathbf{u}^{(2)}(\mathbf{x})$.

D.2 Application of the Reciprocal theorem

Consider the complementary flow problem for a spherical drop translating with velocity \mathbf{U}^* , made dimensionless as in §D.1:

$$\begin{aligned}\nabla \cdot \mathbf{T}^* &= 0 & r > 1 & \quad \nabla \cdot \hat{\mathbf{T}}^* = 0 & r < 1 \\ \nabla \cdot \mathbf{u}^* &= 0 & & \quad \nabla \cdot \hat{\mathbf{u}}^* = 0\end{aligned}\tag{D.22}$$

$$\mathbf{u}^* - \hat{\mathbf{u}}^* = 0 \text{ on } r = 1\tag{D.23}$$

$$\mathbf{u}^* \cdot \mathbf{n}_o = \hat{\mathbf{u}}^* \cdot \mathbf{n}_o = \mathbf{U}^* \cdot \mathbf{n}_o \text{ on } r = 1\tag{D.24}$$

$$\mathbf{t} \cdot [\mathbf{n}_o \cdot \mathbf{T}^* - \lambda \mathbf{n}_o \cdot \hat{\mathbf{T}}^*] = 0 \text{ on } r = 1.\tag{D.25}$$

Here \mathbf{t} is a unit vector tangent to the spherical surface S .

For Stokes flows, we make use of the identities

$$\nabla \cdot (\mathbf{T}^* \cdot \mathbf{u}^{(2)}) = \nabla \cdot (\mathbf{T}^{(2)} \cdot \mathbf{u}^*) \quad \text{and} \quad \nabla \cdot (\hat{\mathbf{T}}^* \cdot \hat{\mathbf{u}}^{(2)}) = \nabla \cdot (\hat{\mathbf{T}}^{(2)} \cdot \hat{\mathbf{u}}^*) \quad (\text{D.26})$$

and the divergence theorem to derive the pair of integral relations

$$\int_S \mathbf{n}_o \cdot \mathbf{T}^{(2)} \cdot \mathbf{u}^* dS = \int_S \mathbf{n}_o \cdot \mathbf{T}^* \cdot \mathbf{u}^{(2)} dS \quad (\text{D.27})$$

$$\int_S \mathbf{n}_o \cdot \hat{\mathbf{T}}^{(2)} \cdot \hat{\mathbf{u}}^* dS = \int_S \mathbf{n}_o \cdot \hat{\mathbf{T}}^* \cdot \hat{\mathbf{u}}^{(2)} dS \quad (\text{D.28})$$

where integrals over bounding surfaces at large distances vanish owing to the sufficiently rapid decay of the integrands. Subtracting λ times (D.28) from (D.27) gives

$$\int_S [\mathbf{n}_o \cdot \mathbf{T}^{(2)} - \lambda \mathbf{n}_o \cdot \hat{\mathbf{T}}^{(2)}] \cdot \mathbf{u}^* dS = \int_S [\mathbf{n}_o \cdot \mathbf{T}^* \cdot \mathbf{u}^{(2)} - \lambda \mathbf{n}_o \cdot \hat{\mathbf{T}}^* \cdot \hat{\mathbf{u}}^{(2)}] dS \quad (\text{D.29})$$

where we have made use of boundary condition (D.23), $\mathbf{u}^* = \hat{\mathbf{u}}^*$ on S .

The solution to the complementary problem (D.22-D.25) for \mathbf{u}^* , \mathbf{T}^* , $\hat{\mathbf{u}}^*$ and $\hat{\mathbf{T}}^*$ is straightforward, and is given by

$$\mathbf{u}^*(\mathbf{r}) = \frac{\lambda}{4(1+\lambda)} \left[\frac{\mathbf{U}^*}{r^3} - 3 \frac{\mathbf{U}^* \cdot \mathbf{r} \mathbf{r}}{r^5} \right] + \frac{2+3\lambda}{4(1+\lambda)} \left[\frac{\mathbf{U}^*}{r} + \frac{\mathbf{U}^* \cdot \mathbf{r} \mathbf{r}}{r^3} \right] \quad (\text{D.30})$$

$$\hat{\mathbf{u}}^*(\mathbf{r}) = \frac{3+2\lambda}{2(1+\lambda)} \mathbf{U}^* - \frac{1}{2(1+\lambda)} [2r^2 \mathbf{U}^* - \mathbf{U}^* \cdot \mathbf{r} \mathbf{r}] \quad (\text{D.31})$$

$$\mathbf{T}^*(\mathbf{r}) = -p_\infty \mathbf{I} - \frac{\lambda}{2(1+\lambda)} \left[3 \frac{\mathbf{U}^* \mathbf{r} + \mathbf{r} \mathbf{U}^* + \mathbf{r} \cdot \mathbf{U}^* \mathbf{I}}{r^5} - 15 \frac{\mathbf{U}^* \cdot \mathbf{r} \mathbf{r} \mathbf{r}}{r^7} \right] - \frac{3(2+3\lambda)}{2(1+\lambda)} \frac{\mathbf{U}^* \cdot \mathbf{r} \mathbf{r} \mathbf{r}}{r^5} \quad (\text{D.32})$$

$$\hat{\mathbf{T}}^*(\mathbf{r}) = -\lambda p_o \mathbf{I} + \frac{1}{2(1+\lambda)} [12 \mathbf{U}^* \cdot \mathbf{r} \mathbf{I} - 3(\mathbf{U}^* \mathbf{r} + \mathbf{r} \mathbf{U}^*)] \quad (\text{D.33})$$

Here p_o and p_∞ are constant pressures inside and outside the drop, respectively.

Thus, for the second order velocity correction we arrive at

$$\mathbf{U}^{(2)} = -\frac{1}{4\pi(2+3\lambda)} \int_S \{ [(1+2\lambda)\mathbf{I} + \mathbf{n}_o \mathbf{n}_o] \cdot \mathbf{C}(\mathbf{n}_o, f) + 3\lambda [\mathbf{I} - 3\mathbf{n}_o \mathbf{n}_o] \cdot \mathbf{A}(\mathbf{n}_o, f) + 3(2+3\lambda) B(\mathbf{n}_o, f) \mathbf{n}_o \} dS. \quad (\text{D.34})$$

The detailed equations presented here differ slightly from those in Haj-Hariri et al. [1990] because of a different choice of reference frame.

Appendix E

The effect of radial and lateral viscosity variations near the Earth's surface on the surface expression of mantle flow

Below we consider briefly the effect of radial and lateral viscosity variations near the Earth's surface, representing for example a lithosphere with a variable thickness, on the stresses and dynamic topography produced by buoyancy-driven flow in the mantle.

E.1 Radial viscosity variations

We begin by investigating the effects of radial viscosity variations on the surface topography induced above an upwelling. The model consists of a buoyant spherical volume a fluid with viscosity μ and density $\rho - \Delta\rho$ beneath a surface layer with viscosity $\gamma\mu$ overlying an infinite half-space mantle with viscosity μ , figure E.1. The surface layer and the mantle both have density ρ . All regions are assumed to be Newtonian fluids. If the amplitude of the surface deflection is small, then the surface

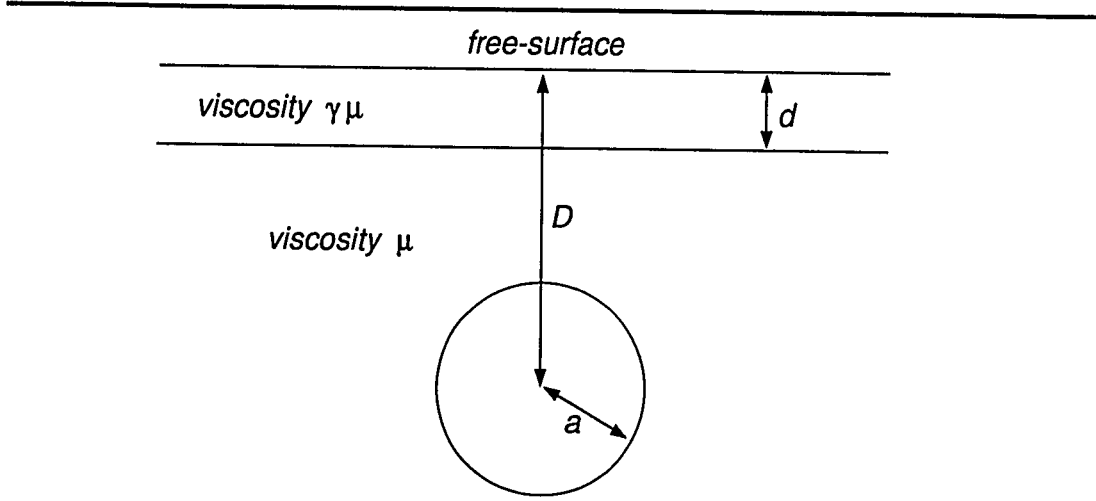


Figure E.1: Geometry of the model used to study radial viscosity variations. The lithosphere (viscosity $\gamma\mu$ and density ρ), underlying mantle (viscosity μ and density ρ), and source of buoyancy (sphere of radius a and density $\rho - \Delta\rho$) are Newtonian fluids.

topography $d(\mathbf{x})$ is found by calculating the normal deviatoric stress and pressure on the surface,

$$d(\mathbf{x}) = [p(\mathbf{x}) + \sigma_{zz}(\mathbf{x})]/\rho g \quad (\text{E.1})$$

where $p(\mathbf{x})$ is the pressure on the surface, $\sigma_{zz}(\mathbf{x}) = 2\mu\partial u_z/\partial z$ is the vertical deviatoric stress and ρ is the density of the mantle.

As previously demonstrated by Morgan [1965] for a two-dimensional geometry, as the viscosity of the surface layer increases the amplitude of the induced topography increases and the wavelength of the topography decreases, figure E.2. The change in amplitude as the viscosity ratio is varied is much larger for an axisymmetric geometry than for a two-dimensional geometry.

We also show in figure E.3 the geoid-topography ratio (maximum geoid divided by maximum topography). As the viscosity ratio decreases (the surface layer becomes less viscous), the geoid-topography ratio decreases. Thus, a low-viscosity layer reduces the magnitude of two geophysical surface observables: (i) dynamic topography (figure

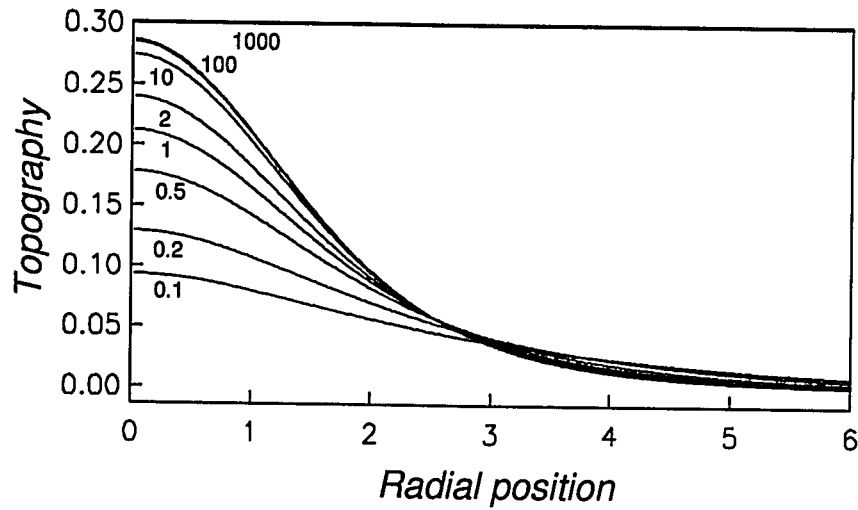


Figure E.2: The steady-state axisymmetric surface topography produced by a sphere of buoyant fluid at a depth $h = 3a$ beneath a surface layer with constant thickness $d = a$ and viscosity ratio γ . The value of γ is labeled on the curves. Surface topography is normalized by $a\Delta\rho/\rho$ and radial position is normalized by the sphere radius a . As the surface layer becomes more viscous, the wavelength of the topography decreases and the amplitude increases.

E.2) and (ii) the geoid-topography ratio (figure E.3). Low geoid-topography ratios may be indicative of the presence of a low-viscosity zone between the Earth's surface and the source of buoyancy. Geoid-topography ratios over oceanic swells are often low, and are interpreted as indications of a low-viscosity zone in the upper mantle [McNutt & Judge 1990]. By contrast, geoid-topography ratios on Venus are very large (geoid-topography ratios on the earth range from -6 to 12 m/km whereas geoid-topography ratios range from 0 to 35 m/km on Venus [Simons et al. 1993]); thus, Venus is inferred to lack a low-viscosity zone and deformation of the lithosphere is thought to be strongly coupled to the convecting mantle [*e.g.* Kiefer et al. 1986]. Since the geoid-topography ratio changes very little for viscosity ratios greater than about 1, the geoid-topography ratio may not be a useful indicator of the presence of high viscosity layers.

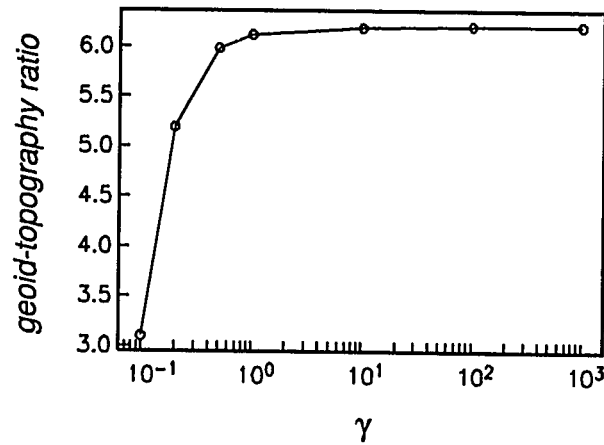


Figure E.3: The steady-state geoid-topography ratio, normalized by $\rho Ga/g$.

E.2 Lateral viscosity variations: Variations of lithosphere thickness

In this section we consider one geometrical example of a problem in which lateral viscosity variations might be expected to arise and demonstrate the potential importance of allowing for lateral viscosity variations in numerical convection calculations. Previous numerical studies, *e.g.* Tackley [1993], have demonstrated the importance of temperature-dependent and stress-dependent viscosity on the wavelength and structure of convective patterns. Forte & Peltier [1994] have demonstrated that long wavelength lateral viscosity variations have only a small effect on dynamic topography and the geoid but do have strong effects on the buoyancy-induced flow field. Here we focus on lateral viscosity variations expected to arise due to variations of lithospheric thickness.

Lateral viscosity variations near the Earth's surface are likely to occur near plate boundaries due to large lateral temperature variations, or may be associated with ocean-continent differences observed seismically in the upper mantle (see §9.4). In a series of two papers, Sabadini and coworkers have investigated some of the consequences of lateral viscosity variations on surface observables using a finite-element

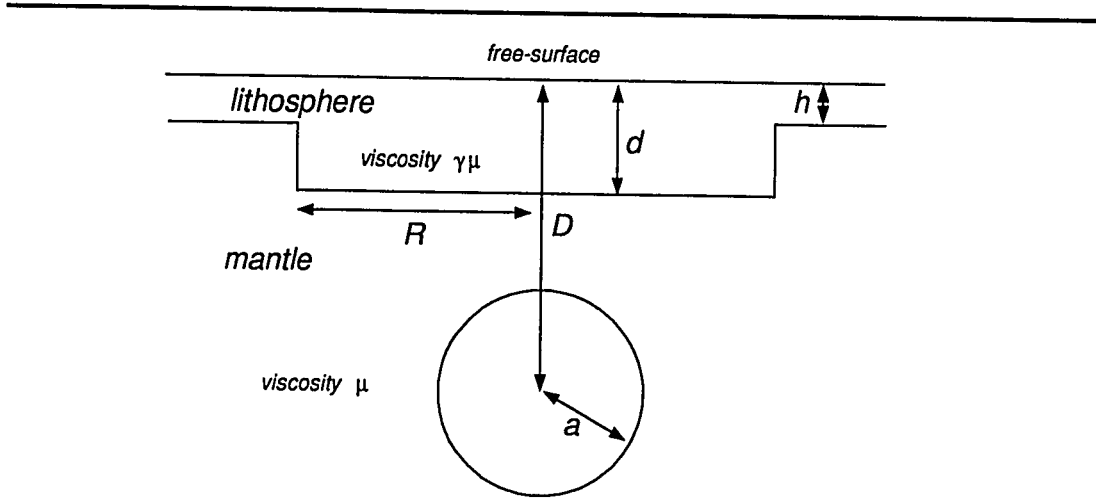


Figure E.4: Geometry of the model used to study variations of lithosphere thickness. The lithosphere (viscosity $\gamma\mu$ and density ρ), underlying mantle (viscosity μ and density ρ), and source of buoyancy (sphere of radius a , viscosity μ and density $\rho - \Delta\rho$) are Newtonian fluids.

model. Lateral viscosity variations are treated numerically as lateral variations of the thickness of the lithosphere, and the surface expression of westward mantle flows [Sabadini et al. 1992], and post-glacial rebound [Gasperini et al. 1990] is calculated.

Here we consider another geometry which might arise in the Earth – an upwelling or downwelling beneath a continent, figure E.4. The lithosphere and mantle are assumed to be a Newtonian fluids with a viscosities $\gamma\mu$ and μ , respectively. Mantle flow is created by a spherical source of buoyancy.

In figure E.5a we present calculated surface topography from equation (E.1) for three models in which the variations of lithospheric thickness are characterized by $h/d = 1, 0.5$ and 0.2 ; $\gamma = 100$, $d/a = 1$, $R/a = 2$ and $D/a = 3$. The interfaces in figure E.4 are described by 300 collocation points so that short wavelength features are well-resolved numerically. In figure E.5b we present deviatoric surface stresses corresponding to the results presented in E.5a. The three deviatoric stresses shown are the vertical stress, $\sigma_{zz} = 2\mu\partial u_z/\partial z$, the radial stress, $\sigma_{rr} = 2\mu\partial u_r/\partial r$, and the

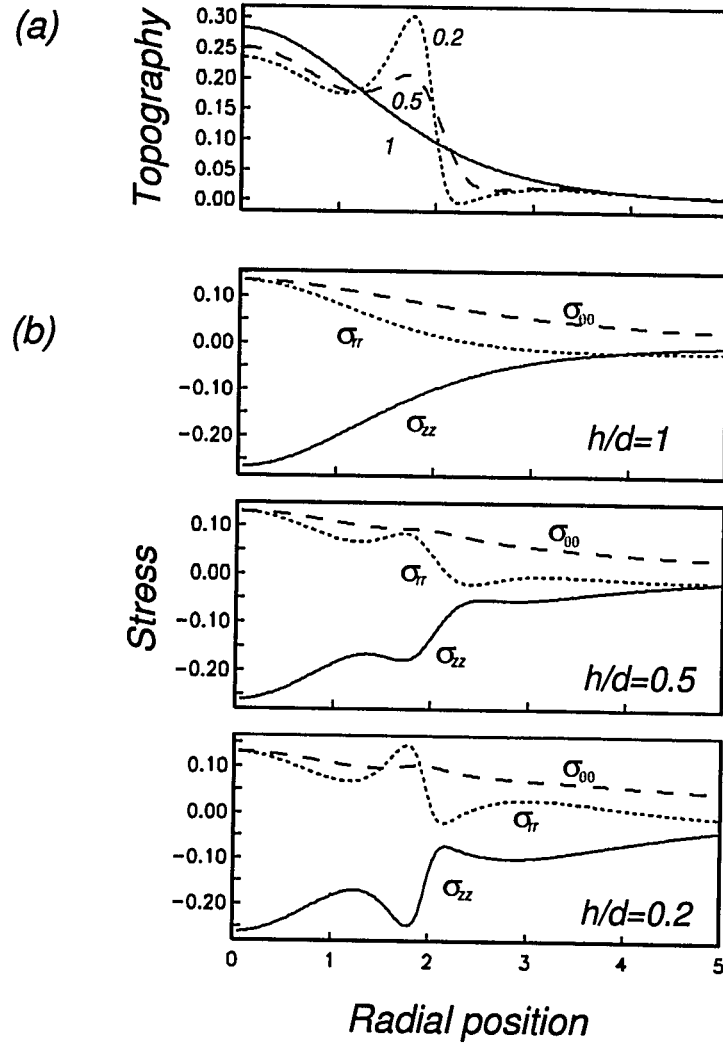


Figure E.5: (a) The steady-state axisymmetric surface topography produced by a sphere (radius a) of buoyant fluid at a depth $D = 3a$ beneath a surface layer with thickness variations $h/d = 1, 0.5$ and 0.2 ; $\gamma = 100$, $d/a = 1$, $R/a = 2$ and $D/a = 3$. Topography is normalized by $a\Delta\rho/\rho$. Radial position is normalized by the sphere radius a . (b) Surface stresses (vertical stress σ_{zz} , radial stress σ_{rr} and hoop stress $\sigma_{\theta\theta}$) produced by a buoyant sphere beneath a surface layer with thickness variations $h/d = 1, 0.5$ and 0.2 corresponding to the results presented in (a). Stresses normalized by $ag\Delta\rho$.

hoop stress $\sigma_{\theta\theta} = 2\mu u_r/r$.

Large variations of lithospheric thickness, for example $h/d = 0.2$, result in topography with a large amplitude and short wavelength above the region where the lithosphere changes thickness. The pattern of deviatoric stresses also changes: for a uniform thickness lithosphere the hoop stress is always the largest stress whereas for $h/d = 0.2$ the radial stress is larger than the hoop stress where the lithosphere changes thickness (and would result in concentric extension rather than radial extension). Since the equations of motion describing flow in a fluid with spatially varying viscosity contain terms which depend on the gradient of viscosity, it is not surprising that surface observables have the largest gradients near regions with lithospheric thickness variations (which may be parameterized as effective viscosity variations).

The geometry and properties of the model described in figure E.4 might be representative of ocean-continent boundaries. The results presented in figure E.5 suggest that the effects of the lateral variations of lithospheric thickness would be concentrated near the ocean-continent boundary. The effects of lateral viscosity variations will have affect the interpretation of sea-level changes due to postglacial rebound which are used to infer the viscosity structure of the mantle and the history of glacial loading [*e.g.* Tushingham & Peltier 1991]. Sea-level changes due to global warming are determined by subtracting postglacial rebound predictions of a spherically symmetric Earth model from observed sea-level changes [*e.g.* Peltier & Tushingham 1989]; lateral variations of the viscosity and structure of the lithosphere will have a significant affect of postglacial rebound rates and thus affect the inferred sea-level change due to global warming [Sabadini & Gasperini 1989; Gasperini et al. 1990].

Bibliography

- Abramowitz, M. & Stegun, I.A. 1972 *Handbook of mathematical functions*. Dover.
- Acrivos, A. 1983 The breakup of small drops and bubbles in shear flows. *4th Int Conf. on physico-chemical hydrodynamics, Ann. N.Y. Acad. Sci.* **404**, 1-11.
- Atkinson, K. 1976 *A survey of numerical methods for the solution of Fredholm integral equations of the second kind*. Soc. for Industrial and Applied Mathematics.
- Ascoli, E.P. & Leal, L.G. 1990 Thermocapillary motion of a deformable drop toward a planar wall. *J. Colloid Interface Sci.* **138**, 220-238.
- Ascoli, E.P., Dandy, D.S. & Leal, L.G. 1990 Buoyancy-driven motion of a deformable drop toward a planar wall at low Reynolds number. *J. Fluid Mech.* **213**, 287-314.
- Aubele, J.C., Crumpler, L.S. & Elston, W.E. 1988 Vesicle zonation and vertical structure of basalt flows. *J. Volc. Geotherm. Res.* **35**, 349-374.
- Austrheim, H. 1991 Eclogite formation and dynamics of crustal roots under continental collision zones. *Terra Nova* **3**, 492-499.
- Baker, G.R., Meiron, D.I. & Orszag, S.A. 1984 Boundary integral methods for axisymmetric and three-dimensional Rayleigh-Taylor instability problems. *Physica* **12D**, 19-31.
- Barnocky, G. & Davis, R. H. 1989 The lubrication force between spherical drops, bubbles and rigid particles in a viscous fluid. *Int. J. Multiphase Flow* **15**, 627-638.
- Batchelor, G.K. 1967 *An introduction to fluid dynamics*, Cambridge University Press.
- Batchelor, G.K. 1970 Slender-body theory for particles of arbitrary cross-section in Stokes flow. *J. Fluid Mech.* **44**, 419-440.
- Batchelor, G.K. 1972 Sedimentation in a dilute dispersion of spheres. *J. Fluid Mech.* **52**, 245-268.
- Bellieni, G., Brotzu, P., Comin-Chiaramonti, P., Ernesto, M., Melfi, A.J., Pacca, I.G. & Piccirillo, E.M. 1984 Flood basalt to rhyolite suites in the southern Parana Plateau (Brazil): Paleomagnetism, petrogenesis and geodynamic implications. *J. Petrol.* **25**, 579-618.
- Bindschadler, D.L. & Parmentier, E.M. 1990 Mantle flow tectonics: The influence of a ductile lower crust and implications for the formation of topographic uplands on Venus. *J. Geophys. Res.* **95**, 21329-21344.
- Bindschadler, D.L., Schubert, G. & Kaula, W.M. 1992 Coldspots and hotspots: Global tectonics and mantle dynamics of Venus. *J. Geophys. Res.* **97**, 13495-13532.
- Blackburn, E.A., Wilson, L. and Sparks, R.S.J. 1976 Mechanisms and dynamics of Strombolian activity. *J. Geol. Soc. Lond.* **132**, 429-440.
- Bott, M.H.P. & Kusznir, N.J. 1979 Stress distributions associated with compensated plateau uplift structures with application to the continental splitting mechanism. *Geophys. J. R. astr. Soc.* **56**, 451-459.
- Blake, J.R. 1971 A note on the image system for a stokeslet in a no-slip boundary. *Proc. Camb. Phil. Soc.* **70**, 303-310.
- Borhan, A. & Mao, C.-F. 1992 Effect of surfactants on the motion of drops through circular tubes. *Phys. Fluids A* **4**, 2628-2640.
- Bottinga, Y. and Weill, D.F. 1972 The viscosity of magmatic silicate liquids: A model for calculation. *Am. J. Sci.* **272**, 438-475.
- Campbell, I.H. & R.W. Griffiths 1992 The changing nature of mantle hotspots through time: Implications for the chemical evolution of the mantle. *J. Geology* **92**, 497-523.

- Chi, B.K. & Leal, L. G. 1989 A theoretical study of the motion of a viscous drop toward a fluid interface at low Reynolds number. *J. Fluid Mech.* **201**, 123-146.
- Courtillot, V., Feraud, G., Maluski, H., Vandamme, D., Moreau, M.G. & Besse, J. 1988 Deccan flood basalts and the Cretaceous/Tertiary boundary. *Nature* **333**, 843-846.
- Cox, R.G. 1970 The motion of long slender bodies in a viscous fluid. Part 1. General theory. *J. Fluid Mech.* **44**, 791-810.
- Crough, S.T. 1983 Hotspot swells. *Annu. Rev. Earth Planet. Sci.* **11**, 169-193.
- Dandy, D.S. 1987 *Intermediate Reynolds number free-surface flows*. PhD thesis, California Institute of Technology, Pasadena, Calif.
- Davies, G.F. & Gurnis, M. 1986 Interaction of mantle dregs with convection: Lateral heterogeneity at the core-mantle boundary. *Geophys. Res. Lett.* **13**, 1517-1520.
- Davis, A.M.J. 1983 Force and torque formulae for a sphere moving in an axisymmetric Stokes flow with finite boundaries: Axisymmetric stokeslets near a hole in a plane wall. *Int. J. Multiphase Flow* **9**, 575-608.
- Davis, R.H. 1984 The rate of coagulation of a dilute polydisperse system of sedimenting spheres. *J. Fluid. Mech.* **145**, 179-199.
- Davis, R. H., Schonberg, J. A. & Rallison, J. M. 1989 The lubrication force between two viscous drops. *Phys. Fluids A* **1**, 77-81.
- deBoor, C. 1978 *A practical guide to splines*, Springer-Verlag.
- deBruijn, R.A. 1989 *Deformation and breakup of drops in simple shear flows*, PhD thesis, Technical University at Eindhoven.
- de Nevers, N. and Wu, J.-L. 1971 Bubble coalescence in viscous fluids. *AIChE J.* **17**, 182-186.
- Delves, L. & Mohamed, J. 1985 *Computational methods for integral equations*. Cambridge University Press.
- Duncan, R.A. & Pyle, D.G. 1988 Rapid eruption of the Deccan flood basalts at the Cretaceous/Tertiary boundary. *Nature* **333**, 841-843.
- Durlofsky, L., Brady, J.F. & Bossis, G. 1987 Dynamic simulation of hydrodynamically interacting particles. *J. Fluid Mech.* **180**, 21-49.
- Einstein, A. 1956 *Investigations on the theory of Brownian motion*. Dover.
- Fordham, S. 1948 On the calculation of surface tension from measurements of pendant drops. *Proc. Roy. Soc. Lond. A* **194**, 1-16.
- Forte, A.M. & Peltier, W.R. 1994 The kinematics and dynamics of poloidal-toroidal coupling in mantle flow: The importance of surface plates and lateral viscosity variations. *Adv. Geophys.*, in press.
- Forte, A.M., Peltier, W.R., Dziewonski, A.M. & Woodward, R.L. 1993 Dynamic surface topography: A new interpretation based upon mantle flow models derived from seismic tomography. *Geophys. Res. Lett.* **20**, 225-228.
- Friedlander, S.K. 1977 *Smoke, dust and haze: Fundamentals of aerosol behavior*. John Wiley & Sons, New York.
- Gable, C.W. & R.J. O'Connell, R.J. 1991 Tomography, the geoid and plate motions, *Rev. Geophys.* **29**, 776-782.
- Gasperini, P., Yuen, D.A. and Sabadini, R. 1990 Effects of lateral viscosity variations on postglacial rebound: Implications for recent sea-level trends. *Geophys. Res. Lett.* **17**, 5-8.
- Geller, A.S., Lee, S.H. & Leal, L.G. 1986 The creeping motion of a spherical particle normal to a deformable interface. *J. Fluid Mech.* **169**, 27-69.
- Gerlach, T.M. and Graeber, E.J. 1985 Volatile budget of Kilauea volcano. *Nature* **313**, 273-277.
- Goff, F.E. 1977. *Vesicle cylinders in vapor-differentiated basalt flows*. PhD thesis, University of California, Santa Cruz.
- Greenland, L.P., Rose, W.J. and Stokes, J.B. 1985 An estimate of gas emissions and magmatic gas content from Kilauea volcano. *Geochim. Cosmochim. Acta* **49**, 125-129.
- Griffiths, R.W. 1986 Particle motions induced by spherical convective elements in Stokes flow, *J. Fluid Mech.* **166**, 139-159.
- Griffiths, R.W. & Campbell, I.H. 1990 Stirring and structure in mantle starting plumes, *Earth*

- Planet. Sci. Lett.* **99**, 66-78.
- Griffiths, R.W. & Campbell, I.H. 1991 Interaction of mantle plume heads with the Earth's surface and the onset of small-scale convection. *J. Geophys. Res.* **96**, 18295-18310.
- Griffiths, R.W., Gurnis, M. & Eitelberg, G. 1989 Holographic measurements of surface topography in laboratory models of mantle hotspots. *Geophys. J.* **96**, 477-495.
- Haber, S., Hetsroni, G. & Solan, A. 1973 Low Reynolds number motion of two drops submerged in an unbounded arbitrary velocity field. *Int. J. Multiphase Flow* **4**, 627-638.
- Hager, B.H. & Clayton, R.W. 1989 Constraints on the structure of mantle convection using seismic observations, flow models and the geoid. In *Mantle convection*, edited by W.R. Peltier, pp. 657-763, Gordon and Breach, New York.
- Haj-Hariri, H., Nadim, A. & Borhan, A. 1990 Effect of inertia on the thermocapillary velocity of a drop. *J. Colloid and Int. Sci.* **140**, 277-286.
- Hansen, U. & Yuen, D.A. 1989 Dynamical influences from thermal-chemical instabilities at the core-mantle boundary. *Geophys. Res. Lett.* **16**, 629-632.
- Hansen, U., Yuen, D.A. & Kroening, S.E. 1990 Transition to hard turbulence in thermal convection at infinite Prandtl number. *Phys. Fluids A* **2**, 2157-2163.
- Happel, J. & Brenner, H. 1965 *Low Reynolds number hydrodynamics*, Prentice-Hall.
- Hartland, S. 1969 The profile of a draining film between a rigid sphere and a deformable fluid-liquid interface. *Chem. Engng Sci.* **24**, 987.
- Hasimoto, H., Kim, M.U. & Miyazaki, T. 1983 The effect of a semi-infinite plane on the motion of a small particle in a viscous fluid. *J. Phys. Soc. Japan* **52**, 1996-2003.
- Head, J.W. and Wilson, L. 1987 Lava fountain heights at Pu'u 'O'o, Kilauea, Hawaii: Indicators of amount and variations of exsolved magma volatiles. *J. Geophys. Res.* **92**, 13715-13719.
- Herd, R.A. and Pinkerton, H. 1993 Bubble coalescence in magmas (abstract). *LPSC XXIV*, 641-642.
- Herrick, R.R. & Phillips, R.J. 1990 Blob tectonics: A prediction for western Aphrodite Terra, Venus. *Geophys. Res. Lett.* **17**, 2129-2132.
- Higdon, J.J.L. 1985 Stokes flow in arbitrary two-dimensional domains: Shear flow over ridges and cavities. *J. Fluid Mech.* **159**, 195-226.
- Hildreth, W. 1981 Gradients in silicic magma chambers: Implications for lithospheric magmatism. *J. Geophys. Res.* **86**, 10153-10192.
- Hill, R.I. 1991 Starting plumes and continental breakup. *Earth Planet. Sci. Lett.* **104**, 398-417.
- Hinch, E. J. 1988 Sedimentation of small particles. In *Disorder and mixing* edited by Guyon, J. P. Nadal & Y. Pomeau, NATO ASI Series, Ser. E, **152**, 153-161.
- Hinch, E. J. 1977 An averaged-equation approach to particle interactions in a fluid suspension. *J. Fluid Mech.* **83**, 695-720.
- Hiram, Y. & Nir, A. 1983 A simulation of surface tension driven coalescence. *J. Colloid Interface Sci.* **95**, 462-470.
- Hocking, L.M. 1964 The behaviour of clusters of spheres falling in a viscous fluid. Part 2. Slow motion theory. *J. Fluid Mech.* **20**, 129-139.
- Hoffman, A.W. & White, W.M. 1982 Mantle plumes from ancient oceanic crust. *Earth Planet. Sci. Lett.* **57**, 421-436.
- Honda, R., Mizutani, H. & Yamamoto, T. 1993 Numerical simulations of Earth's core formation. *J. Geophys. Res.* **98**, 2075-2089.
- Hooper, P.R. 1982 The Columbia River basalts. *Science* **215**, 1463-1466.
- Hooper, P.R. 1990 The timing of crustal extension and the eruption of continental flood basalts. *Nature* **345**, 246-249.
- Houseman, G. & England, P. 1986 A dynamical model of lithosphere extension and sedimentary basin formation. *J. Geophys. Res.* **91**, 719-729.
- Janes, D.M., Squyres, S.W., Bindscadler, D.L., Baer, G., Schubert, G., Sharpton, V.L. & Stofan, E.R. 1992 Geophysical models for the formation and evolution of coronae on Venus. *J. Geophys. Res.* **97**, 16055-16068.
- Jansons, K.M. & Lister, J.R. 1988 The general solution of Stokes flow in a half-space as an integral of the velocity on the boundary. *Phys. Fluids* **31**, 1321-1323.

- Jaswon, M.A. & Symm, G.T. 1977 *Integral equation methods in potential theory and elastostatics*. Academic Press.
- Jaupart, C. and Vergnolle, S. 1988 Laboratory models of Hawaiian and Strombolian eruptions. *Nature* **331**, 58-60.
- Jaupart, C. & Vergnolle, S. 1989 The generation and collapse of a foam layer at the roof of a basaltic magma chamber. *J. Fluid Mech* **203**, 347-380.
- Jeong, J.-T. & Moffatt, H. K. 1992 Free-surface cusps associated with flow at low Reynolds number. *J. Fluid Mech.* **241**, 1-22.
- Jordan, T.H. 1975 The continental tectosphere. *Rev. Geophys. Space Phys.* **13**, 1-12.
- Jordan, T.H. 1978 Composition and development of the continental tectosphere. *Nature* **274**, 544-548.
- Jordan, T.H. 1979 Mineralogies, densities and seismic velocities of garnet Lherzolites and their geophysical implications. In *The mantle sample: Inclusions in Kimberlite and other volcanics*, edited by Boyd, F.R. & Meyer, H.O.A., American Geophysical Union, 1-14.
- Joseph, D. D., Nelson, J., Renardy, M., Renardy & Y. 1991 Two-dimensional cusped interfaces. *J. Fluid Mech.* **223**, 383-409.
- Karrila, S.J. & Kim, S. 1989 Integral equations of the second kind for Stokes flow: Direct solution for physical variables and removal of inherent accuracy limitations. *Chem. Eng. Comm.* **82**, 123-161.
- Karrila, S.J., Fuentes, Y.O. & Kim, S. 1989 Parallel computational strategies for hydrodynamic interactions between rigid particles of arbitrary shape in a viscous fluid. *J. Rheology* **33**, 913-947.
- Kellogg, L.H. 1991 Interactions of plumes with a compositional boundary at 670 km. *Geophys. Res. Lett.* **18**, 865-868.
- Kelmanson, M.A. 1983 Boundary integral equation solution of viscous flows with free surfaces. *J. Eng. Math.* **17**, 329-343.
- Kennedy, M.R., Pozrikidis, C. & Skalak, R. 1994 Motion and deformation of liquid drops, and the rheology of dilute emulsions in simple shear flow. *Computers Fluids* **23**, 251-278.
- Khayat, R.E. & Cox, R.G. 1989 Inertia effects on the motion of long slender bodies. *J. Fluid Mech.* **209**, 435-462.
- Kiefer, W.S. & Hager, B.H. 1991 A mantle plume model for the equatorial highlands of Venus. *J. Geophys. Res.* **96**, 20947-20966.
- Kiefer, W.S. & Hager, B.H. 1992 Geoid anomalies and dynamic topography from convection in cylindrical geometry: Applications to mantle plumes on Earth and Venus. *Geophys. J.* **108**, 198-214.
- Kiefer, W.S., Richards, M.A., Hager, B.H. & Bills, B.G. 1986 A dynamic model of Venus' gravity field. *Geophys. Res. Lett.* **13**, 14-17.
- Kim, S. & Karrila, S.J. 1991 *Microhydrodynamics: Principles and selected applications*, Butterworth-Heinemann Series in Chemical Engineering.
- Knittle, E. & Jeanloz, R. 1989 Simulating the core-mantle boundary: An experimental study of high-pressure reactions between silicates and liquid iron. *Geophys. Res. Lett.* **16**, 609-612.
- Koch, D.L. & Shaqfeh, E.S.G. 1989 The instability of a dispersion of sedimenting spheroids. *J. Fluid Mech* **209**, 521-542.
- Koch, D.M. 1993 *A spreading drop model for mantle plumes and volcanic features on Venus*. PhD Thesis, Yale University, New Haven, Conn.
- Koch, D.M. 1994 A spreading drop model for plumes on Venus. *J. Geophys. Res.* **99**, 2035-2052.
- Koch, D.M. & Ribe, N.M. 1989 The effect of lateral viscosity variations on surface observables. *Geophys. Res. Lett.* **16**, 535-538.
- Koh, C.J. & Leal, L. G. 1989 The stability of drop shapes for translation at zero Reynolds number through a quiescent fluid. *Phys. Fluids A* **1**, 1309-1313.
- Koh, C.J. & Leal, L.G. 1990 An experimental investigation on the stability of viscous drops translating through a quiescent fluid, *Phys. Fluids A* **2**, 2103-2109.
- Kojima, M., Hinch, E. J. & Acrivos, A. 1984 The formation and expansion of a toroidal drop moving

- in a viscous fluid. *Phys. Fluids* **27**, 19-32.
- Ladyzhenskaya, O.A. 1963 *The mathematical theory of viscous incompressible flow*. Gordon and Breach.
- Larson, R.L. & Olson, P. 1991 Mantle plumes control magnetic reversal frequency. *Earth Planet. Sci. Lett.* **107**, 437-447.
- Lay, T., & Helmberger, D.V. 1983 A lower mantle *S* wave triplication and the shear velocity structure of D". *Geophys. J. Roy. Astron. Soc.* **75**, 799-838.
- Leal, L.G. 1992 *Laminar flow and convective transport processes*, Butterworth-Heinemann Series in Chemical Engineering.
- Lee, S.H. & Leal, L. G. 1982 The motion of a sphere in the presence of a deformable interface. II. A numerical study of the translation of a sphere normal to an interface. *J. Colloid Interface Sci.* **87**, 81-106.
- Lee, S.H. & Leal, L.G. 1986 Low-Reynolds number flow past cylindrical bodies of arbitrary cross-sectional shape. *J. Fluid Mech.* **164**, 401-427.
- Lenardic, A., Kaula, W.M. & Bindschadler 1993 A mechanism for crustal recycling on Venus. *J. Geophys. Res.* **98**, 18697-18705.
- Lorentz, H.A. 1896 A general theorem concerning the motion of a viscous fluid and a few consequences derived from it (translated title). *Versl. Kon. Akad. Wetensch. Amsterdam* **5**, 168-174.
- Li, X.Z., Barthes-Biesel, D. & Helmy, A. 1988 Large deformations and burst of a capsule freely suspended in an elongational flow. *J. Fluid Mech.* **187**, 179-196.
- Liron, N. & Mochon, S. 1976 Stokes flow for a Stokeslet between two parallel flat plates. *J. Eng. Math.* **10**, 287-303.
- Liron, N. & Shahar, R. 1978 Stokes flow due to a Stokeslet in a pipe. *J. Fluid Mech.* **86**, 727-744.
- Lister, J.R. 1989 Selective withdrawal from a viscous two-layer system. *J. Fluid Mech.* **198**, 231-254.
- Lister, J.R. & Kerr, R.C. 1989 The propagation of two-dimensional and axisymmetric viscous gravity currents at a fluid interface. *J. Fluid Mech.* **203**, 215-249.
- Liu, M., Yuen, D.A., Zhao, W. & Honda, S. 1991 Development of diapiric structures in the upper mantle due to phase transitions. *Science* **252**, 1836-1839.
- Loper, D.E. & Stacey, F.D. 1983 The dynamic and thermal structure of deep mantle plumes. *Phys. Earth Planet. Inter.* **33**, 304-317.
- Lundgren, T.S. & Mansour, N.N. 1988 Oscillations of drops in zero gravity with weak viscous effects. *J. Fluid Mech.* **194**, 479-510.
- Manga, M. & Stone, H.A. 1994 Interactions between bubbles in magmas and lavas: Effects of deformation. *J. Volc. Geotherm. Res., in press*.
- Manga, M. & Stone, H.A. 1993a Buoyancy-driven interactions between deformable drops at low Reynolds numbers. *J. Fluid Mech.* **256**, 647-683.
- Manga, M. & Stone, H.A. 1993b Interactions between bubbles at low Reynolds numbers, *Phys. Fluids A* **5**, *Gallery of Fluid Motions*, S3.
- Manga, M., Stone, H.A. & O'Connell, R. J. 1993 The interaction of plume heads with compositional discontinuities in the Earth's mantle. *J. Geophys. Res.* **98**, 19979-19990.
- Mangan, M.T., Cashman, K.V. & Newman, S. 1993. Vesiculation of basaltic magma during eruption. *Geology* **21**, 157-160.
- Martinez, M.J. & Udell, K.S. 1989 Boundary integral analysis of the creeping flow of long bubbles in capillaries. *J. Appl. Mech.* **56**, 211-217.
- Martinez, M.J. & Udell, K.S. 1990 Axisymmetric creeping motion of drops through circular tubes. *J. Fluid Mech.* **210**, 565-591.
- McKenzie, D. & O'Nions, R.K. 1983 Mantle reservoirs and ocean island basalts. *Nature* **301**, 229-231.
- McMillan, K., Cross, R.W. & Long, P.E. 1987 Two-stage vesiculation in the Cohasset flow of the Grande Ronde Basalt, south-central Washington. *Geology* **15**, 809-812.
- McNutt, M.K. & Judge, A.V. 1990 The superswell and mantle dynamics beneath the South Pacific. *Science* **248**, 969-975.
- Milliken, W.J., Stone, H.A. & Leal, L.G. 1993 The effect of surfactant on the transient motion of

- Newtonian drops. *Phys. Fluids A* **5**, 69-79.
- Miyazaki, T. & Hasimoto, H. 1984 The motion of a small sphere in fluid near a circular pore in a plane wall. *J. Fluid Mech.* **145**, 201-221.
- Molnar, P., England, P. & Martinod, J. 1993 Mantle dynamics, uplift of the Tibetan plateau, and the Indian monsoon. *Rev. Geophysics* **31**, 357-396.
- Morgan, W.J. 1965 Gravity anomalies and convection currents. 1. A sphere and cylinder sinking beneath the surface of a viscous fluid. *J. Geophys. Res.* **70**, 6175-6187.
- Morgan, W.J. 1971 Convective plumes in the lower mantle. *Nature* **230**, 42-43.
- Newhouse, L.A. & Pozrikidis, C. 1990 The Rayleigh-Taylor instability of a viscous liquid layer resting on a plane wall. *J. Fluid Mech.* **217**, 615-638.
- Newhouse, L.A. & Pozrikidis, C. 1992 The capillary instability of annular layers and liquid threads. *J. Fluid Mech.*, in press.
- Nir, A. 1989 Deformation of some biological particles. *Phys. Fluids A* **1**, 101-107.
- Oguz, H.N. & Prosperetti, A. 1990 Bubble entrainment by the impact of drops on liquid surfaces. *J. Fluid Mech.* **219**, 143-179.
- Olson, P. & Kincaid, K. 1991 Experiments on the interaction of thermal convection and compositional layering at the base of the mantle. *J. Geophys. Res.* **96**, 4347-4354.
- Olson, P. & Nam, I.S. 1986 Formation of seafloor swells by mantle plumes. *J. Geophys. Res.* **91**, 7181-7191.
- Olson, P. & Singer, H. 1985 Creeping plumes, *J. Fluid Mech.* **158**, 511-531.
- Olson, P., Schubert, G. & Anderson, C. 1987 Plume formation in the D" layer of the core-mantle boundary. *Nature* **327**, 409-412.
- Olson, P., Schubert, G., Anderson, C. & Goldman, P. 1988 Plume formation and lithosphere erosion: A comparison of laboratory and numerical experiments. *J. Geophys. Res.* **93**, 15065-15084.
- Peltier, W.R. & Tushingham, A.M. 1989 Global sea level rise and the greenhouse effect: Might they be connected? *Science* **244**, 806-810.
- Philpotts, A.R. & Lewis, C.L. 1987 Pipe vesicles - An alternate model for their origin. *Geology* **15**, 971-974.
- Power, H. 1987 On the Rallison and Acrivos solution for the deformation and burst of a viscous drop in an extensional flow. *J. Fluid Mech.* **185**, 547-550.
- Power, H. & Miranda, G. 1987 Second kind integral equation formulation of Stokes' flows past a particle of arbitrary shape. *SIAM J. Appl. Math.* **47**, 689-698.
- Power, H. 1993 Low Reynolds number deformation of compound drops in shear flow. *Math. Methods App. Sci.* **16**, 61-74.
- Pozrikidis, C. 1987a Creeping flow in two-dimensional channels. *J. Fluid Mech.* **180**, 495-514.
- Pozrikidis, C. 1987b A study of peristaltic flow. *J. Fluid Mech.*, **180**, 515-527.
- Pozrikidis, C. 1988 The flow of a liquid film along a periodic wall. *J. Fluid Mech.* **188**, 275-300.
- Pozrikidis, C. 1989 A study of linearized oscillatory flow past particles by the boundary-integral method. *J. Fluid Mech.* **202**, 17-41.
- Pozrikidis, C. 1990a The instability of a moving viscous drop. *J. Fluid Mech.* **210**, 1-21.
- Pozrikidis, C. 1990b The deformation of a liquid drop moving normal to a plane wall. *J. Fluid Mech.* **215**, 331-363.
- Pozrikidis, C. 1990c The axisymmetric deformation of a red blood cell in a uniaxial straining Stokes flow. *J. Fluid Mech.* **216**, 231-254.
- Pozrikidis, C. 1992a The buoyancy-driven motion of a train of viscous drops within a cylindrical tube. *J. Fluid Mech.* **237**, 627-648.
- Pozrikidis, C. 1992b *Boundary integral and singularity methods for linearized viscous flow*, Cambridge University Press.
- Pozrikidis, C. 1993 On the transient motion of ordered suspensions of liquid drops. *J. Fluid Mech.* **246**, 301-320.
- Pozrikidis, C. 1994 Effects of surface viscosity on the finite deformation of a liquid drop and the rheology of dilute emulsions in simple shearing flow. *J. Non-Newt. Fluid Mech.* **51**, 161-178.
- Pozrikidis, C. & Thoroddsen, S.T. 1991 Deformation of a liquid film flowing down an inclined plane

- wall over a small particle arrested on the wall. *Phys. Fluids A* **3**, 2546-2558.
- Proussevitch, A.A., Sahagian, D.L. & Anderson, A.T. 1993a Dynamics of diffusive bubble growth in magmas: Isothermal case. *J. Geophys. Res.* **98**, 22,283-22,307.
- Proussevitch, A.A., Sahagian, D.L. & Kutolin, V.A. 1993b Stability of foams in silicate melts. *J. Volc. Geotherm. Res.* **59**, 161-178.
- Rallison, J.M. 1981 A numerical study of the deformation and burst of a viscous drop in general shear flows. *J. Fluid Mech.* **109**, 465-482.
- Rallison, J.M. 1984 The deformation of small viscous drops and bubbles in shear flows. *Ann. Rev. Fluid Mech.* **16**, 45-66.
- Rallison, J. M. & Acrivos, A. 1978 A numerical study of the deformation and burst of a viscous drop in an extensional flow. *J. Fluid Mech.* **89**, 191-200.
- Renne, P.R. & Basu, A.R. 1991 Rapid eruption of the Siberian traps flood basalts at the Permo-Triassic boundary. *Science* **253**, 176-179.
- Richards, M.A., Duncan, R.A & Courtillot, V.E. 1989 Flood basalts and hotspot tracks: Plume heads and tails. *Science* **246**, 103-107.
- Richards, M.A., Hager, B.H. & Sleep, N.M. 1988 Dynamically supported geoid highs over hotspots: Observations and theory. *J. Geophys. Res.* **93**, 7690-7708.
- Richards, M.A., Jones, D.L., Duncan, R.A. & DePaolo, D.J. 1991 A mantle plume initiation model for the Wrangellia flood basalt and other oceanic plateaus. *Science* **254**, 263-267.
- Ripepe, M., Rossi, M. & Saccorotti, G. 1993 Image processing of explosive activity at Stromboli. *J. Volcan. Geotherm. Res.* **54** 335-351.
- Sabadini, R. & Gasperini, P. 1989 Glacial isostasy and the interplay between upper and lower mantle lateral viscosity heterogeneities. *Geophys. Res. Lett.* **16**, 429-432.
- Sabadini, R. & Giunchi, C. 1992 Plate motion and dragging of the upper mantle: Lateral variations of lithospheric thickness and their implications for intraplate deformation. *Geophys. Res. Lett.* **19**, 749-752.
- Sahagian, D.L. 1985 Bubble migration and coalescence during the solidification of basaltic lava flows. *J. Geology* **93**, 205-211.
- Sahagian D.L., Anderson, A.T. & Ward, B. 1989 Bubble coalescence in basalt flows: Comparison of a numerical model with natural examples. *Bull. Volcanology* **52**, 49-56.
- Sandwell, D.T. & Schubert, G. 1992 Flexural ridges, trenches, and outer rises around coronae on Venus. *J. Geophys. Res.* **97**, 16069-16083.
- Sano, O. & Hasimoto, H. 1978 The effect of two plane walls on the motion of a small sphere in a viscous fluid. *J. Fluid Mech.* **87**, 673-694.
- Sapir, T. & Nir, A. 1985 A hydrodynamic study of the furrowing stage during cleavage. *Physiochem. Hydrodyn.* **6**, 803-814.
- Sarda, S. & Graham, D. 1990 Mid-ocean ridge popping rocks: Implications for degassing at ridge crests. *Earth Planet. Sci. Lett.* **97**, 268-289.
- Schaber, G.G., Strom, R.G., Moore, H.J., Soderblom, L.A., Kirk, R.L., Chadwick, D.J., Dawson, D.D., Gaddis, L.R., Boyce, J.M. & Russell, J. 1992 Geology and distribution of impact craters on Venus: What are they telling us? *J. Geophys. Res.* **97**, 13257-13301.
- Schubert, G. 1992 Numerical models of mantle convection. *Annu. Rev. Fluid Mech.* **24**, 359-394.
- Schwindinger, K.R. & Anderson, A.T.. 1989 Synneusis of Kilauea Iki olivines. *Contrib. Mineral. Petrol.* **103**, 187-198.
- Sherwood, J.D. 1988 Breakup of fluid droplets in electric and magnetic fields. *J. Fluid Mech.* **188**, 133-146.
- Simons, M., Hager, B.H. & Solomon, S.C. 1994 Regional variations in the geoid/topography admittance of Venus. *Science*, *in press*.
- Sleep, N.M. 1987 An analytical model for a mantle plume fed by a boundary layer. *Geophys. J. R. astr. Soc.* **90**, 119-128.
- Sleep, N.M. 1988 Gradual entrainment of a chemical layer at the base of the mantle by an overlying convection. *Geophys. J.* **95**, 437-447.
- Sleep, N.M. 1990 Hotspots and mantle plumes: Some phenomenology. *J. Geophys. Res.* **95**, 6715-

- 6736.
- Smrekar, S.E. & Phillips, R.J. 1991 Venusian highlands: Geoid to topography ratios and their implications. *Earth Planet. Sci. Lett.* **107**, 582-597.
- Solomon, S.C., Smrekar, S.E., Bindschadler, D.L., Grimm, R.E., Kaula, W.M., McGill, G.E., Phillips, R.J., Saunders, R.S., Schubert, G., Squyres, S.W. & Stofan E.R. 1992 Venus tectonics: An overview of magellan observations. *J. Geophys. Res.* **97**, 13199-13255.
- Sparks, R.S.J. 1978 The dynamics of bubble formation in magmas: A review and analysis. *J. Volcan. Geotherm. Res.* **3**, 1-37.
- Squyres, S.W., Janes, D.M., Baer, G., Bindschadler, D.L., Schubert, G., Sharpton, V.L. & Stofan, E.R. 1992 The morphology and evolution of coronae on Venus. *J. Geophys. Res.* **87**, 13611-13634.
- Stewart, C.A. 1994 The route to chaos in thermal convection at infinite Prandtl number 2: Formation and breakup of the torus. *J. Geophys. Res.*, in press.
- Stilbeck, J.N. & Whitehead, J.A. 1978 Formation of discrete islands in linear chains. *Nature* **272**, 499-501.
- Stofan, E.R., Bindschadler, D.L., Head, J.W. & Parmentier, E.M. 1991 Corona structures on Venus: Models of origin. *J. Geophys. Res.* **96**, 20933-20946.
- Stone, H.A. 1994 Dynamics of drop deformation and breakup in viscous fluids. *Ann. Rev. Fluid Mech.* **26**, 65-102.
- Stone, H.A. & Leal, L. G. 1989a Relaxation and breakup of an initially extended drop in an otherwise quiescent fluid. *J. Fluid Mech.* **198**, 399-427.
- Stone, H.A. & Leal, L.G. 1989b The influence of initial deformation on drop breakup in subcritical time-dependent flows at low Reynolds number. *J. Fluid Mech.* **206**, 223-263.
- Stone, H.A. & Leal, L.G. 1989c A note concerning drop deformation and breakup in biaxial extensional flows at low Reynolds numbers. *J. Colloid Interface Sci.* **133**, 340-347.
- Stone, H.A. & Leal, L.G. 1990a Breakup of concentric double emulsion droplets in linear flows. *J. Fluid Mech.* **211**, 123-156.
- Stone, H.A. & Leal, L.G. 1990b The effects of surfactants on drop deformation and breakup. *J. Fluid Mech.* **220**, 161-186.
- Stoos, J.A. & Leal, L.G. 1989 Particle motion in axisymmetric stagnation flow towards an interface. *AIChE J.* **35**, 196-212.
- Stoos, J.A. & Leal, L.G. 1990 A spherical particle straddling a fluid/gas interface in an axisymmetric straining flow. *J. Fluid Mech.* **217**, 263-298.
- Su, W.-J., Woodward, R.L. & Dziewonski, A.M. 1994 Degree 12 model of shear velocity heterogeneity in the mantle. *J. Geophys. Res.* **99**, 6945-6986.
- Tackley, P.J. 1993 Effects of strongly temperature-dependent viscosity on time-dependent, three-dimensional models of mantle convection. *Geophys. Res. Lett.* **20**, 2187-2190.
- Tackley, P.J. & Stevenson, D.J. 1991 The production of small Venusian coronae by Rayleigh-Taylor instabilities in the uppermost mantle. *EOS* **72**, 287.
- Tackley, P.J., Stevens, D.J., Glatzmaier, G.A. & Schubert, G. 1993 Effects of an endothermic phase transition at 670 km depth in a spherical model of convection in the Earth's mantle. *Nature* **361**, 699-704.
- Tanzosh, J., Manga, M. & Stone, H.A. 1992 Boundary element methods for viscous free-surface flow problems: Deformation of single and multiple fluid-fluid interfaces. In *Boundary element technologies* ed. Brebbia, C.A. & M.S. Ingber, Computational Mechanics Publications and Elsevier Applied Science, Southampton, 19-39.
- Taylor, G.I. 1932 The viscosity of a fluid containing small drops of another fluid. *Proc. Roy. Soc. A* **138**, 41-48.
- Thomas, N., Tait, S. & Koyaguchi, T. 1993 Mixing of stratified liquids by the motion of gas bubbles: Application to magma mixing. *Earth Planet. Sci. Lett.* **115**, 161-175.
- Tjahjadi, M., Stone, H.A. & Ottino, J.M. 1992 Satellite and sub-satellite formation in capillary breakup. *J. Fluid Mech.* **243**, 297-317.
- Tjahjadi, M., Stone, H.A. & Ottino, J.M. 1994 Estimating interfacial tension via relaxation of drop

- shapes and filament breakup. *AIChE J.*, in press.
- Toramoru, A., 1988 Formation of propagation pattern in two-phase flow systems with application to volcanic eruptions. *Geophys. J.* **95**, 613-623.
- Toramoru, A., 1990 Measurement of bubble size distributions in vesiculated rocks with implications for quantitative estimate of eruption processes. *J. Volcan. Geotherm. Res.* **43** 71-90.
- Tran-Cong, T. & Phan-Thien, N. 1989 Stokes problems of multiparticle systems: A numerical method for arbitrary flows. *Phys. Fluids A* **1**, 453-461.
- Tushingham, A.M. & Peltier, W.R. 1991 Ice-3G: A new global model of late Pleistocene deglaciation based upon geophysical predictions of post-glacial relative sea level change. *J. Geophys. Res.* **96**, 4497-4523.
- Unverdi, S.O. & Tryggvason, G. 1992 A front-tracking method for viscous, incompressible, multi-fluid flows. *J. Comp. Phys.* **100**, 25-37.
- van Keken, P. 1993 *Numerical modelling of thermochemically driven fluid flow with non-Newtonian rheology*. PhD Thesis, University of Utrecht, Netherlands.
- van Keken, P., Yuen, D.A. & van den Berg, A. 1992 Pulsating diapiric flows: Consequences of vertical variations in mantle creep laws. *Earth Planet. Sci. Lett.* **112**, 179-194.
- van der Vorst, G.A.L. 1993 Integral methods for a two-dimensional stokes flow with shrinking holes applied to viscous sintering. *J. Fluid Mech.* **257**, 667-689.
- Vergnolle, S. & Jaupart, C. 1990 Dynamics of degassing at Kilauea Volcano, Hawaii. *J. Geophys. Res.* **95**, 2793-2809.
- Walker, G.P.L. 1987. Pipe vesicles in Hawaiian basaltic lava: Their origin and potential as paleoslope indicators. *Geology* **15**, 84-87.
- Walker, G.P.L. 1989 Spongy pahoehoe in Hawaii: A study of vesicle-distribution patterns in basalt and their significance. *Bull. Volcanology* **51**, 199-209.
- Walker, D. & Mullins Jr., O. 1981 Surface tension of natural silicate melts from 1200°–1500° and implications for melt structure. *Contrib. Mineral. Petrology* **76** 455-462.
- Weinbaum, S., Ganatos, P. & Yan, Z.-Y. 1990 Numerical multipole and boundary integral techniques in Stokes flow. *Ann. Rev. Fluid Mech.* **22**, 275-316.
- White, R. & McKenzie, D. 1989 Magmatism at rift zones: The generation of volcanic continental margins and flood basalts. *J. Geophys. Res.* **94**, 7685-7729.
- Whitehead, J.A. & Luther, D.S. 1975 Dynamics of laboratory diapir and plume models. *J. Geophys. Res.* **80**, 705-717.
- Wilson, L. & Head, J.W. 1981 Ascent and eruption of basaltic magma on the Earth and Moon. *J. Geophys. Res.* **86**, 2971-3001.
- Yang, S.M. & Leal, L.G. 1983 Particle motion in Stokes flow near a plane fluid-fluid interface. Part 1. Slender body in a quiescent fluid. *J. Fluid Mech.* **136**, 393-421.
- Yiantsios, S.G. & Davis, R. H. 1990 On the buoyancy-driven motion of a drop towards a rigid or deformable interface. *J. Fluid Mech.* **217**, 547-573.
- Yiantsios, S.G. & Davis, R. H. 1991 Close approach and deformation of two viscous drops due to gravity and van der Waals forces. *J. Colloid Int. Sci.* **144**, 412-433.
- Yiantsios, S.G. & Higgins, B.G. 1989 Rayleigh-Taylor instability in thin viscous films. *Phys. Fluids A* **1**, 1484-1500.
- Young, C.J. & Lay, T. 1990 Multiple phase analysis of the shear velocity structure in the D" region beneath Alaska. *J. Geophys. Res.* **95**, 17385-17402.
- Youngren, G.K. & Acrivos, A. 1975 Stokes flow past a particle of arbitrary shape: A numerical method of solution. *J. Fluid Mech.* **69**, 377-403.
- Youngren, G.K. & Acrivos, A. 1976 On the shape of a gas bubble in a viscous extensional flow. *J. Fluid Mech.* **76**, 433-442.
- Zandt, G. & Carrigan, C.R. 1993 Small-scale convective instability and upper mantle viscosity under California. *Science* **261**, 460-463.
- Zinemanas, D. & Nir, A. 1988 On the viscous deformation of biological cells under anisotropic surface tension. *J. Fluid Mech.* **193**, 217-241.
- Zhang, X. & Davis, R.H. 1991 The rate of collisions due to Brownian or gravitational motion of

- small drops. *J. Fluid Mech.* **230**, 479-504.
- Zhang, X., Wang, H. & Davis, R.H. 1993 Collective effects of temperature gradients and gravity on droplet coalescence. *Phys. Fluids A* **5**, 1602-1613.
- Zhou, H. & Pozrikidis, C. 1993a The flow of ordered and random suspensions of two-dimensional drops in a channel. *J. Fluid Mech.* **255**, 103-127.
- Zhou, H. & Pozrikidis, C. 1993b The flow of suspensions in channels: Single files of drops. *Phys. Fluids*. **5**, 311-324
- Zhou, H. & Pozrikidis, C. 1994 Pressure-driven flow of suspensions of liquid drops. *Phys. Fluids*. **6**, 80-94.
- Zinchenko, A.Z. 1982 Calculations of the effectiveness of gravitational coagulation of drops with allowance for internal circulation. *Prikl. Mat. Mech.* **46**, 58-65.